Analysis of Nano indentation Size effect based on Dislocation Dynamics and Crystal Plasticity

H.J. Chang

▶ To cite this version:

HAL Id: tel-00526500
https://theses.hal.science/tel-00526500

Submitted on 15 Oct 2010

INSTITUT POLYTECHNIQUE DE GRENOBLE

N° attribué par la bibliothèque
|__|__|__|__|__|__|__|__|__|__|

THESE EN COTUTELLE INTERNATIONALE

pour obtenir le grade de

DOCTEUR DE L'Institut polytechnique de Grenoble
et
de Seoul National University

Spécialité : 2MGE : Matériaux, Mécanique, Génie civil, Electrochimie

préparée au laboratoire Science et Ingénierie des Matériaux et des Procédés (SIMaP)
Groupe Génie Physique et Mécanique des Matériaux (GPM2)
dans le cadre de l'Ecole Doctorale I-MEP2
et au laboratoire Material Deformation and Processing (LMDP)
dans la Seoul National Université

présentée et soutenue publiquement

par

Hyung-Jun CHANG

le 15 Juin 2009

TITRE :

Analysis of Nano indentation Size effect based on

Dislocation Dynamics and Crystal Plasticity

Sous la direction de :
Marc FIVEL, Laurent TABOUROT et Marc VERDIER

JURY

M. Yves BRECHET	, Président
M. Samuel FOREST	, Rapporteur
M. Heung Nan HAN	, Rapporteur
M. Kyu Hwan OH	, Examinateur
M. Marc FIVEL	, Directeur de thèse
M. Laurent TABOUROT	, Co-Directeur de thèse
M. Marc VERDIER	, Co-Directeur de thèse

Abstract

This thesis deals with experiments and simulations of nanoindentation in copper single crystals. Indentation experiments are performed with different orientations of the indentation axis and both the load-displacement curve and the surface imprint observed by atomic force microscopy are analysed and compared. Indentation size effect is observed for low penetration of the indenter. Simulations are then performed using crystal plasticity finite element modelling. ABAQUS user subroutines are specially developed in order to account for the physics of dislocation activity in the twelve glide systems of copper crystals. 3D simulations are then performed and comparisons with the experiments give access to key parameters of the constitutive equations. The indentation size effect is reproduced using a simplified size effect theory implanted in the finite element modelling. Finally, a multiscale approach based on discrete dislocation dynamics is used to reproduce (111) indentations of copper single crystals. Molecular dynamics simulations give details of dislocation nucleation beneath the indenter. Dislocation dynamics simulations are then performed and the indentation size effect is addressed.

Keywords: Nanoindentation, Crystal plasticity, Finite element method (FEM), Dislocation dynamics (DD), Molecular dynamics (MD), Indentation size effect, Multi-scale simulation, ABAQUS, TRIDIS, CASTEM

Table of Contents

5

Notations

$\mathbf{A}$ Surface created by the closed dislocation loop

A_j Component of the surface A

A_{projC} Projected contact area during or after nanoindentation

A_{realC} Real contact area during or after nanoindentation

$A_{r,sphere}$ Real surface area of a sphere shape of tip front

$A_{p,sphere}$ Projected area of a sphere shape of tip front

$\mathbf{a^{sp}}$ Matrix for dislocation generation

B^p Phonon drag coefficient

$\mathbf{b}$ Burgers vector

b Norm of the Burgers vector

b_i Component of Burgers vector

C Constrained factor between hardness and yield strerss

C^*_{eq} Equivalent indentation compliance

$C^*_{indenter}$ Indentation compliance of indenter

C^*_{sample} Indentation compliance of sample

$C^*_{experiment}$ Indentation compliance from experiment

$C^*_{simulation}$ Indentation compliance from simulation

$\mathbf{C^C}$ 4th order elastic modules tensor for the relationship between stress and strain measure from Cosserat theory

$\mathbf{C^D}$ 4th order elastic modules tensor for the relationships between curvature and coupled stress from Cosserat theory

$\mathbf{C^E}$ 4th order elastic stiffness matrix

C^ρ Closed dislocation loop

$\mathbf{D}$ Deformation rate tensor

$\mathbf{D^E}$ Elastic deformation rate tensor

$\mathbf{D^P}$ Plastic deformation rate tensor

D_n Normal gradient operators acting on a surface with normal vector n

D_t Tangent gradient operators acting on a surface

D^i Intrinsic dissipation

$D^h(x)$ Homogeneous function of degree 6

d_{max}	Distance form surface center to the maximum stress position
$\mathbf{E}^{*}$	Almansi-Hemel strain tensor
E	Elastic modulus
$E_{indenter}$	Elastic modulus of indenter material
E_{sample}	Elastic modulus of sample
$E_{sapphire}$	Elastic modulus of sapphire
$\mathbf{F}$	Deformation gradient tensor
$\mathbf{F^{E}}$	Elastic deformation gradient tensor
$\mathbf{F^{p}}$	Plastic deformation gradient tensor
$\mathbf{F^{f}}$	Point force vector
F^{f}_{m}	Component of the point force
F_{iter}	Function for Newtonian iteration
f^{sg}	Dissipation potential from strain gradient theory
f_{1}^{c}	Dissipation potential from stress measure at Cosserat theory
f_{2}^{c}	Dissipation potential from coupled stress measure at Cosserat theory
f_{lmk}	Function defined by Willis
g_{lmk}	Function defined by Willis
H	Indentation hardness
H_{0}	Indentation hardness in the absence of any size effect
$\mathbf{h^{sp}}$	Matrix of hardening parameter
$\mathbf{h^{p}}$	Matrix of hardening parameters for latent hardening
h_{0}, s_{s}, a	Hardening parameters from Anand's hardening theorem
h_{0}, n, τ_{0}	Hardening parameters from Asaro and Needelman's hardening theorem
I	Second order identity tensor
k	Boltsman constant
K_{g}	Parameter for dislocation generation
$\mathbf{L}$	Velocity gradient tensor
$\mathbf{L^{E}}$	Elastic velocity gradient tensor
$\mathbf{L^{p}}$	Plastic velocity gradient tensor

$\mathbf{L_0^p}$	Plastic velocity gradient tensor measured by intermediate state
$L^{wil}(\zeta)$	Function for deriving Green function proposed by Willis
L^{cyl}	Contour for the condition given by Willis
L_g	Length scale about global length from theory we proposed
L_{loop}	Length of generated prismatic loop
l	Length between two junction points
l_e	Intrinsic length scale from strain gradient theory
l_g	Length scale about local length from theory we proposed
l_p^{sg}	Characteristic length from strain gradient theory
l_{pc}	Characteristic length from Cosserat theory
l^d	Length of dislocation segment
$\boldsymbol{M}$	Couple stress tensor from Cosserat theory
$\boldsymbol{M^{sg}}$	Couple stress tensor from strain gradient theory
M_{eq}^*	Equivalent indentation modulus
M_{ind}^*	Indentation modulus of indenter
M_{sample}^*	Indentation modulus of sample
$M_{experiment}^*$	Indentation modulus from experiment
$M_{simulation}^*$	Indentation modulus from simulation
$\mathbf{m_{sg}^{sur}}$	Double force vectors on the surface from strain gradient theory
$\mathbf{m^{sur}}$	Couple vectors acting on a surface element from Cosserat theory
$\boldsymbol{m^s}$	Slip direction vector of the sth slip system for a current state of a material
$\boldsymbol{m_0^s}$	Slip direction vector of the sth slip system for an initial state of a material
m^{sg}	Resolved hyper stresses
m^τ	Resolved shear strain from coupled stress at Cosserat theory
m^r	Parameter for rate sensitivity
$N_{mk}(\zeta)$	Homogeneous function of degree 4 in ζ
$\mathbf{n^{sur}}$	Surface normal vector
$\boldsymbol{n}$	Slip plane normal vector
$\boldsymbol{n^s}$	Slip plane normal vector of the sth slip system for a current state of a material
$\boldsymbol{n_0^s}$	Slip plane normal vector of the sth slip system for an initial state of a material
n^{wil}	Parameter for transforming the integral by Willis
$\mathbf{O_{33}}$	3 x 3 matrix fully populated by ones

$P_{criterion}$ Load criterion from nucleation criterion at the given indentation depth

P_{ind} Applied load for given indentation depth

p   Position vector for the material state after plastic deformation

p^{wil} Perpendicular distance from x to the dislocation line

p^{i} Power densities of internal

p^{c} Contact forces

p^{m} Internal material property which affects to local deformation

$\mathbf{q^{sp}}$ Coefficients for self hardening

q   Ratio between the latent hardening and self hardening

R   Distance vector between **r** and **r'**

R   Norm of the vector **R**

R_{cont} Contact radius at the giving indentation depth during nanoindentation

R_{ind} Radius of the sphere indenter

r   Evaluation position vector

r'   Position vector for a dislocation line

S   Indentation stiffness

S^{sur} Arbitrary surface

S^{cyl} Element of area on the cylinder

$\mathbf{T}^{*}$ Second Piola-Kirchhoff stress tensor

T   Temperature

$\mathbf{t^{sur}}$ Traction vectors acting on a surface element

t^{d} Dislocation line vector

u   Displacement vector

u_{m} Components of the displacement vector

$\boldsymbol{u_{mk}}$ Green's function tensor for the elastic displacement

v   Velocity of a dislocation segment

W   Interaction energy

$\boldsymbol{X}$	Position vector of final material state
x_3	Surface displacement through indentation direction
$\boldsymbol{x}$	Position vector of initial material state
$\boldsymbol{x'}$	Coordinate for the point lay on dislocation loop
x^E	End point of arbitrary dislocation segment
x^S	Start point of arbitrary dislocation segment
x_{ind}	Indentation depth
x^*_{ind}	Length that characterizes the depth dependence of the indentation hardness
x^{eq}_{ind}	Total indentation depth
$x^{indenter}_{ind}$	Indentation depth of indenter
x^{sample}_{ind}	Indentation depth of sample
y_c	Minimum dislocation dipole length
Z	Plain defined by Willis
$\boldsymbol{\alpha_{nye}}$	Nye tensor
α	Constant for line tension
$\boldsymbol{\alpha^{sp}}$	Junction strength matrix
ΔG_0	Gibbs free energy
ΔV^*	Volume change
δ_{ij}	Kronecker delta function
ε	Infinitesimal strain tensor (represent global strain)
ε^e	Elastic infinitesimal strain tensor
ε^p	Plastic infinitesimal strain tensor
ε_c	Strain measure defined at Cosserat theory
ε_c^e	Elastic strain measure defined at Cosserat theory
ε_c^p	Plastic strain measure defined at Cosserat theory
$\boldsymbol{\varepsilon_{p,global}}$	Global averaged strain from theory we proposed
$\boldsymbol{\varepsilon_{p,local}}$	Local strain from theory we proposed
$\boldsymbol{\varepsilon_{ijk}}$	Third order permutation tensor
$\boldsymbol{\varepsilon^{con}}$	Convergence factor
$\boldsymbol{\varepsilon^{ext}}$	Deformation field represents the material deformation
ε^{int}	Local deformation at slip system

ϕ	Micro rotation
ϕ_f	Arbitrary function
γ^S	Resolved slip gradient variable
γ^s	Resolved shear strain of the sth slip system
γ^s_0	Initial resolved shear strain rate of the sth slip system
η^p	Plastic strain gradient
η	Strain gradient
η^e	Elastic strain gradient
η^ζ	Normalized element ζ in Fourier space
κ	Second rank tensor for curvature
κ^e	Elastic second rank tensor for curvature
κ^p	Plastic second rank tensor for curvature
λ^{sg}	Plastic multiplier from strain gradient theory
λ_1^c	Plastic multiplier for plastic strain measure from Cosserat theory
λ_2^c	Plastic multiplier for plastic curvature measure from Cosserat theory
λ	Lame constant
μ^s	s^{th} slip system tensor in a material for a current state of a material
μ^s_0	s^{th} slip system tensor for an initial state of a material
μ^{nx}	x directional vector components of the nth slip system tensor (n=1,2…)
μ	Shear modulus
ν	Poisson ratio
$\nu_{indenter}$	Poisson ratio of indenter material
ν_{sample}	Poisson ratio of sample
$\nu_{sapphire}$	Poisson ratio of sapphire
ν^s	Average velocity of the mobile dislocations of the sth slip system
ν_D	Frequency of dislocation passed to obstacles
θ_n	Angle criteria for obtaining contact surface defined
θ	Resolved curvature from Cosserat theory
θ^{wil}	Angle variable by Willis

ρ^{sg}	Coefficient for the relationships at the state low from strain gradient theory
$\rho^{Cosserat}$	Coefficient for the relationships at the state low from Cosserat theory
ρ_g	Geometrically necessary dislocations
ρ_s	Statistically stored dislocations
$\rho_m{}^s$	Density of mobile dislocations
ρ^p	Dislocation density of the pth slip system
ρ^ζ	Norm of the element ζ in Fourier space
$\rho^{\zeta N}$	Norm of the element ζ in Fourier space defined by Willis
$\boldsymbol{\sigma_{extra}}$	Extra stress from theory we proposed
$\boldsymbol{\sigma_c}$	Stress tensors at Cosserat theory
$\boldsymbol{\sigma}$	Cauchy stress tensor (represent global strerss)
$\boldsymbol{\sigma^{app}}$	Applied stress tensor as a boundary condition of DD simulation
$\boldsymbol{\sigma^{int}}$	Internal stress tensor due to dislocation loops
$\boldsymbol{\sigma^{ext}}$	All of the external information obtained by the external boundary conditions
$\sigma^{int}{}_y$	Internal yield stress against local deformation
σ_y	Yield stress
τ^s	Resolved shear strain of the sth slip system
$\tau^s{}_\mu$	Critical resolved shear stress
τ^{*s}	Short range stress field from obstacles or forest dislocations
τ^{pk}	Peach Koehler Forces at a dislocation segment
τ^{lt}	Line tension force at a dislocation segment
τ^{net}	Net force after reducing by lattice friction
$\tau^{peierls}$	Force due to the lattice friction
$\tau_{criterion}$	Resolved shear stress criterion
τ_{max}	Maximum resolved shear stress at the maximum stress position
$\boldsymbol{\Omega}$	Rigid body rotation rate tensor
$\boldsymbol{\Omega^E}$	Elastic rigid body rotation rate tensor
$\boldsymbol{\Omega^P}$	Plastic rigid body rotation rate tensor
Ω	Solid angle
ω	Element on the unit sphere $|\eta^\zeta|=1$
ξ	Vector normal to both slip the slip direction vector and the slip plane normal vector

ψ	Tip angle of cone shape indenter between tip axis and tip surface
Ψ	Free energy density
ζ	Position vector at Fourier space
ζ^{N}	Position vector at Fourier space by Willis

I. Introduction

<u>Indentation experiments and related sized effect</u>

Indentation has recently become a widely used method to measure mechanical properties of metals and ceramics. Recent advances in indentation technique have led to the development of very low load with depth sensing indentation also called *nanoindentation*. This nondestructive examination allows estimating local material properties using a measurement of the penetration depth into extremely small regions of material. Therefore, it is now widely used for probing local material properties of bulk solids or welding joints but also to test confined materials such as multiphase materials, thin films, or when the volume of materials is limited like for irradiated samples.

The usual objective of nanoindentation test is to find out the hardness of the probed material. This is defined by the ratio of the indentation force and the current contact area during load. Note that this is different from the conventional hardness measurements (Vickers, Brinell and Rockwell) where the contact area is measured on the imprint left after the indenter removal. For elastic solids for example, this difference implies that a Vickers hardness is infinite (residual contact area being null) whereas there is a finite value for nanoindentation measures. Although the force can be measured directly (see figure I-1(a) for example), it is not the case for the contact area which has to be estimated. This is classically done using Oliver-Pharr method [OP92], but the accuracy depends on the mechanical properties of the tested material. An alternative way consists of measuring the contact area by atomic force microscopy (AFM) which gives access to the actual surface shape after indentation.
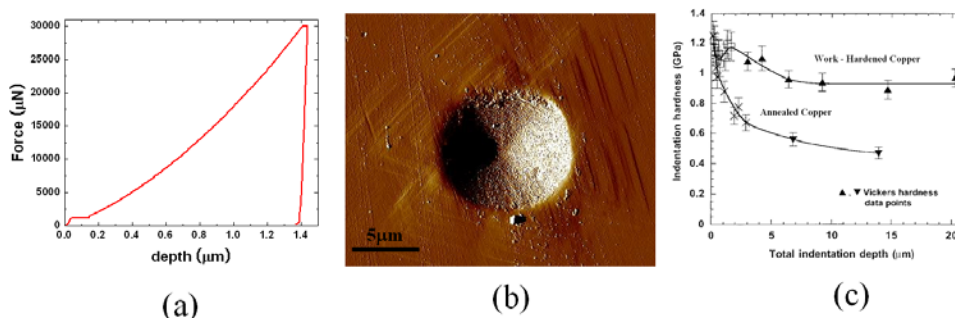

Figure I-1 (a) Typical load displacement curve during nanoindentation,
(b) Residual imprint of (111) copper surface after a 1400nm indentation.
(c) Typical indentation size effect of copper single crystal

Figure I-1(b) shows the residual imprint left on a (111) surface of copper single crystal after a conical indentation at a depth 1400nm. Such a picture can then be exploited in order to measure the contact area between the indenter and the surface at the maximum load.

Even when most attention is paid to the measurement of the contact area, it is found that the value of the hardness depends on the indentation depth: hardness increases when the depth is decreased. In copper single crystals for example, this so called *Indentation Size Effect* (ISE) is observed for a large range of penetration depths as shown in figure I-1(c). As a conclusion, the hardness of a given sample is not a constant value and should always refer to tip geometry and penetration depth (or load). Consequently, the modeling of indentation requires constitutive equations that account for the physics at the origin of the plasticity of the materials. In the case of copper crystals, this can be done in the frame of continuum mechanics using crystal plasticity modeling where the discrete character of plastic slip is taken into account through the definition of the crystal slip systems.

Finite element modeling of indentation using crystal plasticity (CPFEM)

Crystal plasticity (CP) is a general framework of deformation theory based on continuum mechanics devoted to modeling the mechanical behavior of crystalline materials. Such modeling is based on two main ingredients: (i) a theoretical framework designed to describe the kinematics of the deformation, and (ii) a set of constitutive equations needed to reproduce the physics of the plastic deformation. For crystalline materials, plasticity is mainly developed by the motion of dislocation lines on crystallographic planes. In the case of FCC crystals, there are twelve {111} slip systems. Thus, the local deformation is by nature discrete (see slip lines in figure I-1 (b)) and the collective motion of the dislocations line may introduce plastic anisotropy that homogeneous description of plasticity could not reproduce. Figure I-2 shows a typical result obtained by crystal plasticity in the case of a polycrystalline aggregate deformed by tension. The colors indicate the plastic strain accumulated in the different finite elements.

In such modeling, the constitutive equations consist of analytical expressions relating the plastic strain rate to the applied stress state. This is usually defined through a flow law involving a yield stress. This law should be complemented by a hardening equation which gives the evolution of the yield stress with the plastic deformation. Some theories introduce internal variables whose role is to reflect the physics. One possibility is to introduce the dislocation densities on the different slip systems. This requires adding a third equation which specifies the evolution of the dislocation densities with the plastic deformation. Although these efforts spent to fit to reality, these models are scale independent and thus, they cannot reproduce size effects. One need to modify these equations in order to introduce an intrinsic length like in theories of generalized continuum mechanics.
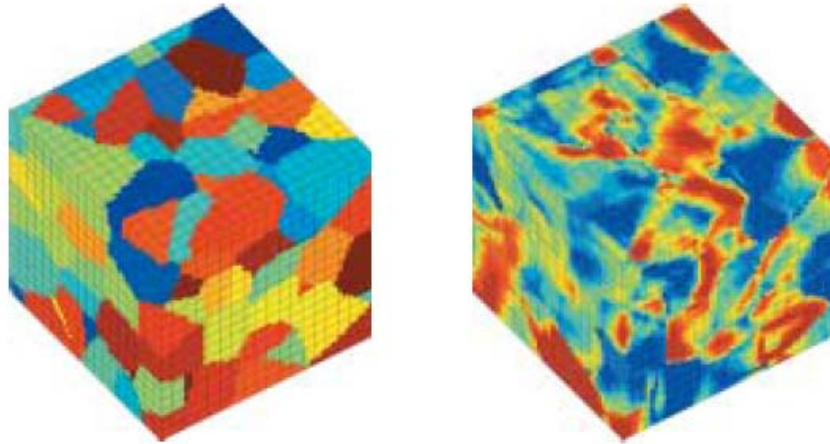
Figure I-2 Example of application of CPFEM in the case of Zinc polycrystal aggregates loaded in tension. Second figure shows plastic deformation on basal slip systems [FF04].

Generalized continuum mechanics of materials

The terminology of generalized continuum mechanics includes different extensions of the classical theory of continuum mechanics. On one hand there is the higher level medium for which additional degrees of freedom are introduced in the formalism but only first order gradients are used like in the classical theory. Micromorphic medium where a local micro-strain tensor is introduced is an example of higher level medium. Cosserat theory which introduces couple stresses as local variables is also a part of these media. On the other hand, there are the higher order media which use second or above gradients of the displacement field in their description. Examples of these theories are the second order theory which accounts for the gradient of the strain and all the media of gradient of internal variables.

Although different in their descriptions, these theories have a common advantage which other classical continuum mechanics don't have: they can reproduce size effects. Figure I-3 shows the lattice rotations computed in γ/γ' single crystals within the frame of classical plasticity and the same quantity computed from Cosserat modeling.

Despite this better description of material behavior, generalized media are still a field of research and not widely used in the industry. The main reason is certainly the computing time which dramatically increases with the model complexity (number of degrees of freedom, high order non-linearities, and so on).

Finally, these models are still continuum descriptions whereas the plastic behavior of crystalline materials is discrete. Only discrete models where the dislocation lines are individually simulated can reproduce this feature.
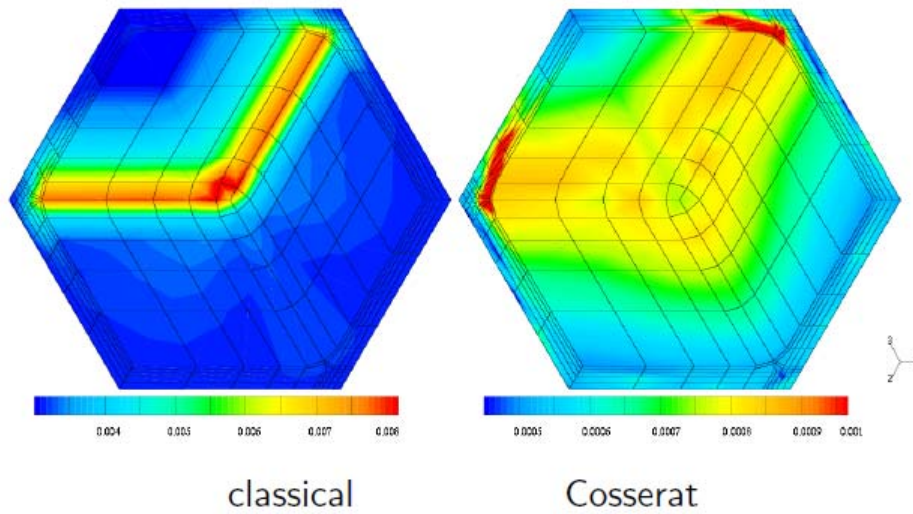
Figure I-3 Comparison of lattice rotations computed in classical continuum mechanics and using Cosserat modeling [For07].

Dislocation dynamics modeling (DD)

The concept of 3D dislocation dynamics method has been imagined in the early 1990s. In such modeling, the dislocation lines are discretized in sets of segments embedded in a continuum medium. Each of the segments can then move in the simulation box according to local rules describing the local reactions that may occur during the flight (phonon drag, junctions, cross-slip, and so on). The DD approach can be used to analyze plasticity in confined volumes. Because of computation constraints, the amount of cumulated plasticity is limited to a few percents.   Consequently, these models generally focus the understanding of the initial stage of plasticity as shown for example in figure I-4 in the case of low amplitude fatigue simulations.
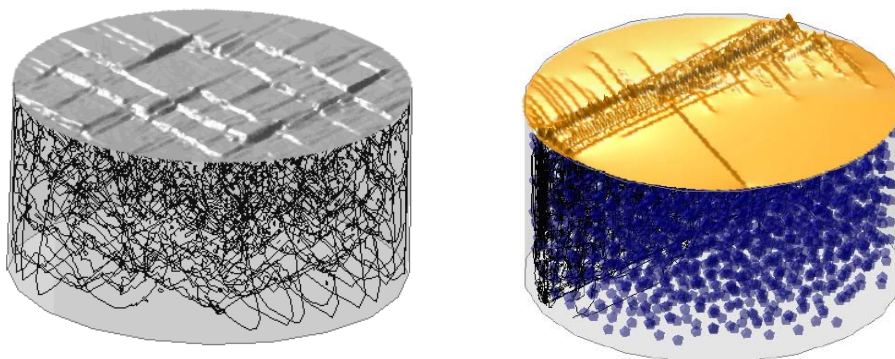
Figure I-4 Typical DD simulation of the fatigue behavior of 316L stainless steels [Dép04] and precipitate hardened material [Shi04].

17

The figure also shows that this description gives access to the discrete character of plastic strain: slip lines are printed in the surface when dislocations shear the crystal. The model can reproduce size effects since it makes use of an internal length which is the Burgers vector of the dislocation lines that is to say the elemental carrier of crystal plasticity.

<u>Outline of the thesis</u>

In this thesis, nanoindentation experiments of copper single crystals are analysed and compared to numerical analysis. The numerical investigation is performed using different models: classical finite element crystal plasticity, strain gradient model, and dislocation dynamics.

Firstly, the state of the art in the different modeling used in this thesis is introduced in chapter II.

- Section II-1 concerns crystal plasticity modeling. The general framework of continuum mechanics is recalled and dislocation based constitutive equations are introduced. The model is then implanted in UMAT and VUMAT subroutines supported in ABAQUS package and validation of the code is performed in the case of a simple tensile test of copper single crystal.

- Non-local theories are presented in section II-2. After a brief recall of Cosserat and second gradient theories, a simplified strain gradient theory is proposed. The model is integrated by FEM and applied to reproduce size effect both in case of tensile and shear deformation.

- Section II-3 described the basic ingredients of discrete dislocation dynamics modeling. The code TRIDIS is modified and extended to treat anisotropic media.

The case of nanoindentation is treated in chapter III.

- Section III-1 presents the analysis methods we have developed to measure the actual contact area in the simulations. It also describes several correction methods needed to compare simulation results with experiments.

- Section III-2 shows results of indentation experiments performed with different orientations of the indentation axis. Both the load-displacement curve and the surface imprint observed by atomic force microscopy are analysed and compared.

- Numerical analysis is then performed using crystal plasticity finite element modelling in section III-3.

- The numerical results are quantitatively compared to the experiments in section III-4, which gives access to key parameters of the constitutive equations of the dislocation density based crystal plasticity model.

- In section III-5, the indentation size effect is reproduced using the simplified strain gradient theory proposed in section II-2.

- Finally, dislocation dynamics simulations of indentation are presented in section III-6. A

nucleation criterion is proposed from atomic considerations. The nanoindentation loading is applied using a coupling with finite element modelling (code CAST3M) and results are given in the case of a (111) spherical indentation.

II. State of the art of crystal plasticity modeling

1. Crystal plasticity theories

Crystal plasticity theory is a deformation theory based on continuum mechanics developed for understanding the mechanical behavior of crystalline materials. Most of the crystal plasticity theories were developed during the early 20th century, from 1900 to 1938 [ER00, BB33, TE23, TE25, Tay34, Pol22 and Sch24]. For most of the loading conditions, plastic deformation is mainly due to the movement of dislocations. Dislocations are line defects of the crystals that carry the plastic deformation through a slip vector: the Burgers vector. Dislocation lines lie and move on specific planes imposed by the crystal lattice. The combination of one specific planes and one specific Burgers vector defines a slip system. As an example, there are 12 slip systems in FCC crystals as shown in table II-1-1.

01(C1)	02(C3)	03(C5)	04(A2)	05(A3)	06(A6)
(1 1 -1)	(1 1 -1)	(1 1 -1)	(1 -1 -1)	(1 -1 -1)	(1 -1 -1)
[0 1 1]	[1 0 1]	[1 -1 0]	[0 1 -1]	[1 0 1]	[1 1 0]
07(D1)	08(D4)	09(D6)	10(B2)	11(B4)	12(B5)
(1 -1 1)	(1 -1 1)	(1 -1 1)	(1 1 1)	(1 1 1)	(1 1 1)
[0 1 1]	[1 0 -1]	[1 1 0]	[0 1 -1]	[1 0 -1]	[1 -1 0]

Table II-1-1. The slip systems for a FCC crystal

A slip system can then be defined by the Schmid matrix $\boldsymbol{\mu^s}$ expressed as the tensor product of the slip vector $\mathbf{m^s}$ and the normal to the slip plane $\mathbf{n^s}$:

$$\boldsymbol{\mu^s} = \mathbf{m^s} \otimes \mathbf{n^s} \tag{II-1-1}$$

When dislocations move on the slip systems, they contribute to the global plastic deformation. In practice, crystal plasticity theory is a mathematical description of empirical or physical rules relating the local behavior of the dislocations and the global deformation of the volume.

In crystal plasticity models, generally, the deformation and stress field ($\boldsymbol{\varepsilon^{ext}}$, $\boldsymbol{\sigma^{ext}}$) are discretized as functions of local deformation and stress field (ε^{int}, σ^{int}_y) for each slip systems (s).

$$\left(\boldsymbol{\sigma^{ext}}, \boldsymbol{\varepsilon^{ext}}\right) = \sum_s f\left(\sigma^{int,s}_y, \varepsilon^{int,s}\right) \tag{II-1-2}$$

The local deformation (ε^{int}) is given by the *flow law*:

$$\varepsilon^{int} = f\left(\boldsymbol{\sigma^{ext}}, \sigma^{int}_y, p^m\right) \tag{II-1-3}$$

where $\boldsymbol{\sigma^{ext}}$, σ^{int} and p^m represent external information due to a boundary conditions, local yield

against given local deformation and internal variables which affect the local deformation. The local yield stress (σ^{int}_y) is obtained from another local rule: the *hardening law*:

$$\sigma^{int}_y = f\left(\mathbf{\sigma}^{\mathbf{ext}}, \varepsilon^{int}, p^m\right) \tag{II-1-4}$$

Normally, the effect of p^m is ignored for simplicity. However, some attempts have tried to link the physical properties of the material (p^m) to the constitutive equations in order to give back the anisotropic behavior [TH98]. In these approaches, the physical property is obtained from another local rule: the *evolution law*.

$$p^m = f\left(\mathbf{\sigma}^{\mathbf{ext}}, \varepsilon^{int}, \sigma^{int}_y\right) \tag{II-1-5}$$

Following the first development of mathematical crystal plasticity model proposed by Taylor [Tay38], many authors have developed and proposed different crystal plasticity models [Hil66, HR72, AR77, HR82, Asa, TF97, PAN83, BW91, CO92, MC91, Wen87 and Oha87]. In these models, an attention has been paid to the description of the visco-plastic deformation of crystalline metals using phenomenological laws [Hil62]. More recently, Tabourot *et al.* have proposed a complete crystal plasticity model based on dislocation dynamics theories [TF97].

In this section, details of crystal plasticity models based on empirical rules are introduced. Then, the rules are linked to the physical theory based on dislocation dynamics. Finally the dislocation based model is implanted in FEM routines and tested in several simple loading conditions.

1.1 Crystal plasticity theory based on empirical rules

Global deformation and local deformation

The global deformation of a single crystal material is related to the plastic deformation cumulated on the different slip systems. Figure II-1-1 depicts a schematic description of two slip systems with the related global deformation. In this figure, μ^{1x} and μ^{2x} are x directional vector components of the 1st and 2nd slip system tensor which is defined by direction cosine value between each slip systems and global x direction, respectively. Local deformations of 1st or 2nd slip system are represented by shear strains (γ^1 and γ^2) and shear stresses (τ^1 and τ^2) resolved on each slip systems and the global macroscopic quantities are represented by the global strain (ε) and stress (σ).

Although the global deformation is produced by the local deformations accumulated on each slip systems, not all the slip systems are required to accommodate the global deformation. Mathematically, the slip system with the highest Schmid factor will multiply the first. If two or more slip systems have the same highest value of Schmid factor, they are activated

simultaneously.
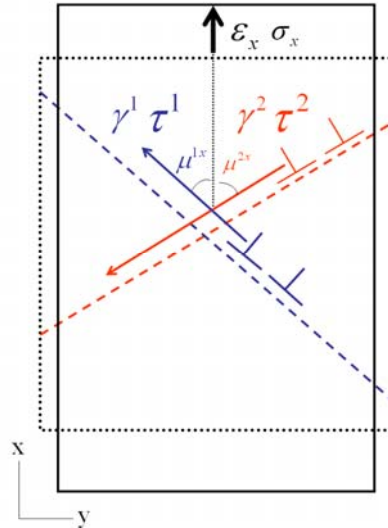
Figure II-1-1. Schematic description of two interacting slip systems loaded in tension.

Figure II-1-2 depicts the slip systems activated in the case of uniaxial tensile deformation for FCC materials. In this stereographic projection, if the loading direction falls within a triangular domain, the slip system indicated in figure II-1-2 will feel the highest Schmid factor (see table II-1-1 for slip system description).

If the projection falls on the lines delimitating two adjacent triangles in figure II-1-2, both slip systems beside the line are simultaneously activated. Similarly, if it lays on the line intersections, all the slip systems surrounding the intersection point are activated simultaneously. As an example there are respectively 4, 6 and 8 slip systems activated simultaneously when the tensile direction is aligned with directions (110), (111) and (001) whereas only B4 slip system is activated when the direction is inside the domain delimitated by the projections of [0 0 1], [0 1 1] and [-1 1 1].
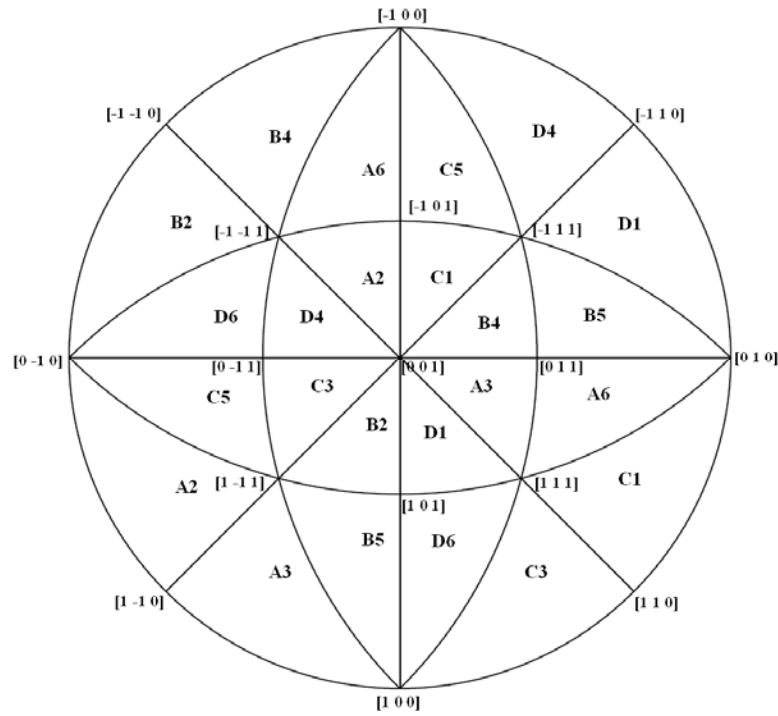
Figure II-1-2. Stereographic projection of the slip systems activated in tension for different orientations of the tensile direction

Mathematical description of crystal plasticity

Let define the deformation gradient (**F**) as:

$$d\mathbf{x} = \mathbf{F} \cdot d\mathbf{X} \tag{II-1-6}$$

where d**X** and d**x** are position vectors of initial and final state respectively.

As shown in figure II-1-3, the final state of deformation is obtained by a composition of plastic and elastic strains. The plastic strain is the irreversible part of the deformation due to the movement of dislocations and the elastic deformation is the remaining material deformation including the rigid rotation of the material. Hence, the deformation gradient (**F**) can be decomposed into the elastic deformation gradient (**F**$^{\mathbf{E}}$) and the plastic deformation gradient (**F**$^{\mathbf{p}}$) [Asa].

$$\mathbf{F} = \mathbf{F}^{\mathbf{E}} \cdot \mathbf{F}^{\mathbf{p}} \tag{II-1-7}$$

23
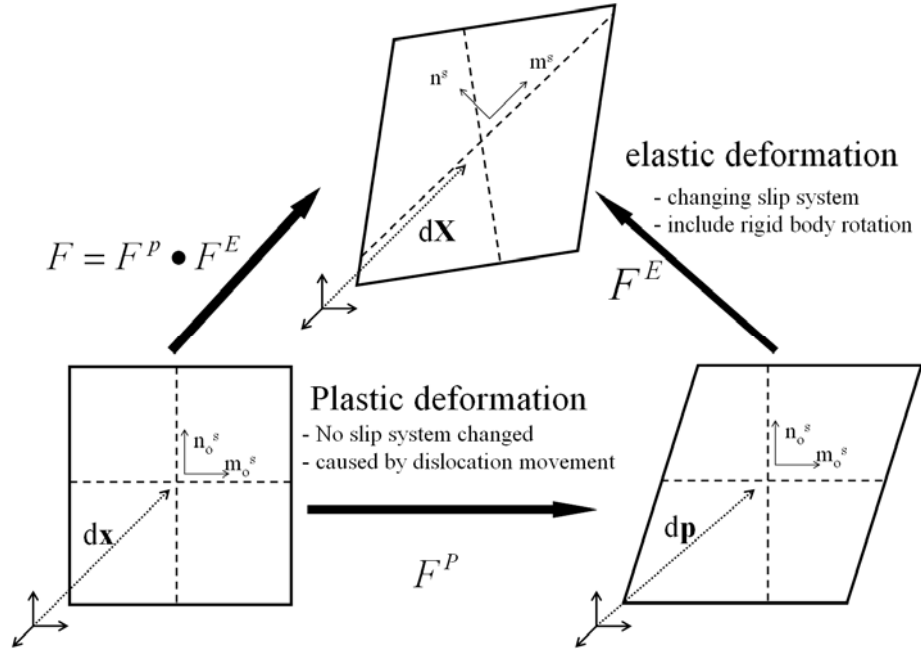
Figure II-1-3. Schematic description of the transformation decomposition into elastic and plastic deformations

Then the plastic deformation gradient ($\mathbf{F^p}$) transforms a vector d$\mathbf{X}$ into a deformed state d$\mathbf{p}$ as

$$d\mathbf{p} = \mathbf{F^p} \cdot d\mathbf{X} \tag{II-1-8}$$

The plastic deformation gradient ($\mathbf{F^p}$) can be expressed from the local plastic strain (γ^s) cumulated on each slip systems as:

$$\mathbf{F^p} = \sum_s \mathbf{F^{ps}} = \sum_s \left(\mathbf{I} + \gamma^s \mathbf{\mu_0^s} \right) \tag{II-1-9}$$

where $\mathbf{I}$, $\mathbf{\mu_0^s}$ are second order identity tensor and tensor matrix of sth slip system at the initial state, respectively.

Similarly, the elastic deformation gradient ($\mathbf{F^E}$) can be defined by following equation.

$$d\mathbf{x} = \mathbf{F^E} \cdot d\mathbf{p} \tag{II-1-10}$$

This elastic deformation gradient represents not only all the elastic deformation but also the rigid body rotation of the crystal lattices (note that the crystal lattice is not modified by the plastic deformation).

Since, both slip plane and slip direction are changed after the elastic deformation, their orientations at the current state are expressed as a function of the elastic deformation gradient.

$$\mathbf{m^s} = \mathbf{F^E} \cdot \mathbf{m_0^s} \tag{II-1-11}$$

$$\mathbf{n^s} = \mathbf{n_0^s} \cdot \mathbf{F^{E-1}} \tag{II-1-12}$$

where $\mathbf{m}^s_0$ and $\mathbf{n}^s_0$ are the slip direction and slip plane of system s at the initial state respectively. The previous relationships are illustrated in figure II-1-3. The bottom left picture represents the initial state of a single crystal material. Horizontal and vertical dashed lines depict the crystal lattice orientations of the materials represented by the slip direction ($\mathbf{m}^s$) and the normal to the slip plane ($\mathbf{n}^s$). The bottom right picture depicts the intermediate state of the single crystal obtained after plastic deformation: the material shape is changed but the dotted lines are not modified. The top picture depicts the current state of the single crystal after both elastic and plastic deformations: both material shape and dashed lines are changed.

The velocity gradient parameter ($\mathbf{L}$) is also needed the crystal plasticity theory. It is expressed by

$$\mathbf{L} = \dot{\mathbf{F}} \cdot \mathbf{F}^{-1} = \dot{\mathbf{F}}^E \cdot \mathbf{F}^{E-1} + \mathbf{F}^E \cdot \dot{\mathbf{F}}^p \cdot \mathbf{F}^{p-1} \cdot \mathbf{F}^{E-1} = \mathbf{D} + \mathbf{\Omega} \qquad \text{(II-1-13)}$$

where the velocity gradient ($\mathbf{L}$) is divided into the deformation rate ($\mathbf{D}$) and the rigid body rotation rate ($\mathbf{\Omega}$). The deformation rate ($\mathbf{D}$) is defined by the symmetry part of the velocity gradient ($\mathbf{L}$) and the rigid body rotation rate ($\mathbf{\Omega}$) is defined by skew symmetry part of the velocity gradient ($\mathbf{L}$).

$$\mathbf{D} = \frac{1}{2}\left(\mathbf{L} + \mathbf{L}^T\right) \quad , \quad \mathbf{\Omega} = \frac{1}{2}\left(\mathbf{L} - \mathbf{L}^T\right) \qquad \text{(II-1-14)}$$

Both the deformation rate and rigid body rotation rate are decomposed into two parts as done for the deformation gradient.

$$\mathbf{D} = \mathbf{D}^E + \mathbf{D}^p \quad , \quad \mathbf{\Omega} = \mathbf{\Omega}^E + \mathbf{\Omega}^p \qquad \text{(II-1-15)}$$

The dislocation movements induce a plastic strain rate which is represented by the plastic deformation rate ($\mathbf{D}^p$) and the plastic spin ($\mathbf{\Omega}^p$). The other deformation of the material is called elastic deformation and it is expressed by elastic deformation rate ($\mathbf{D}^E$) and elastic spin ($\mathbf{\Omega}^E$).

Using equation (II-1-13) and (II-1-15), new relationships among plastic and elastic parts of all the $\mathbf{L}$, $\mathbf{D}$, $\mathbf{\Omega}$ and $\mathbf{F}$ can be induced as followed

$$\mathbf{L}^E = \mathbf{D}^E + \mathbf{\Omega}^E = \dot{\mathbf{F}}^E \cdot \mathbf{F}^{E-1} \qquad \text{(II-1-16)}$$

$$\mathbf{L}^p = \mathbf{D}^p + \mathbf{\Omega}^p = \mathbf{F}^E \cdot \dot{\mathbf{F}}^p \cdot \mathbf{F}^{p-1} \cdot \mathbf{F}^{E-1} = \mathbf{F}^E \cdot \mathbf{L}^p_0 \cdot \mathbf{F}^{E-1} \qquad \text{(II-1-17)}$$

where $\mathbf{L}_0^p$ is the velocity gradient measured at the intermediate state before any crystal lattice deformation. This parameter can be estimated from the resolved shear strain rate and slip system tensor.

$$\mathbf{L}^p_0 = \sum_{s=1}^{n} \mathbf{L}^{ps}_0 = \sum_{s=1}^{n} \dot{\gamma}^s \mathbf{\mu}^s_0 \qquad \text{(II-1-18)}$$

$\mathbf{L}^p$ can also be expressed from the shear strain rate and slip system tensor by using equation (II-1-1), (II-1-11), (II-1-12), (II-1-17) and (II-1-18).

$$\mathbf{L^p} = \mathbf{F^E} \cdot \mathbf{L_0^p} \cdot \mathbf{F^{E-1}} = \sum_{s=1}^{n} \dot{\gamma}^s \boldsymbol{\mu^s} \tag{II-1-19}$$

Constitutive equations

Constitutive equations are needed to relate the stress to the strain. At the macroscopic level, it is written as:

$$\mathbf{T^*} = \mathbf{C^E}\left[\mathbf{E^*}\right] \tag{II-1-20}$$

where $\mathbf{C^E}$, $\mathbf{E^*}$ and $\mathbf{T^*}$ are 4th order elastic stiffness matrix, Almansi-Hemel strain tensor and second Piola-Kirchhoff stress tensor, respectively. The strain tensor and stress tensor can be written as functions of deformation gradient and Cauchy stress tensor.

$$\mathbf{E^*} = \frac{1}{2}\left\{\mathbf{F^{ET}F^E} - \mathbf{I}\right\} \tag{II-1-21}$$

$$\mathbf{T^*} = \mathbf{F^{E-1}}\left\{\left(\det \mathbf{F^E}\right)\boldsymbol{\sigma}\right\}\mathbf{F^{E-T}} \tag{II-1-22}$$

where $\boldsymbol{\sigma}$ is the Cauchy stress tensor.

At the microscopic level, the flow law relates the resolved shear stress τ^s to the resolved shear strain rate for each slip systems as:

$$\dot{\gamma}^s = \dot{\gamma}_0^s \left|\frac{\tau^s}{\tau_\mu^s}\right|^{\frac{1}{m^r}} sign\left(\tau^s\right) \tag{II-1-23}$$

where s is the system index and $\dot{\gamma}_0^s$, τ_μ^s and m^r are the initial shear strain rate, the critical resolved shear stress and the strain rate sensitivity, respectively.

Figure II-1-4 illustrates the meaning of the flow law. The resolved shear strain is generated on system at a rate $\dot{\gamma}_0^s$ if the resolved shear stress is reaching the critical value (τ_μ^s). Once the resolved shear stress overcomes the critical resolved shear stress, the shear strain increases at a rate imposed by the strain rate sensitivity coefficient (m^r). Hence, the meaning of the critical resolved stress is a minimum value to generate a shear strain rate. In other words, the critical resolved stress is a minimum stress value for starting plastic deformation so that it defines a yield criterion and consequently the parameter for the isotropic hardening.

Resolved shear stress is expressed as a function of second Piola-Kirchhoff stress tensor.

$$\tau^s = \left(\mathbf{F^T F T^*}\right) : \boldsymbol{\mu_0^s} \approx \mathbf{T^*} : \boldsymbol{\mu_0^s} \tag{II-1-24}$$
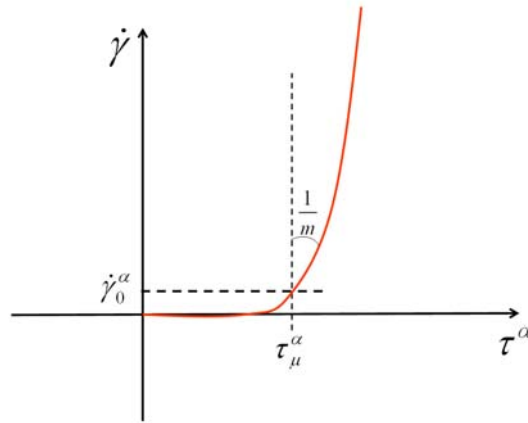
Figure II-1-4. Illustration of the flow law relating resolved shear strain rate to shear stress

The dependency between the resolved shear strain rate and the resolved shear stress depends on quantity of strain rate sensitivity variable (m^r). A large value for m^r would lead to a small power exponent ($1/m^r$) and consequently enhances the sensibility of the strain rate to the stress. On the other hand, a small m^r induces no dependence between them since the shear strain rate will quickly change from zero to $\dot{\gamma}_0^s$ when the shear stress increases.

<u>Hardening law</u>

In general, most of materials increase their strength when the plastic deformation is increased. This is known as the deformation hardening. In the models developed and proposed by many authors [Hil66, HR72, AR77, HR82, Asa, TF97, PAN83, BW91, CO92, MC91, Wen87 and Oha87], an attention has been paid to the description of the anisotropic work hardening of crystalline metals available for large strain using phenomenological laws [Hil62]. Bassani and Wu [Bas90 and BW91] have proposed a model in which the hardening matrix is diagonally dominant, and Pierce and co-workers [PAN83] model latent hardening effects by means of a hardening matrix in which the off-diagonal terms are dominant. These theories are commonly adopted for the interpretation of latent hardening experiments [Bas90, Koc70, RKC65, KB66 and FBZ80]. Following is the description of several representative hardening rules.

For a given slip system, the hardening can be induced not only by the plastic deformation cumulated on itself (the so called self hardening) but also by the plastic deformation accumulated on the other slip systems i.e. the latent hardening. Many authors have reported experimental results about the hardening [Koc70, KB66 and JB67] and these results give the fundamental of mathematical hardening rule which is expressed by following form.

$$d\tau_\mu^s = \sum_{p=1}^{n} \mathbf{h^{sp}} d\gamma^p \tag{II-1-25}$$

where $\mathbf{h^{sp}}$ is the matrix of hardening parameters. Many authors have proposed mathematical

expression of the $\mathbf{h^{sp}}$ [PAN83, Wen87, NK66, HS77 and AN85]. Nakada and Keh proposed hardening rules based on two independent hardening coefficients: one (h^p) for self hardening and the second ($\mathbf{q^{sp}}$) for latent hardening [NK66]. The model is expressed by following equation.

$$d\tau_\mu^s = \sum_{p=1}^{n} \mathbf{q^{sp}} h^p d\gamma^p \qquad \text{(II-1-26)}$$

where h^p and $\mathbf{q^{sp}}$ are self hardening coefficient and matrix of hardening parameters for latent hardening. For FCC crystals with 12 slip systems, $\mathbf{q^{sp}}$ can be expressed by followed equation [AN85]

$$\mathbf{q^{sp}} = \begin{Bmatrix} \mathbf{O_{33}} & q\mathbf{O_{33}} & q\mathbf{O_{33}} & q\mathbf{O_{33}} \\ q\mathbf{O_{33}} & \mathbf{O_{33}} & q\mathbf{O_{33}} & q\mathbf{O_{33}} \\ q\mathbf{O_{33}} & q\mathbf{O_{33}} & \mathbf{O_{33}} & q\mathbf{O_{33}} \\ q\mathbf{O_{33}} & q\mathbf{O_{33}} & q\mathbf{O_{33}} & \mathbf{O_{33}} \end{Bmatrix} \qquad \text{(II-1-27)}$$

where q is the ratio between the latent hardening and self hardening and $\mathbf{O_{33}}$ is 3 x 3 matrix fully populated by ones.

h^p is identical for each systems. Anand and co-workers have proposed mathematical description for h^p as the following power-law type expression [KBA92, BKA89 and BKA92].

$$h^p = h_0 \left(1 - \frac{\tau_\mu^p}{s_s} \right)^a \qquad \text{(II-1-28)}$$

where h_0, a and s_s are slip system hardening parameters which are taken to be identical for all slip systems. In the equation (II-1-28), the self hardening is directly related to the critical resolved shear stress (τ^p_μ).

Asaro and Needelman proposed another power-low type description for h^p [AN85] as followed

$$h^p = h_0 \left(\frac{h_0 \gamma^p}{n \tau_0} + 1 \right)^{n-1} \qquad \text{(II-1-29)}$$

where h_0, n and τ_0 are self hardening parameters which are also taken to be identical for all slip systems. Here the hardening rule is a function of the resolved shear strain on the slip system.

Since all of these mathematical hardening rules are just based on empirical fitting of experimental results, parameters of the rules are not easy to explain with physical arguments and the values of the parameters for a material are obtained by fitting experimental results. Therefore, a full physical description of hardening rules is still challenging today and it motivates many other groups in the world since people do want to get rid of any fitting sequence.

1.2 Dislocation based theories of crystal plasticity

The development of constitutive equations for crystal plasticity model is still challenging today. The objective is to derive a set of behavior laws with physics based theory and physical meaningful parameters. The physics based plastic deformation behavior has been studied since the early sixties [Teo75]. Recently, Tabourot *et al.* proposed a full crystal plasticity model based on dislocation dynamics theory [TF97]. Each rule of this model is derived from physical considerations of dislocation motions. In this section, details of the model proposed by Tabourot *et al.* are introduced.

Origin of the flow law

The flow rule can be derived from the motion of each single dislocation gliding on slip system s by Orowan equation.

$$\dot{\gamma}^s = \rho_m^s b v^s \tag{II-1-30}$$

where ρ_m^s, b, v^s are the density of mobile dislocations, normalized value of the Burgers vector and average velocity of the mobile dislocations, respectively.

The average velocity can be derived from the velocity of a single dislocation moving in a heterogeneous stress field. In the FCC crystal structure, it is admitted that the dislocation motion is governed by the obstacle which can be classified in two categories. The first one includes the obstacles inducing long range stresses (τ_μ^s) which do not depend on temperature, like dislocations stored at grain boundaries or around precipitates and the second one accounts for the obstacles including a short range stress field (τ^{*s}) which are thermally activated, such as forest dislocations or impurities.

Figure II-1-5 depicts the spatial evolution of the stress components induced by the two types of obstacles.

When considering only the isotropic hardening, the stress evolution of the athermal stress (τ_μ^s) is similar to a periodic function with a null average and a large wave length. When a dislocation meets an obstacle which induces a short range stress within few atomic distances to the dislocation position, it needs an additional stress (τ^{*s}) to pass the obstacle. Therefore the resolved shear stress needed for the dislocation movement could be expressed by the sum of the two stresses.

$$\tau^s = \tau_\mu^s + \tau^{*s} \tag{II-1-31}$$
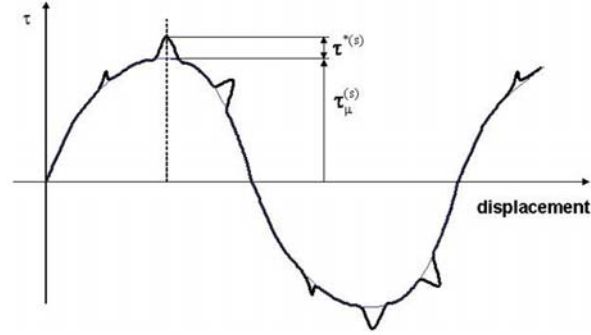
Figure II-1-5.　　　Spatial evolution of the different stress components which affect the dislocation movement

Teodosiu and Sidoroff proposed the following expression of the dislocation velocity within the assumption that the time for the dislocation flight is negligible in comparison to the waiting time in front of the obstacles [TS76].

$$v = \frac{bv_D}{e^{\frac{\Delta G_0}{kT}} \times \left(2\sinh\left(\frac{\tau^{*s}\Delta V^*}{kT}\right)\right)^{-1}} \qquad \text{(II-1-32)}$$

where v_D, ΔG_0, k, T and ΔV^* are Debye frequency, Gibbs free energy, Boltzmann constant, temperature and volume change, respectively. The term with sinh function in equation (II-1-32) models the probability for passing the obstacles, which includes reverse directional jumping probability.

The τ^{*s} can be replaced by τ_μ^s- τ^s because of equation (II-1-31). When the resolved shear stress is less than 70% of stress value at 0K (τ_0^{*s}), one can neglect the reverse directional jumping probability so that the sinh part in equation (II-1-32) can be replaced by the negative exponential function.

$$v = bv_D \exp\left(\frac{-\Delta G_0 + \left(\tau^s - \tau_\mu^s\right)\Delta V^*}{kT}\right) = bv_D \exp\left(\frac{-\Delta G_0 + \tau_\mu^s\left(\frac{\tau^s}{\tau_\mu^s} - 1\right)\Delta V^*}{kT}\right) \qquad \text{(II-1-33)}$$

The exponential term can be approximated by first order Taylor approximation.

$$v = bv_D \exp\left(\frac{-\Delta G_0}{kT}\right)\left|\frac{\tau^s}{\tau^s_\mu}\right|^{\frac{\tau^s_\mu \Delta V^*}{kT}} sign(\tau^s) \qquad \text{(II-1-34)}$$

Assuming that the average velocity for all the mobile dislocations follows a similar expression, one can replace v in Orowan equation (II-1-30) and obtain:

$$\dot{\gamma}^s = \rho^s_m b^2 v_D \exp\left(\frac{-\Delta G_0}{kT}\right)\left|\frac{\tau^s}{\tau^s_\mu}\right|^{\frac{\tau^s_\mu \Delta V^*}{kT}} sign(\tau^s) \qquad \text{(II-1-35)}$$

Equation (II-1-35) is similar to equation (II-1-23) if we write:

$$\dot{\gamma}^s_0 = \rho^s_m b^2 v_D \exp\left(\frac{-\Delta G_0}{kT}\right), \quad m^r = \frac{kT}{\tau^s_\mu \Delta V^*} \qquad \text{(II-1-36)}$$

These relationships give a physical meaning of the parameters involved in equation (II-1-23).

Hardening rule

Isotropic strain hardening is defined by the increase of the athermal stress τ^s_μ with the internal variables like the dislocation densities. Figure II-1-6 depicts a physical origin of the mathematical expression for such a relationship. Let consider a dislocation moving on slip system (s) (normal $n^{(s)}$) through a population of dislocations piercing the slip plane.
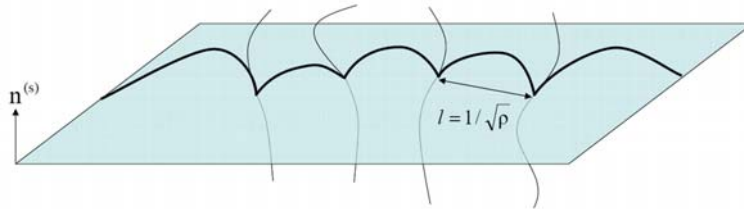
Figure II-1-6. Illustration of the Taylor expression for forest hardening

These dislocations, called as forest dislocations, are impacting the slip plane at many points separated from an average distance $l=1/\sqrt{\rho}$. According to line tension theory, the resolved shear stress needed to bend a dislocation pinned on two points separated of l is given as

$$\tau^s_\mu = \tau_{lt} = \frac{\alpha\mu b}{l} = \alpha\mu b\sqrt{\rho_F} \qquad \text{(II-1-37)}$$

where μ, α and ρ_F are the shear modulus, a constant for line tension and the forest dislocation density respectively. Such a relationship between the critical resolved shear stress and the dislocation density is known as the Mecking and Kocks equation [MK81].

This equation can be split over the 12 slip systems of the FCC crystal using a matrix α which corresponds to the slip system interactions.

$$\tau_\mu^s = \mu b \sqrt{\sum_{p=1}^{12} \boldsymbol{\alpha}^{\mathbf{sp}} \rho^p} \qquad\qquad \text{(II-1-38)}$$

where, $\boldsymbol{\alpha}^{\mathbf{sp}}$ and ρ^p are junction strength matrix and dislocation density on slip system p, respectively. For FCC crystals, $\boldsymbol{\alpha}^{\mathbf{sp}}$ is a 12×12 matrix, but because of symmetry, only 6 coefficients are independent. They are denoted as the self (α_1), coplanar (α_2), hirth (α_3), glissile (α_4), lomer (α_5) and collinear (α_6) coefficients. Table II-1-2 details the junction matrix for FCC crystal [Fiv97].

	A2	A3	A6	B2	B4	B5	C1	C3	C5	D1	D4	D6
A2	α_1	α_2	α_2	α_6	α_4	α_4	α_3	α_4	α_5	α_3	α_5	α_4
A3		α_1	α_2	α_4	α_3	α_5	α_4	α_6	α_4	α_5	α_3	α_4
A6			α_1	α_4	α_5	α_3	α_5	α_4	α_3	α_4	α_4	α_6
B2				α_1	α_2	α_2	α_3	α_5	α_4	α_3	α_4	α_5
B4					α_1	α_2	α_5	α_3	α_4	α_4	α_6	α_4
B5						α_1	α_4	α_4	α_6	α_5	α_4	α_3
C1							α_1	α_2	α_2	α_6	α_4	α_4
C3								α_1	α_2	α_4	α_3	α_5
C5					symmetric				α_1	α_4	α_5	α_3
D1										α_1	α_2	α_2
D4											α_1	α_2
D6												α_1

Table II-1-2. Values of the system interaction matrix for FCC crystals

In order to get the closed forms of the strain hardening equations it is needed to specify the evolution rule of the dislocation densities with the deformation. The evolution can be explained from statistic considerations of dislocation production and annihilation [ML70 and EM67].

$$\dot{\rho}^s = \frac{1}{b}\left(\frac{\sqrt{\sum_{p=1}^{12} \mathbf{a}^{\mathbf{sp}} \rho^p}}{K_g} - 2 y_c \rho^s \right)\left|\dot{\gamma}^s\right| \qquad\qquad \text{(II-1-39)}$$

where $\mathbf{a}^{\mathbf{sp}}$ and K_g are parameters for dislocation generation and y_c is the annihilation distance. Here again $\mathbf{a}^{\mathbf{sp}}$ is a 12×12 matrix, like $\boldsymbol{\alpha}^{\mathbf{sp}}$. Recently, Kubin *et al*. has proposed that the matrix for dislocation generation ($\mathbf{a}^{\mathbf{sp}}$) is the same matrix as that of the junction strength ($\boldsymbol{\alpha}^{\mathbf{sp}}$) [KDH08]. Note that this equation implies that the dislocation densities saturate for a given system when

the production term equals the annihilation term, which will lead to a saturation of the isotropic hardening when all the dislocations densities have saturated.

Finally, the general form of the hardening rule at crystal plasticity model like equation (II-1-25) is defined by the combination of the two equations (II-1-38) and (II-1-39).

$$d\tau_\mu^s = \sum_p \mathbf{h^{sp}} d\gamma^p = \sum_p \frac{\mu \boldsymbol{\alpha^{sp}}}{2\sqrt{\sum_q \boldsymbol{\alpha^{sq}} \rho^q}} \left(\frac{\sqrt{\sum_p \mathbf{a^{sp}} \rho^p}}{K_g} - 2y_c \rho^p \right) d\gamma^p \qquad \text{(II-1-40)}$$

Since all the rules in this frame work are based on physical considerations, the corresponding parameters have a physical meaning and could be estimated through dislocation dynamics simulations [DKH06 and DF02] or nano scale experiment [KWD01 and CFP05].

A benefit of this model is that the dislocation evolution during macroscopic deformation can be analyzed. The model gives also access to the orientation change, resolved shear stress and strain on the slip systems during the macroscopic deformation.

1.3 Applications of the model

<u>Tensile test – a simple integration</u>

Since tensile deformation behavior of FCC single crystal is one of the most well known behaviors both theoretically and experimentally, we will first check the model in this configuration.

The test calculations have been done by simple integration routine to get a stress field from Newtonian iteration method, given the strain field and the crystal plasticity model. For simplicity, the algorithm is started from the relationship between Cauchy stress and infinitesimal strain field.

$$d\boldsymbol{\sigma} = \mathbf{C^E} d\boldsymbol{\varepsilon^e} = \mathbf{C^E}\left(d\boldsymbol{\varepsilon} - d\boldsymbol{\varepsilon^p}\right) \qquad \text{(II-1-41)}$$

where we assumed that the plastic infinitesimal strain filed could be earned by the flow rule in equation (II-1-23).

$$d\boldsymbol{\varepsilon^p} = \sum_{s=1}^{12}\left(d\gamma^s \cdot \boldsymbol{\mu^s}\right) = \sum_{s=1}^{12}\left[\gamma_0 \left(\frac{\boldsymbol{\sigma} : \boldsymbol{\mu^s}}{\tau_\mu^s} \right)^{\frac{1}{m^r}} \cdot \boldsymbol{\mu^s} \right] \qquad \text{(II-1-42)}$$

The following equation is obtained from equation (II-1-41) and (II-1-42).

$$\mathbf{F}_{\mathbf{iter}} = d\boldsymbol{\sigma} - \mathbf{C}^{\mathbf{E}}d\boldsymbol{\varepsilon} - \mathbf{C}^{\mathbf{E}}\left\{\sum_{s=1}^{12}\left[\gamma_0\left(\frac{\boldsymbol{\sigma}:\boldsymbol{\mu}^{\mathbf{s}}}{\tau_\mu^s}\right)^{\frac{1}{m^r}}\cdot\boldsymbol{\mu}^{\mathbf{s}}\right]\right\} \qquad \text{(II-1-43)}$$

Therefore, we can have a Cauchy stress field ($\boldsymbol{\sigma}$) from a given infinitesimal strain field ($\boldsymbol{\varepsilon}$) by following simple iteration equation.

$$d\boldsymbol{\sigma}_{\mathbf{new}} = d\boldsymbol{\sigma}_{\mathbf{old}} - \left(\frac{\partial\mathbf{F}_{\mathbf{iter}}}{\partial\boldsymbol{\sigma}}\right)^{-1}\mathbf{F}_{\mathbf{iter}} \qquad \text{(II-1-44)}$$

Table II-1-3 gives the values for the parameters corresponding to copper single crystals [Fiv97]. The shear modulus (μ) and the Poisson ratio (ν) are set to 42000 MPa and 0.3, respectively. The initial resolved shear strain rate (γ_0) and the strain rate sensitivity variable (m^r) in the flow rule equation (II-1-23) are 0.001 /sec and 0.005, respectively. Junction strength matrix (α) and Burgers vector (b) for hardening equation (II-1-38) are 0.09 for all the invariant at α matrix and 2.56×10^{-10} m, respectively. Finally parameters, $\mathbf{a}^{\mathbf{sp}}$, K, y_c and initial dislocation density on the slip system (ρ_0^s) are (0.01, 0.4, 0.4, 0.75, 1.0, 0.4), 56, 1.43×10^{-9}m and 10^8m^{-2}.

In the following simulations the macroscopic tensile strain is increased up to 1.0. Six initial tensile directions are tested: [-1 2 5], [-1 3 5], [-2 3 5], [-5 6 10], [-14 15 25] and [-3 3 5], respectively. Results will be analyzed in term of orientation change, resolved shear stress versus resolved shear strain relationship, number of activated slip systems and dislocation density evolutions. Finally the effect of initial orientation on the mechanical response will be discussed.

Elastic property	μ	42000 MPa
	ν	0.3
Flow rule property	γ_0	0.001 /sec
	m	0.005
Hardening property	b	2.56×10^{-10} m
	$\alpha_{1\sim6}$	(0.09, 0.09, 0.09, 0.09, 0.09, 0.09)
Dislocation evolution property	$a_{1\sim6}$	(0.01, 0.4, 0.4, 0.75, 1.0, 0.4)
	K	56.0
	y_c	1.43×10^{-9} m
	ρ_0^s	1.0×10^8 /m^2

Table II-1-3. General parameter values of copper single crystal

Figure II-1-7 shows the orientation change in the case of [-1 2 5] orientation of the tensile axis. Since [-1 2 5] orientation lays in the triangle delimitated by [001], [011] and [-1 1 1], B4 slip system activates the first (see figure II-1-2). B4 slip direction being [-1 0 1], the initial

orientation moves towards [-1 0 1] direction until it meets a line between [0 0 1] and [-1 1 1]. When the tensile direction reaches this line, Both B4 and C1 slip systems are simultaneously activated. Consequently, the tensile direction moves to the [-1 1 2] direction which is summation of slip directions of B4 ([-1 0 1]) and C1 ([0 1 1]).

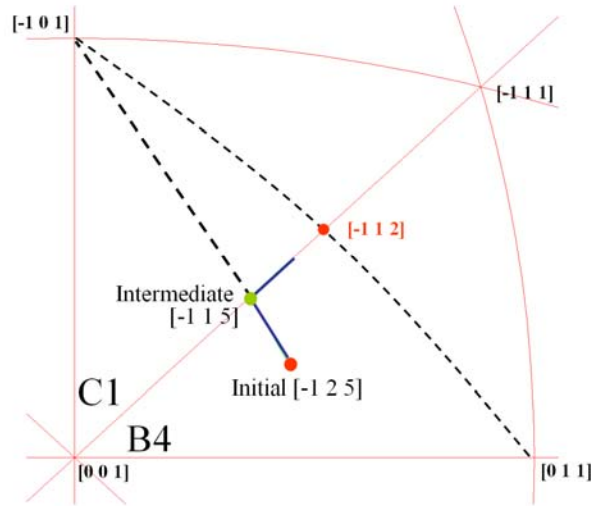Figure II-1-7. Orientation change during <-1 2 5> directional tensile deformation

Figure II-1-8 gives the relationship obtained between the shear stress and the shear strain resolved on system B4 during the [-1 2 5] tensile deformation. The evolution of the resolved shear stress is dictated by the rule given in equation II-1-40. Hence, it depends on the total dislocation density stored on the different slip systems and the dislocation generation matrix ($a_{1\sim6}$).
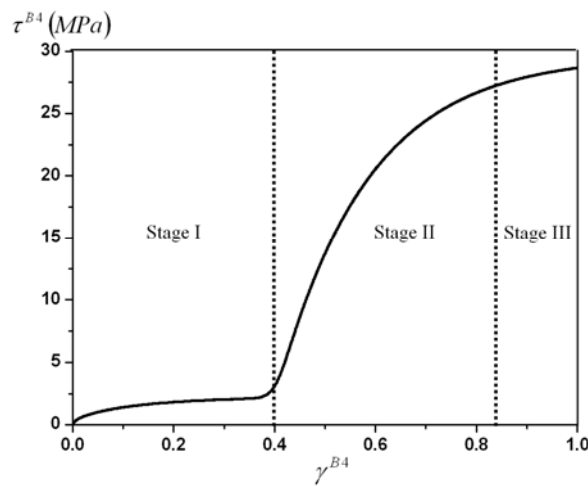

Figure II-1-8. Resolved shear stress versus resolved shear strain computed on slip system B4 during <-1 2 5> tensile test

Since slip system B4 activates at the beginning of the tensile test, the resolved shear stress on B4 is mainly imposed by the resolved shear strain γ(B4) and the self hardening parameter, a_1,. The value of a_1 being smaller than the others, the initial resolved shear stress rate is low. This correspond to the Stage I behavior of single crystals. After 40% of cumulated resolved shear strain, however, the resolved shear stress rate strongly increases. This coincides to the instant when the second slip system (C1) starts to activate. This second activated slip system implies the interaction parameter (a_5), which has a much higher value than a_1. This directly influences the rate of the resolved shear stress and leads to the Stage II behavior of single crystals. At last, after a large deformation of about 60% of cumulated resolved shear strain, the increasing rate of the resolved shear stress is decreasing with the increasing resolved shear strain. This is because the increasing dislocation density on the activated slip system is disturbed by the dislocation annihilations. Indeed, when the dislocation production rate equals the annihilation rate for all the slip systems, all the dislocations densities have saturated, which will lead to a saturation of the resolved shear stress and the well-known Stage III behavior of single crystals.

The instant when the second slip system activates can be estimated by plotting the shear strain resolved on system (C1) versus the shear strain cumulated on system (B4) as given in figure II-1-9.
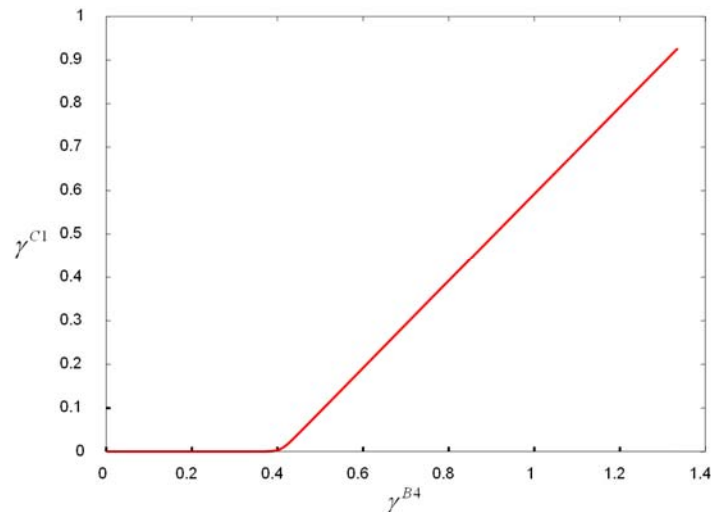

Figure II-1-9. Shear strain resolved on C1 slip system plotted versus the shear strain resolved on B4 slip system

It appears that system C1 activates when the shear strain cumulated in system (B4) reaches 40%. Then the slope of the curve is closed to 1.00 which demonstrates that the two slip systems are simultaneously activated with an identical Schmid factor.

Figure II-1-10 shows the evolution of the dislocation densities on B4 and C1 slip systems. It also gives information about single slip or double slip system activation during the tensile test. Initially, the dislocation density on system B4 increases dramatically whereas the density on C1 remains constant and equal to the initial value. After 15% of global shear strain, i.e. at the beginning of stage II, the dislocation density on system B4 dramatically increases together with that of system C1.
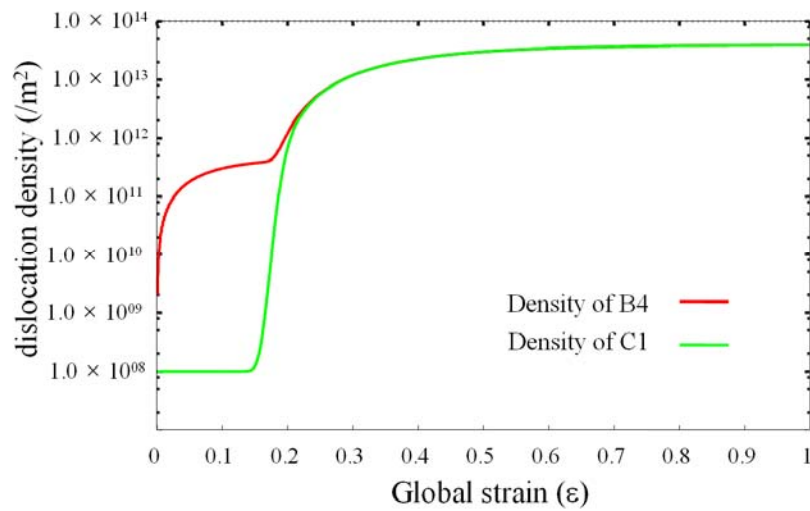

Figure II-1-10. Evolution of dislocation density at B4 and C1 slip systems

The increasing rate of dislocation density on C1 appears to be much higher than the initial increasing rate on B4. This comes from the evolution rule for the dislocation densities on the slip systems which depend on the dislocation densities stored on all the slip systems. Thus, the total dislocation density at the time of C1 slip system activation being much higher than the initial total dislocation density, the slope of ρ(C1) is increased and so does the slope of B4. At the end of the tensile test, both dislocation densities on C1 and B4 slip systems are saturating to values close to 8×10^{13}/m^2.

Figure II-1-11 gives the orientation of the tensile axis in the crystal frame for tensile tests conducted up to 100% of tensile strain and for the different tensile directions investigated. Since, every tensile directions except [-3 3 5] lay inside a triangular region made from [001], [011] and [-1 1 1], B4 slip system always activates at the beginning of the simulation and the orientation of the tensile axis move toward the glide direction [-1 0 1] until second slip system C1 is activated. The second slip system activation changes the tensile axis direction so that all the projections move to [-1 1 2]. As a consequence, although the initial tensile direction is different they all converge to the same final direction [-1 1 2] after a given amount of plastic deformation.
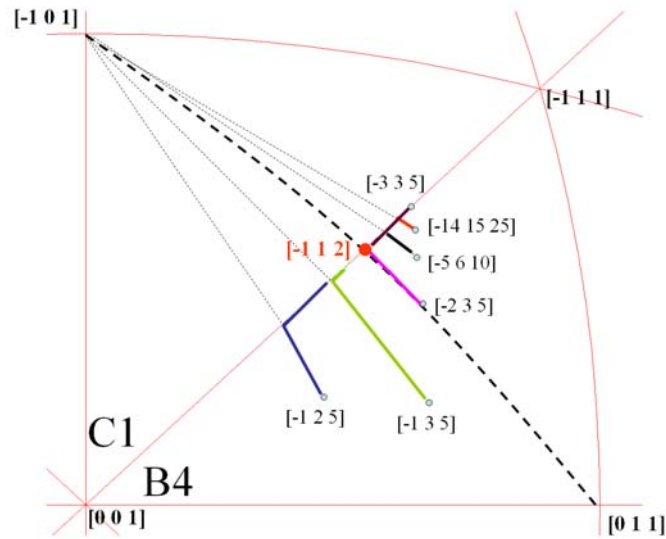
Figure II-1-11. Orientation changes for several tensile directions of the tensile axis

Figure II-1-12 shows the mechanical response of the deformed samples for different orientations. The resolved shear stresses on B4 slip systems are plotted as a function of the global tensile strain.
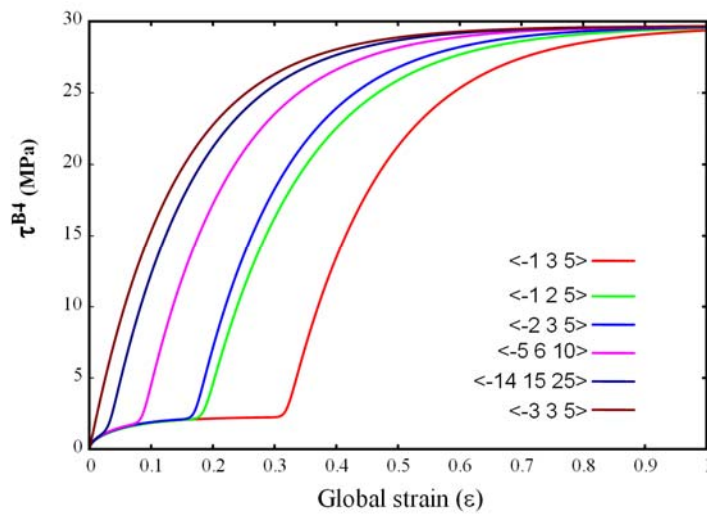
Figure II-1-12. Shear stresses resolved on slip system B4 plotted versus the global tensile strain for different orientation of the tensile axis

The figure shows that when the slopes for stage I and stage II are all similar although they do not begin at the same time. The [-1 3 5] orientations leads to the longest stage I (ε~30%) and the initial double glide configuration [3 3 5] display no Stage I and directly starts in Stage II. For all

the orientations the resolved shear stresses saturate at 30MPa. The reason is that the saturation density with double slip systems activation does not depends on the initial tensile directions.

Tensile test - FEM integration

The above results have been obtained by using a simple integration algorithm. The Tabourot *et al*. model described above can be implemented in FEM codes so that complex loading conditions and heterogeneous stress states can be investigated. In this study, we have implanted the set of constitutive equations into ABAQUS software [ABA04]. In order to simulate a tensile test, the sample has been chosen to be parallelepiped with dimensions (6mm×6mm×30mm). A slender shape of the sample has been chosen in order to limit the boundary effects and promote a homogeneous stress state as done experimentally for dog-bones specimens. The volume is meshed into 512 elements eight-node elements as shown in figure II-1-13 (a). For the boundary conditions, two points at the center of dog-bones specimen as shown in figure II-1-13 (a) are fixed to prohibit rigid body movement and rotation and all of the nodes on both sides of specimen are stretched out through the tensile direction, simultaneously. Parameters for the calculations are the same as given in table II-1-3. Orientation for the initial tensile direction is [-1 2 5]. After the calculation, the results of shear stress, strain and dislocation density cumulated on activated systems are picked at the center element of the specimen shown by red dotted cube in figure II-1-13 (a).
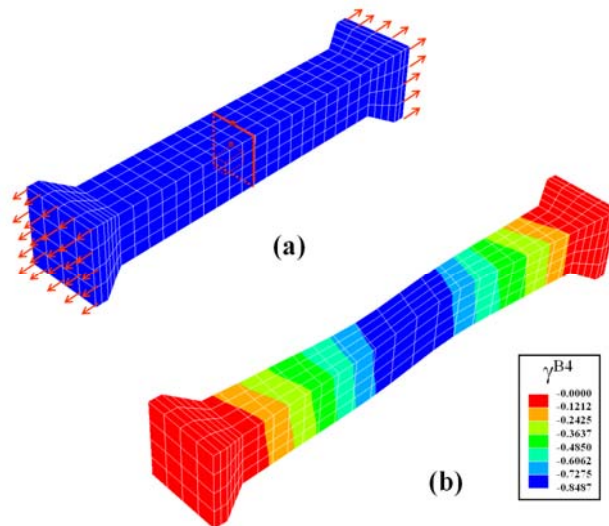

Figure II-1-13. (a) 512 element mesh and boundary conditions used for FEM tensile simulation along direction is <-1 2 5> (b) Deformed shape and resolved shear strain distribution on slip system B4 after up to 33% of global tensile deformation

Figure II-1-13 (b) shows the deformed mesh obtained after 40% of macroscopic plastic strain. The isovalues indicate the local resolved shear strain cumulated on system B4. It is found to be maximum resolved shear strain at the center of the specimen. One can notice the 'S' like curved shape of the deformed sample. This is directly related to the rotations induced by the activation of the slip systems.

Figure II-1-14 shows the comparison between results from FEM calculation and simple integration algorithm during the [-1 2 5] tensile deformation.
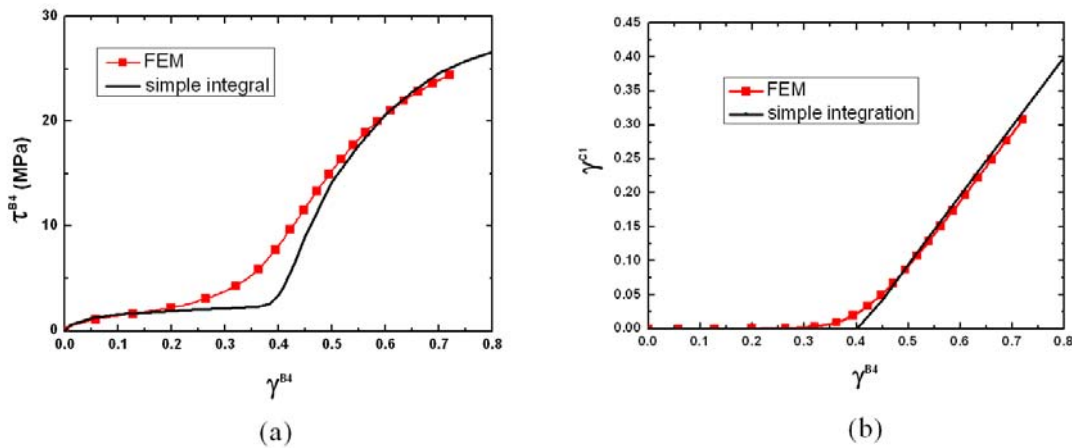

Figure II-1-14. Comparison between FEM calculation and simple integration (a) Resolved shear stress with resolved shear strain on slip system B4 during <-1 2 5> tensile test

(b) Shear strain resolved on slip system C1 plotted versus the shear strain resolved on B4

The relationships obtained between the shear stress and the shear strain resolved on system B4 from FEM calculation and simple integration algorithm are depicted in figure II-1-14 (a). The evolution of the shear strain resolved on system (C1) versus the shear strain cumulated on system (B4) from the two kinds of calculation methods are given in figure II-1-14 (b), where the black line and red line with square symbols depict the results from simple integration algorithm and FEM calculation, respectively.

The simple integration method makes a clear distinction between Stage I and II behavior when the shear strain cumulated in system (B4) reaches 40%. However, the FEM calculation makes a more gradual change from Stage I to Stage II. The resolved shear stress rate from FEM calculation does not show any strong increase, but it rather increases gradually with the resolved shear strain as shown in figure II-1-14 (a). It appears from FEM calculation that system C1 starts to activate with very weak slope when the shear strain cumulated in system (B4) reaches about 20% and the slope of the curves increasing gradually with resolved shear strain, where the slope of the curve is closed to 1.00 only after the shear strain cumulated in system (B4) reaches

about 50% as shown in figure II-1-15 (b). On the other hand, after about 60% of resolved shear strain, both curves of resolved shear stress from the two calculation methods decrease their slope, which means that both the calculation methods give the Stage III behavior. These are due to the difference of boundary conditions. The simple integration method calculates the response with free boundary condition (except for the tensile direction constraint), whereas the FEM does not allow 100% of free boundary condition: each element interacts with its neighbor elements, which in term disturbs the free motion of the element.

Figure II-1-15 shows the evolution of the dislocation densities on B4 and C1 slip systems calculated from FEM. It also gives information about gradual changing between Stage I and II.
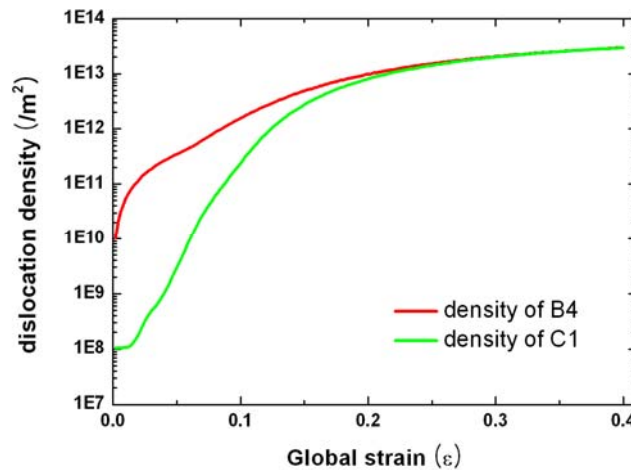
Figure II-1-15. Evolution of dislocation densities on slip system B4 and C1 obtained from FEM calculation

Initially, the dislocation density on system B4 increases dramatically whereas the density on C1 increases with very weak increasing rate, but the increasing rate of density on system C1 is increasing with strain. Therefore, the density difference between system B4 and C1 is reducing gradually. After about 20% of global shear strain, the two curves which depict the dislocation density on system B4 and C1 meet together and show the same increasing tendency. After about 40% of the tensile test, the dislocation density on system B4 and C1 have reached values close to $4 \times 10^{13} m^{-2}$ which is similar to the values obtained at the same global strain with the simple integration algorithm.

All of the simulation results during tensile deformation from figure II-1-7 to figure II-1-15 are exactly the same as the theoretical expectations, which verify that the model gives excellent results about deformation behavior of single crystal material.

1.4 What should be retained from this section

- Crystal plasticity Model composed by

  - Flow rule $\qquad \dot{\gamma}^s = \dot{\gamma}_0^s \left| \dfrac{\tau^s}{\tau_\mu^s} \right|^{\frac{1}{m^r}} sign(\tau^s)$

  - Hardening rule $\qquad \tau_\mu^s = \mu b \sqrt{\displaystyle\sum_{p=1}^{12} a^{sp} \rho^p}$

  - Evolution rule $\qquad \dot{\rho}^s = \dfrac{1}{b} \left(\dfrac{\sqrt{\displaystyle\sum_{p=1}^{12} \mathbf{a}^{sp} \rho^p}}{K_g} - 2 y_c \rho^s \right) |\dot{\gamma}^s|$

- The model implanted into ABAQUS successfully

2. Generalized continuum mechanics to understand size effect

Experimentally, size effects are observed for micrometric sample sizes and for various modes of plastic deformation. Generally, a smaller size gives a stronger response for a given deformation field. This was evidenced for elastic bending experiments of marble [EVK01] and epoxy polymeric beams [LYC03]. It was also found in porous media, such as bones or foams [YL81, Lak86 and Aif99]. When the size effects have been observed, the need for advanced continuum formulations was also recognized, since in all cases, the classical theories substantially fail to predict the experimental results.

The recent advanced theories were derived from the approximation of the average strain by a Taylor expansion [MA91]. These theories all introduce an intrinsic material length and an additional hardening rule that can be related to the strain gradient or to the lattice curvature as first proposed by Nye [Nye53]. Nye noticed that after bending or torsion a crystal contains excess dislocations of a definite sign that gives rise to lattice curvature.

Later, it was commonly admitted that the dislocations can be divided into dislocations needed for the accommodation of the lattice curvature and the others (statistically stored). According to Ashby [Ash70], dislocations may store in a plastically non-homogeneous solid for two reasons. The first one is that dislocations are either required for the compatible deformation of various parts of the specimen and the other is that they accumulated by trapping each other in a random way. This gives rise on the one hand to the density of so-called geometrically necessary dislocations (GND) ρ_g and on the other hand to the density of statistically stored dislocations (SSD) ρ_s.

The density of GND can be computed approximately in some situations like plastic bending or punching. This quantity comes out directly from the continuum theory of dislocations and corresponds to the components of the dislocation density tensor so called Nye tensor. In contrast, the density ρ_s belongs to the second group of variables that have been listed and called hardening variables. However, as shown by Ashby [Ash70], geometrically necessary dislocations may lead to additional hardening. The relative importance of GND and SSD depends on the amount of overall plastic deformation. Clearly GND can dominate in the case of strong deformation gradients and it is believed that the character of GND is at the origin of size effect. Therefore, the recent advanced theories widely use the concept of GND.

Recent theories such as the Cosserat theory [FCS97] or the strain gradient theory [FH97 and SF99] were demonstrated their ability to reproduce the experimental evidence of size effects. As examples, they could predict particle size effects [Ash70], indentation size effects [NG98 and GHN99] and size effect in micro torsion [FMA94] or thin beams bending [SE98] as well as in multi-phase materials [FBC00].

However, in the case of the advanced theories involving higher order derivatives such as strain gradient theories, it was shown that their implementation into the FEM is rather limited. The performance of the implementation was reported to be poor in the context of strain gradient theories [XH96] and the extension to a three-dimensional interpolation is considered to be too much complex. There are several way to implement these recent theories into FEM codes [ZPV01], but one always need to define a very large number of additional nodal degrees of freedom which will increase the calculation time dramatically. To make it worse, contact theory based on these theories have not been developed yet. Hence, FEM simulations with contact problem like nano indentation could not be easily calculated with these advanced theories yet. Therefore it is worth developing a simple size effect theory without any extra constitutive equations or degree of freedom.

In this section, two advanced theories for size effect are introduced: strain gradient theory and Cosserat theory. Then we propose an alternative theory for accounting of size effect in plasticity which does not require any extra constitutive equation and degree of freedom. Finally, a simple example is shown in order to test the proposed model.

2.1 Recent theories for size effect

In the continuum theory of dislocations, the notion of geometrically necessary dislocations is associated with that of the dislocation density tensor introduced by Nye [Nye53] and the recent theories consist of introducing the dislocation density tensor into the single crystal constitutive equations.

The starting point is the famous relation by Nye that relates the dislocation density tensor to the lattice curvature. This is the key ingredient of the Cosserat crystal plasticity model detailed in [FCS97]. It is also well-known that the dislocation density tensor is also related to the curl of the plastic deformation, which in turn led to the second grade approach settled by Mindlin [ME68] and more recently by Fleck and Hutchinson [FH97].

One should note that the approach proposed by Aifantis [Aif87] is not directly related to the dislocation density tensor although it also accounts for size effects in plasticity. The basic ingredient of this theory is related to the dislocation patterning during deformation and not from the GND. In the previous Aifantis models, the internal variable is then limited to the scalar dislocation density (so-called density of statistically stored dislocations) or the cumulative plastic strain.

In the following, two representative theories for size effect are presented: the Cosserat theory and the strain gradient theory.

Cosserat plasticity

The degree of freedom and modeling variables of the Cosserat theory are the displacement **u**, the micro-rotation **φ** and their gradients.

$$(\mathbf{u}, \mathbf{\varphi}, \nabla\mathbf{u}, \nabla\mathbf{\varphi}) \tag{II-2-1}$$

Until now, the physical meaning of micro-rotation **φ** has not been specified. It is in fact intended to coincide with the notion of crystal lattice rotation, so that the Cosserat directors are simply lattice directions defined in the released isoclinic configuration introduced in [Man73].

For the strain measure, Cosserat strain $\mathbf{\varepsilon_c}$ and second rank tensor for curvature $\mathbf{\kappa}$ are introduced and these can be divided into elastic and plastic quantities.

$$\mathbf{\varepsilon_c} = \nabla\mathbf{u} + \mathbf{\varepsilon_{ijk}} \cdot \mathbf{\varphi} = \mathbf{\varepsilon_c^e} + \mathbf{\varepsilon_c^p} \tag{II-2-2}$$

$$\mathbf{\kappa} = \nabla\mathbf{\varphi} = \mathbf{\kappa^e} + \mathbf{\kappa^p} \tag{II-2-3}$$

where $\mathbf{\varepsilon_{ijk}}$ is the third order permutation tensor whose components give the sign of the micro-rotation. The definition of Cosserat relative deformation implies that the skew-symmetric part of elastic deformation $\mathbf{\varepsilon_c^e}$ measures the difference between lattice and Cosserat rotation. The constraint that $\mathbf{\varepsilon_c}$ has to be symmetric must therefore be added for the micro-rotation to have the wanted physical meaning.

The free energy $\Psi(\mathbf{\varepsilon_c^e}, \mathbf{\kappa^e})$ is a function of elastic deformation and curvature. The state laws for defining the stress measures are defined by the free energy function, where the state laws are deduced from the analysis of the entropy principle.

$$\mathbf{\sigma_c} = \rho^{Cosserat} \frac{\partial\Psi}{\partial\mathbf{\varepsilon_c^e}} \tag{II-2-4}$$

$$\mathbf{M} = \rho^{Cosserat} \frac{\partial\Psi}{\partial\mathbf{\kappa^e}} \tag{II-2-5}$$

where $\mathbf{\sigma_c}$ and $\mathbf{M}$ are stress tensors and couple stress tensor, respectively and $\rho^{Cosserat}$ is a coefficient. This leads to the following intrinsic dissipation.

$$D^i = \mathbf{\sigma_c} : \dot{\mathbf{\varepsilon}}_c^p + \mathbf{M} : \dot{\mathbf{\kappa}}^p \tag{II-2-6}$$

Here, two constitutive equations are deduced. The elastic constitutive equations require two symmetric fourth rank tensors of elastic modulii $\mathbf{C^C}$ and $\mathbf{C^D}$ having the dimension of MPa and MPa·m^2, respectively.

$$\mathbf{\sigma_c} = \mathbf{C^C} : \mathbf{\varepsilon_c} \tag{II-2-7}$$

$$\mathbf{M} = \mathbf{C^D} : \mathbf{\kappa} \tag{II-2-8}$$

We resort here to two dissipation potentials $f_1^c(\mathbf{\sigma}, R)$ and $f_2^c(\mathbf{M}, R)$. This corresponds to a multi-criterion framework, involving two plastic multipliers.

$$\dot{\boldsymbol{\varepsilon}}_\mathbf{c}^\mathbf{p} = \lambda_1^c \frac{\partial f_1^c}{\partial \boldsymbol{\sigma}_\mathbf{c}} \tag{II-2-9}$$

$$\dot{\boldsymbol{\kappa}}^\mathbf{p} = \lambda_2^c \frac{\partial f_2^c}{\partial \mathbf{M}} \tag{II-2-10}$$

Note that the choice of the proper plastic multiplier to be used in the evolution equation for hardening variable (II-2-9) and (II-2-10) depends on the specific type of hardening laws and number of internal variables. Let us specify the potentials retained to model Cosserat crystal plasticity.

$$f_1^c = |\tau|, \quad with \quad \tau = \boldsymbol{\sigma}_\mathbf{c} : (\mathbf{m} \otimes \mathbf{n}) \tag{II-2-11}$$

$$f_2^c = |m^\tau|, \quad with \quad m^\tau = \mathbf{M} : (\boldsymbol{\xi} \otimes \mathbf{m}) \tag{II-2-12}$$

where

$$\boldsymbol{\xi} = \mathbf{n} \times \mathbf{m} \tag{II-2-13}$$

A coupling must exist between the different hardening variables of the model to give rise to size effects. In contrast, in the specific second gradient model, the coupling is introduced directly by a single criterion and plastic multiplier. Within the present Cosserat model, the flow rules become.

$$\dot{\boldsymbol{\varepsilon}}_\mathbf{c}^\mathbf{p} = \dot{\gamma}(\mathbf{m} \otimes \mathbf{n}) \tag{II-2-14}$$

$$\dot{\boldsymbol{\kappa}}^\mathbf{p} = \frac{\dot{\theta}}{l_{pc}}(\boldsymbol{\xi} \otimes \mathbf{m}) \tag{II-2-15}$$

where γ, θ and l_{pc} are resolved shear strain, resolved curvature and a characteristic length, respectively.

The two plastic multipliers are rewritten according to (II-2-9)~(15).

$$\lambda_1^c = \dot{\gamma} sign(\tau) \tag{II-2-16}$$

$$\lambda_2^c = \frac{\dot{\theta}}{l_{pc}} sign(m^\tau) \tag{II-2-17}$$

The meaning of the second plastic multiplier therefore is that of a scalar curvature rate, for example, the ratio of a rotation rate by a characteristic length.

The power densities of internal forces p^i and contact forces p^c are used to derive two balance equations, named balance of momentum and balance of moment of momentum.

$$p^i = \boldsymbol{\sigma}_\mathbf{c} : \dot{\boldsymbol{\varepsilon}}_\mathbf{c} + \mathbf{M} : \dot{\boldsymbol{\kappa}} \tag{II-2-18}$$

$$p^c = \mathbf{t^{sur}} \cdot \dot{\mathbf{u}} + \mathbf{m^{sur}} \cdot \boldsymbol{\varphi} \tag{II-2-19}$$

where the traction and couple vectors acting on a surface element are denoted by $\mathbf{t^{sur}}$ and $\mathbf{m^{sur}}$.
The balance and boundary conditions then read.

$$div\,\boldsymbol{\sigma}_c = 0, \quad div\,\mathbf{M} - \boldsymbol{\varepsilon}_c : \boldsymbol{\sigma}_c = 0 \tag{II-2-20}$$

$$\mathbf{t^{sur}} = \boldsymbol{\sigma}_c \cdot \mathbf{n^{sur}}, \quad \mathbf{m^{sur}} = \mathbf{M} \cdot \mathbf{n^{sur}} \tag{II-2-21}$$

Second grade constitutive framework

The degree of freedom and the modeling quantities of the theory are the displacement field and its first and second gradients.

$$\left(\mathbf{u}, \nabla\mathbf{u}, \nabla\nabla\mathbf{u}\right) \tag{II-2-22}$$

The corresponding strain measures are the second order strain tensor ε, which is the same as the classical definition, and its gradient ($\boldsymbol{\eta} = \nabla\boldsymbol{\varepsilon}$). They are split into elastic and plastic contributions.

$$\boldsymbol{\varepsilon} = \boldsymbol{\varepsilon}^\mathbf{e} + \boldsymbol{\varepsilon}^\mathbf{p} \tag{II-2-23}$$

$$\boldsymbol{\eta} = \boldsymbol{\eta}^\mathbf{e} + \boldsymbol{\eta}^\mathbf{p} \tag{II-2-24}$$

Here it is assumed that the plastic strain gradient ($\boldsymbol{\eta}^\mathbf{p}$) is not equal to the gradient of plastic strain ($\boldsymbol{\varepsilon}^\mathbf{p}$) in the theory in [FH97].

The stress tensor and couple stress tensor are defined from the energy density and previous strain measures as:

$$\boldsymbol{\sigma} = \rho^{sg}\frac{\partial\Psi}{\partial\boldsymbol{\varepsilon}^\mathbf{e}} \tag{II-2-25}$$

$$\mathbf{M^{sg}} = \rho^{sg}\frac{\partial\Psi}{\partial\boldsymbol{\eta}^\mathbf{e}} \tag{II-2-26}$$

The authors in [FH97] and [SFV01] propose a simplified version of elasticity constitutive equations including the usual four-rank tensor of elasticity modulii $\mathbf{C^E}$ and additional intrinsic length scale l_e.

$$\boldsymbol{\sigma} = \mathbf{C^E} : \boldsymbol{\varepsilon}^\mathbf{e} \tag{II-2-27}$$

$$\mathbf{M^{sg}} = l_e^2 \mathbf{C^E} : \boldsymbol{\eta}^\mathbf{e} \tag{II-2-28}$$

The intrinsic dissipation can be written as followed

$$D^i = \boldsymbol{\sigma} : \dot{\boldsymbol{\varepsilon}}^\mathbf{p} + \mathbf{M^{sg}} \vdots \boldsymbol{\eta}^\mathbf{p} \tag{II-2-29}$$

In contrast to two plastic potentials used in the Cosserat theory, only one potential function $f^{sg}(\boldsymbol{\sigma}, \mathbf{M})$ is used for defining plastic strain measures.

$$\dot{\boldsymbol{\varepsilon}}^\mathbf{p} = \lambda^{sg}\frac{\partial f^{sg}}{\partial\boldsymbol{\sigma}} \tag{II-2-30}$$

$$\dot{\mathbf{\eta}}^{\mathbf{p}} = \lambda^{sg} \frac{\partial f^{sg}}{\partial \mathbf{M}^{\mathbf{sg}}} \tag{II-2-31}$$

where λ^{sg} is the plastic multiplier of strain gradient theory. If we assumed the particular case of rate-independent plasticity for simplicity, The potential functions are derived by extended Schmid law with not only resolved shear stresses but also resolved hyper stresses and related constitutive length l_p^{sg}.

$$f = |\tau| + \frac{|m^{sg}|}{l_p^{sg}}, \quad with \ \tau = \mathbf{\sigma} : (\mathbf{m} \otimes \mathbf{n}), m^{sg} = \mathbf{M}^{\mathbf{sg}} : (\mathbf{m} \otimes \mathbf{n} \otimes \mathbf{m}) \tag{II-2-32}$$

Hence, the plastic strain and strain gradient rates follow from the normality rules.

$$\dot{\mathbf{\varepsilon}}^{\mathbf{p}} = \dot{\gamma}(\mathbf{m} \otimes \mathbf{n}) \tag{II-2-33}$$

$$\dot{\mathbf{\eta}}^{\mathbf{p}} = \dot{\gamma}^{S}(\mathbf{m} \otimes \mathbf{n} \otimes \mathbf{m}) \tag{II-2-34}$$

For the sake of simplicity, we have introduced only the effect of slip gradient in the slip direction m, although the original model also contains a contribution of slip gradient in the slip normal direction n. It must be noticed that the slip gradient variable γ^S does not coincide with the gradient of slip $\triangledown\gamma$.

Both are related to the plastic multiplier λ^{sg} according to (II-2-30) ~ (34).

$$\lambda^{sg} = \dot{\gamma} sign(\tau) = l_p^{sg} \dot{\gamma}^{S} sign(m^{sg}) \tag{II-2-35}$$

Therefore, for monotonous loading, the slip gradient variable γ^S turns out to be equal to the amount of slip γ divided by l_p^{sg}.

These stress tensors and associated strain measure make the power densities of internal and contact forces.

$$p^i = \mathbf{\sigma} : \dot{\mathbf{\varepsilon}} + \mathbf{M}^{sg} \vdots \dot{\mathbf{\eta}} \tag{II-2-36}$$

$$p^c = \mathbf{t}^{\mathbf{sur}} \cdot \dot{\mathbf{u}} + \mathbf{m}_{\mathbf{sg}}^{\mathbf{sur}} \cdot D_n \mathbf{u} \tag{II-2-37}$$

where D_n, $\mathbf{t}^{\mathbf{sur}}$ and $\mathbf{m}_{\mathbf{sg}}^{\mathbf{sur}}$ are the normal gradient operators acting on a surface with normal vector $\mathbf{n}$, the traction vectors and double force vectors on the surface, respectively.

The balance and boundary conditions are derived as followed.

$$div \ \mathbf{\tau}^{\mathbf{sg}} = 0, \quad with \ \mathbf{\tau}^{\mathbf{sg}} = \mathbf{\sigma} - div \ \mathbf{M}^{sg} \tag{II-2-38}$$

$$\mathbf{t}^{\mathbf{sur}} = \mathbf{\tau}^{\mathbf{sg}} \cdot \mathbf{n} + 2R\mathbf{M}^{sg} : (\mathbf{n} \otimes \mathbf{n}) - D_t (\mathbf{M}^{sg} \cdot \mathbf{n}), \mathbf{m}_{\mathbf{sg}}^{\mathbf{sur}} = \mathbf{M}^{sg} : (\mathbf{n} \otimes \mathbf{n}) \tag{II-2-39}$$

Where D_t is a tangent gradient operators acting on a surface.

2.2 Proposition of a simplified strain gradient model

As shown above, the recent theories for size effects generally need extra degrees of freedoms and additional constitutive rules. It means that these theories strongly increase the calculation time and they can not be easily implanted into general FEM. Besides, any of these theories do not have a general solution for complex contact boundary conditions. Therefore, FEM simulations using these theories can only be realized for simple loading conditions or very small deformations. They can not solve nanoindentation problems for which contact boundary conditions are required.

In this work, we propose an alternative theory which can also reproduce size effects, which has no extra degree of freedom and no extra constitutive rules. Hence it can be easily implanted in general FEM solvers and with few extra costs in term of computation time. In this theory, size effect comes from an extra stress measure induced by the difference between the local deformation and the global averaged deformation.

First, the origin of the extra stress source is introduced, which gives physical back ground of the theory. Then, the proposed theory is presented.

Microscopic effect of Nye tensor as an origin of extra stress

Many authors insist that Nye tensor, which is vector summation within a given volume, induces extra stress related to size effect. Therefore most of recent theories for size effect are based on mathematical effect of the Nye tensor, but they all focus on the effect of the Nye tensor as a macroscopic point of view. The Nye tensor can also be considered as a microscopic contributor to the size effect. As an example, one could consider the effect of the Nye tensor on the dislocation movement.

We have verified the effect of Nye tensor on the dislocation motion using simple dislocation dynamics simulation. This gives several clues about the effect induced on the global plastic deformation of materials.

Nye tensor, $\boldsymbol{\alpha_{nye}}$, is defined as the following quantity implying both the line direction and the Burgers vector at a given material point $\mathbf{x}$ averaged over a volume: $\boldsymbol{\alpha_{nye}} = <\mathbf{b(x)} \otimes \boldsymbol{\xi}(\mathbf{x})>$.

For sake of simplicity, in the following, the definition of Nye tensor is simplified as the equivalent vector produced by the simple summation of Burgers vectors within a given volume. It is named $\mathbf{S_{Nye}}$.

$$\mathbf{S_{Nye}} = \sum \vec{\mathbf{b}} \qquad \text{(II-2-40)}$$

Figure II-2-1 depicts two sets of dislocations array with the same number of dislocations, but

different orientations of the Burgers vector. Since all the dislocations in figure II-2-1 (a) have the same directions, Burgers vectors of these dislocations are the same, so that S_{Nye} should be 6**b**. On the other hand in figure II-2-1 (b), half of the dislocations have opposite Burgers vectors, which make a zero component of the S_{Nye}.
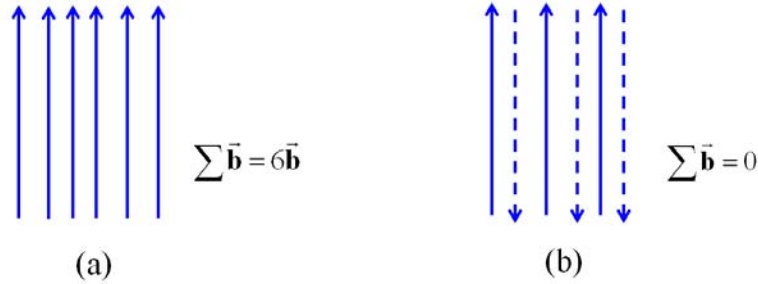

Figure II-2-1. Examples of dislocation arrays
(a) all of the Burgers vector are the same → high Nye tensor
(b) Mixed Burgers vectors with half and half ratio → zero Nye tensor

These two arrays should have a different effect on the dislocation movement since the induced internal stress is very different. According to recent theories, dislocation array like figure II-2-1 (a) makes more extra hardening that can be related to size effect than the array in figure II-2-1 (b). We can image in that a dislocation will have more difficulties to move in presence of an array with a high value of Nye tensor, i.e. a large number of polarized dislocations in its neighborhood. Therefore, dislocation dynamics simulation is a suitable tool that can be used to test the effect of the Nye tensor on dislocation movement.

First, a dislocation is forced to move through the two arrays as depicted in figure II-2-2 and results are analyzed in terms of Nye tensor effect. Figure II-2-2 (a) corresponds to the case of a dislocation moving through forest dislocations with the same directional Burgers vector. When the moving dislocation meet the first forest dislocation, the two dislocations reacts in order to minimize the line energies. This could lead to the formation of a junction if the configuration is favorable. Thus, the moving dislocation changes its shape to minimize the interaction energy. If the moving dislocation has enough energy to break the junction, it will move through the first forest dislocation with a modified shape. After the first reaction, the moving dislocation does not need to change its shape anymore when it meets another forest dislocation because it already has the shape needed for minimizing the breaking energy of the junction. Therefore the moving dislocation moves through the other forest dislocations without any need of changing the shape and consequently it does not require any increase of the applied stress.

On the other hand, figure II-2-2 (b) shows the case of a mobile dislocation moving through a statistic (none polarized) set of forest dislocations made of two opposite directional Burgers

vectors. When the moving dislocation meets the first forest dislocation, it will make a junction with the forest dislocation like in situation in figure II-2-2 (a). Then it changes its shape to minimize the energy needed for breaking the junction and moves through the first forest dislocation with the changed shape. After moving through the first forest, the moving dislocation will meet another forest dislocation with a different Burgers vector direction. Hence, it should stop to make another type of junction and changes its shape again to minimize the interaction energy for breaking the new junction. After changing into its new shape again, it can move through the second forest dislocation. Every time the moving dislocation encounters a forest dislocation the same feature is repeated: the moving dislocation stops to make a junction, changes its shape for minimum energy and moves through the forest dislocation.
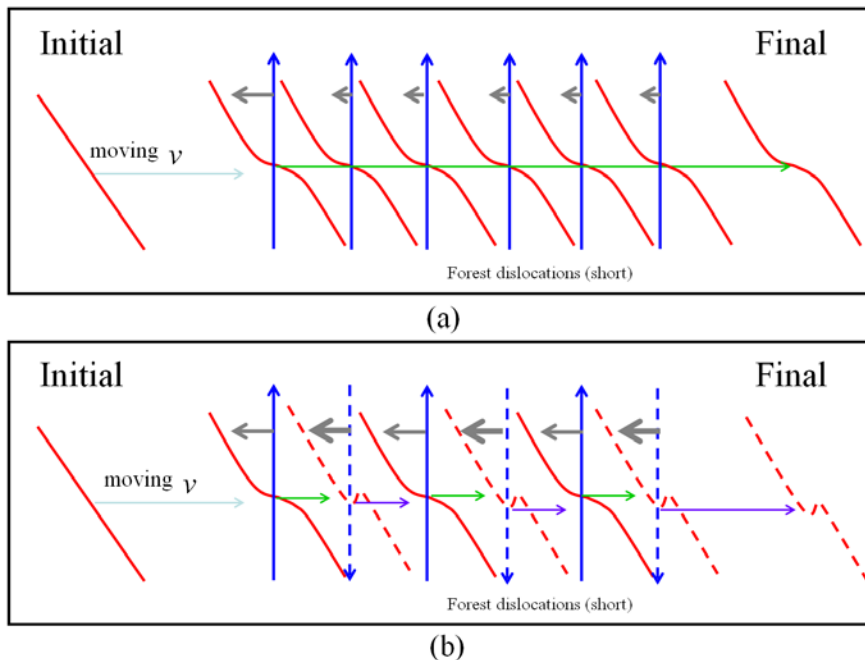

Figure II-2-2. Synopsis of dislocation movement through two kinds of dislocation array
(a) through array with high value of Nye tensor (b) through array with low value of Nye tensor

This repetition will take much time and energy to move the dislocation. Therefore, the figure II-2-2 shows that a smaller S_{Nye} magnitude makes it harder to move a dislocation. In other words, smaller Nye tensor values will give higher stress for plastic deformation. It is exact opposite results to the belief about a role of Nye tensor. Following this reasoning one could think that the Nye tensor should not affect dislocation motion.

However, reality can be different, especially when we account for long range stresses. Another situation is depicted in figure II-2-3. A dislocation moves in proximity to two arrays of forest

dislocations inducing long range forces. For sake of simplicity, the array of forest dislocations is assimilated to a single super dislocation whose Burgers vector is equivalent to that induced by the resulting Nye tensor. On one hand, the dislocation group sharing the same directional Burgers vector induces a strong long range stresses. On the other hand, the dislocations with different Burgers vectors decrease the stress field amplitude. In other world, higher value of Nye tensor increases the long range stress field and vice versa. Hence, moving a dislocation near the forest dislocation array with a high value of Nye tensor is more difficult, than moving a dislocation near the forest dislocation array with a zero value of the net Burgers vector. The results shown in figure II-2-3 are then opposed to the previous situation. The Nye tensor effect should affect dislocation motion through the long range forces.
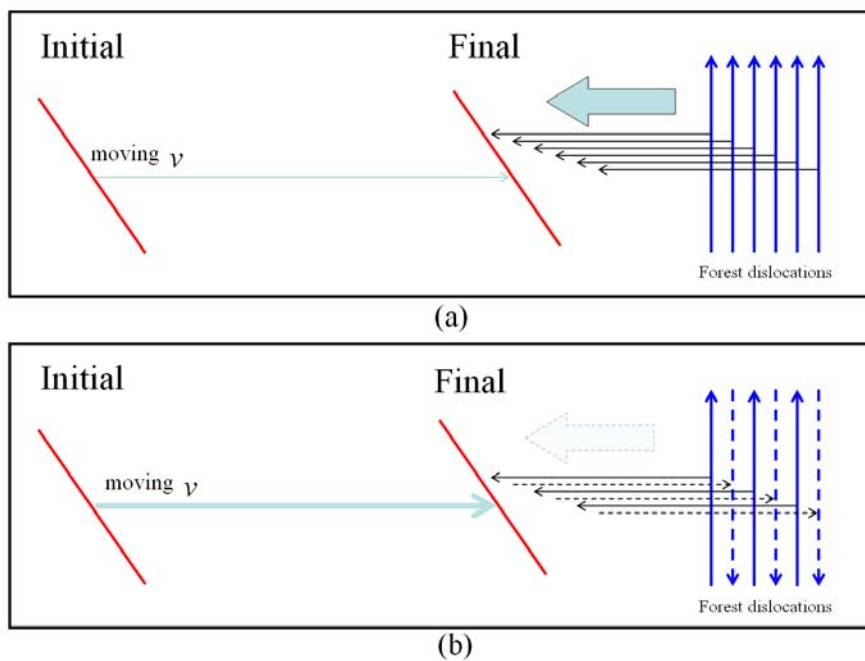

Figure II-2-3. Synopsis of dislocation movement beside two kinds of dislocation array

(a) through array with high Nye tensor (b) through array with low Nye tensor

Figure II-2-4 shows a last situation helpful for understanding the effect of Nye tensor of dislocation mobility. It corresponds to the case of a moving dislocation pushed through an array of forest dislocations located near another array of polarized forest dislocations. Figure II-2-4(a) depicts that the moving dislocation moves through the forest dislocation array with a high Nye tensor value, changes its shape and is also affected by the long range forces induced by the other forest dislocation group nearby. If the shape of the moving dislocation minimizes the energy needed to shear the forest dislocation array with a given Nye tensor value, the new shape must

also minimize the long range force induced by any forest dislocation array in the neighborhood provided the Nye tensor is similar to that of the sheared forest dislocations. Inversely, the shape should also maximize the long range force induced by a forest dislocation array with the opposite Nye tensor. Therefore, a moving dislocation as shown in figure II-2-4 (a) is affected with a minimum long range force whereas the moving dislocation shown in figure II-2-4 (b) is strongly affected by the long range forces induced by the forest dislocation group nearby. This result indicates that there exists a complex coupling between local reactions and long-range forces.
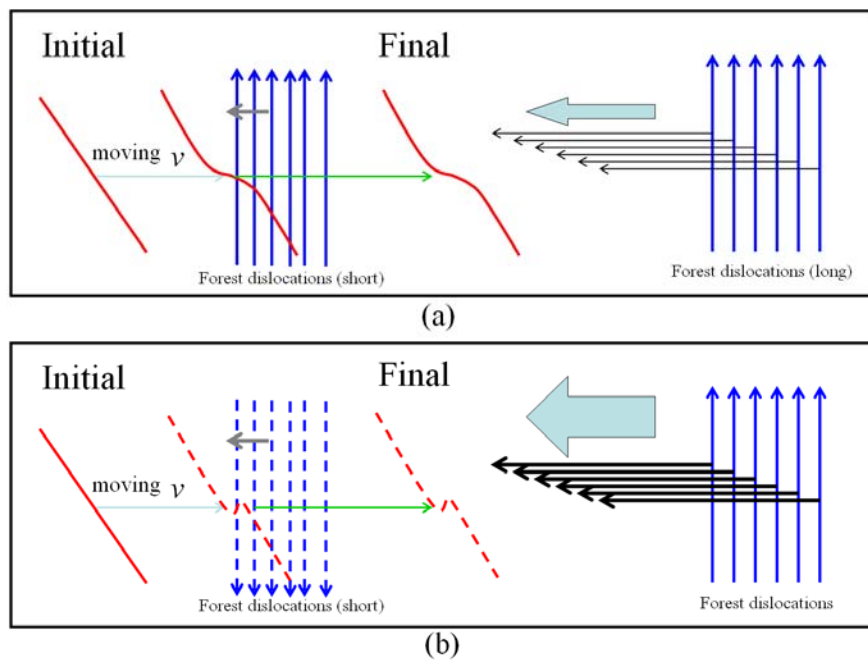

Figure II-2-4. Synopsis of dislocation movement through dislocation array near forest dislocations (a) two arrays with same Nye tensor (b) two arrays with opposed Nye tensor

Figure II-2-5 gives a schematic diagram about the effect of forest dislocation groups with a given Nye tensor on dislocation mobility. A dislocation moves with two types of interactions due to different forest dislocation groups. One corresponds to a short range interaction and the other one to long range forces. The classical crystal plasticity theory like the model described in Chapter II-1 only considers the short range interactions.

In order to account for size effects, however, the long range forces should also be considered. Therefore we need to describe the long range interactions in the frame of continuum mechanics. The key parameters are the distance between the moving dislocation and the forest dislocation group and the difference in term of Nye tensors between the short range forest dislocation

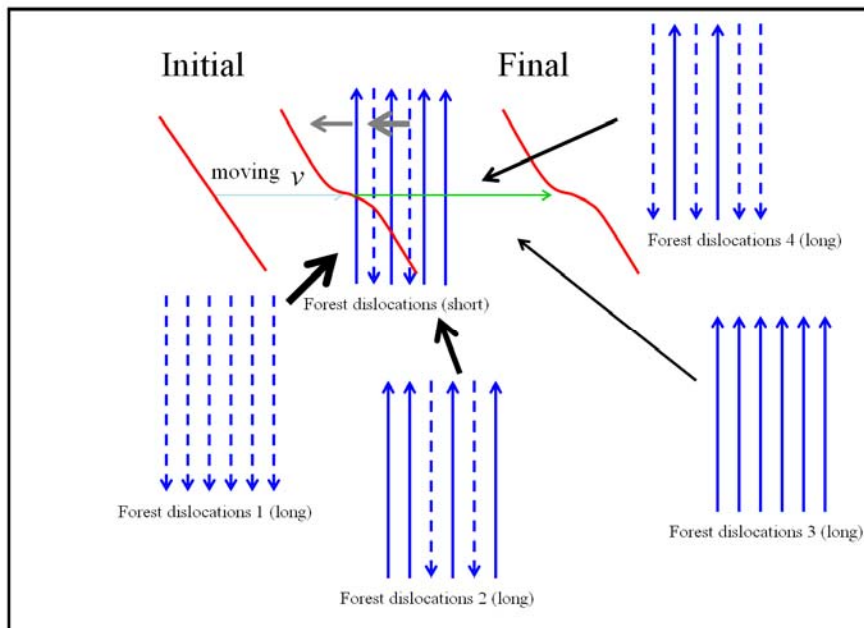groups and the long range forest dislocation groups.

Figure II-2-5. Synopsis of dislocation motion through forest dislocation groups with different Nye tensor

There exists recent theories which could explain size effects but they are usually complex because they use additional degrees of freedom and more constitutive laws. Here, we introduce a new concept without any extra degree of freedom or any new constitutive equation which in turn will reduce the CPU time and facilitate the implantation in general FEM softwares.

Model for size effect based on averaged strain

The global deformation of a material is closely related to the dislocations stored inside the material. The three figures in figure II-2-6 show schematically both the shape of a piece of material and the associated dislocations located inside the material. Figure II-2-6 (a) depicts the initial state of the material and the initial dislocation microstructure. When the material is loaded (here in pure shear), it starts to deform by movement of dislocations. Figure II-2-6 (c) depicts the final state of the material after the applied forces are removed. During the deformation process, the total number of dislocations inside the material increases because of the dislocation interactions. Here there is no need to introduce size effect theory and classic theories perfectly explain this situation very well mathematically using the classical Orowan equation.

The deformation state is homogeneous everywhere inside the material, at least for the two states

described in figure II-2-6 (a) and (c). On the opposite, the plastic strain is not homogeneous during the deformation process and this may induce size effects. Let's take the intermediate state as shown in figure II-2-6 (b).
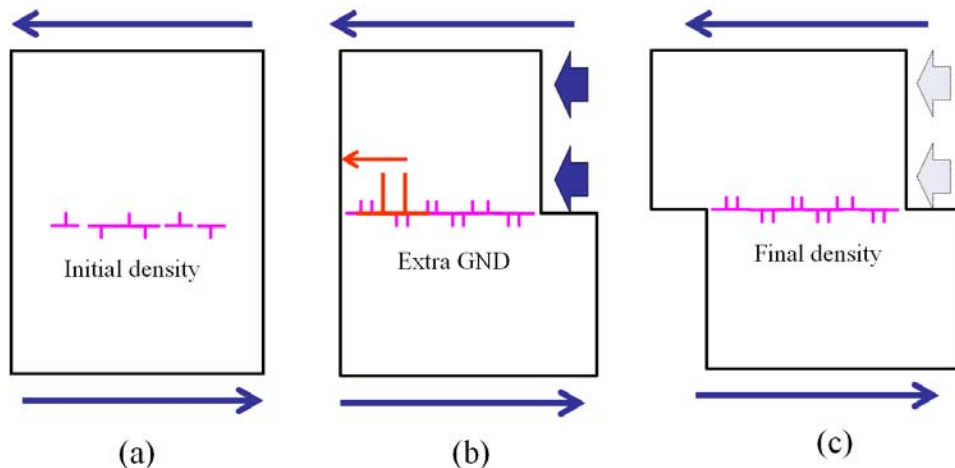

Figure II-2-6. Scheme describing both the shape of a deformed material with the associated dislocations. (a) initial state of the material (b) intermediate state (c) final state.

At this deformation stage, the piece of material is deformed heterogeneously. GNDs and extra forces are generated to compensate for the heterogeneous shape. By definition, the GND can move by the application of the applied loading. When the GND move through a free surface of the material the GND and the extra forces disappear and give raise to the homogeneous like in figure II-2-6 (c). In other words, we assumed that the theories for size effect like theories of GNDs, Cosserat and strain gradient are closely related to non-homogeneous and transient deformation inside a strained material.

Note that this description is similar to the strain gradient theory or Cosserat theory which explains that the extra forces at the origin of size effects are due to strain gradients or local rotations inside the material. Figure II-2-7 explains the non-homogeneous deformation state from several theories.

Figure II-2-7 (a) shows a description in term of dislocation dynamics. The big red dislocations represent GND and the others represent SSD. GNDs are related to material deformation and especially curvature of the crystal lattice. When the material is deformed, the GND is generated to accommodate the applied loading one can imagine that the GND induce extra force related to size effect.

The point of view expressed by strain gradient theories or Cosserat theory is shown in figure II-2-7 (b). In these theories, each local site in the material has its own strain and strain gradient or local rotation between neighbor sites. The extra forces related to size effects come from the

strain gradient or local rotations. The GND in figure II-2-7 (a) is represented by the strain gradient or local rotations in figure II-2-7 (b).
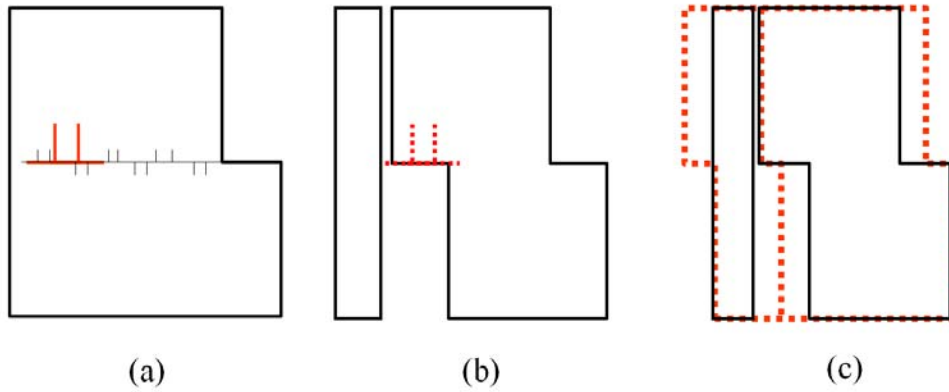

Figure II-2-7. Explanation of different non-homogeneous deformation state
(a) from GND theory (b) from Strain gradient or Cosserat theory
(c) from difference of local and global deformation

Because we assumed that a lower force is needed when the material deforms homogeneously, the source of extra hardening related to size effect can also be explained by the difference between the local deformation and a virtual global homogeneous deformation as shown in figure II-2-7 (c). The virtual homogeneous deformation can be estimated by averaging the local deformation inside the material. This assumption relies on the same concept as the strain gradient theory in the sense that a difference of strain generates the extra force.

The originality of this proposition is that the extra forces come from strain difference between local strain and its global averaged strain, not the difference between neighbor local strains. Then, we do not need any extra degree of freedom and more constitutive equations. We just need to calculate the average strain and to compare it with the local strain. This will generate extra local force explicitly.

In the following, we will detail the method used to get an extra force from the strain difference between local and global averaged strain. We should consider two types of differences: the global strain could be higher than the local strain or it could lower as shown in figure II-2-8. In practice, we don't need to differentiate the two cases since both cases can be converted into one simple compaction as shown in two blue boxes in figure II-2-8. Therefore, we used the simple compression equation for calculating the extra forces.

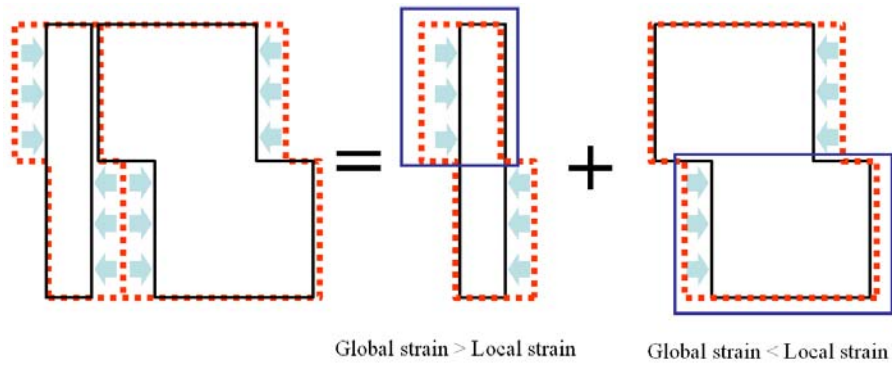Global strain > Local strain   Global strain < Local strain

Figure II-2-8. Comparison between the global averaged strain (red dot) and the local strain (black line). Though global strain could be greater or smaller than the local strain these two configurations can be represented by simple compaction (blue box)

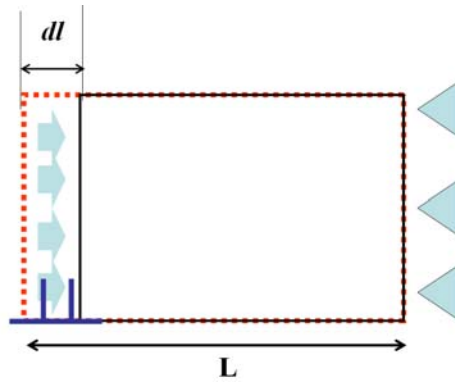Figure II-2-9 depicts the basic situation explaining the extra compression force.

Figure II-2-9. The schematic diagram for extra compression forces and related variables

Compression stresses can be written by the simple elastic equation.

$$\sigma = E\frac{dl_g}{L_g} = 2(1-\nu)\mu\frac{dl_g}{L_g} \tag{II-2-41}$$

In this equation, there are two length scale parameters, L_g and dl_g. L_g is the length related to the piece of material deformed homogeneously, i.e. the global length scale. This should be the same as the grain size or material size when we explain a grain size effect or material size effect, or it can also represent the size of the plastic zone when we explain a nano-indentation size effect. The dl_g represents the difference between global averaged strain and local strain. The length of difference can be written as followed.

$$dl_g = \left|\varepsilon_{p,global} - \varepsilon_{p,local}\right| \times l_g \tag{II-2-42}$$

where $\varepsilon_{p,global}$ and $\varepsilon_{p,local}$ are global averaged strain and local strain. Here l_g is the length for

57

calculating the local strain, i.e. the local length scale. It can be related to the dislocation mean free path as used in dislocation dynamics theory.

$$l_g = l = \frac{K}{\sqrt{\rho}} \qquad \text{(II-2-43)}$$

Finally, the extra stress σ_{extra} can be estimated by merging equation (II-2-41) ~ (II-2-43).

$$\boldsymbol{\sigma}_{\mathbf{extra}} = \frac{2(1-\nu)K\mu}{L_g\sqrt{\rho}}\left|\boldsymbol{\varepsilon}_{\mathbf{p,global}} - \boldsymbol{\varepsilon}_{\mathbf{p,local}}\right| \qquad \text{(II-2-44)}$$

This extra stress will be added to the general stress computed from classical crystal plasticity theory like adding extra kinematic hardening stress.

2.3 Applications of the model

A benefit of the size effect theory proposed here relies in its simplicity. There is no extra degree of freedoms and no new constitutive equation. It just requires simple calculations to get the average strain and to derive the extra stress. Another benefit of this theory is that it is easy to implant to general FEM softwares since it has the same number of degrees of freedoms and constitutive equations as in general FEM formulations. In the following, this theory is introduced in the dislocation dynamics based crystal plasticity theory as shown in section II-1. It has been implanted into the user material subroutine (UMAT) available in ABAQUS packages [ABA04].

The numerical model is now tested in simple loading conditions. Shape and meshes used for the test are shown in figure II-2-10. It consists of a 3-dimensional cubic shape for which each edge is meshed into 5 eight-nodes elements with reduced integration. Therefore, a total number of 125 elements are used for this simple simulation. The material property used for the test simulation is chosen to represent copper single crystals as given in table II-1-3 section II-1. The bottom face of the cube is fixed, and the opposite top face has two kinds of loading conditions: either pure shear displacement (condition a) is imposed on component 13 or pure longitudinal displacement (condition b) is applied along normal direction 3. After each calculation the global stress is calculated by averaging all the stress tensors of all the elements and the global strain is directly estimated from the applied boundary conditions. Here, the global length scale, L represents the size of the plastic deformation; it is calculated by the cube root of the total volume of the plastically deformed elements. Generally, the value found for L is close to the edge length of the cube which will vary within 50, 200 and 600 μm for the different simulations. For comparison purpose, simulations with the original crystal plasticity code without extra hardening for size effect are also performed. Results are referred as the original calculation.
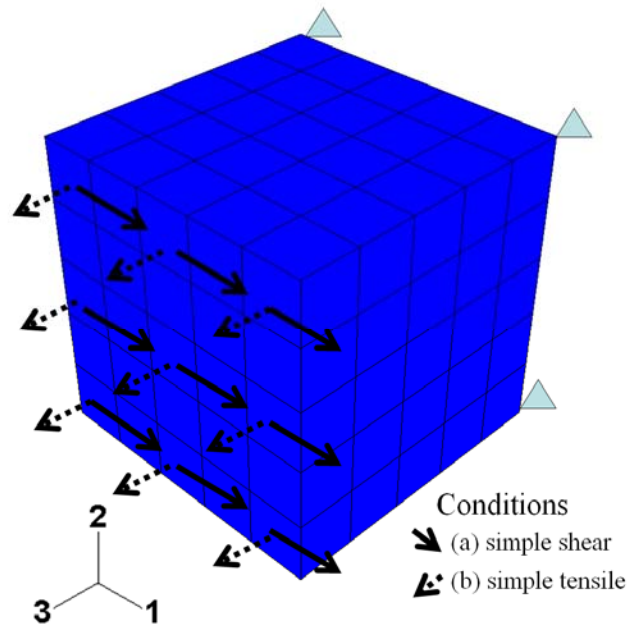
Figure II-2-10. Mesh and boundary conditions used for the test simulation.

Figure II-2-11 depicts the global loading curves plotting the global stress versus the global strain and for the different cubic sizes. Without extra hardening, the original code gives a shear stress of about 130MPa for a cumulated strain of 50 percents. The modified model shows that smaller sizes of the simulated volume give higher shear stresses. The shear stress reached for a 600 μm volume is close to 150MPa whereas for 50 μm we obtain 300 MPa, which is about 2.5 times higher than the shear stress obtained with the original code.

For tensile loading conditions (b), the tensile stress obtained at 25% of global plastic strain without extra stress is about 160MPa as shown in figure II-2-11 (b). Once again, a smaller size of the cube gives a higher tensile stress but globally, the size effect is weaker than in shear loading condition. The smaller size of 50 μm of cubic size gives only a shear stress of 220MPa, which is about 1.3 times higher than the original model.

The difference of sensibility to the volume size comes from the homogeneity of the plastic strain during the deformation process. Figure II-2-12 depicts the local strain recorded in each element versus the global strain.
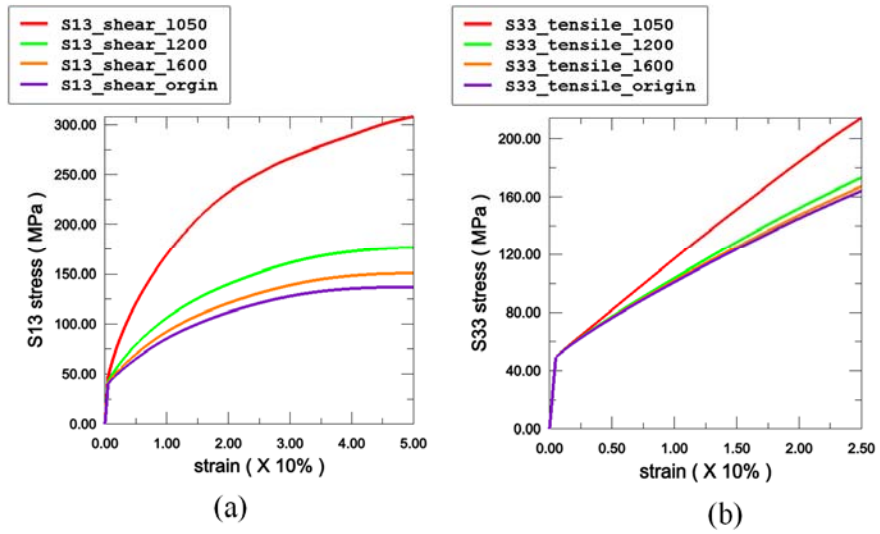
Figure II-2-11. Global loading curves plotted against the global strain

(a) shear stress for difference element sizes (b) tensile stress for difference element sizes
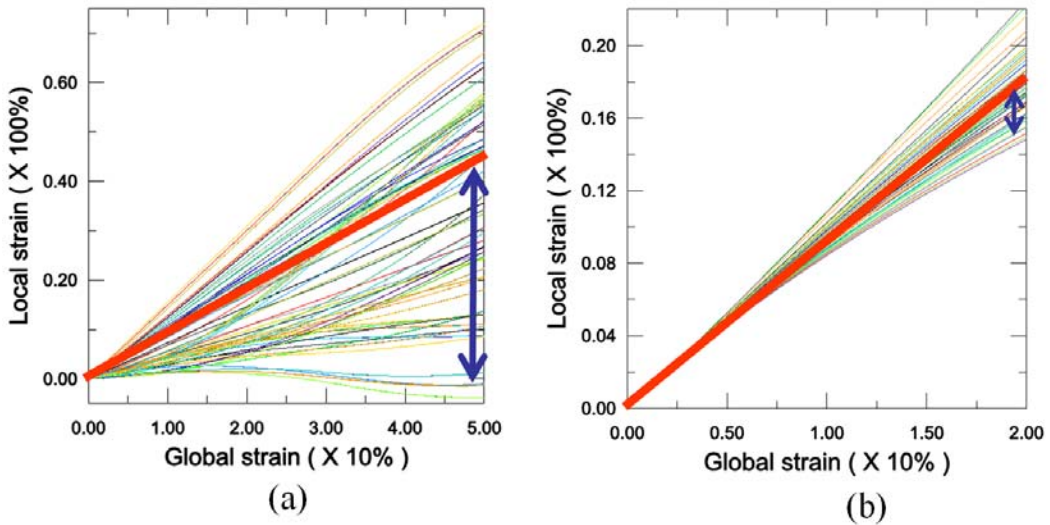
Figure II-2-12. Local strain in all the elements as function of the global strain

(a) from shear loading condition (b) from tensile loading condition

The thick red line represents the global averaged shear strain. For the shear loading conditions shown in figure II-2-12 (a), the distribution of the local strain during the deformation is very wide. In some elements the shear strain reaches negative values and in others it can be as high as twice the global shear strain. This wide distribution gives higher extra stress since the extra stress derived from the difference between local and global strains.

On the other hands, for the tensile deformation as shown in figure II-2-12 (b), the local strain distributions nearly follows the global averaged tensile strain. Although there is still a deviation to the global strain, the difference is rather small compared to the shear loading conditions. This is the main reason why tensile loading conditions display a smaller size effect. In the proposed model, a higher heterogeneity gives a larger amount of size effect.

Figure II-2-13 depicts contour of extra stress after final strain, which will show maximum extra stress regions. Both loading conditions are shown in figure II-2-13 (a) and (b).
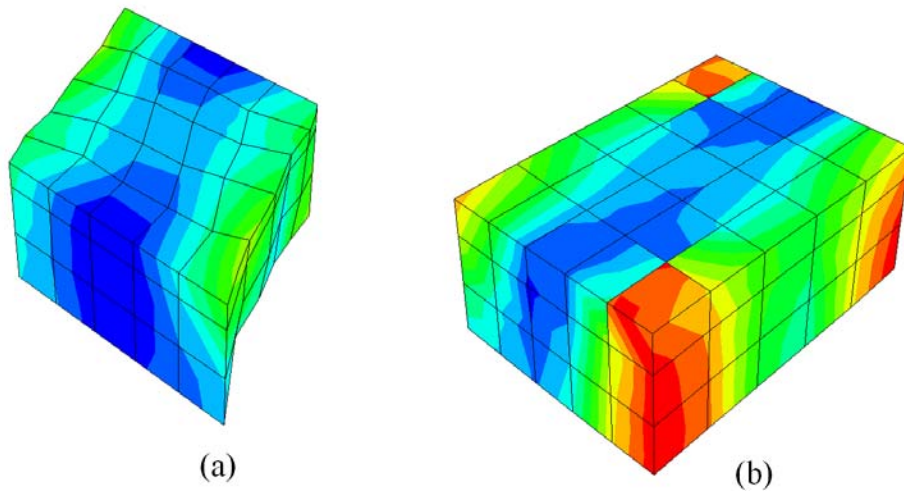
Figure II-2-13. Contour of extra stress developed at the final applied strain
(a) from shear strain condition (b) from tensile strain condition

It is shown that the top and bottom faces of the cube have the lowest extra stress. This is because the two faces are the region of the applied boundary conditions. Indeed, these regions have high tendency for the local strain to follow the global strain, which will consequently reduce the extra stress. On the other hands, the other two front and back faces of the cube are the location of the maximum extra stress. Since, the two faces are free boundary conditions region these have low constraints to the global deformation. This free constraint at the surface should give high differences to the global strain, and thus, a large extra hardening.

2.4 What should be retained from this section

- **Recent theories for size effect use**
  - Extra degree of freedoms
  - Extra constitutive equations
  - → Complexity ↑, Time consumption ↑

- **Simplified theory proposed in this section**
  - No extra degree of freedoms and constitutive equations
  - Extra stress due to size effect

$$\sigma_{extra} = \frac{2(1-\nu)K\mu}{L_g\sqrt{\rho}}\left|\varepsilon_{p,global} - \varepsilon_{p,local}\right|$$

- **The simplified model implanted into ABAQUS successfully**

3. Dislocation dynamics theory

Though, continuum theory of plasticity is a good way to investigate material behavior, it should rely on physical background in order to be predictive. This can be provided by experimental database. However it can be difficult to extrapolate the experimental database outside its range of measurements. Experiments also fail to provide some of the internal parameters such as the inherent length scale [HGW03]. This difficulty can be overcome by using dislocation dynamics (DD) approaches that directly simulate the dynamics of dislocation ensembles. Many authors have reported about this type of modeling [AG90, KCC92, RZH98, VFG98 and Sch99].

In the DD approach, the dislocation lines are discretized piecewise. The elastic stress field of the dislocation ensemble is determined within the simulation volume using dislocation theory [HL82]. Then, this stress tensor is added to the applied stress tensor enforcing the boundary conditions and the Peach-Kohler force is computed on each dislocation segments. The integrated resultant force is finally used to determine the velocity of the dislocation segments. The different DD codes differ in some details but the general algorithm is always the same: discretization of the dislocation lines, computation of the Peach Koehler Forces, derivation of the mobility law, updating the dislocation positions.

Once resolved on the dislocation moving direction, the Peach Koehler force induces a shear stress (τ^{pk}) on a given dislocation segment that can be expressed from the applied and internal stress as:

$$\tau^{pk} = \left\{\left(\mathbf{\sigma^{app}} + \mathbf{\sigma^{int}}\right)\cdot \mathbf{n}\right\}\cdot \mathbf{b} + \tau^{lt} \tag{II-3-1}$$

where $\mathbf{\sigma^{app}}$ and $\mathbf{\sigma^{int}}$ are the applied stress resulting from the boundary conditions and the internal stress induced by the dislocation segments, respectively and $\mathbf{n}$ is slip plane normal vector of given dislocation segment.

The Peierls forces should then be subtracted to get the net shear stress τ^{net}:

$$\tau^{net} = \tau^{pk} - sign\left(\tau^{pk}\right)\cdot \tau^{peierls} \tag{II-3-2}$$

Finally, the dislocation velocity can be obtained from the net shear stress as:

$$v = \frac{\tau^{net}b}{B^p} \tag{II-3-3}$$

where B^p is a Phonon drag coefficient. For a given time step dt, equation (II-3-3) allows updating the position of dislocation segment according to v.dt.

For all the DD simulation, one of the key ingredients is then the formula for calculating the stress field ($\mathbf{\sigma^{int}}$) induced by a dislocation segment. Main DD codes use analytical expressions of dislocations segments given by Li [Li65] or deWitt [Wit67]. However these expressions are only valid in the case of isotropic elasticity and in some metals such as copper, the anisotropy may play a crucial role. In the following, we propose to set up expressions of dislocation stress

fields in anisotropic media.

Next section recalls how to establish the stress field of a dislocation segment in the case of isotropic medium. Then these expressions are extended to the case of anisotropic medium. The two expressions are compared in section II-3.3.

3.1 Stress field from dislocation segment in isotropic media

<u>Displacement due to dislocation segment in isotropic media</u>

The displacement and derivation of the displacements associated with a dislocation loop of arbitrary shape is obtained in the frame of linear elasticity theory. Let consider a material of infinite extent, and suppose that a closed dislocation loop C^ρ with Burgers vector **b** produces some displacement $u(\mathbf{r})$ at point **r**. If a point force F^f acts at **r** while the dislocation is created, it induces a work given by following

$$W = \mathbf{F^f} \cdot \mathbf{u}(\mathbf{r}) = F_m^f u_m(\mathbf{r})$$
(II-3-4)

where u_m and F^f_m are the components of *u* and $\mathbf{F^f}$, respectively. If the displacement relieves the point force, it decreases the interaction energy by an amount W. Therefore, a positive value of W in equation (II-3-4) represents a decrease in the system energy. Since, there is no cross term in the elastic energy between the stress field of the dislocation and the stress field produced by the force F^f and since the dislocation line is not a sink of interaction energy, the entire energy W can also be written as the work dissipated on a surface A defined by closed loop (C^ρ) (see figure II-3-1) [HL82],
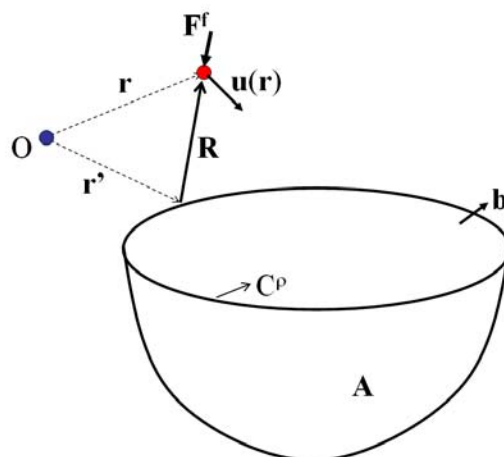

Figure II-3-1. Definition of dislocation configuration used to get the displacement field

$$W = -\int_A dA_j b_i F_m^f \sigma_{ijm}(\mathbf{r}' - \mathbf{r}) \tag{II-3-5}$$

where $F_m^f \sigma_{ijm}(\mathbf{r}'-\mathbf{r})$ is the stress σ_{ij} at $\mathbf{r}'$ caused by the components F_m^f of a point force F^f at $\mathbf{r}$. The b_i is the components of $\mathbf{b}$ and dA_j is the components of $\mathbf{dA}$, respectively.

In terms of the $u_{mk}(\mathbf{r}'-\mathbf{r})$ which is so-called Green's function and is that m[th] component of displacement caused by a unit point force applied in the kth direction at the origin, the equation (II-3-5) can be written as

$$W = -\int_A dA_j b_i C_{ijkl}^E \frac{\partial}{\partial x_l'} F_m^f u_{mk}(\mathbf{r}' - \mathbf{r}) \tag{II-3-6}$$

where the u_{mk} can be substituted in the elastic isotropic media.

$$u_{mk}(\mathbf{r}) = \frac{1}{8\pi\mu}\left(\delta_{mk}\nabla^2\mathbf{r} - \frac{\lambda+\mu}{\lambda+2\mu}\frac{\partial^2\mathbf{r}}{\partial x_m \partial x_k}\right) \tag{II-3-7}$$

where λ and δ_{ij} are the Lame constant and Kronecker delta function with the properties

$$\delta_{ij} = \begin{cases} 0 & i \neq j \\ 1 & i = j \end{cases} \tag{II-3-8}$$

Equaling equations (II-3-4) and (II-3-6) with only one non vanishing component of F^f, one obtains the displacement field u_m due to the dislocation by canceling F_m^f,

$$u_m(\mathbf{r}) = -\int_A dA_j b_i C_{ijkl}^E \frac{\partial}{\partial x_l'} u_{mk}(\mathbf{r}' - \mathbf{r}) \tag{II-3-9}$$

Equation (II-3-9) is called Burgers integral expression and is the general formula used to establish dislocation stress field.

Displacement gradient due to dislocation segment in isotropic media

Mura has demonstrated that the Burgers integral expression in equation (II-3-9) can be transformed to a line integral for the gradient of $u_m(\mathbf{r})$ [Mur63]. Because the coordinates in equation (II-3-9) are relative coordinates $d\mathbf{x}'=-d\mathbf{x}$, so the derivative of equation (II-3-9) can be written with $\mathbf{R}$

$$\frac{\partial u_m(\mathbf{r})}{\partial x_s} = b_i C_{ijkl}^E \int_A dA_j \frac{\partial^2 u_{mk}(\mathbf{R})}{\partial x_s' \partial x_l'} \tag{II-3-10}$$

where the vector $\mathbf{R}$ is the distance between the $\mathbf{r}$ and $\mathbf{r}'$.

$$\mathbf{R} = \mathbf{r}' - \mathbf{r} \tag{II-3-11}$$

This quantity enters the strains, which must be continuous across the cut A. In accord with the equilibrium equations of classical elasticity, we obtain

$$C_{ijkl}^E \frac{\partial^2 u_{mk}(\mathbf{R})}{\partial x_j' \partial x_l'} = 0 \tag{II-3-12}$$

where the **R** should not be zero.

This condition is similar to the requirement for mechanical equilibrium in the strain field of a point force. Since the surface area A can always be chosen so that $\mathbf{R} \neq 0$ on the cut surface, equations (II-3-10) and (II-3-12) can be combined to give

$$\frac{\partial u_m(\mathbf{r})}{\partial x_s} = b_i C_{ijkl}^E \int_A \left[dA_j \frac{\partial^2 u_{mk}(\mathbf{R})}{\partial x_s' \partial x_l'} - dA_s \frac{\partial^2 u_{mk}(\mathbf{R})}{\partial x_j' \partial x_l'} \right] \qquad \text{(II-3-13)}$$

Application of Stokes' theorem to equation (II-3-13) yields the line integral

$$\frac{\partial u_m(\mathbf{r})}{\partial x_s} = \varepsilon_{jsn} b_i C_{ijkl}^E \oint_C \frac{\partial}{\partial x_l'} u_{mk}(\mathbf{R}) dx_n' \qquad \text{(II-3-14)}$$

where the Stokes' theorem has the form.

$$\int_A \left(\frac{\partial \phi_f}{\partial x_j'} dA_i - \frac{\partial \phi_f}{\partial x_i'} dA_j \right) = \varepsilon_{ijk} \oint_C \phi_f dx_k' \qquad \text{(II-3-15)}$$

Equation (II-3-14) is called Mura's formula. When the dislocation is in the isotropic media, the equation (II-3-14) could be substituted by introducing the Green function in isotropic media as shown in equation (II-3-7).

$$\begin{aligned}
\frac{\partial u_m(\mathbf{r})}{\partial x_s} &= \varepsilon_{jsn} b_i C_{ijkl}^E \oint_C \frac{1}{8\pi\mu} \left(-\frac{3(\lambda+\mu)}{\lambda+2\mu} \frac{x_l' x_m' x_k'}{R^5} - \delta_{mk} \frac{\lambda+3\mu}{\lambda+2\mu} \frac{x_l'}{R^3} \right. \\
&\left. + \delta_{ml} \frac{\lambda+\mu}{\lambda+2\mu} \frac{x_k'}{R^3} + \delta_{lk} \frac{\lambda+\mu}{\lambda+2\mu} \frac{x_m'}{R^3} \right) dx_n'
\end{aligned} \qquad \text{(II-3-16)}$$

where the R is norm of the vector **R**.

<u>Stress field due to dislocation segment in isotropic media</u>

The stress field due to any arbitrary dislocation loop can be derived from the displacement gradient shown in equation (II-3-16) and following equation.

$$\sigma_{ij}^{\text{int}} = C_{ijms}^E \frac{\partial u_m(\mathbf{r})}{\partial x_s} \qquad \text{(II-3-17)}$$

This can also be a starting point to obtain the stress field from a dislocation segment as usually used in DD codes. The analytical expressions of stress field due to dislocations segment is proposed by Li [Li65].

$$\sigma_{11}^{\text{int}} = \frac{-b_1 r_2 - b_2 r_1}{R(R-r_3)} - \frac{r_1^2 (b_1 r_2 - b_2 r_1)(2R-r_3)}{R^3 (R-r_3)^2} \qquad \text{(II-3-18)}$$

$$\sigma_{22}^{\text{int}} = \frac{b_1 r_2 + b_2 r_1}{R(R - r_3)} - \frac{r_2^2(b_1 r_2 - b_2 r_1)(2R - r_3)}{R^3(R - r_3)^2} \qquad \text{(II-3-19)}$$

$$\sigma_{33}^{\text{int}} = \frac{r_3(b_1 r_2 - b_2 r_1)}{R^3} - \frac{2\nu(b_1 r_2 - b_2 r_1)}{R(R - r_3)} \qquad \text{(II-3-20)}$$

$$\sigma_{23}^{\text{int}} = \frac{r_2(b_1 r_2 - b_2 r_1)}{R^3} - \frac{\nu b_1}{R} + \frac{(1 - \nu)b_3 r_1}{R(R - r_3)} \qquad \text{(II-3-21)}$$

$$\sigma_{13}^{\text{int}} = \frac{r_1(b_1 r_2 - b_2 r_1)}{R^3} + \frac{\nu b_2}{R} - \frac{(1 - \nu)b_3 r_2}{R(R - r_3)} \qquad \text{(II-3-22)}$$

$$\sigma_{12}^{\text{int}} = \frac{b_1 r_1 - b_2 r_2}{R(R - r_3)} - \frac{r_1 r_2(b_1 r_2 - b_2 r)(2R - r_3)}{R^3(R - r_3)^2} \qquad \text{(II-3-23)}$$

3.2 Stress field from dislocation segment in anisotropic media

Equation (II-3-14) is generally valid for both isotropic and anisotropic materials. Therefore, the stress and strain fields caused by arbitrary dislocation loop in anisotropic media can be calculated once the Green's function $u_{mk}(\mathbf{R})$ for the anisotropic media is defined. Until now there is no closed form of the Green function, but many authors proposed explicit expressions to get the Green function in anisotropic media.

For a finite straight dislocation, the elastic stress field in anisotropic media can be explicitly obtained through the evaluation of a sextic equation or line integration [Wil70, Bar72, AHB73 and MM76]. Using the results for a straight segment, Willis derived a line integral expression for a curved dislocation loop [Wil70]. Mura also developed a line integral for the stress field of an arbitrarily curved dislocation loop [Mur63]. Other procedures for the elastic field of anisotropic crystals were also developed by a number of investigators. Indenbom and Orlov obtained a solution for a curved dislocation loop, which contains higher derivatives of the straight dislocation solution [IO68]. On the other hand, Lothe [Lot67] and Brown [Bro67] developed alternate solutions for the in-plane field of a planar loop. The general anisotropic theory of dislocations has been discussed by Bacon *et al*. [BBS80], Hirth and Lothe [HL82] and Mura [Mur87].

In this section, derivation of an expression based on Willis' paper is described.

Displacement and displacement gradient in anisotropic media

Equation (II-3-14) is the starting point in the analysis of Willis [Wil70], whose approach gives an integral representation for the Green function $u_{mk}(\mathbf{R})$. Using Fourier transforms, the Green's

function $u_{mk}(R)$ is immediately obtained that

$$u_{mk}(\mathbf{R}) = \frac{1}{8\pi^3} \iiint d\zeta_1 \zeta_2 \zeta_3 \frac{N_{mk}(\zeta)}{D^h(\zeta)} e^{(-i\zeta \cdot \mathbf{R})} \qquad \text{(II-3-24)}$$

In (II-3-24)

$$D^h(\zeta) = \left| L^{wil}(\zeta) \right| \qquad \text{(II-3-25)}$$

and

$$N_{mk}(\zeta) = \left(adj\ L^{wil}(\zeta) \right)_{mk} = \left(L^{wil^{-1}}(\zeta) \right)_{mk} D^h(\zeta) \qquad \text{(II-3-26)}$$

where

$$L_{ik}^{wil}(\zeta) = C_{ijkl}^E \zeta_j \zeta_l \qquad \text{(II-3-27)}$$

It should be noted for future reference that, in general, $N_{mk}(\zeta)$ is a homogeneous function of degree 4 in ζ, $D^h(\zeta)$ is a homogeneous function of degree 6 and $D^h(\zeta)=0$ only when $\zeta=0$, if all three components of ζ are real.

Equations (II-3-9) and (II-3-24) yield to the displacement field in anisotropic media.

$$u_m(\mathbf{r}) = \frac{-i}{8\pi^3} b_i C_{ijkl}^E \int_A dA_j(\mathbf{r'}) \times \iiint d\zeta_1 \zeta_2 \zeta_3 \frac{N_{mk}(\zeta)}{D^h(\zeta)} \exp(-i\zeta \cdot (\mathbf{r'} - \mathbf{r})) \qquad \text{(II-3-28)}$$

The displacement gradient field in equation (II-3-14) can also be described as the following.

$$u_{m,s}(\mathbf{r}) = \frac{-i}{8\pi^3} \varepsilon_{jsn} b_i C_{ijkl}^E \oint_C dx_n' \times \iiint d\zeta_1 \zeta_2 \zeta_3 \frac{N_{mk}(\zeta)}{D^h(\zeta)} \exp(-i\zeta \cdot (\mathbf{r'} - \mathbf{r})) \qquad \text{(II-3-29)}$$

Displacement gradient from dislocation segment in anisotropic media

Equation (II-3-28) and (II-3-29) are quite explicit but these will be reduced to usable forms especially for arbitrary dislocation segment (**r'**) which is expressed as following.

$$\mathbf{r'} = \mathbf{x^S} + t(\mathbf{x^E} - \mathbf{x^S}) \quad 0 \le t \le 1 \qquad \text{(II-3-30)}$$

Using equation (II-3-30), equation (II-3-29) thus reduces to:

$$\begin{aligned} u_{m,s}(\mathbf{r}) = \frac{-i}{8\pi^3} \varepsilon_{jsn} b_i C_{ijkl}^E \left(x_n^E - x_n^S \right) \times \int_0^1 dt \\ \times \iiint \zeta_l \frac{N_{mk}(\zeta)}{D^h(\zeta)} \exp\left(-i\zeta \cdot \left(\mathbf{x^S} - \mathbf{r} + t(\mathbf{x^E} - \mathbf{x^S})\right)\right) d\zeta_1 d\zeta_2 d\zeta_3 \end{aligned} \qquad \text{(II-3-31)}$$

In this simplified equation, several functions are set.

$$\boldsymbol{\eta}^\zeta = \frac{\zeta}{\rho^\zeta} \quad \rho^\zeta = |\zeta| \qquad \text{(II-3-32)}$$

$$d\zeta_1 d\zeta_2 d\zeta_3 = \rho^{\zeta^2} d\omega \qquad \text{(II-3-33)}$$

where $d\omega$ is an element on the unit sphere $|\boldsymbol{\eta}^{\zeta}|=1$. Remembering the homogeneity of $N_{mk}(\boldsymbol{\zeta})$ and $D^h(\boldsymbol{\zeta})$.

These substitutions reduce (II-3-31) to

$$u_{m,s}(\mathbf{r}) = \lim_{\varepsilon^{con} \to 0} \frac{-i}{8\pi^3} \varepsilon_{jsn} b_i C_{ijkl}^E \left(x_n^E - x_n^S\right) \times \int_0^1 dt \iint_{|\eta^\zeta|=1} d\omega \eta_l^\zeta \frac{N_{mk}(\boldsymbol{\eta}^\zeta)}{D^h(\boldsymbol{\eta}^\zeta)} \int_0^\infty \rho^\zeta d\rho^\zeta$$
$$\times \exp\left[-\rho^\zeta \left\{\varepsilon^{con} + i\boldsymbol{\eta}^\zeta \cdot \left(\mathbf{x}^S - \mathbf{r} + t\left(\mathbf{x}^E - \mathbf{x}^S\right)\right)\right\}\right]$$

(II-3-34)

The convergence factor ε^{con} having been inserted to enable the integrals to be evaluated in any desired order. Integrating first with respect to ρ^ζ and then with respect to t reduces (II-3-34) to the form

$$u_{m,s}(\mathbf{r}) = \lim_{\varepsilon^{con} \to 0} \frac{-i}{8\pi^3} \varepsilon_{jsn} b_i C_{ijkl}^E \left(x_n^E - x_n^S\right) \times \iint_{|\eta^\zeta|=1} d\omega \eta_l^\zeta \frac{N_{mk}(\boldsymbol{\eta}^\zeta)}{D^h(\boldsymbol{\eta}^\zeta)}$$
$$\times \frac{1}{\left\{\varepsilon^{con} + i\boldsymbol{\eta}^\zeta \cdot \left(\mathbf{x}^S - \mathbf{r}\right)\right\}\left\{\varepsilon^{con} + i\boldsymbol{\eta}^\zeta \cdot \left(\mathbf{x}^E - \mathbf{r}\right)\right\}}$$

(II-3-35)

To proceed further, we first define

$$\mathbf{n}^{wil} = \frac{\left(\mathbf{x}^S - \mathbf{r}\right) \wedge \left(\mathbf{x}^E - \mathbf{r}\right)}{\left|\left(\mathbf{x}^S - \mathbf{r}\right) \wedge \left(\mathbf{x}^E - \mathbf{r}\right)\right|}$$

(II-3-36)

We now transform the integral over the unit sphere to one over the circular cylinder, with sides parallel to n and unit radius, defined by

$$\left|\boldsymbol{\zeta} \wedge \mathbf{n}^{wil}\right| = 1$$

(II-3-37)

Then the following equation is obtained by the operation of projection

$$d\omega = \frac{dS^{cyl}}{\rho^{\zeta 3}}$$

(II-3-38)

where dS^{cyl} is the element of area on the cylinder.

The two following equations are also obtained by the projection.

$$\eta_l^\zeta \frac{N_{mk}(\boldsymbol{\eta}^\zeta)}{D^h(\boldsymbol{\eta}^\zeta)} = \rho^\zeta \frac{\zeta_l N_{mk}(\boldsymbol{\zeta})}{D(\boldsymbol{\zeta})}$$

(II-3-39)

$$\left\{\varepsilon^{con} + i\boldsymbol{\eta}^\zeta \cdot \left(\mathbf{x}^S - \mathbf{r}\right)\right\}\left\{\varepsilon^{con} + i\boldsymbol{\eta}^\zeta \cdot \left(\mathbf{x}^E - \mathbf{r}\right)\right\}$$
$$= \frac{\left\{\rho^\zeta \varepsilon^{con} + i\boldsymbol{\zeta} \cdot \left(\mathbf{x}^S - \mathbf{r}\right)\right\}\left\{\rho^\zeta \varepsilon^{con} + i\boldsymbol{\zeta} \cdot \left(\mathbf{x}^E - \mathbf{r}\right)\right\}}{\rho^{\zeta 2}}$$

(II-3-40)

Therefore, the equation (II-3-35) can be reproduced as

$$u_{m,s}(\mathbf{r}) = \lim_{\varepsilon^{con} \to 0} \frac{-i}{8\pi^3} \varepsilon_{jsn} b_i C^E_{ijkl}\left(x^E_n - x^S_n\right) \times \oint_{L^{cyl}} dS^{cyl} \int_{-\infty}^{\infty} dZ \frac{\zeta_l N_{mk}(\zeta)}{D^h(\zeta)}$$

$$\times \frac{1}{\left\{\rho^\zeta \varepsilon^{con} + i\zeta \cdot \left(\mathbf{x^S} - \mathbf{r}\right)\right\}\left\{\rho^\zeta \varepsilon^{con} + i\zeta \cdot \left(\mathbf{x^E} - \mathbf{r}\right)\right\}}$$

(II-3-41)

where

$$Z = \zeta \cdot \mathbf{n^{wil}}$$

(II-3-42)

and L^{cyl} is the contour of

$$\zeta = 0, \quad \left|\zeta \wedge \mathbf{n^{wil}}\right| = 1$$

(II-3-43)

The integral with respect to Z can be performed by noting that the integrand is $O(Z^{-3})$ when $|Z| \to \infty$. Therefore by closing the contour in the upper half of the complex Z plane and using Cauchy's theorem, we obtain

$$u_{m,s}(\mathbf{r}) = \lim_{\varepsilon^{con} \to 0} \frac{1}{4\pi^2} \varepsilon_{jsn} b_i C^E_{ijkl}\left(x^E_n - x^S_n\right) \times \sum_{N=1}^{3} \oint_{L^{cyl}} dS^{cyl} \frac{\zeta^N_l N_{mk}(\zeta^N)}{n^{wil}_k \dfrac{D^h(\zeta^N)}{\partial \zeta_k}}$$

$$\times \frac{1}{\left\{\rho^{\zeta^N} \varepsilon^{con} + i\zeta \cdot \left(\mathbf{x^S} - \mathbf{r}\right)\right\}\left\{\rho^{\zeta^N} \varepsilon^{con} + i\zeta \cdot \left(\mathbf{x^E} - \mathbf{r}\right)\right\}}$$

(II-3-44)

where

$$\zeta^N = \zeta + \mathbf{n^{wil}} Z$$

(II-3-45)

ζ being restricted to lie on L^{cyl} and $Z^N(N=1,2,3)$ are the roots of the equation

$$D^h\left(\zeta + \mathbf{n^{wil}} Z^N\right) = 0$$

(II-3-46)

which have positive imaginary parts.

The symbol $\rho^{\zeta N}$ is defined as $\rho^{\zeta^N} = \left\{1 + \left(Z^N\right)^2\right\}^{1/2}$

the branch of square root being chosen so that it is positive whenever Z^N is real. This means that $\rho^{\zeta N}$ always has a positive real part and (II-3-44) can be expressed in the simpler form

$$u_{m,s}(\mathbf{r}) = \frac{-1}{4\pi^2} \varepsilon_{jsn} b_i C^E_{ijkl}\left(x^E_n - x^S_n\right) \times \sum_{N=1}^{3} \oint_{L^{cyl}} dS^{cyl} \frac{\zeta^N_l N_{mk}(\zeta^N)}{n^{wil}_k \dfrac{D^h(\zeta^N)}{\partial \zeta_k}}$$

$$\times \frac{1}{\left\{\zeta \cdot \left(\mathbf{x^S} - \mathbf{r}\right) - 0i\right\}\left\{\zeta \cdot \left(\mathbf{x^E} - \mathbf{r}\right) - 0i\right\}}$$

(II-3-47)

The term $[\zeta(\mathbf{x^S}\text{-}\mathbf{r})\text{-}0i]^{-1}$, $[\zeta(\mathbf{x^E}\text{-}\mathbf{r})\text{-}0i]^{-1}$ behave rather like delta functions.

The result of evaluating the integral in (II-3-47) is

$$u_{m,s}(\mathbf{r}) = \frac{i}{2\pi} \varepsilon_{jsn} b_i C^E_{ijkl} \frac{\left(x^E_n - x^S_n\right)}{\left|\mathbf{x^E} - \mathbf{x^S}\right| p^{wil}} \left[f_{lmk}\left\{\zeta^*\left(\mathbf{x^S}\right)\right\} - f_{lmk}\left\{\zeta^*\left(\mathbf{x^E}\right)\right\}\right]$$

(II-3-48)

where

$$f_{lmk}(\zeta) = \sum_{N=1}^{3} \frac{\zeta_l^N N_{mk}(\zeta^{\mathbf{N}})}{n_k^{wil} \frac{\partial D^h(\zeta^{\mathbf{N}})}{\partial \zeta_k}} \qquad \text{(II-3-49)}$$

$\zeta^*(\mathbf{x^S})$ and $\zeta^*(\mathbf{x^E})$ are unit vectors in the plane of $\mathbf{r}$, $\mathbf{x^S}$ and $\mathbf{x^E}$ which are perpendicular to $(\mathbf{r} - \mathbf{x^S})$ and $(\mathbf{r} - \mathbf{x^E})$ respectively, and p^{wil} is the perpendicular distance from $\mathbf{r}$ to the dislocation line, as shown in figure II-3-2.
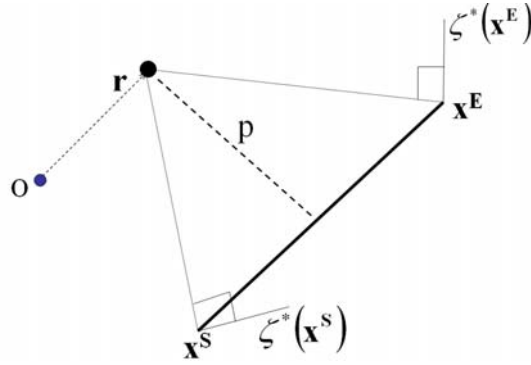

Figure II-3-2. Definition of the parameters used in Willis expression valid for anisotropic media

Equation (II-3-48) shows that the displacement gradient from arbitrary dislocation segment in anisotropic media is closed form in Fourier space. In real space, it is described as the line integral formula.

$$u_{m,s}(\mathbf{r}) = \frac{1}{4\pi^2} \varepsilon_{jsn} b_i C_{ijkl}^E \frac{(x_n^E - x_n^S)}{|\mathbf{x^E} - \mathbf{x^S}| p^{wil}} \int_0^\pi \left[g_{lmk}\{\eta^{\zeta^*}(\mathbf{x^S})\} - g_{lmk}\{\eta^{\zeta^*}(\mathbf{x^E})\} \right] \frac{1}{\sin \theta^{wil}} d\theta^{wil} \quad \text{(II-3-50)}$$

where

$$g_{lmk}(\boldsymbol{\eta}^\zeta) = \frac{\eta_l^\zeta N_{mk}(\boldsymbol{\eta}^\zeta)}{D^h(\boldsymbol{\eta}^\zeta)} \qquad \text{(II-3-51)}$$

The distortions due to any polygonal loop may be found by forming a finite sum of term like (II-3-50).

Stress field from dislocation segment in anisotropic media

Equation (II-3-50) and (II-3-17) yield to the stress field from any dislocation segment in anisotropic media.

71

$$\sigma_{pr}^{\text{int}}(\mathbf{r}) = \frac{1}{4\pi^2} \varepsilon_{jsn} b_i C_{pqms}^E C_{ijkl}^E \frac{\left(x_n^E - x_n^S\right)}{\left|\mathbf{x}^E - \mathbf{x}^S\right| p^{wil}} \int_0^\pi \left[g_{lmk}\left\{\eta^{\zeta^*}\left(\mathbf{x}^S\right)\right\} - g_{lmk}\left\{\eta^{\zeta^*}\left(\mathbf{x}^E\right)\right\} \right]$$

$$\times \frac{1}{\sin \theta^{wil}} d\theta^{wil}$$

(II-3-52)

In DD code, the integration is calculated using numerical method such as Gaussian integration method.

3.3 Comparison between equations for isotropic and anisotropic media

Stress field from dislocation loops in isotropic and anisotropic media

In order to compare the analytic formulas of isotropic and anisotropic media, stress results are computed from dislocation loops using equation (II-3-18~23) and (II-3-47).

The calculation conditions are shown in figure II-3-3. A dislocation loop made of four dislocation segment whose Burgers vector is (1 0 0) and length is 260 nm is introduce in the (z=0) plane. Two dislocation segments are edge dislocations and the other two are screw dislocations. The stress fields due to the dislocation loops are obtained at the calculation points shown by red spots forming a regular grid as shown in the figure. The calculation grid is located 26nm above the dislocation loops through the z direction. The range of calculation grid is from -5200nm to 5200nm through x and y direction. Each calculation line has 100 or 1000 points. Hence, the total number of calculation points is 10^4 or 10^6.
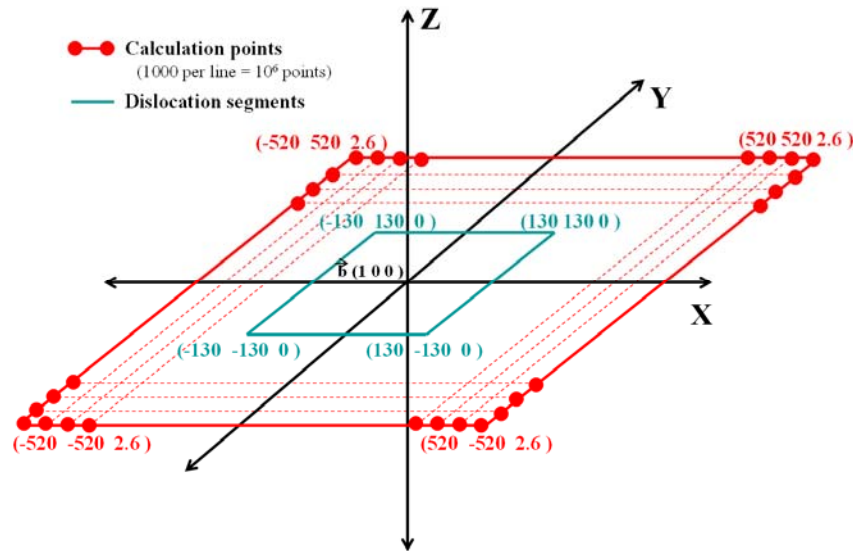

Figure II-3-3. Configuration of the dislocation loop and calculation points

The calculations need information about Burgers vectors and stiffness matrix. The length of Burgers vector is set to 0.254 nm. The stiffness matrix for isotropic media is defined by the two independent parameters, λ and μ. The stiffness matrix for the anisotropic media has three independent parameters, C_{11}, C_{12} and C_{44}. The properties for copper material are shown in table II-3-1.

Burgers vector	$\vec{\mathbf{b}}$	(1 0 0)
	$|\mathbf{b}|$	2.54 nm
Stiffness (isotropy)	λ	77.32 MPa
	μ	42.00 MPa
Stiffness (anisotropy)	C_{11}	168.40 MPa
	C_{12}	121.40 MPa
	C_{44}	75.40 MPa

Table II-3-1 Material properties for copper

Contours of shear stress field computed from both the isotropic and anisotropic media are depicted in figure II-3-4 (a) and (b) respectively. The tendencies of stress contours are quite similar. Both show that the region inside and outside the dislocation loops have negative and positive stress field, respectively and the shear stress decreases with the increasing distance from dislocation loops. On the other hand, the specific distributions near the dislocation loop, especially at the corner of the loop, are a bit different. Stress contour in isotropic media near dislocation loop has homogeneous distribution including corner region, but the contour in anisotropic media has heterogeneous distribution especially at the corner regions. The black color region which has less than -80MPa of shear stress at anisotropic media is a bit larger that one at isotropic media.
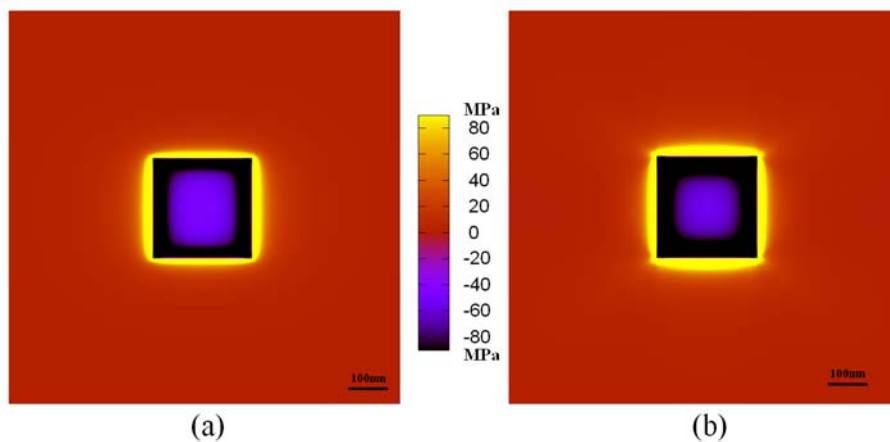

Figure II-3-4. Internal shear stress computed in (a) isotropic medium (b) anisotropic medium

The formulas for isotropic and anisotropic media are described by closed form and integral form, respectively. Since the formula of anisotropic media is described with integrals, the Gaussian integration method is used for the formula. Here for example we used 51 Gauss points on each segment. Therefore, the calculation for anisotropic media needs much time because of the integration part. The calculation time from the two calculations is summarized in table II-3-2.

# of calculations	10,000	1,000,000
Isotropic Formula	< 1 sec	1min 04 sec
Anisotropic Formula	122 sec	202min 40 sec

Table II-3-2. Calculation time needed for estimating the internal stress

For the 10000 calculation, the formula for anisotropy need about 100 times larger calculation time than the formula for isotropy. For the 1000000 calculation, the time difference between them is about 200 times.

Limitation of the formula for anisotropic media

Since the anisotropy may play a crucial role in some metals such as copper, the expressions of stress field due to dislocation loops in anisotropic media may be an important element of future DD code needed to increase the accuracy especially for the stress field near the dislocation loops.

However, the difference between the formulas decreases with increasing the distance between the dislocation loop and the calculation point. Moreover the formula for anisotropic media is not a closed form but an integration form. This consumes a lot of calculation time. The DD code for anisotropic media is about 100 times slower than the DD code for isotropic media and the difference of time consumption between isotropic and anisotropic media should be increased with the continuously increasing number of dislocation segments. This problem of time consumption makes the DD code for anisotropic media hard to be applicable to DD simulations with large deformation such as nanoindentation simulation. Because of these reasons, the DD calculation for nanoindentation described at section III-6 will be done using isotropic expressions of the dislocation stress field.

3.4 What should be retained from this section

- Formula for internal stress in anisotropic media

$$\sigma_{pr}^{int}(\mathbf{r}) = \frac{1}{4\pi^2}\varepsilon_{jsn}b_i C_{pqms}^E C_{ijkl}^E \frac{\left(x_n^E - x_n^S\right)}{\left|\mathbf{x}^E - \mathbf{x}^S\right| p^{wil}}$$

$$\times \int_0^\pi \left[g_{lmk}\left\{\eta^{\varsigma^*}(\mathbf{x}^S)\right\} - g_{lmk}\left\{\eta^{\varsigma^*}(\mathbf{x}^E)\right\}\right]\frac{1}{\sin\theta^{wil}}d\theta^{wil}$$

  - Integral form (solved by numerical solution)
  - About 200 times slower than isotropic formula

III. Indentation of copper single crystal

Indentation experiments have been used since the 18th century at least in geology to measure the hardness of materials [Tab51], thereby characterizing the strength of solids. Specific indenter geometries such as spherical or pyramidal tests have been traditionally used for material characterization of metals and ceramics [OP92, SP01 and GS90]. In addition to the mechanical characterization of microstructures of metals and ceramics, this test has been successfully applied to biological materials [LSB02] and thin film materials [DN86, OP92, FS93, BAS75, Sne65 and NG98].

In a typical instrumented indentation test, an indenter tip is driven into the material of interest at either a constant loading, displacement or deformation rate until a certain load or depth has been reached. After a short hold period, the load is gradually removed from the indenter. During this process, both load and displacement are recorded continuously. Usually, the principle goal of such test is to extract the elastic modulus and hardness of the specimen from the load displacement curve. If instrumented with "nano-" resolution in depth and load, the test is commonly called nanoindentation. The experimental recording can characterize not only elastic property and hardness, but also define the nature of theology law (visco-elastic, elasto-visco plastic etc...) and quantify some of the parameters [KLB08] of great concern for metals deforming at room temperature which is the core of this work such as elasto-plastic properties obtained in uniaxial testing (yield stress and work hardening) [FS95, TZK98, KM01, HT99, NEB02, HPO01, CL04 and CHA06]. Recently, Charleux have published a study to extract the plastic properties of materials by using inversion approach from indentation curves [CHA06]. The method has been evaluated for a wide range of material properties.

Theoretical analysis of indentation

On the other hand, analytical and experimental analysis of deformation and stress field beneath the indenter is an active field of study, since the methods for extracting the material properties are based on this analysis. These studies have been carried out for Vickers [GLV94], Berkovich [LSG96] and conical [Joh70] indenters. Many authors have also proposed analytical models. Tabor [Tab48] and Stilwell and Tabor [ST61] have shown that the recovery of the indentation during unloading can be calculated from the theory of elasticity for spherical and conical indenters. Subsequently, Johnson's spherical cavity model [Joh70] was used to predict the relationship between hardness and yield strength.

$$H = C\sigma_y$$
(III-1-1)

where H, C and σ_y are the indentation hardness, the constrained factor and yield stress,

respectively.

The methods of determining the area of contact from depth measurements are founded upon the elastic equations of contact of Hertz for a sphere and Sneddon for a cone (more generally a parabolic revolution) [Len896 and Sne65].

Doerner and Nix [DN86] and Pharr *et al*. [POB92] have modeled the loading and unloading process of indentation test by considering the contact of an indenter with an elastic half space. Most of these approaches are using isotropic elasticity.   However, micro and nanoindentation experiments are often performed on single grains or on textured or single crystal epitaxial thin films, which are elastically anisotropic.

For analysis of anisotropic material, it is assumed that elastic properties are some polycrystalline average of the elastic constants [FWK89] or correspond to the elastic modulus in the direction of the indentation [CSK90 and Doe87]. Recently, Joost J. Vlassak *et al*. [VN93, VN94 and VCB03] have shown that the indentation modulus can be calculated for arbitrary anisotropic solids using a semi-inverse approach first given by Willis [Wil66].

Indentation size effect

Size effect characterizes the observation that in some solids, hardness depends on the scale of load or depth used. This is known for a long time, and it usually manifests as "smaller is harder". Fleck *et al.* [FMA94] have pointed out that the well-known indentation size effect (ISE) for metals especially in the sub-micrometer depth regimes. This same physical description was given earlier by Stelmashenke *et al*. [SWB93] and De Guzman *et al*. [DNF93] to account for the depth dependence of the hardness.

This is in contrast to classical continuum mechanics plasticity theory where it is usually assumed that the mechanical properties of a material do not depend on the scale. Therefore, earlier researchers had proposed environmental explanation for the ISE, such as the presence of oxide layer [TS81], chemical contamination [PT79] of surface layers, inadequate measurement capability and elastic recovery of indents [Sam86], indenter-specimen friction [LGH93] and edge effects for small indents [MC95]. All of these suggestions have some merit and are likely to have contributed to the ISE. However, it has become clear that the inherent size dependence in many cases is not an artifact caused by unwanted environmental effects [SWB93, FMA94, MC95, PAF96, SE98, NG98, Gur02, ES02, KPM06, RMP07 and RMP08].

The size effect can be interpreted by models dealing with a strain gradient in the deformation field and geometrically necessary dislocations (GNDs) to accommodate this strain gradient [GHN99, AB00, HGN00, FH01, ES03 and Mug04]. Ma and Clarke [MC95] used the same physical description and recognized its connection to strain gradient plasticity. In these descriptions, statistically stored dislocations, which are created by homogeneous strain, and

geometrically necessary dislocations, which are related to strain gradients, both contribute to the flow stress. Nix and Gao [NG98] have proposed a model of GND to describe the depth dependence of hardness of crystalline materials. They assumed that the indentation is accommodated by circular loops of GNDs as shown in figure III-1-1.
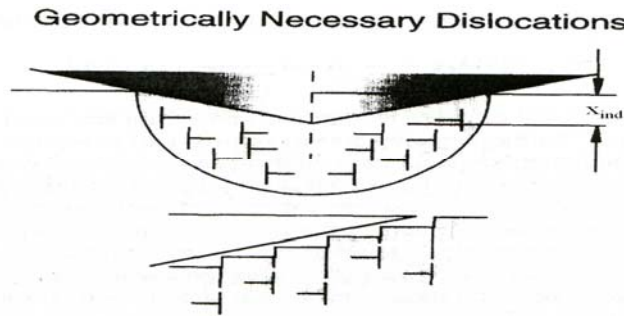

Figure III-1-1. Schematic description of conical indentation accommodated by GNDs [NG97]

The relationships between hardness and indentation depth derived by Nix and Gao can be written by following formula.

$$\frac{H}{H_0} = \sqrt{1 + \frac{x^*_{ind}}{x_{ind}}}$$
(III-1-2)

where H_0, x^*_{ind} and x_{ind} are the indentation hardness in the absence of any size effect, the length that characterizes the depth dependence of the indentation hardness and the indentation depth, respectively.

However, despite several different strain-gradient based theoretical development [FMA94, MC95, NG98, GHN99, HGN00 and FH01], no direct evidence between the strain gradient length parameter and some physical parameter of the structure of the solid has been obtained yet.

Numerical simulation of indentation

Finite element simulations have been used for explanation of mechanism of indentation experiments. Such continuum based simulations have provided an insight into the contact mechanics and the effect of strain hardening solids during nanoindentation (for isotropic material see [HSZ89, GLV94, BS95, BFN93, MF99, CV01, MAA02, MAS04, BK04, FRS04, GJS06 and MCA06] and for anisotropic materials see [WRK04, LBY05, ZRS06, EG07, COA07, ACO08 and ZRR08]). However, these simulation methods have covered one or few case of experimental results. Because these modeling incorporate phenomenological deformation law they can be used only within the experimental database used for their adjustment, and it is too difficult to extrapolate the results outside the range of measurements

using continuum theory [HGW03].

To overcome the weakness of the continuum theory at small scale, the other spectrum of simulation approach, such as atomistic and discrete dislocation dynamics simulations have been used for analyzing ultra low-load nanoindentation experiments (e.g. [KPH98, FRC98, LZF03, FDS03, MY03, ZVO04, SL04, YKJ04, LPK05, SMC05, SM06, MAS06 and TS07]). Although the results from these simulation methods are quite important for understanding the physics of indentation in terms of defect nucleation, interaction between them etc, the simulation scale and time regime of these methods are too small to cover the analysis of mechanics of nanoindentation at micro scale indentation depth.

These are the reasons why the three kinds of simulation methods, which are molecular dynamics, dislocation dynamics and finite element simulation, required to be merged in a so called multi-scale approach.

This section is dedicated to an analysis of nanoindentation of copper single crystal by various experiments and numerical simulations. Quantitative comparison between both approaches is presented. For this purpose, several new analysis methods are proposed in section III-1. Results concerning the effect of crystal surface orientation and initial dislocation densities are described in section III-2 and III-3, respectively. In section III-4, the two results from experiment and simulations are compared quantitatively. Section III-5 presents an example of the effect of a gradient of dislocation density introduced below the surface. Finally, nanoindentation simulations using a multi-scale scheme from molecular dynamics to FEM simulation are presented in section III-6.

1. Analysis methods

Indentation testing is a well known experimental method used for determination of the constitutive properties of conventional materials such as metals and alloys, [Tab51, Joh70, Joh85, DN86 and Mot56]. Usually, the main goal of such testing is to extract indentation modulus and hardness of the specimen from experimental readings of indenter load, depth of penetration and of the residual projected area, where the residual area refers to the area of the indentation measured after the indenter has been completely unloaded from the sample. An analysis of the initial portion of the unloading response and residual area give an estimate of the indentation modulus of the indented material, because the initial portion of the unloading is assumed to be purely elastic. The hardness value is obtained by dividing the load by the residual projected area of the indentation.

 Therefore, the method to get the contact area is of great importance to obtain material properties with high accuracy; however there is no general method to obtain a contact area from

an anisotropic material.

On the other hand, most of the numerical simulations of nanoindentation test have used the rigid body indenter assumption because the calculations usually focus on the deformation of material not of the indenter. However, the deformation of the indenter may affect the applied load and indentation stiffness with penetration depth. Especially, we have observed that the results from experimental indentation carried out with a sapphire indenter which has relatively low elastic modulus compared to diamond are different to the results from indentation test with rigid body indenter. This is the reason why we need the correction of the test results for including the effect of deformation of indenter.

In this section, the new methods for obtaining contact area from the indentation test with anisotropic material are presented and the correction methods for the difference of indenter properties are also described.

1.1 Determination of contact area

Several methods for getting the contact area have been developed. [Len896, POB92 and DN86]. The general method is to use a criterion based on surface displacement after the nanoindentation experiment or simulation. The displacement criterion to evaluate a boundary of contact area depends on the type of surface morphology. There are two kinds of surface displacement which are called *pile-up* or *sink-in* morphology (see figure below) and which depend on a dimensionless ratio (flow stress/elastic modulus).
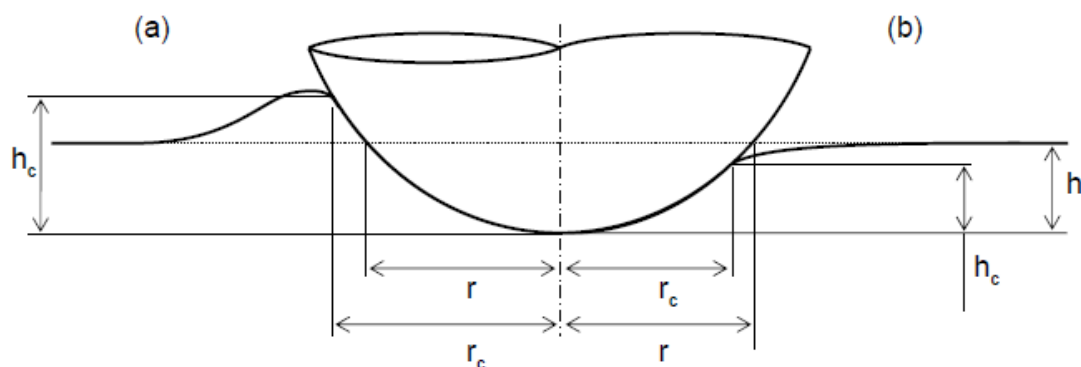

Figure II-1-2 Description of the contact area in (a) pile-up and (b) sink-in mode.

However, these methods are based on the assumption that the material can be considered as an isotropic media. Therefore, the contact boundary profile from these methods is a homogeneous shape with respect to the angular direction.

Copper single crystal presents a non negligible elastic anisotropy (depending on the crystal orientation in uniaxial loading, the modulus varies between 94 and 140 Gpa) and of course its intrinsic plastic flow along octahedral slip systems (111)[110]. As a matter of fact, we observed that both pile-up and sink-in behavior can be present on a single indented surface. This makes it very complex to define the contact area, since general methods used for isotropic material have not been verified to give a realistic contact area for anisotropic material. We have proposed several methods to evaluate the surface area for anisotropic material under load and after unloading in such a way that the procedure could be applied to both experiments and simulations or at least to allow precise comparison between the loaded and unloaded situations.

Direct method to get a contact area from FEM simulation

One very obvious method to get a contact area in anisotropic material is to use the simulation results. One of commercial FEM package, ABAQUS [ABA04] can provide the real contact area not a projected area. Therefore, the value of contact area from ABAQUS post processing should be converted to projected area because all of the analyses after nanoindentation are based on projected contact area, not on the real contact area.

Real contact area is simply converted to projected contact area by using the tip angle (ψ).

$$A_{projC} = \sin^2 \psi \times A_{realC} \qquad \text{(III-1-3)}$$

where ψ is tip angle between tip axis and tip surface which is 71.2° in our nanoindentation experiment or simulation and A_{projC} and A_{realC} are projected contact area and real contact area, respectively. The real contact area, A_{realC} is given by ABAQUS post processing program. This equation (III-1-3) is only for nanoindentation using cone type indenter because the angle ψ of cone type indenter is constant. If the indenter has a spherical shape, the tip angle ψ should depend on the indentation depth. Hence, an integration of equation (III-1-3) with indentation depth is needed for obtaining the projected contact area. Therefore, the equation is modified for our indenter tip which has a sphero-conical shape.

$$A_{projC} = \sin^2 \psi \times \left(A_{realC} - A_{r,sphere} \right) + A_{p,sphere} \qquad \text{(III-1-4)}$$

where $A_{r,sphere}$ and $A_{p,sphere}$ are surface area of sphere shape at our indenter which is about 4.1895 μm^2, projected area of the sphere shape which is about 4.0214 μm^2, respectively. Good point of this method is its simplicity because this equation (III-1-4) could allow getting the value of contact area from ABAQUS directly. However, accuracy of contact area value from this method depends on the contact mesh size and it provides it only during the loading state.

<u>Indirect method to get a contact area from contact pressure distribution</u>

Another obvious method for getting contact area is to use the contact pressure distribution from the FEM simulation. Figure III-1-3 (a) shows a two dimensional map of contact pressure distribution from FEM simulation.
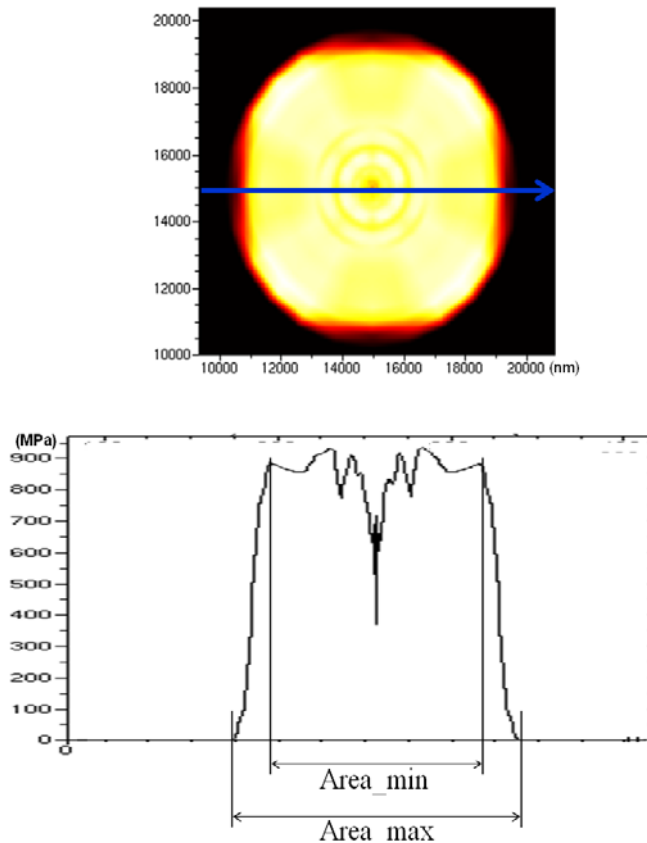

Figure III-1-3. Contact pressure distribution from FEM simulation,
(a) two dimensional mapping of the contact pressure distribution from FEM simulation,
(b) pressure value through the blue line in figure III-1-1 (a)

The contrast in the figure III-1-3 (a) depicts the amount of contact pressure value. This shows the contact boundary directly, because contact pressure values can have non-zero value only if the surface of material contacts to the indenter tip. However, the contact boundary line is not a sharp line, but a broadened area made from the red region. Therefore, there are two type of contact boundary, the one is boundary from the outside of the bright yellow region and the other is a boundary from the outside of the red region.

Figure III-1-3 (b) depicts the pressure value through the blue line in figure III-1-3 (a). Contact pressures within the contact are about 900 MPa but the others are zero. We can see a linear

transition region between the contact and the non-contact zone, which is the same region as the broad red one: this is a direct effect of the mesh. Hence, obtained value of contact area depends on the criterion of the minimum pressure threshold selected as due to the contact. Higher pressure criterion value gives smaller contact area and vice versa. In our simulation, three kinds of pressure criterion are used, which are an absolute value of 1MPa, a relative quarter and relative half of maximum pressure value, are used to find out minimum and maximum value of contact area. The uncertainty in determining the contact area is due to the fact that it can be located inside a mesh element and depends on its size. However, this method is not able to apply for obtaining contact area from experimental results and it can not be used as well for the unloaded state.

Indirect method to get the contact area from surface normal angle distribution

The last method proposed for obtaining contact area is by using the surface normal vector. If the surface of material is in contact with the indenter, its surface normal vector should be same as the surface normal vector of the tip. Hence, the angle between normal vector from the material surface and indentation axis could be good criteria for obtaining contact area.

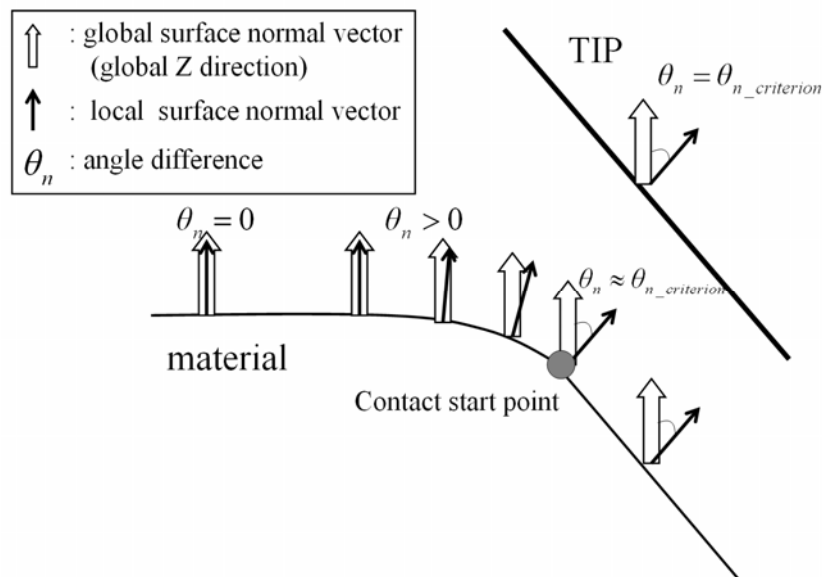Figure III-1-4 explains the reason why the surface normal angle could be a criterion of contact boundary.

Figure III-1-4. Detection of the contact area with the surface normal angle

The surface displacement during or after indentation from both experiment and simulation can be defined by a function as followed:

$$x_3 = F_{sur}(x_1, x_2) \tag{III-1-5}$$

Then local surface normal vector was obtained by differentiating the function F_{sur} in equation (III-1-5).

$$n_{sur} = \left(\frac{dF_{sur}}{dx_1}, \frac{dF_{sur}}{dx_2}, 1 \right) \tag{III-1-6}$$

Since, in general, the surface displacement function could not be defined theoretically, the surface normal vector is obtained by numerical differentiating method such as Bi-cubic 2D spline method. After having the surface normal vector, an angle (θ_n) between indentation axis and local surface normal vector (n_{sur}) is defined by :

$$\theta_n = \cos^{-1} \left(\frac{1}{\sqrt{1 + \left(\frac{\partial x_3}{\partial x_1}\right)^2 + \left(\frac{\partial x_3}{\partial x_2}\right)^2}} \right) \tag{III-1-7}$$

Figure III-1-5 depicts the surface angle (θ_n) distribution, where the black and white color in the figure III-1-5 shows the angle value of 0° and 18°, respectively. Note the presence of the spherical apex.
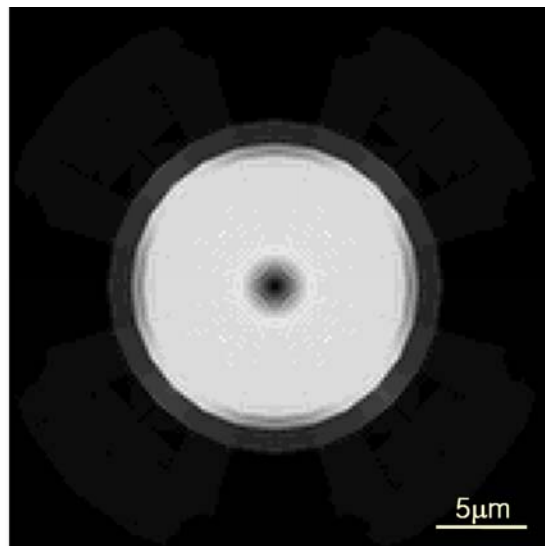

Figure III-1-5. Surface angle (θ_n) distribution from the simulation results of 1400 nm depth. Black and white colors depicts the angle value of 0° and 18°, respectively.

If the surface angle is close to 18°, which is the same as the surface normal angle of the tip surface, it means that the surface have been contacted with the indenter tip. This distribution shows very sharp boundary line and that means there is a big difference between inside and outside of the contact line. We can also see the mesh shape around the contact boundary from the figures. This means that there is only one surface angle value inside a mesh. It is just because that we use the 8 nodes linear cubic element. Theoretically, differentiation the displacement inside 8 nodes mesh is always constant.

The contact area value from the surface angle criteria do not depend on criteria so much, compared to the pressure criteria method. Like a pressure criterion, in our calculation, three angle criteria which are 18.8°, 17° and 9.4° are used for minimum and maximum contact area value respectively.

The advantage of this method is that it can be used to get a contact area from experimental results and simulation results during loading and after unloading state because it just uses information of surface displacement. Therefore, the contact areas from both experiment and simulation results are comparable to each other directly by using the same analyzing method based on surface angle criterion. Of course this method depends on the mesh size and shape very much, so shape and value of contact area may be unreasonable if these come from coarse meshes.

1.2 Correction of material properties from indentation results

Stiffness and indentation modulus

The contact stiffness is the slope of the load displacement curves during elastic loading a material, which can be expressed by a differentiation of applied load or a function of indentation modulus and contact area.

$$S = \frac{\partial P_{ind}}{\partial x_{ind}} = \frac{2}{\sqrt{\pi}} M^*_{eq} \sqrt{A_{projC}}$$
(III-1-8)

where P_{ind} and x_{ind} are the applied load for given indentation depth, and indentation depth, respectively, and S, and M^*_{eq} are indentation stiffness and equivalent indentation modulus, respectively. The equivalent indentation modulus is assumed to be given by the serial spring sum of indentation modulus of indenter ($M^*_{indenter}$) and sample (M^*_{sample}).

$$\frac{1}{M^*_{eq}} = \frac{1}{M^*_{indenter}} + \frac{1}{M^*_{sample}}$$
(III-1-9)

If the indenter and sample are isotropic material, the indentation modulus can be obtained from their elastic modulus and Poisson ratio.

$$M^*_{indenter} = \frac{E_{indenter}}{1 - \nu^2_{indenter}}$$

(III-1-10)

$$M^*_{sample} = \frac{E_{sample}}{1 - \nu^2_{sample}}$$

On the other hand, the measurement of indentation modulus for anisotropic material is still a challenging task. Few have reported about it [VN93, VN94 and VCB03]. Until now, the best way to get an indentation modulus for anisotropic material is obtained from indentation stiffness value and imaging its contact area after the indentation experiment. The ways of getting contact area from anisotropic material were already described in previous section. In the following we detail the method for obtaining the indentation stiffness from experiments or numerical simulations.

During an indentation experiment, the contact stiffness at any depth can be obtained directly by using the continuous stiffness measurement mode providing adequate synchronous detection, and the remained contact area after the indentation could be obtained by the method described at previous section with AFM for example. After that, we can calculate the indentation modulus value from the obtained indentation stiffness and the contact area value by using the Sneddon equation.

$$M^*_{eq} = \frac{\sqrt{\pi}}{2\sqrt{A_{projC}}} S$$

(III-1-11)

However, for the numerical simulation, there is no direct way to obtain the contact stiffness. Because the definition of the indentation stiffness is the slope of applied load curve with indentation depth due to the elastic property of a material, we can calculate the indentation stiffness from the differentiating the applied load at the given indentation depth if we simulate the nanoindentation simulation with elastic material properties only. We can calculate the contact area during the nanoindentation simulation even with pure elastic condition. After that, the indentation modulus value is obtained by the indentation stiffness, the contact area and the equation (III-1-11).

The method using the nanoindentation simulation elastic condition is a good way to get the indentation modulus and to compare the value to the one taken out from the experiment. The interest of establishing the elastic stiffness (depth) curve is, as Vlassak and Chen have shown : for two materials, either elastic or elastic-plastic, their contact stiffness are equal if they share the same area of contact. However, without knowing the equivalent indentation modulus, we can not compare the indentation stiffness at the given indentation depth between the experiment and the simulation with pure elastic condition directly. Since, the copper material can not assume the pure elastic material, the contact area with given depth from the experiment should

be different to the contact area from the elastic simulation. We can not compare the indentation stiffness at the given contact area between them neither, because there is no way to get a contact area with given indentation depth during the nanoindentation from the experiment.

For getting indentation stiffness from the applied load with indentation depth curve of experiment or simulation with material condition of crystal plasticity, differentiation of unloading load is used. Since, load decrease at the unloading state is assumed to be due to elastic recovery. Here, there will be a big difference between indentation modulus from indentation stiffness of the experiment and simulation. It is because the indentation stiffness is a function of equivalent indentation modulus, not the sample's indentation modulus. The indenter for the experiment is made of a sapphire single crystal, whose elastic modulus is about 345GPa, and the imaginary rigid indenter which has infinite elastic modulus is used for the simulation. The difference of elastic modulus of indenter between experiment and simulation will make the difference of equivalent indentation modulus between them though the same sample's indentation modulus property is used. Therefore, we should compare the indentation modulus and indentation stiffness from the experiment and the simulation just after correction of the difference of indenter's elastic modulus.

The relationship between indentation modulus from experiment and simulation could be described from the equation (III-1-8) and (III-1-9).

$$\frac{1}{M^*_{exp\,eriment}} = \frac{1 - v^2_{sapphire}}{E_{sapphire}} + \frac{1}{M^*_{simulation}} \qquad \text{(III-1-12)}$$

The relationship between indentation stiffness from experiment and simulation is also described from equation (III-1-8) and (III-1-12), if the contact area from experiment and simulation is the same.

$$\frac{1}{S_{exp\,eriment}} = \frac{\sqrt{\pi}}{2\sqrt{A_{projC}}} \frac{1 - v^2_{sapphire}}{E_{sapphire}} + \frac{1}{S_{simulation}} \qquad \text{(III-1-13)}$$

Load verse depth curve

Since a different elastic modulus of indenter between experiment and simulation also affects the applied load, we should also compare the applied load with given indentation depth from the experiment and the simulation just after correction of the difference of indenter's elastic modulus.

The effect of the modulus of the tip to an applied load curve can be obtained with two assumptions. The first assumption is that the indenter shape is a cone. The other assumption is that both indenter and sample material can be considered as elastic material. The two

assumptions will make the two relationships about the loading and about the indentation depth. At first, an applied load with indentation depth can be described by square type equation of indentation depth, when the elastic material is indented by cone type indenter, and because of energy equilibrium, applied load at the indenter, sample and total media are always same among them.

$$P_{ind} = C_{eq}^*\left(x_{ind}^{eq}\right)^2 = C_{indenter}^*\left(x_{ind}^{indenter}\right)^2 = C_{sample}^*\left(x_{ind}^{sample}\right)^2 \qquad \text{(III-1-14)}$$

where C_{eq}^*, $C_{indenter}^*$ and C_{sample}^* are indentation compliance of equivalent, indenter and sample materials, respectively, and x_{ind}^{eq}, $x_{ind}^{indenter}$ and x_{ind}^{sample} are indentation depth of total, indenter and sample materials, respectively.

The second relationship is the relationship between the indentation depth of total, indenter and sample materials.

$$x_{ind}^{eq} = x_{ind}^{indenter} + x_{ind}^{sample} \qquad \text{(III-1-15)}$$

Using the equation (III-1-14) and (III-1-15), the relationship among the compliances can be described.

$$\frac{1}{\sqrt{C_{eq}^*}} = \frac{1}{\sqrt{C_{indenter}^*}} + \frac{1}{\sqrt{C_{sample}^*}} \qquad \text{(III-1-16)}$$

If we assume that the indenter follows an elastic behavior, the indentation compliance can be described as a function of elastic modulus of the indenter material.

$$C_{indenter}^* = \frac{2}{\pi} M_{ind}^* \tan\psi = \frac{2\tan\psi \times E_{indenter}}{\pi\left(1 - \nu_{ndenter}^2\right)} \qquad \text{(III-1-17)}$$

Although, the above relationship is based on elastic material behavior, it is proved that the applied load with sample, which has the elasto-plastic deformation behavior, is also expressed by a square type equation like equation (III-1-14) (see for ex. [Fis02]). Therefore, the relationship as shown in equation (III-1-16) can apply to the sample followed by elasto-plastic behavior if the indenter could be assumed that it has only pure elastic deformation.

Finally, the relationship between indentation compliance and applied load from experiment and simulation is also described by following equation, like the relationship of indentation stiffness between them:

$$\frac{1}{\sqrt{C_{experiment}^*}} = \sqrt{\frac{\pi\left(1 - \nu_{sapphire}^2\right)}{2\tan\psi E_{sapphire}}} + \frac{1}{\sqrt{C_{simulation}^*}} \qquad \text{(III-1-18)}$$

$$P_{ind}^{experiment} = \frac{C_{experiment}^*}{C_{simulation}^*} P_{ind}^{simulation} \qquad \text{(III-1-19)}$$

1.3 What should be retained from this section

- To get a contact area
  - Using ABAQUS output variable
  - Using pressure distributions
  - Using surface normal vector distributions

- Correction for indenter stiffness
  - Stiffness correction

$$\frac{1}{S_{experiment}} = \frac{\sqrt{\pi}}{2\sqrt{A_{projC}}} \frac{1-v_{sapphire}^2}{E_{sapphire}} + \frac{1}{S_{simulation}}$$

  - Compliance correction

$$\frac{1}{\sqrt{C_{experiment}^*}} = \sqrt{\frac{\pi\left(1-v_{sapphire}^2\right)}{2\tan\psi E_{sapphire}}} + \frac{1}{\sqrt{C_{simulation}^*}}$$

2. Experimental indentation

Recently, interest in the indentation test has grown with the development of very low-load, depth-sensing indentation instruments [DN86, OP92 and PHO83]. These instruments allow one to make indentations as shallow as a few nanometers. The nanoindentation test is, therefore, particularly well-suited for the measurement of mechanical properties extremely small volume of material. These instruments also allow recording the applied load-depth curves and stiffness-depth curves directly. The properties are obtained during the test by using recent indentation technique. Hence, in the last few years these techniques have also been used to measure material properties such as the hardness, Young's modulus [DCV01, DN86 and OP92], and plastic properties [DCV01, BSF03, CDS03, GS99, FWT01, Gia02, CC03, MA03, DY03, BSS04, MA04, CL04a and CL04b].

Experimental analysis of surface deformation beneath the imprint after indentation test is another interest of nanoindentation. Such observations are important to understand the deformation mechanism of anisotropic materials. However, few authors have reported about the observation and analyze the surface deformation morphology of indented anisotropic material, such as copper single crystal, and they have used pyramidal indenter for the nanoindentation test of anisotropic material. Though the indentation test with pyramidal indenter is used widely as a standard indentation method, the indenter shape has weak point to analyze the effect of anisotropy because of the geometrical anisotropy of the indenter itself. The anisotropy effect from the nanoindentation test with pyramidal indenter is due to the both of anisotropy of material and geometry of indenter. For the exact observation of anisotropy effect, wide range of nanoindentation test with conical indenter, which has geometrically isotropy, is required.

In this section, we present the results of indentation test of different copper single crystal. The analysis about the effect of surface orientation and initial dislocations and about the mechanism of slip system activation are also described by using the experimental results of applied load-depth curves, indentation stiffness-depth curves during the indentation test and surface deformation morphology after the indentation test.

2.1 Sample preparation

Bulk copper single crystals of a minimum thickness of 5 mm have been used. Four different single crystals are used to vary both surface normal orientation and initial dislocation density. The orientations of the samples are shown in figure III-2-1.
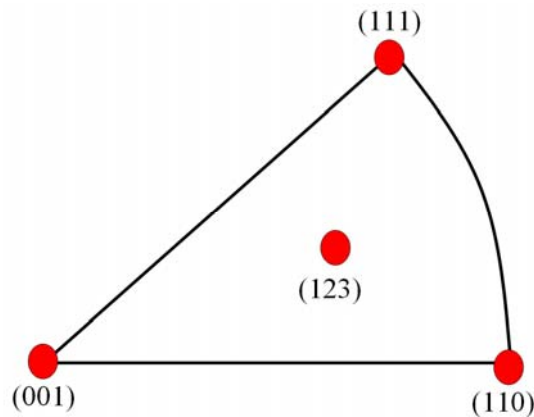
Figure III-2-1. Pole figures used to define the normal orientations of the prepared samples for nanoindentation experiments

Initial dislocation densities of the samples are not the same among them because of different growth methods for the single crystal samples. A very low initial dislocation density crystal was grown from high purity Cu using Bridgman technique in a graphite mold along a <541> direction with a square section geometry. The orientations of the other sections are (111) and (123) planes, respectively. The low density crystal is supplied by Prof. M. Niewczkas at McMaster University is characterized and reported in [Nie]. The crystal sample are used for nanoindentation in the (123) and (111) surface orientation. Three other crystals with (110), (111) and (001) surface normal plane were cut by spark erosion from neutron mirror bulk single crystal. Hence, their initial dislocation density is not as low as the first crystal, since a controlled minute bending was introduced during their growth. These crystals are kindly supplied by the Institute Laue Langevin- ILL Grenoble and we use these for nanoindentation in the (110), (111) and (001) surface orientations.

Surfaces of all the four crystals are polished mechanically before electrochemical polishing at 1.65V in a (25%H3PO4 - water) solution. The mechanical polishing step was required to flatten the surfaces to allow detailed observations of rosette of dislocation slip systems around the indents by Atomic Force Microscopy (AFM), though the mechanical polishing increase the initial dislocation densities. On the other hands, one side of (123) crystal, (111) orientation, was not flattened mechanically but only polished electrochemically. This (111) surface without mechanical flattening was used for analyzing initial density effect with same surface orientation with mechanical polishing. All instrumented indentations were carried out within a few hours after surface preparation to avoid roughness development due to oxide layer.

Table III-2-1 shows the surface orientations orientation miscut, and Bragg peak broadening around the diffraction vector direction (θ−2θ) and in its perpendicular direction (θ scan).

Orientation surface	Miscut χ (°)	θ (°)	FWHM (111) (θ-2θ °)	FWHM (111) (θ scan °)
[111] ILL	1.3	-0.1	0.06	0.57
[002] ILL	0.8	0.6	0.1	0.56
[022] ILL	7	3	0.32	1.35
[123] B. ([111] B.)	0.8 (0.7	0.2 0.01)	0.04 (0.038)	0.2 (0.084)

Table III-2-1. Surface orientations and misfit. Band broadness through diffraction vector direction (θ−2θ °) and its perpendicular direction (θ scan °).

The surface orientations are not exactly ideal as in the numerical simulation, the respective miscut are small enough to be negligible (all but for the (110) crystal where 7° miscut is recorded). The Bragg peak width in the (θ−2θ °) scan is proportional to the internal residual microstrain which is proportion to the square root of the initial dislocation density, whereas in the (θ scan) geometry, the width expresses the crystallographic mosaicity (presence of small misorientation due to subgrains for example).

The crystal whose surface has (123) orientation presents a weaker peak broadening than the others, which is due to the sample growing method difference. Especially, the other surface of this crystal which is a (111) surface orientation, has also the lowest value of peak broadening. The peak broadening of the other crystals are all a bit higher than one of crystal with (123) orientation. The maximum value of peak broadening is more than 10 times higher than the minimum value of the (123) crystal. Therefore, we can assume that the initial dislocation density differences among the crystals are as big as the differences of peak broadening among them.

2.2 Indenter properties

For the nanoindentation of the Cu single crystals, a sphero-conical type geometry tip is used, because this study focuses on comparison between experiments and finite element modeling (FEM) using crystal plasticity model. This sphero-conical type geometry avoids the threefold symmetry and edge effects from traditional pyramidal tip geometry such as the Berkovich or Cube corner geometry classically used in nanoindentation.

Manufacturing perfect conical tip with small tip apex is difficult with diamond, therefore we use [0001] sapphire single crystal. This tip geometry was characterized by measuring its real height-area function by direct AFM scan. The radius and height of tip which has sphere shape geometry is about 3.3 μm and 200 nm, respectively, and angle between tip axis and tip surface is 71.2^o as shown in figure III-2-2 [Cha06].
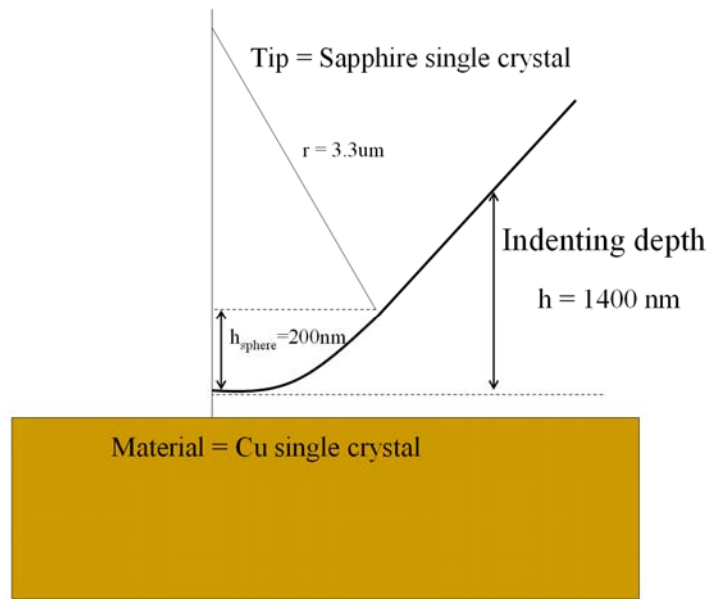
Figure III-2-2. Description of the tip geometry used in the nanoindentation experiments

A MTS XP nanoindenter machine is used for testing the various copper single crystals. A continuous stiffness measurement mode was used with frequency of 50 Hz and displacement amplitude of 2 nm. At the final depth of 1400 nm, good control of the oscillation is insured, contrary to the first 200 nm depth. After the nanoindentation experiments, both load (P_{ind}) and contact stiffness (S) with total displacement depth (x_{ind}) are obtained.

Standard indentation procedures are carried out with the following parameters [SP04 and TP04]. During the indentation experiment up to 1400 nm of indentation depth, the strain rate is controlled constant at 5×10^{-2} s^{-1}. Thermal drift is corrected by correction method [SP04 and TP04] recorded at the end of each individual indents. Only tests with a minimum average drift less than 0.05 nm/s are retained. At least 5 indents were processed on each sample to make sure of reproducible mechanical data.

Surface topography on residual indents was investigated using an AFM (Veeco 3100 commercial system) in tapping mode. Typical scan of indents consisted of a minimum 30×30 μm^2 square area, large enough to include flat surface reference around the indents, with a 512^2 data sampling. From the AFM investigation, the residual rosette of dislocation slip systems with the various surface orientations and height of deformed surface are obtained.

The height measurement data are used for post data processing to calculate the angle between the indentation axis and the local surface normal axis. This allowed us to obtain contact shape and area of the highly anisotropic shape of the residual indents. For getting the angle, 2D bicubic spline surface fitting method is used [Sci]. Details are described in the section III-1.

2.3 Experimental Results

<u>Crystal orientation effect</u>

Figure III-2-3 shows the applied load versus the depth curves for four different surface orientations from the nanoindentation experiments. The loading part follow a typical parabolic curve, but applied loads at the same indentation depth are different with surface orientations. The highest load is around 60 mN with 1400nm of indentation from (110) surface orientation. Increasing amount of applied loads for (001) and (111) surface orientations are quite similar which is about 55mN with 1400 nm of indentation depth, although loads for (111) surface orientation is a bit higher than one for (001) orientation. The lowest load with final indentation depth is about 38mN for the (123) crystal orientation. It shows more than 55% difference comparing to highest load value with same indentation depth.
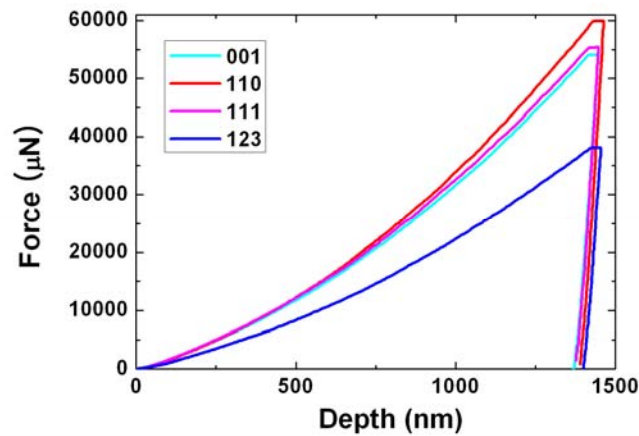
Figure III-2-3. Experimental load-displacement curves obtained for different orientations

The table III-2-2 presents the contact areas with various surface orientations after nanoindentation experiments, which are different for the various surface orientations. The highest value of contact area is about 69μm^2, which for the (110) crystal orientation and the lowest value of one is about 57μm^2 for the (123) surface orientation. The contact areas from (001) and (111) orientation are quite similar between them, which is about 68μm^2. The tendency of the contact area differences among the various orientations is the same as for the final applied load, though the difference between maximum and minimum contact area is about 20% which is smaller than the 55 % difference between maximum and minimum applied loads.

Criterion Orientation	18.8	17	9.4
110	68.592 (μm^2)	69.077 (μm^2)	72.778 (μm^2)
111	66.910 (μm^2)	67.669 (μm^2)	73.941 (μm^2)
001	67.284 (μm^2)	67.755 (μm^2)	72.197 (μm^2)
123	54.811 (μm^2)	56.913 (μm^2)	64.229 (μm^2)

Table III-2-2. Remaining contact areas for various surface orientations after 1400nm indentation

Two kinds of effects could be a reason for the contact area and applied load differences among the orientations. The one is their surface orientation effect. The surface orientation could make a difference of elastic modulus through the indentation axis and number of activated slip system. This one will make the plastic hardening difference among surface orientations and that one will make elastic response discrepancy among them. Moreover, the surface orientation can affect the contact area because of their characteristic symmetry. The other is their initial density effect. Their initial density is closely related to the yield stress which is a criterion between elastic and plastic behavior of Cu single crystal. Higher initial dislocation density induces higher yield stress and this increase amount of elastic response from the material. This can also affect to the contact area because the ratio between elastic and plastic response is an important parameter of remained contact area.

As a result, the applied load and contact area differences with various surface orientations are due to the complex mechanism mixed by several reasons, but it is not known yet which factor affect to differences predominantly. It is hard to count how big each reason makes the amount of the differences quantitatively by using experimental technique, because this requires extremely well controlled sample preparation. Therefore, for detail quantitative analysis, these results should be compared with the results from numerical simulations. The detailed simulation results are shown in section III-3 and detailed comparisons between experiment and simulation results are in section III-4.

Figure III-2-4 plots the stiffness versus the indentation depth for several surface orientations. Stiffness curves with indentation depth show weak oscillation which is due to the continuous stiffness measurement technique. The four stiffness traces are very similar among each other. At the beginning, the stiffness increases with high slope and the slope is decreasing with indentation depth. It is due to the spherical shape of the tip front. After the tip front region, the stiffness increases linearly as expected with indentation depth due to the cone shape indenter tip. The four orientations can be divided into two by the amount of stiffness. The stiffness from (110) and (111) orientations, which is about 1.00 MN/m for 1400nm indentation depth are a bit higher than the stiffness from (001) and (123) orientations with same indentation depth, which

is about 0.85 MN/m.

In general, the stiffness result has been used for analyzing the elastic property, because stiffness is calculated from elastic property once the area is known using the extension of Sneddon relation. The difference of stiffness curves among surface orientations depicts the difference of the elastic property due to the elastic anisotropy. However, for detailed analysis, contact area effect should be also considered since stiffness is a result from combination of indentation modulus which is purely elastic material property and its contact area as shown in equation (III-1-8). Even though, the elastic property is same, the stiffness could be varied due to the contact area difference. Therefore, to see an elastic anisotropic effect exactly it is more useful to analyze the indentation modulus with orientations.
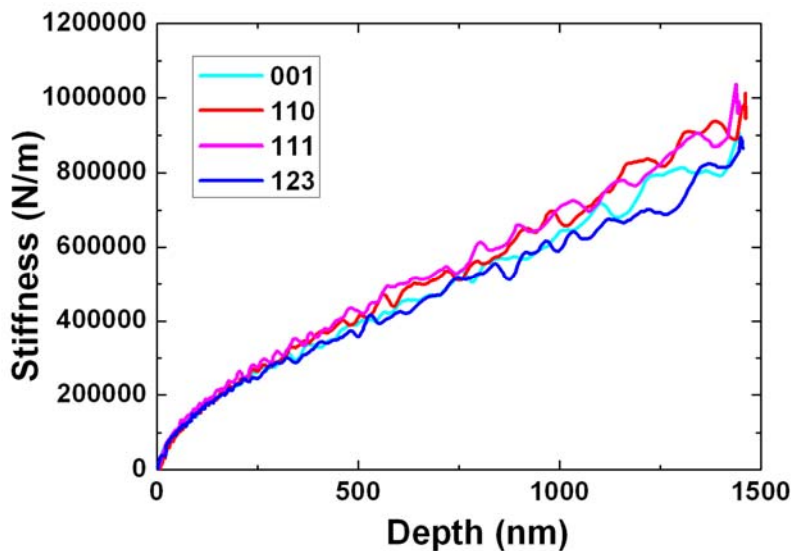
Figure III-2-4. Experimental stiffness plotted in function of the indentation depth

Figure III-2-5 depicts the indentation modulus with different surface orientations from nanoindentation experiments.

Because of the indentation modulus is just material property based on elasticity of the material, the difference of indentation modulus among the surface orientations should be caused by elastic anisotropy of the copper single crystal. The highest indentation modulus is about 105 GPa which for (111) orientation and the lowest one is about 90GPa for the (001) orientation. Indentation modulus with (110) and (123) orientation is just between them, which is about 100 GPa and 98 GPa, respectively and close to the value of (111) surface orientation. The tendency of indentation modulus with surface orientation is the same as elastic modulus with surface orientations. This is because of the relationship between elastic modulus and indentation modulus. It is indeed a well known relationship recalled in equation (III-1-8) and valid for

isotropic materials. It has published recently that the relationship is still accepted even for anisotropic materials [VN93 and VN94]. The result from figure III-2-5 confirms the recent reports.
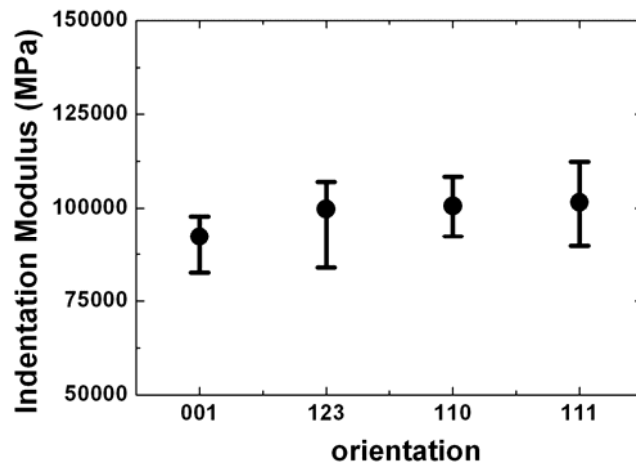

Figure III-2-5. Indentation modulus obtained experimentally for different surface orientations

Figure III-2-6 depicts the surface displacement morphology with different surface orientations from AFM experiments. Figure III-2-6 (a-d) depicts the surface displacement morphology of (001), (110), (111) and (123), respectively. Every orientation presents both pile-up and sink-in regions simultaneously. It is because of anisotropy of the copper material. Hence, each of the surface morphology in figure III-2-6 depicts their own symmetry, which is same as the symmetry of plastic slip system array projected on the surface crystal plane. The symmetries due to the surface orientations are 4-fold symmetry for (001), 2-fold symmetry for (110) and 3-fold symmetry for (111), respectively. Surface morphology from (123) orientation has weak 2-fold symmetry but the height of the four upheaval are different among them. Maximum heights from the other surface orientations are different among them. Maximum height of (110), and (001) surface orientation are about 300 nm high but the height of (111) and (123) orientations are just about 200 nm high.

In general, the pile-up height depends on the yield stress and plastic work hardening but these relationships are observed for isotropic material. Few reports about pile-up height for the anisotropic material have been published. Qualitatively speaking, because of the indentation, some slip systems are activated and dislocations at the activated slip systems are start to move to the specific direction, which generate the surface pile-up morphology. The other regions are not affected by the dislocation movement at the activated slip system shows sink-in morphology. Therefore, the pile-up and sink-in morphology are due to the activated slip system differences just below the surface.
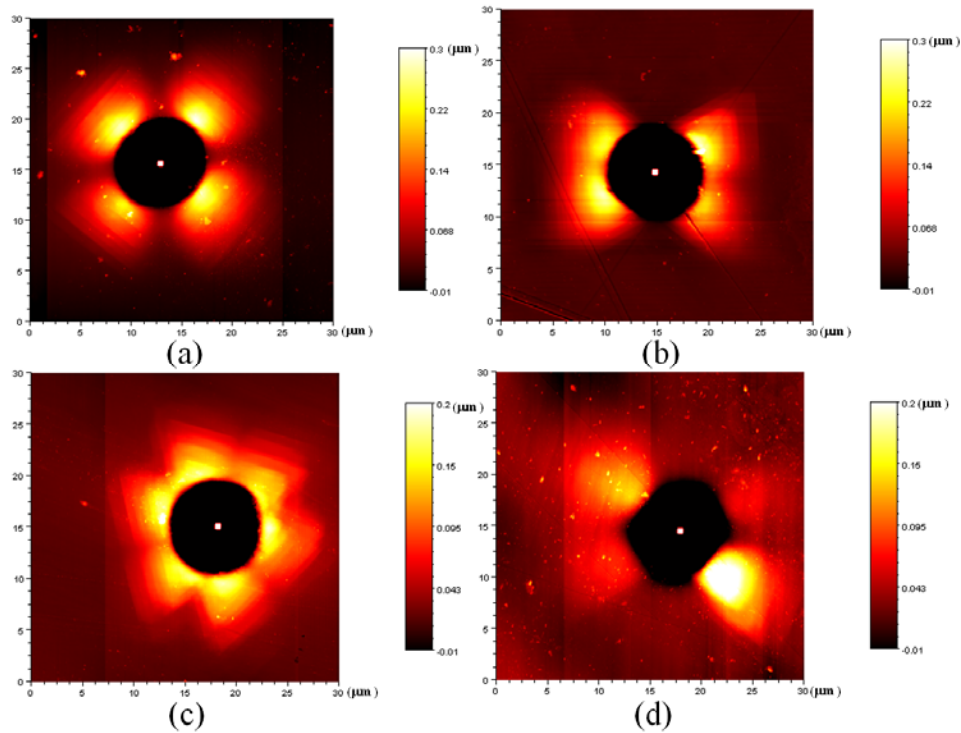
Figure III-2-6 AFM surface displacement morphology measured for different surface
orientations (a) (001) surface orientation, (b) (110) surface orientation,
(c) (111) surface orientation (d) (123) surface orientation

Quantitative analysis about it is not reported yet, because of its complexity. We should analyze first the slip system activation and dislocation evolution around the indentation region quantitatively. These are not easy to do by experiment (it requires various Focus Ion Beam cross section and detailed subsequent crystal rotation analysis by Electron Back Scatter Pattern, see the recent work of [KPM06, RMP07 and RMP08] for example). Therefore, for detail quantitative analysis for the surface morphology, the results from numerical simulations is needed. The detailed simulation results about the surface morphology are shown in section III-3 and the detailed comparison between experiment and simulation results are presented in section III-4.

Initial dislocation density effect
To understand initial density effect, 111 orientations with two different initial densities are compared in figure III-2-7 for the applied load depth curves. Though their surface orientations are the same, applied load values with same indentation depth are quite different between each other, where the load for final indentation depth with high initial dislocation density is 55mN and the load with low initial dislocation density is about 30mN, respectively.
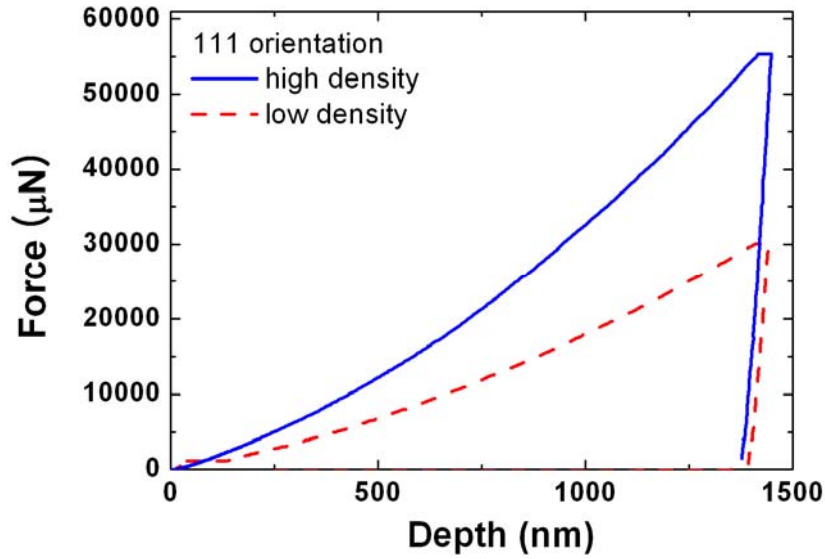
Figure III-2-7. Experimental load-depth curves for (111) indentation in two samples having different initial dislocation densities

High initial density needs more than 80% higher applied load than required with low initial dislocation density. It is quite reasonable because higher initial dislocation density increase yield stress which means that the material becomes harder.

Table III-2-3 shows the different remaining contact areas of (111) surface orientations with high and low initial dislocation density from experiments.

Orientation \ Criterion	18.8	17	9.4
111 high density	66.910 (μm^2)	67.669 (μm^2)	73.941 (μm^2)
111 low density	53.979 (μm^2)	54.340 (μm^2)	61.023 (μm^2)

Table III-2-3. Remaining contact areas of (111) surface orientations with high and low initial dislocation density measured by AFM after indentation experiments

The contact area from (111) surface orientation with high initial dislocation density is about $68\mu m^2$ and the one from same surface orientation with low initial dislocation density is about 54 μm^2, respectively. The contact area difference between two different dislocation densities is about 25% which is the same tendency as applied load difference between two difference dislocation densities.

The results from figure III-2-7 and table III-2-3 support the assumption that one of the important reason of applied load and contact area differences among surface orientations in figure II-2-3. Figure III-2-3 and table III-2-2 have a difference in initial dislocation density. The difference in

ratio between minimum and maximum from figure III-2-7 and table III-2-3 explains the difference in ratio from figure III-2-3 and table III-2-2, respectively. The other reason is that it is quite reasonable that the low initial dislocation density of (111) surface orientation is similar to the initial dislocation density of (123) surface orientation, because the two surface orientation comes from the same sample, although mechanical polished (123) surface could be higher than the non mechanical polished (111) surface. In the same way, the high initial dislocation density of (111) surface orientation should be similar to the initial dislocation density of (110) surface orientation because the two samples are grown by the same method (bending for neutron mirror purpose).

Figure III-2-8 presents the surface morphology of the (111) surface orientation with two different initial dislocation densities.
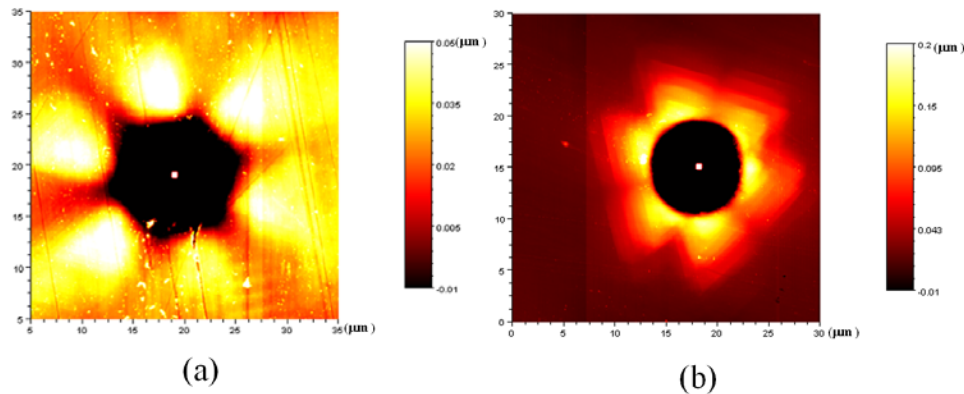
Figure III-2-8. Surface morphology of the (111) surface orientation with two different initial dislocation densities measured from nanoindentation experiments
(a) low initial density   (b) high initial density

Although the same indentation condition, surface morphologies with two different initial dislocation densities are very different between each other. (111) surface orientation with low initial density as shown in figure III-2-8 (a) gives 6-fold symmetry with 6 pile-up picks and the height of the maximum pile up site is about 50nm. On the other hand, (111) surface orientation with high initial density as shown in figure III-2-8 (b) shows a 6 pile-up upheaval which height is about 200 nm but the surface morphology looks like a 3-fold symmetry not a 6-fold symmetry as shown in figure III-2-8 (a). It is shown that the initial dislocation density is a very important parameter for both the surface morphology and maximum pile-up height. We can explain the mechanism qualitatively. At first, the low initial dislocation density produces 6 picks with 6-fold symmetry. If the initial dislocation density is increased, 2 peaks of them are getting closer to each other and join. Finally, they make a 'bundle', which produces surface morphology

with 3-fold symmetry when the initial dislocation density is high enough.

For detailed analysis about applied load, stiffness, surface morphology and maximum pile-up height with surface orientation or with initial dislocation density, it is needed that the experimental results are compared to the simulation results with same indentation conditions. Hence, details of experimental results are described and compared to results of numerical simulation which is shown in section III-4.

Slip system activation effect

Figure III-2-9 (a-d) depict AFM image of slip bands with (001), (110), (111) and (123) surface orientations, respectively. The images about the slip bands show the symmetry same as shown in figure III-2-6 due to their surface orientation. The (001), (110) and (111) surface orientations have 4-fold, 2-fold and 3-fold symmetries of the slip band morphology, respectively. (123) orientations has only one directional slip band. We can assume that the pile-up heights in figure III-2-6 are closely related to slip band distribution in figure III-2-9, because the maximum pile-up height region is exactly the same as the slip band region.

A qualitative explanation about it is already mentioned above. The symmetry of surface morphology is due to symmetry of the slip system projected to surface orientation. Figure III-2-10 (a), (b) and (c) depicts the projected slip system to its own surface orientations which is (001), (110) and (111) surface orientation, respectively, where the blue arrows are activated slip systems. The projected slip systems shows exactly same symmetry as the one of surface morphology.

(001) surface orientation as shown in figure III-2-10 (a) has 4-fold symmetry from both surface morphology and projected slip system. The positions of the 4 Burgers vectors and 8 slip system's normal planes explain the reason of 4-fold symmetry of surface morphology.
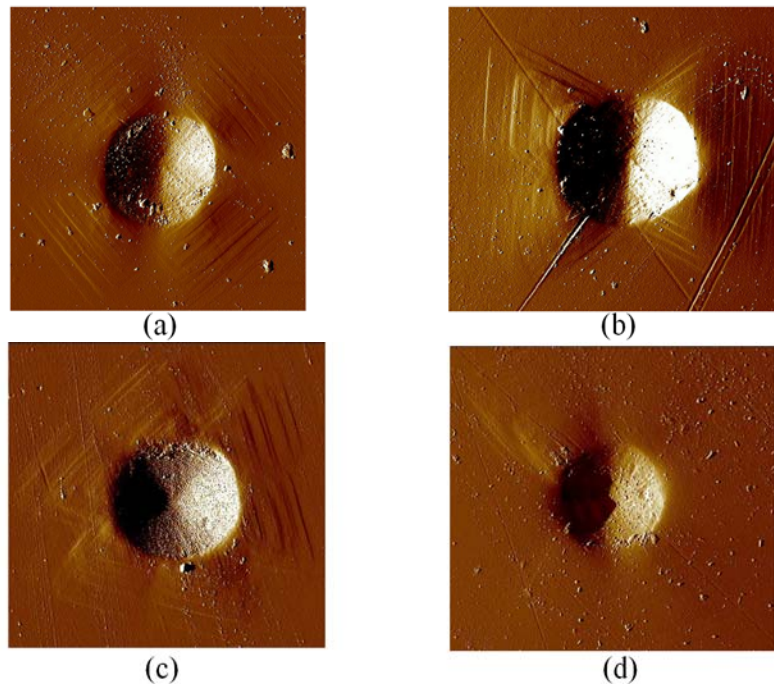
Figure III-2-9. AFM images showing slip bands surrounding the imprint for
(a) (001) orientation, (b) (110) orientation, (c) (111) orientation (d) (123) orientation
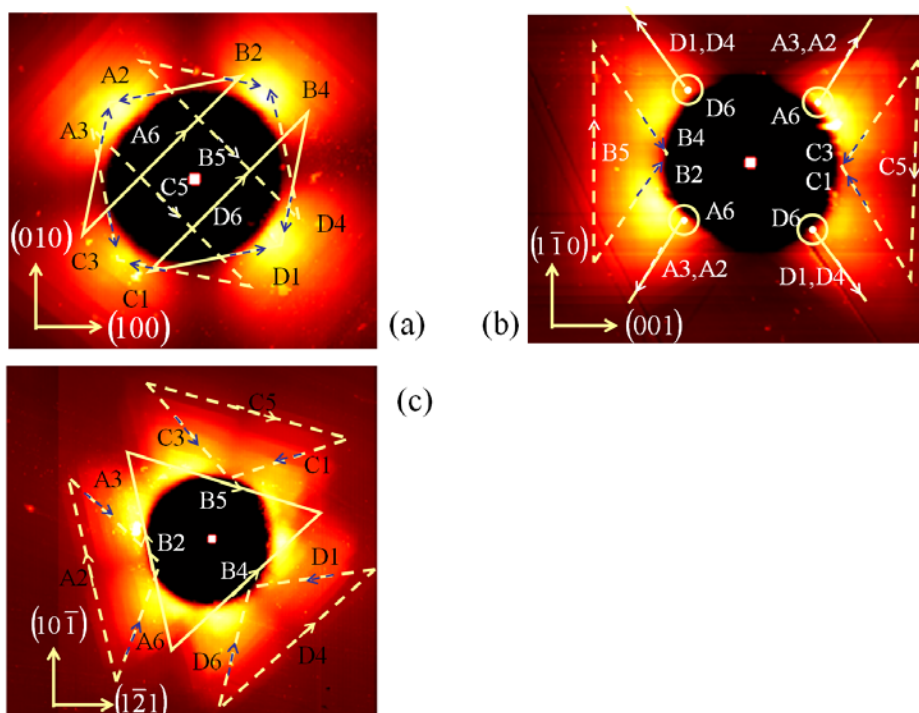

Figure III-2-10. Symmetry of the projected slip system to its own surface orientations
(a) (001) surface orientation (b) (110) surface orientation (c) (111) surface orientation

Because for the surface orientation (001) two Burgers vector named 5 and 6 lay perpendicular to the surface normal orientation, therefore slip system with the two Burgers vectors are not activated. The two Burgers vector are also perpendicular to each other. The other 4 Burgers vectors named 1, 2, 3 and 4 lay with a slope of 45° compare to 5 or 6 Burgers vectors, and slip systems including the four Burgers vectors are activated. Four slip system's normal planes named A, B, C and D lay with direction to top left, top right, bottom left and bottom right pile-up site. Now, we can figure out easily that the pile up of top left is just due to the A2 and A3 slip system activation, the pile-up of top right is due to the B2 and B4 slip system activation, the pile up of bottom left is due to the C1 and C3 slip system activation and the pile-up of bottom right is due to the D1 and D4 slip system activation, respectively.

(110) surface orientation as shown in figure III-2-10 (b) has 2-fold symmetry from both surface morphology and projected slip system. The positions of 4 Burgers vectors and 4 slip system's normal planes explain the reason of 2-fold symmetry of surface morphology.

For the surface orientation (110), one Burgers vector named 6 is parallel to the surface normal orientation and other Burgers vector named 5 is perpendicular to the surface normal orientation, so the slip system including the two Burgers vectors are not activated. The Burgers vectors named 2 and 4 and slip plane named B has a direction on the left side of (110) surface orientation and the 1 and 3 Burgers vectors and C slip plane lay with a direction on the right side of the (110) surface. The other 2 slip plane normal is perpendicular to the (110) surface orientation. Now, we can figure out easily that the two pile up sites at left are just due to the B2 and B4 slip system activation, the two pile-up peaks at right are due to the C1 and C3 slip system activation, respectively.

(111) surface orientation as shown in figure III-2-10 (c) has 3-fold symmetry from both surface morphology and projected slip system. The positions of the 3 Burgers vectors and 6 slip system's normal planes explain the reason of 3-fold symmetry of surface morphology. Because surface orientation is (111), one slip plane normal named B is parallel to surface normal orientation, the slip systems including B slip plane is not activated. Three Burgers vector named 2, 4 and 5 also lay perpendicular to the surface normal orientation, therefore slip system with the three Burgers vectors are neither activated. The other 3 Burgers vectors named 1, 3 and 6 lay with an angle of 60° between them. The slip systems including this 3 Burgers vectors are activated. Three slip system's normal planes named A, C and D lay with directions to the three pile-up sites. Now, we can figure out easily that the 6 pile-up peaks are just due to the A3, A6, D6, D1, C1 and C3 slip system activation, respectively.

As a result, slip systems projected to the various surface orientation can give the reason for the observed symmetry of the various surface morphology and the activated slip systems tell the reason of pile-up sites, respectively. However, these arguments are simple and details only what

happens at or just below the surface: it is not easy to tell the reason of the pile-up height difference among the surface orientations. This is the reason why complete 3D simulation is needed to get the complex plastic crystal flow around the indenter tip

2.4 What should be retained from this section

- The load displacement curve
  - (110) > (111) > (001) > (123)
- The stiffness (Indentation modulus) curve
  - (111) > (110) > (123) > (001)
- Surface Morphology
  - (110) : 2 fold symmetry (4 pile up picks)
  - (111) : 3 fold symmetry (6 pile up picks)
  - (001) : 4 fold symmetry (4 pile up picks)
  - (123) : 4 heterogeneous pile up picks

3. FEM simulations of indentation

<u>State of the art of continuum simulations of indentation</u>

Finite element simulations (e.g. [HSZ89, GLV94, MF99, MAA02, MAS04, BK04, FRS04, GJS06 and MCA06]) are used to reproduce the nanoindentation of wide variety of crystalline solids. In spite of the fact that the elastoplastic behavior of the material is considered as isotropic, such simulations allow to settle fundamental understanding of indentation test [MF99, HSZ89, BS95, BFN93 and CV01].

However, instrumented indentation experiments are often performed on single grains or on textured or single crystal epitaxial thin films, which are anisotropic. Only finite element simulation making use of models that takes into account crystal plasticity is able to give back experimental evidence corresponding to nanoindentation inside a grain. This has been the object of recent work presented in [WRK04, LBY05, ZRS06, EG07 and COA07]. Some investigations aim to reproduce applied load-penetration depth curves of instrumented indentation made with a spherical indenter [WRK04 and LBY05]. They also analyze the surface morphology underneath the spherical tip in connection with anisotropy [ZRS06]. Casals *et al*. [COA07] explore nanoindentation of annealed and strain-hardened copper single crystals thanks to crystal plasticity finite element simulations. of nanoindentation. The pyramidal indenter is of Vickers and Berkovich type. Zaafarani *et al*. [ZRS06 and ZRR08] have captured and explained crystallographic orientation patterns of copper single crystalline induced by conical indenter. J. Alcala *et al*. [ACO08] analyze sharp indentation experiments performed in a variety of FCC crystals by using the crystal plasticity simulation.

In spite of the fact that the finite element simulation making use of crystal plasticity is a good way to retrieve experimental material behavior, they still have a lack of physical reality if the deformation law used is phenomenological. Due to this fact, models can be used only for cases that correspond with experimental condition of model parameters identification. Other applications like nanoindentation lead to risky extrapolation [HGW03].

In this section, original results issued from nanoindentation simulations are presented. A fully physically based constitutive behavior law has been implemented in a user material routine. Because the theory is fully physically based [Koc94], all the parameters have a physical sense. Thus, they can be identified with numerical computations at a lower scale such as dislocation dynamics simulation (see for example [Fiv97]). Due to the generic features of the model, the simulation can cover a wide range of indentation conditions without any restriction due to the identification process.

The results concern the applied load-depth curves, the contact stiffness-depth curves during the indentation test and surface deformation morphology after unloading. In section III-3, general

results from finite element methods using the crystal plasticity are presented and in the section III-4, quantitative comparison between simulation and experiment are presented.

3.1 Model framework

<u>Geometry</u>

Various nanoindentation tests on a copper single crystal with various surface orientations and initial dislocation densities are simulated with finite element method (FEM). Figure III-3-1 (a) shows the cylinder which is used to describe the sample submitted to nanoindentation. This volume is meshed with 8 nodes cubic elements. The mesh is composed of 10959 nodes and 10308 elements. The radius and depth of the mesh shape are 50μm and 100μm, respectively. The mesh is composed of 24 circumferential elements, 34 elements along radial direction (on the surface) and 35 elements along the height (in the center of the cylinder).

(a)

(b)
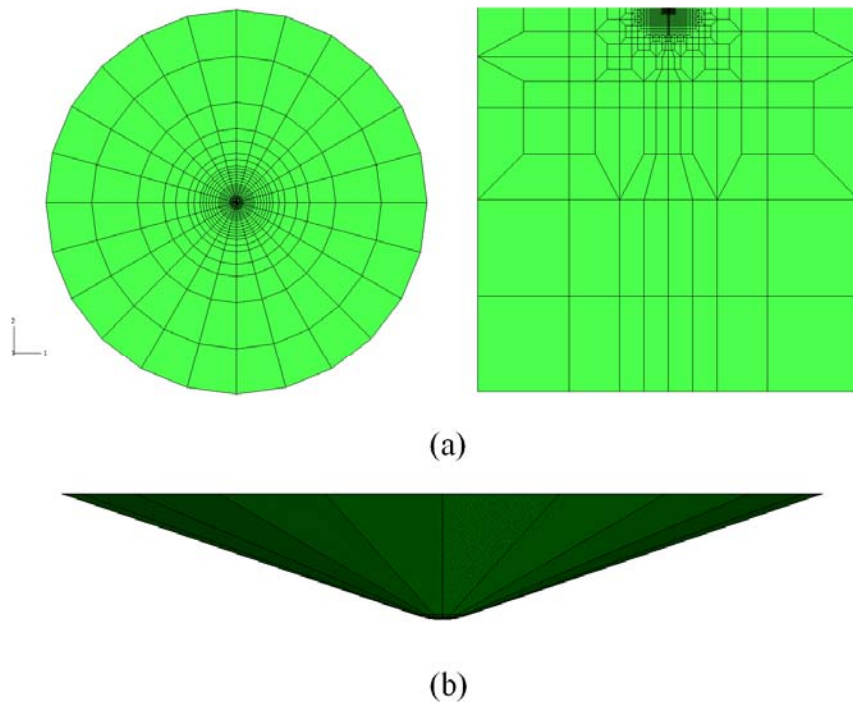
Figure III-3-1. (a) Cylindrical shape of the FEM mesh used for simulations
(b) Modeled indenter defined as a sphere-cone type

Figure III-3-1 (b) shows the indenter used in the simulation. It is of conical shape ended with a sphere at the top. The sphere radius is 3.3μm. The height of the spheroid part is about 200nm. After 200nm, the indenter is conical with an angle of about 71.8°. The total radius and height of

the indenter are about 15µm and 5µm, respectively. The modeled indenter is not composed by rigid body type elements, but described with analytical equation supported by commercial FEM solution packages named ABAQUS [ABA04]. The geometry of the modeled indenter tip reproduces exactly the geometry of the experimental indenter tip.

Plastic Behavior

The plastic behavior of the material is described with the physically based model, proposed by Tabourot *et al*.[TF97] and described in section II-1. This model is implanted into a finite element method (FEM) using the material user subroutine (VUMAT) in ABAQUS [ABA04]. The material parameters of the constitutive behavior laws are given in table III-3-1 for copper single crystal.

Elastic property	C^E_{11}	168.4 GPa
	C^E_{12}	121.4 GPa
	C^E_{44}	75.4 GPa
Flow rule property	γ_0	0.001 /sec
	m^r	0.005
Hardening property	μ	75.4 GPa
	b	2.56×10^{-10} m
	$\alpha_{1\sim6}$	(0.09, 0.09, 0.09, 0.09, 0.09, 0.09) or (0.122, 0.122, 0.07, 0.137, 0.122, 0.625)
Dislocation evolution property	$a_{1\sim6}$	(0.01, 0.4, 0.4, 0.75, 1.0, 0.4)
	K	36.0
	y_c	1.43×10^{-9} m
	ρ_0	$9.0 \times 10^{12} \sim 1.5 \times 10^{14} /m^2$

Table III-3-1. Material parameters used in the FEM elasto-plastic model.

Since the mechanical behavior of copper single crystal is anisotropic, three parameters are necessary to build the anisotropic stiffness matrix (see table III-3-1). The other values used in relations that describe hardening rule and dislocation evolution are determined by recent dislocation dynamics simulation [DKH06, Fiv97 and KDH08]. Only the value of initial dislocation density is considered as an adjustable parameter. As initial dislocation density is one of the most influencing parameters on load, surface morphology and contact area as shown in the previous section, various values are used to quantify the effect of initial dislocations density on results.

The hardening matrix (α^{sp}) is given with a reduced set of only six independent parameters. Two different sets are used during simulations.

1. The value 0.09 is taken for all 6 independent parameters when hardening on system is supposed to be homogeneous [Fiv97].
2. The values of the independent parameters are (0.122, 0.122, 0.07, 0.137, 0.122, 0.625) when non-homogeneous hardening is induce by self, coplanar, ortho, glissile, lomer and collinear interactions, respectively [DKH06].

The matrix parameters (a^{sp}) which controls the dislocation evolution is also described with a set of 6 independent parameters. Two sets are tested.

1. The value of the parameters are (0.01, 0.4, 0.4, 0.75, 1.0, 0.4) as proposed by M. Fivel *et al.* in [Fiv97]
2. The values for (a^{sp}) are similar to the (α^{sp}) values following the assumption of Kubin *et al.*'s [KDH08].

Four different surface orientations are used in simulation in order to determine orientation effects. Correspondence between local and global axis for each orientation is shown in figure III-3-2, where the global Z direction coincides with 4 different indentation crystallographic axis (001), (110), (111) and (123).
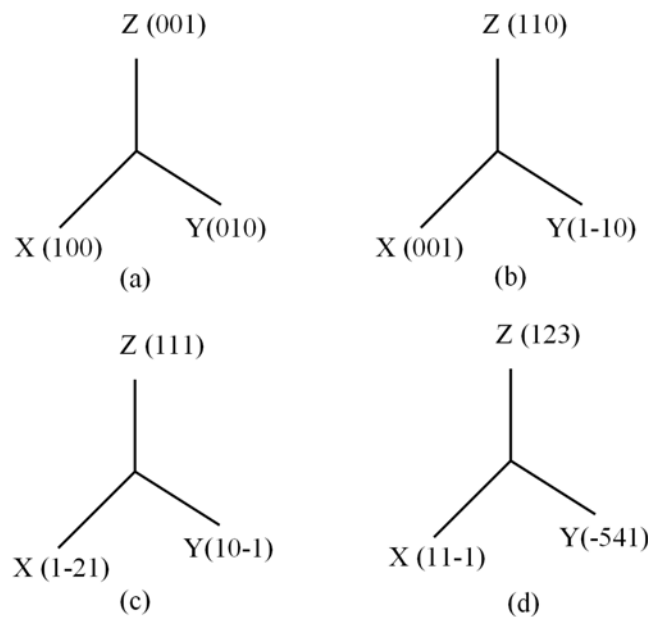
Figure III-3-2. Local and global axis definition for (a) (001) surface orientation
(b) (110) surface orientation (c) (111) surface orientation (d) (123) surface orientation

The transformation from the global axes to the local crystallographic axes is defined by 3 Euler angles. These three angles are used to find surface orientation in the simulations. The Euler angles corresponding to (001), (110), (111) and (123) crystallographic surface orientation as

shown in figure III-3-2 are given in table III-3-2.

Surface orientation $(Z=[z_1\ z_2\ z_3], X=[x_1\ x_2\ x_3])$	Euler angles (ϕ_1, Φ, ϕ_2)
Z=[0 0 1], X=[1 0 0]	(0.00, 0.00, 0.00)
Z=[1 1 0], X=[0 0 1]	(90.0, 90.0, 45.0)
Z=[1 1 1], X=[1 -2 1]	(30.0, 54.7, 45.0)
Z=[1 2 3], X=[1 1 -1]	(285., 36.7, 26.6)

Table III-3-2. Euler angles defining the crystallographic orientation of the crystal.

3.2 Solver method

Integration

One of the possible integration schemes when dealing with finite element technique is implicit method. For most cases, implicit method guarantees the stability of the calculation. However, the implicit method consumes huge calculation time if contact boundary limit conditions are involved during simulation. Especially, the implicit method leads to a critical problem during the nanoindentation simulation.

Figure III-3-3 gives an overview of the problem. The deformed mesh as shown in figure III-3-3 is obtained after a simulation done with implicit scheme. The material behavior is purely elastic.

(a)   (b)
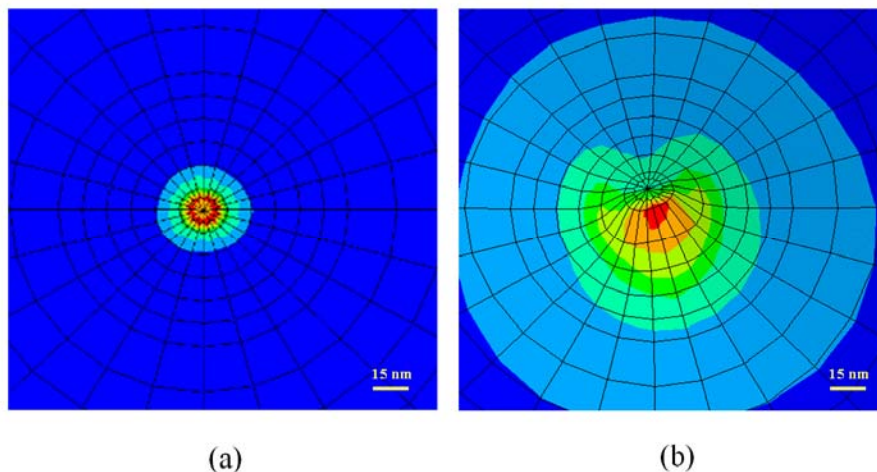
Figure III-3-3. Overview of diverging mesh effect due to the implicit method
(a) initial mesh and initial stress results from nanoindentation of (111) surface orientation
(b) deformed mesh obtained after deeper nanoindentation.

Figure III-3-3 (a) shows the initial mesh. Indentation axis is coincident with the (111) crystallographic orientation. The whole mesh is fine enough to avoid simulation problem. However, the meshes and stress results diverge during the nanoindentation simulation as shown in figure III-3-3 (b). Central point which should remain on indentation axis is moving upwards. Hence, the neighboring elements are widely distorted. The mesh distortion may be due to the numerical instability which breaks the force equilibrium of the central point. When the position is changed, the instability is increased leading to an acceleration of the movement.

Consequently, stress distribution in figure III-3-3 (b) is not really realistic. Indeed, stress results should exhibit a 3-fold symmetry due to the symmetry induce by a (111) surface orientation.

This mesh distortion does not occur during nanoindentation simulation with explicit integration scheme using Arbitrary Lagrangian and Eulerian (ALE) method. This method consumes much less time than the implicit method for the present nanoindentation simulations. Table III-3-3 shows time consumption of the two integration methods for a given nanoindentation calculation, whose final indentation depth is 1400nm indentation depth. The two methods use same meshes and the same elastoviscoplastic behavior is considered for the material.

	Integral method	
	Implicit	Explicit with ALE
Time consume	3 weeks	30 hrs

Table III-3-3. Comparison of the CPU time required for two integration methods

Nevertheless, this technique takes into account acceleration effect and thus boundary conditions have to be carefully controlled in order to impose quasi-static loading. Therefore, the velocity of indenter is monitored in order to minimize the kinematic energy. The explicit integration is then retained for all the nanoindentation simulations.

Boundary condition

Imposed velocity profile of the indenter is shown in figure III-3-4. This smoothed velocity variation is an excellent way to minimize kinematic energy and to obtain quasi static material behavior during simulation.

During the loading stage at a constant velocity, the indenter moves downwards to a depth of 1400nm. Then, the indenter penetrates 50nm deeper during the interval where velocity is decreasing. This smooth transition is also needed to minimize the kinematic energy. If this smooth transition is not respected, the indented material would be given a huge kinematic energy generated by the important acceleration induced by the strong velocity variation between loading and unloading.
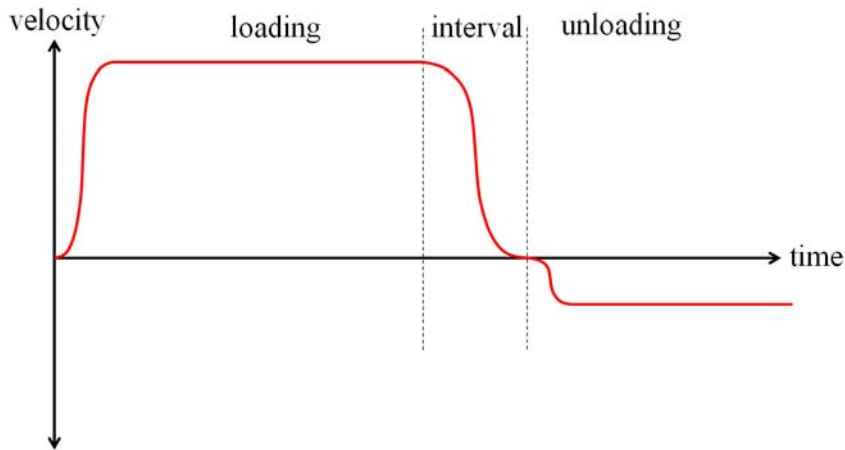
Figure III-3-4. Prescribed indenter velocity during one nanoindentation cycle (load and unload).

In the third stage the indenter starts to move upwards 10 times slower than its loading velocity. This unloading velocity is also imposed progressively in order to limit kinematic energy as well. When the indenter tip is not in contact anymore with the materials, the simulation is stopped automatically.

It is therefore necessary to check if these conditions keep the explicit finite element simulation in quasi static regime. To reach this objective, the corresponding results are compared with the results obtained with implicit simulation which is under quasi-static calculation.

For a simple verification, the comparison between implicit and explicit are performed under the condition of indentation an elastic material with 4 different surface orientations which are (001), (110), (111) and (123). Figure III-3-5 shows the applied load versus indentation depth curves of 4 different orientations and two kinds of simulation methods, where the standard and explicit designations means respectively implicit and the explicit method. The two simulation methods give quite similar results.

There is one missing triangle point at the indentation depth of 0.04μm for the (110) surface orientation. The calculation stops due to a mesh distortion problem. For the same reason, the implicit method fails to give results at a depth of 0.05μm for all the four surface orientation. As a conclusion, the boundary conditions guarantee stable calculation even with very deep indentation depth. In this latter case, simulation can not be achieved with implicit integration.

3.3 Important parameter analysis

Surface orientation effect
In figure III-2-3, a big difference is noticed between the experimental load displacement curves

corresponding to the indentation of crystals with 4 different orientations. The reasons of the difference could be found either in the effect of surface orientation, either in the effect of the initial amount of dislocations in the sample. Numerical simulation is the convenient mean to test the effect of surface orientation with an initial dislocation density kept constant.

For these FEM simulations, hardening coefficients of the model are those of table III-3-1. The hardening coefficients are 0.09 for all the 6 independent parameters of matrix (a^{sp}) and initial dislocation density is set to 4.8×10^{11}/m^2 for any of the slip systems and for all sample whatever the surface orientation is.
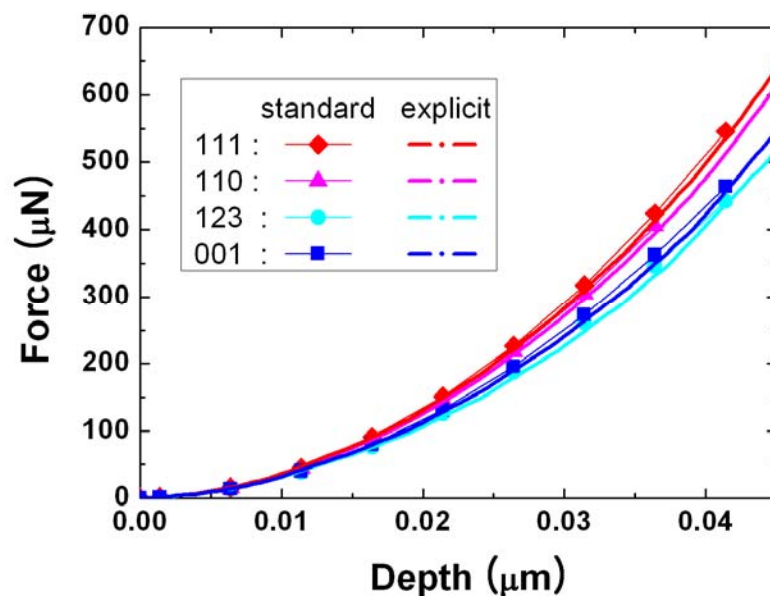
Figure III-3-5. Applied load versus indentation depth curves for the indentation of an elastic sample with 4 different orientations obtained in the case of implicit and explicit finite element simulation.

Figure III-3-6 shows the computed load-depth curves in the case of four surface orientations. The figure shows that the surface orientations induce difference between applied loads at a given indentation depth. Nevertheless, these differences are not really big when compared to the differences observed in the experimental results as shown on figure III-2-3.
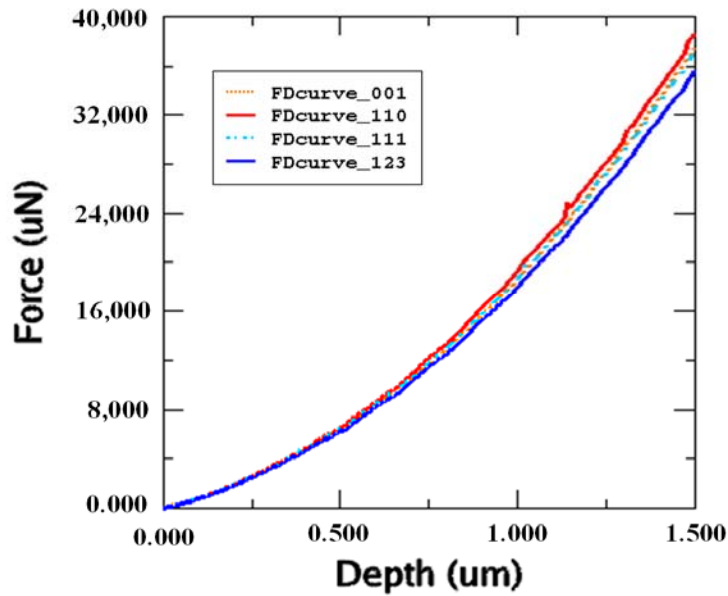
Figure III-3-6. Load versus indentation depth for 4 different surface orientations obtained by FEM simulation including homogeneous plastic hardening coefficients

The maximum applied load, for the (110) surface orientation, is about 39200µN at 1500nm depth whereas the minimum applied load for the (123) surface orientation is about 36000µN at 1500nm depth. Hence, the difference between maximum and minimum applied load at a given indentation depth is less than 8%. The values of applied loads obtained in the case of (001) and (111) orientations are just between the values obtained with (110) and (123) orientation, namely 37600µN at 1500nm depth i.e. about 3% lower than the value obtained in the case of the (110) surface orientation. In the experimental results, the applied load at a given indentation depth and for (110) surface orientation is about 55% higher than that corresponding to the (123) surface orientation and about 10% higher than that corresponding to (001) and (111) surface orientations.

Besides, the surface orientation affects the indentation modulus and the plastic hardening slope. The influence of the surface orientation on the value of elastic modulus is shown in figure III-3-5 where the material behavior is purely elastic. Thus, the order of the applied load displacement curves due to the crystal anisotropy is (111), (110), (123) and (001). This order is different when plasticity is involved during deformation as can be seen on figure III-2-3 and figure III-3-6. This order is (110), (111), (001) and (123). It shows that the elastic anisotropy can not explain the order of applied load versus displacement curves in both experimental and simulation results.

Surface orientations affect strain-hardening because activated slip systems are not the same due to modification in Schmid factor distribution. Identical hardening coefficients reduce naturally difference due to surface orientation effect. Therefore, it is a reasonable assumption that surface

orientation effect on strain hardening may be enhanced by using the non-identical hardening coefficients. Therefore, non-homogeneous hardening coefficients may increase applied load difference among surface orientations.

In order to check if this assumption is correct, nanoindentation is now simulated using non-identical hardening coefficients. Figure III-3-7 shows the applied load displacement curves corresponding to the 4 surface orientations obtained from these simulations.
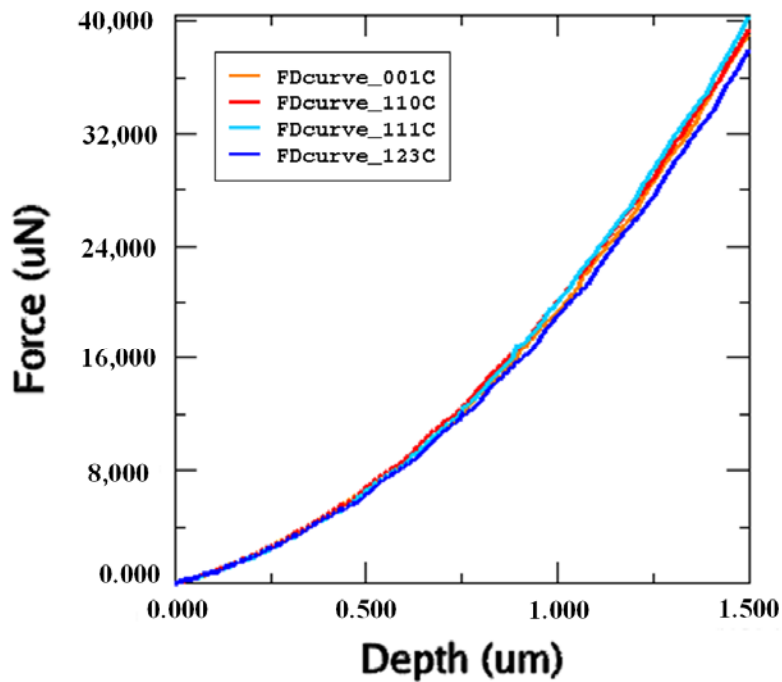

Figure III-3-7. Load versus indentation depth for 4 different surface orientations. Results obtained from FEM simulation where hardening coefficients are non homogeneous.

Initial dislocation density is set to $4.8 \times 10^{11}/m^2$ for all the surface orientations. Applied load differences are smaller than the difference shown in figure III-3-6. The applied load at 1500nm depth in the case of (111) surface orientation is 40000µN, and the applied load at the same indentation depth in the case of (123) surface orientation is 38000µN. The difference between (001), (111) and (110) is less than 2%. This means that use of non-identical hardening coefficients reduces differences, which is a result opposite to initial expectations. This is due to the high increase induced by the (111) and (123) surface orientation which is about 2400µN and a smaller increase for (001) and (110) which is about 800µN.

In conclusion, the chosen surface orientations induce differences about 8% with identical hardening coefficients and 5% with non-homogeneous hardening coefficients. This is not really a big difference compared to experimental one which is about 55%. Therefore, the maximum

55% of difference at the applied load with various surface orientations from the experiment is not only due to the surface orientation difference but to different initial densities in the crystals used for experimentation.

Initial dislocation density effect

The indentation experiment is widely used for getting the yield stress at an industrial level because it is proved that hardness value from the indentation experiments is closely related to its yield stress [AT65]. In the frame of crystal plasticity theory presented in section II-1, the yield stress is calculated with initial dislocation density and hardening coefficients as following equation (II-1-35). Therefore, initial dislocation density deeply affects to results of the nanoindentation.

Figure III-3-8 shows applied load displacement curves with 3 different initial densities for in the case of a (111) surface normal orientation.
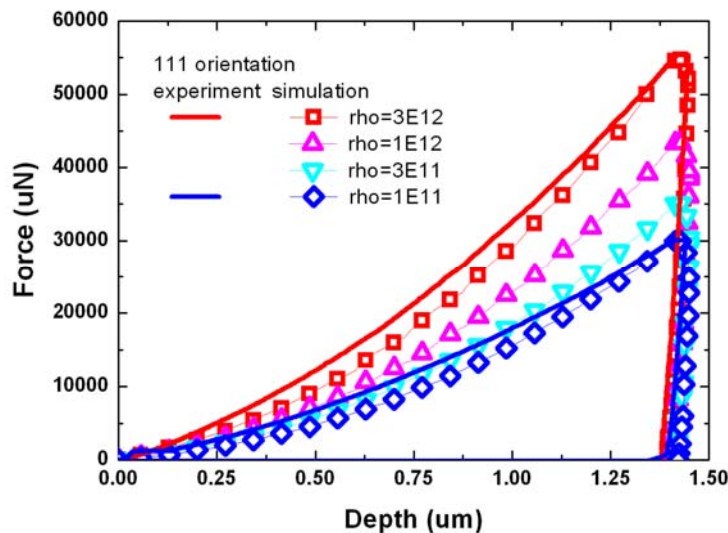
Figure III-3-8. Load versus indentation depth curves obtained from (111) nanoindentation simulations for four different initial dislocation densities. Experimental curves with two different initial dislocation densities are superimposed in thick lines.

Increasing initial dislocation density results in increasing applied load for a given indentation depth. The applied load for 1400nm indentation depth with 3.6×10^{13} /m^2 initial dislocation density is 55000 μN and the one with 1.2×10^{13}/m^2, 3.6×10^{12}/m^2 and 1.2×10^{12} /m^2 initial dislocation densities are about 45000 μN, 35000 μN and 30000 μN, respectively.

As a result, 3 times higher initial dislocation density multiplies applied load by 1.2 for a given indentation depth. The applied load on the sample with 1.2×10^{12}/m^2 initial dislocation density is

quite similar with the applied load obtained experimentally in the case of (111) surface orientation. The applied load on a sample with $3.6 \times 10^{13}/m^2$ initial dislocation density is quite similar to the applied load obtained experimentally in the case of test on one another (111) surface orientation. The curvatures of the load displacement curves are a bit different between the experiments and simulations. It means that it is possible to fit experimental applied loads displacement curves by using only one parameter, the initial dislocation density.

Figure III-3-9 gives the relationship between hardness and yield stress in the case of a (111) surface normal orientation.
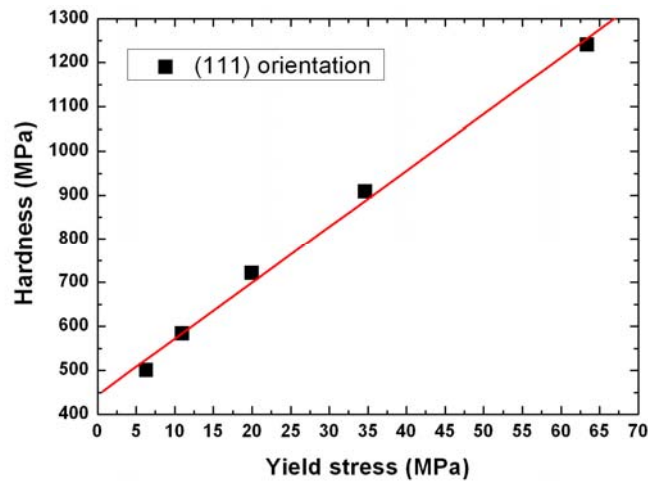
Figure III-3-9. Relationship between hardness and yield stress obtained from (111) nanoindentation simulations

The hardness values are calculated as the maximum force from the indentation simulations divided by the related contact area (see figure III-3-9 and table III-2-3). The yield stresses are obtained from total dislocation density and equation II-1-37. In this figure, the hardness values have a linear relationship with yield stress, where the red line in figure III-3-9 shows the best linear fitting curve. The fitting slope is about 12.8 and the curve intercepts 444.17 of y axis.

Figure III-3-10 shows experimental applied load versus displacement curves in the case of the 4 different surface orientations compared to those obtained numerically. Appropriate initial dislocation densities are determined in order to obtain a good agreement between experimental and numerical data. The curvatures of the load versus displacement curves are a bit different between experiments and simulations. The initial dislocation densities of (110), (111) and (001) surface orientations are quite similar to each others but the initial dislocation density of (123) surface orientations is lower than the others. This is probably due to the difference of sample preparation method as described in previous sections.
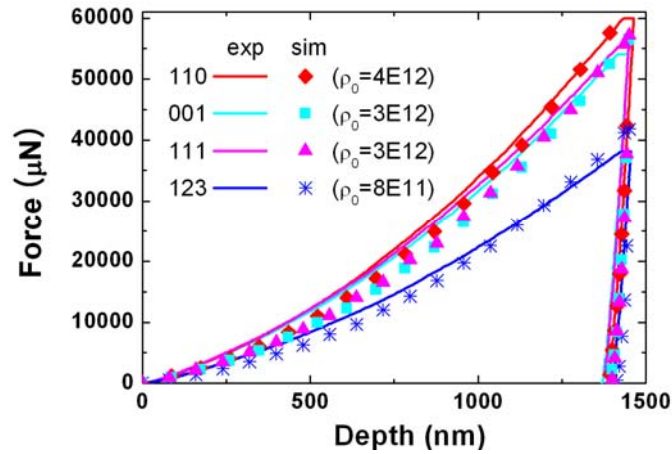
Figure III-3-10. Experimental applied load versus indentation depth obtained for 4 samples with different surface orientations. Initial dislocations are fitted in order to retrieve the data in the case of numerical simulation

<u>Plastic crystal flow effect</u>

The various orientations induce also various morphologies of the imprint. For each surface orientation, figure III-3-11 gives the surface displacement obtained by FEM simulations.
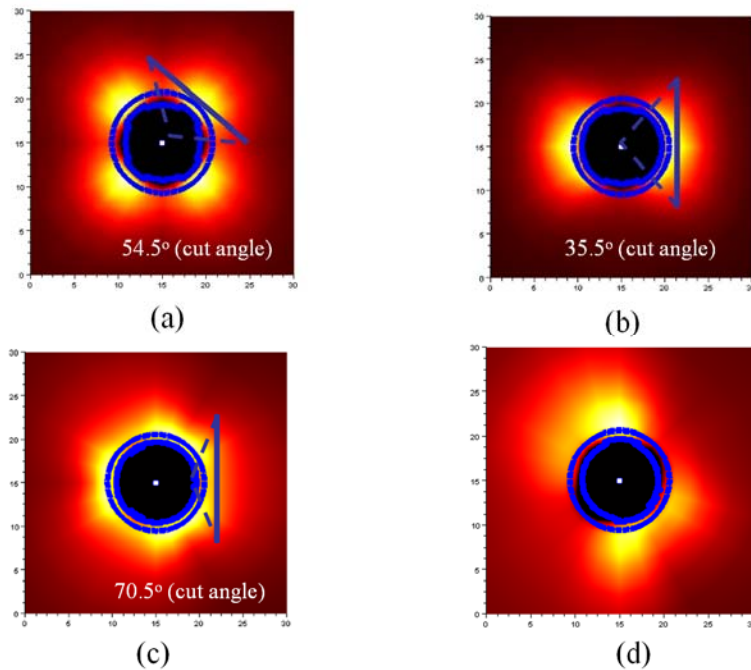

Figure III-3-11. The surface displacement morphology with different surface orientations from FEM simulation (a) (001) surface orientation, (b) (110) surface orientation, (c) (111) surface orientation (d) (123) surface orientation

To obtain such presentation, FEM simulations results are post processed with a routine developed under the Scilab software environment [Sci]. The surface profiles obtained with FEM simulation are quite similar to the experimental ones when referring to figure III-2-6. Each of the surface morphologies in figure III-3-11 has its own typical symmetry. The symmetries due to the surface orientations are 4-fold symmetry for (001), 2-fold symmetry for (110) and 3-fold symmetry for (111), respectively. Surface morphology from (123) orientation has weak 2-fold symmetry but the height of the 4 pile-up picks are different among them. The symmetry of the morphologies is connected to projection of active slip systems as shown in figure III-2-10.

Every orientation induces both pile-up and sink-in regions simultaneously. It is assumed from figure III-2-9 and figure III-2-10 that the pile-up peaks are caused by the activated dislocations. Figure III-3-11 (a), (b) and (c), shows the geometry of a cutting layer including a maximum pile-up peak. Such layer corresponds indeed to the plane of locally activated slip system. The cutting angles for getting the layers are 54.5^o for (001) surface orientation, 35.5^o for (110) surface orientation and 70.5^o for (111) surface orientation, respectively. Because the cutting layer is parallel to the slip plane of the activated slip system, the regions of high dislocation densities are distributed through the slip direction of the activated slip system.

The dislocation densities and moving direction of the dislocations of the activated slip systems, at the cutting layer from (001) surface orientation are given in figure III-3-12.
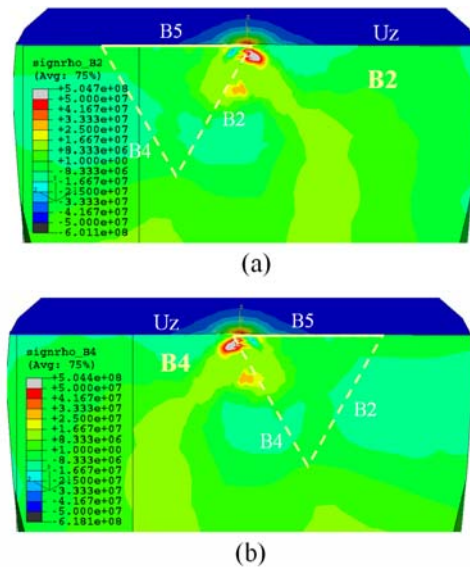

Figure III-3-12. Dislocation densities and moving direction of the dislocations in the activated slip systems in the cutting layer for (001) surface orientation

(a) dislocation density of slip system B2 (b) dislocation density of slip system B4

The cutting layer is parallel to B slip plane. The activated slip systems for pile-up peak at the cutting layer are B2 slip system, whose dislocation density is shown in figure III-3-12 (a), and B4 slip system, whose dislocation density is shown in figure III-3-12 (b), as expected in figure III-2-10 (a). The sign of dislocation density depicts the moving direction of the dislocation at the slip system, where the plus sign depicts the dislocation moving upward and vice verse. Therefore, we can observe the flow of dislocation movement from this figure. Below the pile-up peak, there is a high density spot, whose color is the red. Hence, the dislocations at the high density spot are moving through upward direction. Besides the high dislocation density moving upward, it is observed that another high dislocation densities, whose color is blue, moves downward. We can also observe from the figure that the high dislocation density regions are laid through the slip direction of the activated slip system, exactly.

The dislocation densities and moving direction of the dislocations of the activated slip systems in the cutting layer for (110) surface orientation are given in figure III-3-13.
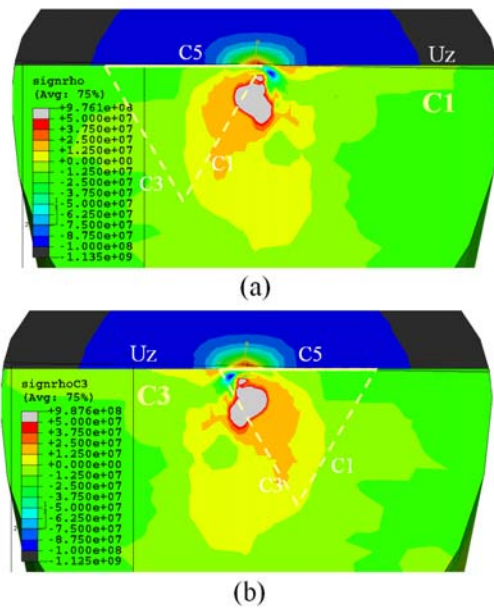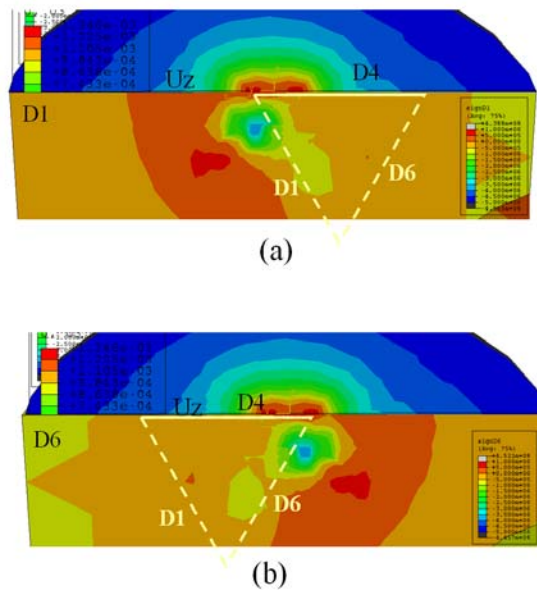

Figure III-3-13. Dislocation densities and moving direction of the dislocations of activated slip system in the cutting layer for (001) surface orientation (a) dislocation density of C1 slip system (b) dislocation density of C3 slip system

This cutting layer is parallel to C slip plane. The activated slip systems responsible of pile-up peak in the cutting layer are C1 and C3. The corresponding dislocation densities are shown in figure III-3-13 (a) and (b). For the latter system, it can be also referred to figure III-2-10 (b). The positive sign of dislocation density indicates the upward moving direction of the dislocation on the slip system. In the figure III-3-12, this convention is applied. Below the pile-up peak, there is a high density spot, whose color is red and whose moving direction is upward.

Backward through slip direction of the C1 and C3 slip systems, it is observed one another spot of high dislocation densities, whose color is blue. Consequently, the dislocations move downward. A third high dislocation spot with upward moving direction is also noticeable. We can also observe from the figure that the line made from the three high dislocation density regions is parallel to the slip direction of the C1 and C3 slip systems, too.

The dislocation densities and moving direction of the dislocations of the activated slip systems in the cutting layer for (111) surface orientation is given in figure III-3-14.

Figure III-3-14. Dislocation densities and moving direction of the dislocations in the activated slip systems in the cutting layer for (001) surface orientation
(a) dislocation density in slip system D1 (b) dislocation density in slip system D6

The cutting layer is parallel to D slip plane. The activated slip systems for pile-up peak in the cutting layer are D1 slip system, whose dislocation density is shown in figure III-3-14 (a), and D6 slip system, whose dislocation density is shown in figure III-3-14 (b) : it can be compared to figure III-2-10 (c). Below the pile-up peak, there is a small high density spot, whose color is red and whose moving direction is upward. The high density region is smaller than the other high density regions below the pile-up peaks at the figure III-3-12 and III-3-13. It may be due to the value of the angle between the surface and the slip plane normal which is close to 90$^{\text{o}}$. This could explain that the pile-up height for (111) surface orientation is lower than the pile-up height for (001) or (110) surface orientation. Backward through slip direction of the D1 and D6 slip systems, it is observed that other big spots of high dislocation densities, whose color is blue. The line made from the two high density regions is parallel to the slip direction of the D1 and D6 slip systems, exactly.

As a result, the dislocation's upward movement at the activated slip system causes the pile-up peak morphology of (001), (110) and (111) surface orientations.

3.4 What should be retained from this section

- Surface orientation effect : weak
- Initial density effect : strong
  - Increase applied load with same indentation depth
  - Increase Hardness
- Surface morphology
  - Determined from symmetry of activated slip systems

4. Quantitative comparison between simulations and experiments

4.1 Correction of stiffness and load-depth curves

<u>Correction of elastic compliance for comparison of load displacement curves</u>

The real indenter is made of sapphire, whose elastic modulus and Poisson ratio are 345GPa and 0.34, respectively. In the simulation, the indenter is modeled as a rigid body whose elastic modulus is infinite. This differs from reality and affects the comparison between experiment and simulation. Therefore, for a clear comparison between experiments and simulations, the results of simulation should be corrected.

Figure III-4-1 zooms on numerical and experimental applied load displacement curves in the zone defined by the transition between loading and unloading. In the simulation each orientations have their own fitted initial dislocation densities, which are $4.8 \times 10^{13}/m^2$, $3.6 \times 10^{13}/m^2$, $3.6 \times 10^{13}/m^2$ and $9.6 \times 10^{12}/m^2$ for (110), (111), (001) and (123) surface orientations, respectively. With those parameters, the simulated applied load displacement curves are quite well superimposed to the experimental ones in the loading phase as shown in figure III-3-9. However, a gap exists between experimental and numerical results in the unloading phase as shown in figure III-4-1. Especially, the initial slopes of the 4 simulated curves are much higher than the initial slopes of experimental curves.
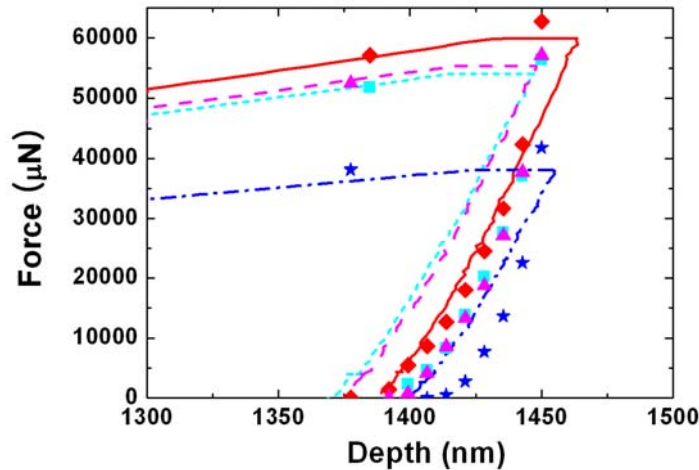

Figure III-4-1. Load-displacement curves during unloading state from experiments with 4 different surface orientations and from simulations using appropriate initial dislocation densities to fit the experimental curves

As mentioned above, this is mainly due to the infinite stiffness of the indenter and correction should be introduced on the numerical results. Following equation (III-1-14), square root of the applied load is a linear function of the indentation depth, and the slope is related to the square root of the indentation compliances ($\sqrt{C^*}$). Therefore, the correction of the simulation results can be done.

Figure III-4-2 (a-d) shows the square root of applied load displacement curves extracted from 4 simulations with different surface orientations of the sample. The curves are not linear at the beginning.
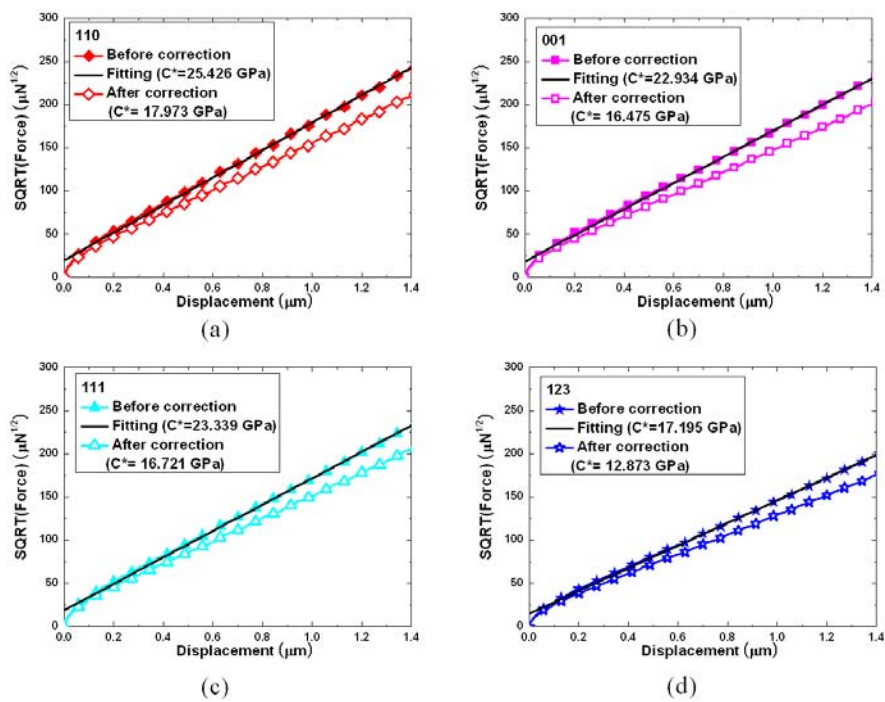
Figure III-4-2. Square root of the applied loads versus indentation depth extracted from simulations with 4 different surface orientations, (a) for (001) surface orientation, (b) for (110) surface orientation, (c) for (111) surface orientation, (d) (123) surface orientation

This non-linearity is due to the non-conical (spherical) part on the top of the indenter. Once the conical part is sufficiently inside the material (i.e. after 0.2 μm displacement), the curve becomes linear. The sample compliances (C^*_{sample}) are then obtained by least squares minimization for each surface orientation. Compliances for (110), (001), (111) and (123) surface orientations are 25.4GPa, 22.9GPa, 23.3GPa and 17.2GPa, respectively. As indenter is modeled by a rigid body in the simulation, the comparison between experimental and numerical results requires a correction of these compliances should be corrected as described in section III-1-2. The elastic coefficients of sapphire are 345GPa for elastic modulus and 0.34 for Poisson ratio

[Cha06]. Then, the compliance $C^*_{indenter}$ of the sapphire indenter is estimated with equation (III-1-17) to the value of 709GPa. The bulk material's compliances are then corrected following equation (III-1-18). The corrected compliances for (110), (001), (111) and (123) surface orientations are finally 18GPa, 16.5GPa, 16.7GPa and 12.9GPa, respectively. Original and corrected curves are presented in figure III-4-2 (a-d). Application of the correction tends to lower the curves as presented on the figure above.

Figure III-4-3 shows the effect of the correction applied in the case of an indentation on a sample with a (111) surface orientation.
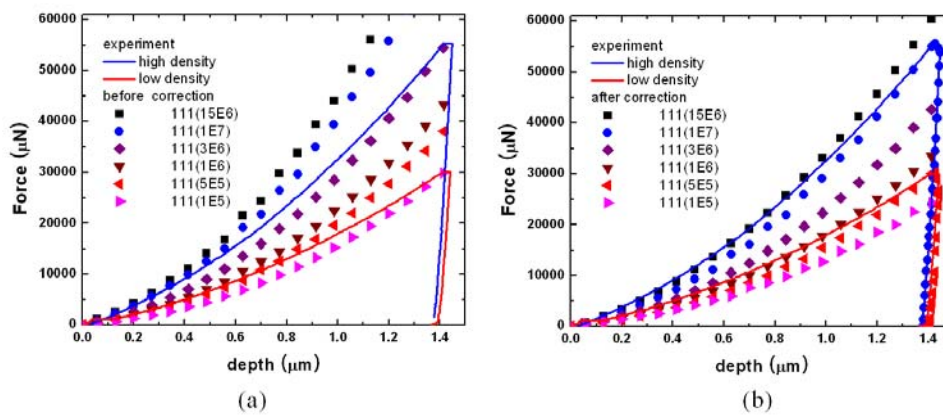
Figure III-4-3. Simulated applied load versus indenter displacement curves for indentation of (111) surface oriented samples with various initial dislocation densities (a) before correction of the simulation results, (b) after correction of the simulation results

Simulations are done with six initial dislocation densities. In order to have experimental reference, the corresponding curves for nanoindentations on sample with two different initial dislocation densities are also reported. Figure III-4-3 (a) refers to results without any correction while (b) stands for the corrected ones.

Before correction as shown in figure III-4-3 (a), the applied load displacement curve for $1.2\times10^{12}/m^2$ and $3.6\times10^{13}/m^2$ initial dislocation density values are quite similar with the two experimental curves corresponding to low and high initial dislocation densities, though the curvatures of experimental and simulated curves are a bit different. As the correction lowers simulated curves, the curves for $1.2\times10^{12}/m^2$ and $3.6\times10^{13}/m^2$ initial dislocation densities become lower than the experimental reference curves. Instead, the curves for $6.0\times10^{12}/m^2$ and $1.2\times10^{14}/m^2$ initial dislocation densities become quite similar to experimental reference curves. After introducing correction due to the elasticity of the sapphire indenter, $6.0\times10^{12}/m^2$ and $1.2\times10^{14}/m^2$ are considered as reasonable initial dislocation densities to fit experimental results. Using the same procedure, the initial dislocation densities in the case of (001), (110) and (123)

oriented samples are recalculated. Those results are use to obtain the curves presented in figure III-4-4 (a) and (b).

Figure III-4-4 (b) focuses on the transition between loading and unloading phases. It becomes clear, that with these corrections, the unloading phase is well described by the numerical results.
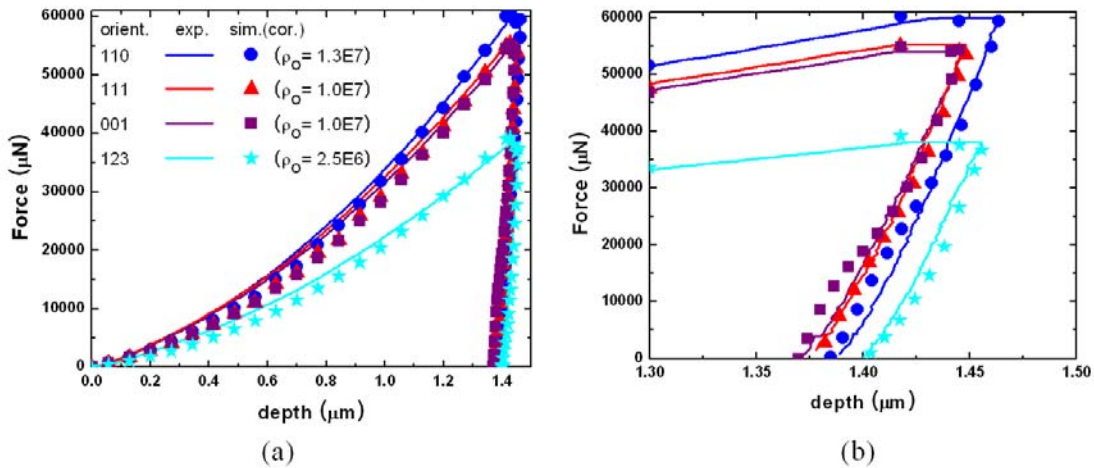

Figure III-4-4. Simulated applied loads versus displacement curves of samples with different surface orientation after correction of indenter elasticity effect (a) during loading state (b) during unloading state

Correction of the indentation modulus for comparison of the stiffness-depth curves

One way to obtain the indentation stiffness value is based on the use of the applied load displacement curve. As described in section III-1-2 (see equation (III-1-8)), the indentation stiffness is obtained by differentiating the applied load with respect to indentation depth when the indentation is done in such a way that strains remain elastic. Another way to get stiffness is to differentiate applied load with respect to indentation depth just after starting unloading in the case of the elastoviscoplastic material. In our calculations, the stiffness at a given indentation depth is obtained from simulations where the material is considered to have pure elastic behavior as shown in figure III-3-5 and from simulations where the material has elastoviscoplastic behavior.

Figure III-4-5 (a-d) show the applied load displacement curves obtained by simulations of indentation on samples with (110), (001), (111) and (123) surface orientations. The material behavior is elastoviscoplastic. During the loading phase, 10 indentations depths are considered to start simulations of unloading phase and get corresponding indentation stiffnesses. The 10 unloading curves for (110), (001), (111) and (123) surface orientation are gathered in figure III-4-5 (a-d).
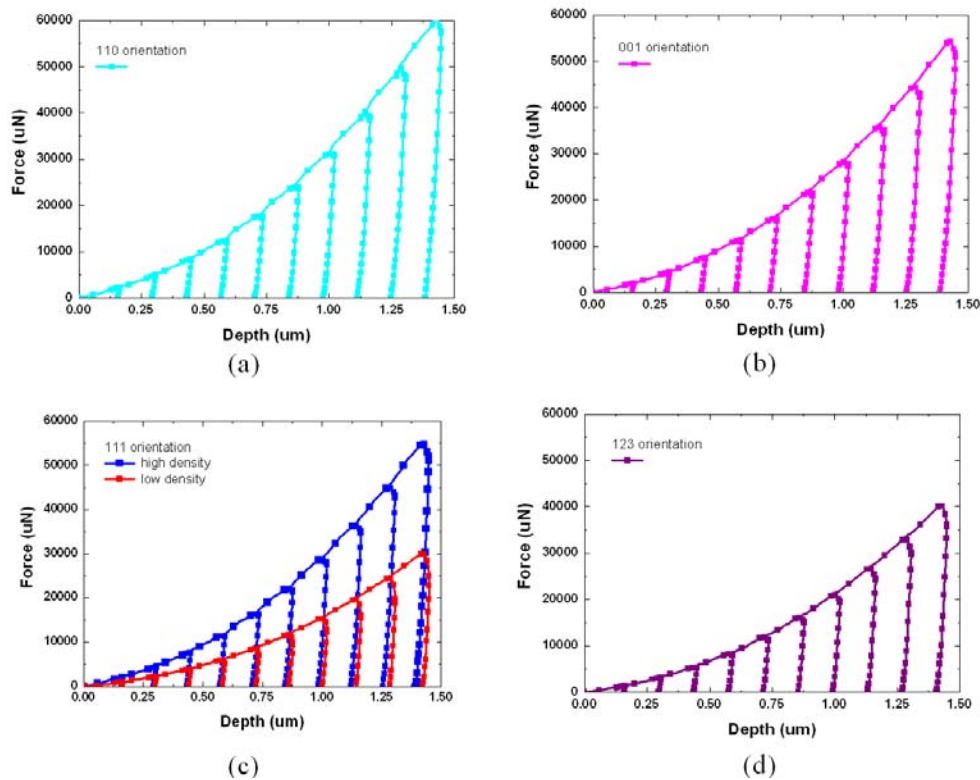
125

Figure III-4-5. Applied load versus indentation depth for loading and unloading states from the 10 different indentation depths (a) for (110) surface orientation, (b) for (001) surface orientation, (c) for (111) surface orientation (d) for (123) surface orientation.

The beginning of the curve in unloading phase are used to get the slope which should correspond to the stiffness at the given indentation depth. The results are plotted in figure III-4-6. Figure III-4-6 (a-d) shows the evolution of indentation stiffness for samples with (110), (111), (001) and (123) surface orientations with respect to contact area extracted from simulations of indentation of a material with pure elastic behavior or elastoviscoplastic behavior.

Contact area is an important parameter in the determination of stiffness. To make comparable the values of stiffness determined either with elastic material or with elastoviscoplastic material, same contact area determination should be used. When the indentation is carried on elastic material, one determines the contact area, simply by calling specific function of Abaqus which provides value of contact area between indenter and specimen. A complementary computation is necessary to obtain the projected area used in the relationship for stiffness determination. The green symbols are indentation stiffness for each surface orientation with respect to contact area extracted by calling specific function of ABAQUS from the simulation for a material with pure elastic behavior. For the elastoplastic material indentation, determination area takes place once the material is unloaded. A method based on surface normal angle criterion as described in

126

section III-1-1 is then available to estimate the area of the residual deformed cavity induced formally by the indenter.
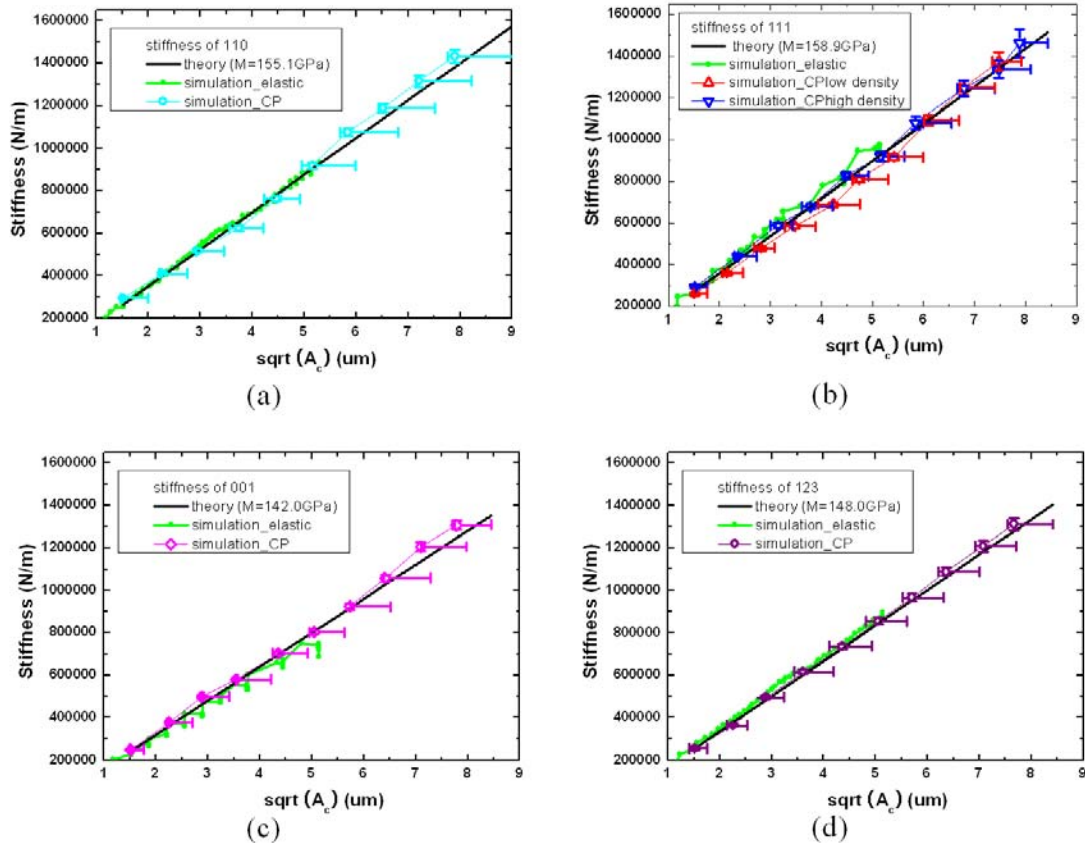

Figure III-4-6. Indentation stiffness versus square root of contact area curves obtained from simulations of indentation of purely elastic samples and elastoplastic material (a) for (110) surface orientation, (b) for (111) surface orientation, (c) for (001) surface orientation (d) (123) surface orientation

The color symbols except for green one in the figure III-4-6 correspond to contact area values provided by the method with 17 ^{o} angle criterion. The method with 18.8 ^{o} and 9.4^o angle criterions is used to get the minimum and maximum values of contact area at the given indentation depth. The extremities of horizontal error bars are obtained by plotting the minimum and maximum contact areas at the given indentation depth.

The stiffness values obtained either for elastic material or after removing the indenter in the case of indentation of an elastoplastic material are similar to each other. It is also seen that the indentation stiffness values at a given contact area do not depend on initial dislocation density as shown in figure III-4-6 (b) which allows to be confident in the simulation.

Stiffness depends only on elastic behavior. For the isotropic material, it is well known that the

stiffness values from the simulations of indentation of elastic material are the same as stiffness values for elasto-plastic materials [Fis02]. However, it has not been confirmed that this rule apply to anisotropic material. Now, Because of results of figure III-4-6, we can say that stiffness do not depend on the plastic properties including initial dislocation density even for anisotropic material.

Equation (III-1-8) implies that stiffness should increase linearly with the square root of contact area. The indentation modulus is then obtained by determining the slope of the stiffness vs. square root of contact area curve. The black lines shown in figure III-4-6 corresponds to theoretical stiffness values computed by equation (III-1-8), where the indentation modulus is taken as the best fitting slopes of the simulation data. The indentation modulus of (110), (111), (001) and (123) are 155.1GPa, 158.9GPa, 142.0GPa and 148.0GPa, respectively. Ordering the surface orientations on their corresponding indentation modulus value basis is (111), (110), (123), (001) (decreasing order). It is not the same order when the sorting criterion is funded on values of applied load at a given depth which is (110), (111), (001), (123).

The objective is now to compare the stiffness values between experiment and simulation. One way is the comparison on the indentation stiffness vs. square root of contact area curves. One difficulty is that there is no way to calculate the contact area during the loading phase of a nanoindentation experiment. The only measurable geometry is the residual contact area value after unloading state. Before comparing the indentation stiffness values from experiment and simulation therefore, first thing to do is to see whether the contact areas from experiment and simulation are identical or not.
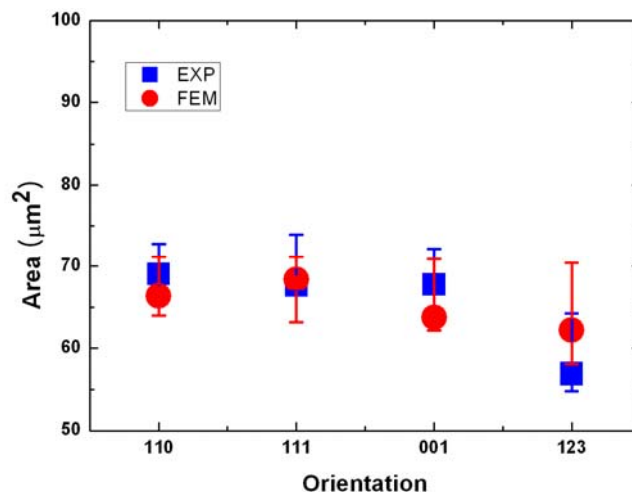

Figure III-4-7. Contact area values for various surface orientations after unloading obtained from experiments and simulations

The figure III-4-7 gives the contact area values in function of the surface orientations after unloading obtained from experiment and simulation. Blue squares are used for contact area values from experiment using an angle criterion to get the contact area of 17°, while blue error bar extremities are obtained with the minimum and maximum values of contact area for an angle criterion of 18° and 9°, respectively. Red circle are used to plot contact area from simulation using an angle criterion of 17° angle. The red error bar extremities are obtained following the experimental prescriptions as well (angle criterion of 18° and 9°).

The contact areas in the case of (110) and (001) surface orientations issued from simulation are 66.4 μm^2 and 63.7μm^2. They are a bit lower than the values issued from experiments but the difference ratio is less than 5%. The simulated contact area for (111) surface orientation is about 68.4 μm^2 which is quite similar to the value determined from experiment, which is 67.7 μm^2. The simulated contact areas for (123) surface is 62.2 μm^2. It is a bit higher than the experimental value. The difference between experiment and simulation for (123) surface orientation is about 9%. From this comparison, it is retained that the contact area from simulation is determined with a good approximation since the maximum difference between experiment and simulation is less than 10%.

The values of indentation modulus for each surface orientation from both experiment and simulation are plotted in figure II-4-8.
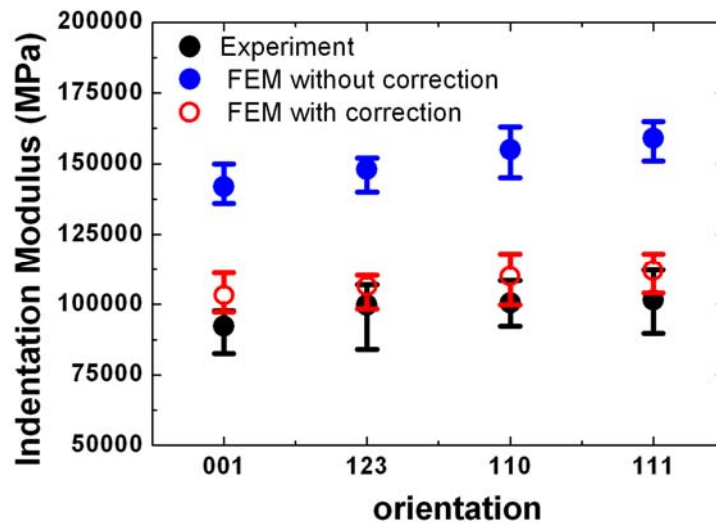

Figure III-4-8. Indentation modulus for various surface orientations obtained both from experiments and simulations

The blue and black symbols are used for the values extracted from numerical simulation and experiment by mean of equation (III-1-11).The corrected modulus by means of equation (III-1-12) (taking into account sapphire elasticity) is plotted with the red symbols. Error bars for

experimental data are due to the fluctuation of stiffness value and contact area variation when different angle criterions are used. Error bars for simulation data are due to contact area variation when different angle criterions are used.

The highest experimental indentation modulus is about 105GPa obtained for the (111) surface orientation and the lowest one is about 90GPa for (001) surface orientation. Indentation modulus for (110) and (123) orientations are 100GPa and 98GPa, respectively. The indentation modulus determined numerically without correction are respectively 142.0GPa, 148.0GPa, 155.1GPa, 158.9GPa for the (001), (123), (110) and (111) surface orientations. These values are reduced after application of the correction. They are respectively 103.3GPa, 106.4GPa, 110.7GPa and 111.9GPa for (001), (123), (110) and (111) surface orientation. Though there is about 10% difference between indentation modulus from experiment and simulation, the difference is not as big as their error range.

Figure III-4-9 compares the evolution of indentation stiffness for the various surface orientations in function of indentation depth obtained from experiment and by simulation.
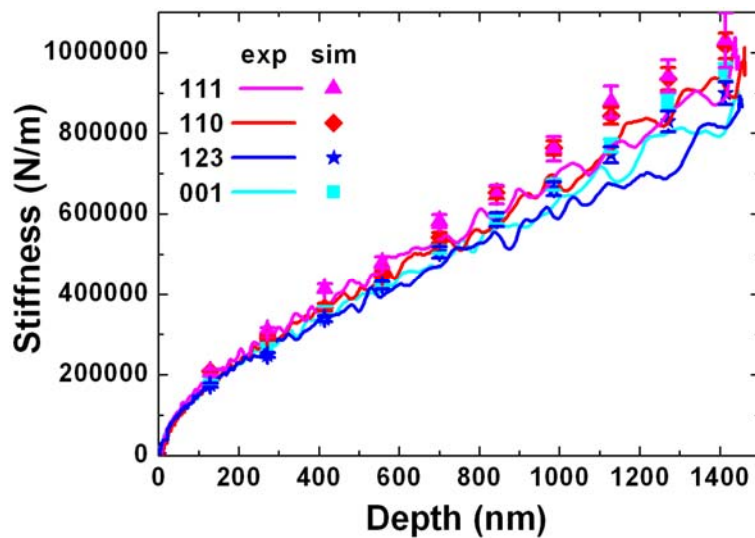

Figure III-4-9. Experimental and simulated indentation stiffness versus indentation depth curves for samples with different surface orientations.

The elasticity of indenter is introduced by making use of equation (III-1-13). At the beginning, the indentation stiffness values from experiment and simulation are similar, but a growing difference between results is noticed when indentation depth increases. The maximum difference is about 10% for the final indentation depth. It is nevertheless considered that the numerically determined stiffness is rather in good accordance with experimental results.

4.2 Effect of hardening parameters

Model explanation and simulation conditions

In order to carry on a refined study of nanoindentation of a copper single crystal with a (111) surface orientation a new finite element model with refined mesh is designed.

Figure III-4-10 shows the cylinder shape finite element mesh, composed of 30924 elements and 32509 nodes. The elements are 8 nodes cubic elements. Dimensions are 50μm for the radius and 100μm for the height. The mesh is composed of 72 circumferential elements, 34 radial elements and 35 elements along the height. The cross section of the fine meshes for detailed nanoindentation simulation is the same as the previous mesh (see figure III-3-1), but the number of circumferential elements increases by a ratio of 3. This refinement is necessary for detailed observation of surface morphology and pile up height distribution through section of the specimen. Figure III-4-10 (a) shows a top view of the mesh, on which the high mesh density in circumferential direction can be seen.

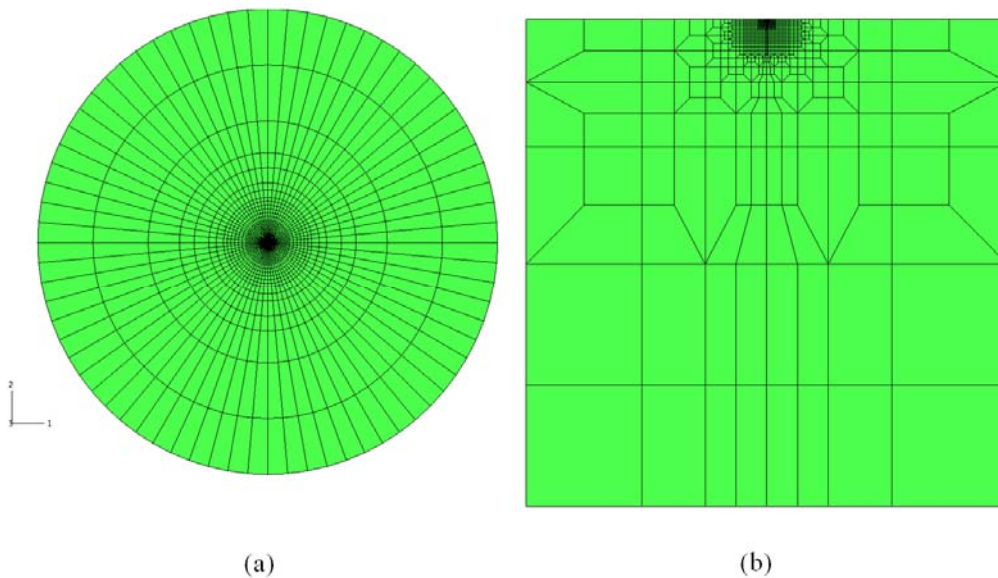
(a)   (b)

Figure III-4-10. Cylindrical mesh used (a) top view (b) front section view

Figure III-4-10 (b) shows front view which looks similar to the previous meshes shown in figure III-3-1 (a). The sphere-cone type rigid body indenter is used in this simulation as previously described in the figure III-3-1 (b).

The behavior model is the same as the one used previously in paragraph III-3.1. The material parameters are the same as those proposed in table III-3-1 apart from the hardening parameters and those involved in dislocation evolution rule. The initial dislocation density for the bulk

material is set to 1.2×10^{14} /m^2 for (111) surface orientation (see table III 3-1).

Six combinations involving hardening rule and dislocation evolution rule parameters are used for analyzing the effect of the plastic parameters on indentation test. The 6 different combinations are shown in table III-4-1.

dislocation evolution ($a_{1\sim6}$) / hardening ($\alpha_{1\sim6}$)	Taylor (0.090, 0.090, 0.090, 0.090, 0.090, 0.090)	Hetero (0.122, 0.122, 0.07, 0.137, 0.122, 0.625)
Normal (0.010, 0.400, 0.400, 0.750, 1.000, 0.400)	K=36	K=36
Same same value as Hardening parameters ($\alpha_{1\sim6}$)	K=36	K=36
High K (0.010, 0.400, 0.400, 0.750, 1.000, 0.400)	K=100	K=100

Table III-4-1. Various parameters set for hardening rule and dislocation evolution rule

Two kinds of matrix for hardening rule (α^{sp}) are used. The first one is designed to give back homogeneous hardening on all system and is named Taylor matrix. The second one which considers heterogeneous hardening rule on the different slip system is named Hetero. It takes into account the various junction strengths including very high collinear junction strength. The matrix coefficients for Taylor hardening rule (α^{sp}) are all equal and their value is 0.09. For the Hetero hardening rule, the 6 independent parameters are 0.122, 0.122, 0.07, 0.137, 0.122, 0.625. Dislocation evolution rule requires the determination of the matrix coefficients (a^{sp}) and a storage variable (K_g). Three sets of parameters are used. They are named "normal", "same" and "high K".

- The parameter set "normal" has the following values: (0.01, 0.4, 0.4, 0.75, 1.0, 0.4) and K_g value is 36.
- The parameter set named "high K" is defined by (0.01, 0.4, 0.4, 0.75, 1.0, 0.4) and K_g value is 100 which induce a very weak dislocation storage.
- The matrix parameters for the set named "same" are identical to the parameters set used for hardening coefficients, as proposed by Kubin *et al*. [KDH08] and K_g value is 36.

To avoid mesh distortion during simulation, the finite element simulation was carried out with explicit integration method. The monitoring of the indenter displacement is done as in the previous paragraph in order to minimize the transformation of applied work into kinetic energy.

Parameters for plastic property effect

Figure III-4-11 shows the applied load displacement curves for the six sets of plastic parameters (see table III-4-1). Experimental results are also reported on this figure. The maximum and minimum applied loads at a depth of 1400nm are 66000μN and 48000μN for the parameters set Hetero+normal and Taylor+highK, respectively.
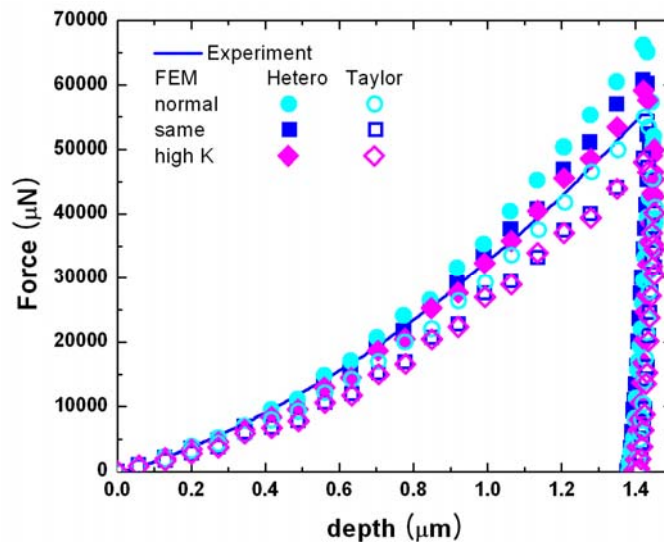

Figure III-4-11. Load versus indentation depth curves obtained from simulations with six plastic parameters sets in the case of (111) surface orientation.

The value of minimum applied load is about 30% lower than the maximum applied load. The applied loads for the other parameter sets at the same indentation depth are 60700μN for Hetero+same, 59100μN for Hetero+highK, 55000μN for Taylor+normal and 48700μN for Taylor+same, respectively.

The applied loads from the three Hetero hardening parameter sets are above 60000 μN. On the other side, the applied loads from the three parameter sets involving Taylor coefficients are below 55000 μN. They are 20% lower than the value from sets involving Hetero hardening coefficients with dislocation evolution which is similar in both cases. For a given hardening set (Taylor or Hetero) changing from parameter sets highK to same parameters set has practically no influence, but they are about 10% lower than the applied load from parameter set named normal.

As a conclusion of this study, the hardening coefficients are among the important parameters which control the applied load evolution during loading. The load itself results from stresses inside the specimen. The evolution of resolved shear stress is related to total dislocation densities through the 6 values of hardening matrix (α^{sp}). The average value of Taylor hardening

parameters is 0.3, whereas this average is 0.5 for Hetero hardening parameters. Therefore, change from Taylor to the Hetero parameters will increase the applied load about 20% at the same indentation depth.

The matrix for dislocation evolution (a^{sp}) and K_g are related to storage ratio between generated dislocations and total dislocations. Mean ratios are obtained by dividing the average values of a^{sp} by the K_g. These ratios are 0.02, 0.01 and 0.007 for parameter set normal, same and high K, respectively. It can be seen that decreasing the storage ratio will decrease the applied load by 10% at a given indentation depth. It is due to subsequent decrease of the total dislocation density. Figure III-4-12 shows the values of the area after indentation for the six sets of plastic parameters. The contact area from nanoindentation experiment is also plotted on this figure. The H, T same and H hK notations on the x axis stand for the name of parameter set, i.e. Hetero+normal, Taylor+same and Hetero+highK, respectively.

The maximum and minimum simulated contact areas are 73.0μm^2 and 66.6μm^2 correspond to parameter set Taylor+highK and Hetero+normal, respectively. All values from the various simulations are just within the error interval of experimental measurement, which ranges from 66.9μm^2 to 74.0μm^2. Hence, the range of contact areas induced by the different set of plastic parameters is smaller than experimental incertitude on contact area measurement.

However, plastic parameters play a significant role in the contact area. It is detectable in table III-4-2.

Criterion / Parameter set	18.8	17	9.4
Hetero+normal	63.528 (μm²)	66.618 (μm²)	73.471 (μm²)
Hetero+same	67.868 (μm²)	71.384 (μm²)	79.926 (μm²)
Hetero+high K	69.818 (μm²)	72.043 (μm²)	84.567 (μm²)
Taylor+normal	63.721 (μm²)	68.994 (μm²)	73.787 (μm²)
Taylor+same	69.818 (μm²)	72.263 (μm²)	86.916 (μm²)
Taylor+high K	69.791 (μm²)	72.949 (μm²)	88.646 (μm²)
EXP	66.910 (μm²)	67.669 (μm²)	73.941 (μm²)

Table III-4-2. Contact area values with their corresponding parameters sets

Even if the contact area induced by the Hetero+normal parameters seems to be not really different from the contact area from the Taylor+normal parameters set, there is a difference between values which is 3%. Furthermore, the contact area is affected by the dislocation storage term which is determined when to the matrix for dislocation evolution (a^{sp}) and K_g are chosen Low storage value of (a^{sp}) or high K_g value increases contact radius. The contact radii determined with parameters sets named same, or highK are about 9% higher value than the

contact radius determined with the parameters set named normal.

For isotropic materials, it is well known that smaller hardening stiffness and smaller yield stress induce bigger contact areas, and vice versa [CV01]. The main reason is that smaller hardening stiffness and yield stress promote surface piled up, which increases contact radius. This explains the results from the figure III-4-12.
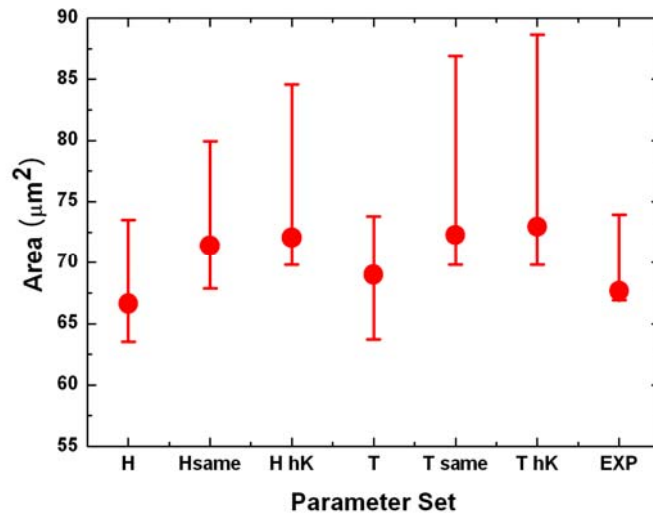

Figure III-4-12. Simulated residual contact area in the case of the indentation of a sample with (111) surface orientation for six plastic parameter sets

parameters	Taylor normal	Taylor same	Taylor highK	Hetero normal	Hetero same	Hetero highK	Exp
Hardening	low	low	low	High	High	High	
Storage	large	small	small	large	small	small	
Force (mN)	66	58	48	66	60,7	59,1	55
Area (μm^2)	69	72	73	67	71	72	68
figures	(a)	(b)	(c)	(d)	(e)	(f)	
morphology	3 fold 2 pile ups	3 fold	3 fold	3 fold 2 pile ups	3 fold	3 fold	3 fold 2 pile ups
maximum pile up height (nm)	110	200	200	110	200	200	200

Table III-4-3. Synthetic comparison of experimental and simulated results

The use of parameter set named Hetero implies higher yield stress than the parameter set named Taylor. Regarding the effect of storage term, the parameter set named highK or same gives smaller hardening stiffness than the parameter set named normal. The associated contact areas on figure III-4-12 respect the ranking induced by hardening stiffness. In conclusion, it is verified

that he relationship between contact radius and hardening stiffness for isotropic material [CV01] are still applicable to the anisotropic material, too.

Figure III-4-13 shows the various surface morphologies for each set of parameters. Maximal heights are tabulated in table III-4-3. Hence, it is assumed that the maximum pile up height depends on the dislocation storage term that is deduced from the a^{sp} and K_g values. The smaller storage term from (a^{sp}) or high K_g increases the maximum pile up height.
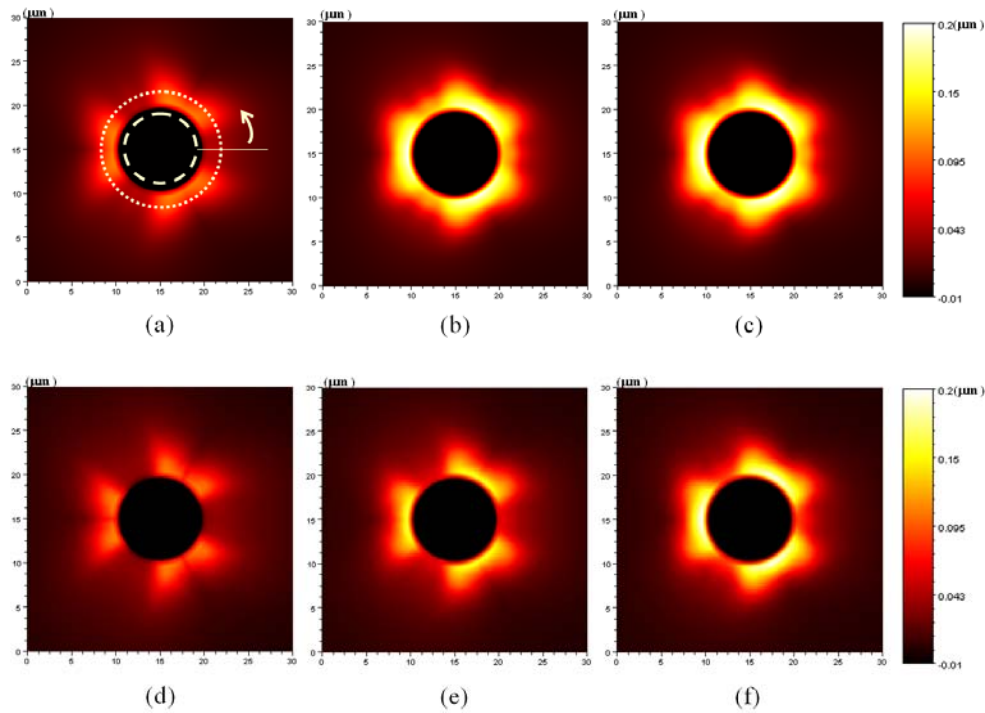
Figure III-4-13. Surface morphology of (111) surface orientation obtained from nanoindentation simulations in the case of six plastic parameters sets (a) Taylor normal (b) Taylor same (c) Taylor highK (d) Hetero normal (e) Hetero same (f) Hetero highK

There are two kinds of morphology after indentation. The first one is detected in the figure III-4-13 (a) and (d). It shows 3-fold symmetry which split into two pile-up peaks. Between two pile-up peaks, there is a radial channel especially noticeable in the figure III-4-13 (d), where the channel morphology is very similar in the case of experimental results as shown in figure III-2-6 (c).

The other morphologies are present in figure III-4-13 (b), (c), (e) and (f). They still reveal the 3-fold symmetry with 3 sets of two pile-up peaks but the two peaks are merged. They look then like one broad pile-up peak. The radial channel is very smooth compared to the figure III-4-13 (d). It is also observed 3 sink-in trenches. On the other hand, the heights in the sink-in regions in

figure III-4-13 (b) and (c) are a bit higher than the height in the figure III-4-13 (e) and (f), so the height differences between pile-up and sink-in region in the figure III-4-13 (b) and (c) are a bit smaller than the differences from the others.

The high value of storage term induces 6 sharp pile-up peaks, though the heights of the pile-up peaks are much smaller than the pile-up height from experiment results. The radial channel between two neighboring pile-up peaks is therefore clearly visible. On the other hand, the small value of storage term makes the two pile-up peaks merged and it smoothes the channel between two neighboring peaks. Especially, the radial channel almost disappears in the figure III-4-13 (c) due to the really small storage term in the case of Taylor highK. The Taylor hardening matrix reduces the differences of surface displacement of pile-up and sink-in regions. It may be due to the fact that homogeneous hardening matrix with small storage terms reduces heterogeneity of material.

Figure III-4-14 (a) to (f) shows the elevation along a circle which is indicated with a dashed line in figure III-4-13 (a).
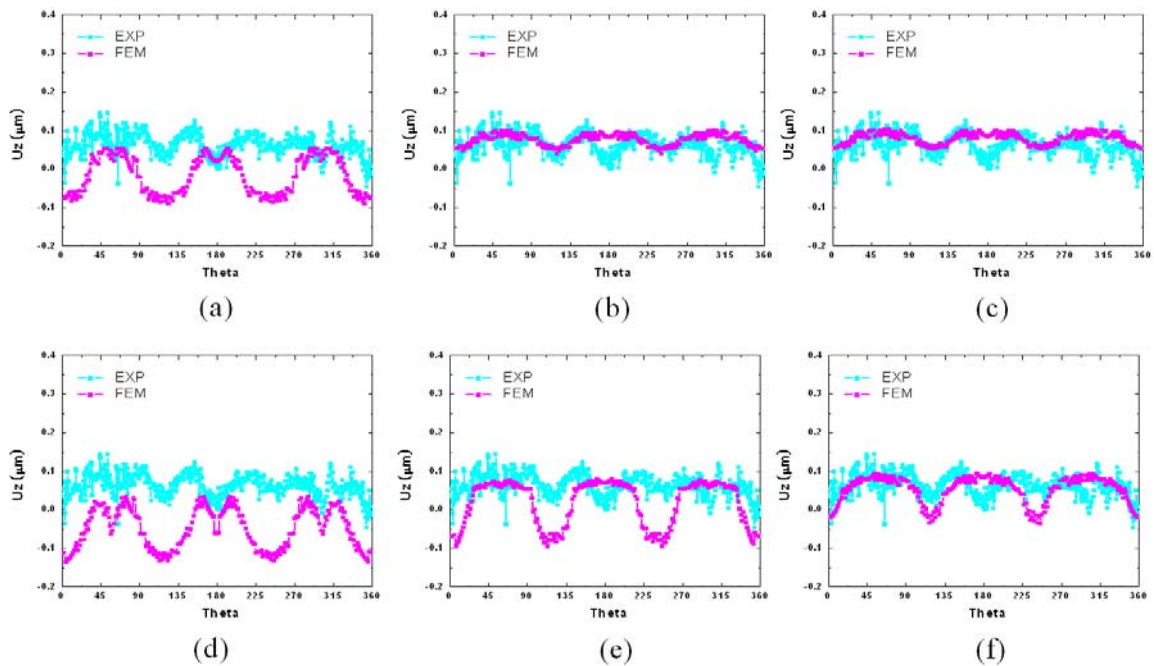

Figure III-4-14. Surface displacement along the contact line indicated as a dashed line in figure III-4-13 (a), from nanoindentation simulation with (a) Taylor normal, (b) Taylor same, (c) Taylor highK, (d) Hetero normal, (e) Hetero same, (f) Hetero highK

The displacements extracted from simulations results exhibit 3 main undulations with 3 regularly spaced maximum and minimum values whereas the experimental displacement has 6 undulations with 6 regularly spaced maximum and minimum.

There are three kinds of curve distributions. The first one is the distribution of figure III-4-14 (a) and (d), which corresponds to a parameters set which has a higher storage term than the others. The displacement level extracted from the simulations is about 0nm, which is about 100nm lower than the displacement level from experiment. The evolution of elevation presents 6 peaks especially at the figure III-4-14 (d).

The second distribution is presented in figure III-4-14 (b) and (c). It is obtained when small storage term and homogeneous hardening parameters named Taylor are used for the simulation. The peak height of the displacement distribution from simulations is about 100nm which is similar with the peak height of displacement distribution from experiment. The minimum height from the simulations is about 50nm, which is a bit higher than the minimum height from the experiment which is below the 0nm. It looks like that the amplitude between maximum and minimum height is reduced by the homogeneous hardening matrix named Taylor.

The third distribution is observed in figure III-4-14 (e) and (f), which corresponds to parameter sets with small storage parameters and heterogeneous hardening parameters. The maximum and minimum height from the simulation is 100nm and -100nm in the figure III-4-14 (e) and 100nm and 0nm in the figure III-4-14 (f), respectively, which is similar to the displacement distribution from the experiment. The difference between simulation and experiment is that there is only three peaks from the simulation while experimental results reveal 6 ones.

As a result, the height, amplitude and number of peaks are related to the plastic parameters. The high storage term gives similar distribution to the experiment, qualitatively and the small storage term with heterogeneous hardening parameter gives quantitatively similar distribution to the experiment.

Figure III-4-15 shows the elevation along a circle which is indicated in dotted line in figure III-4-13 (a). The experimental displacement evolution along the circle has 6 waves. One wave is bigger than the others. The difference between those maximum points is about 50nm. The maximum and minimum heights are about 200nm and 100nm, respectively.

The numerical curves have different typical shapes. The first shape is visible on figure III-4-15 (a) and (d) and corresponds to simulations which present higher storage term than the others. The maximum height from the simulations is about 100nm, which is about 100nm lower than the experimental displacement. The minimum height from the simulation is about 50nm, which is also lower than the experimental displacement. However, the displacement evolutions determined by the simulations are qualitatively similar to those measured experimentally result. These results extracted from simulations have 6 peaks and are similar to experimental results, especially in the figure III-4-15 (d).
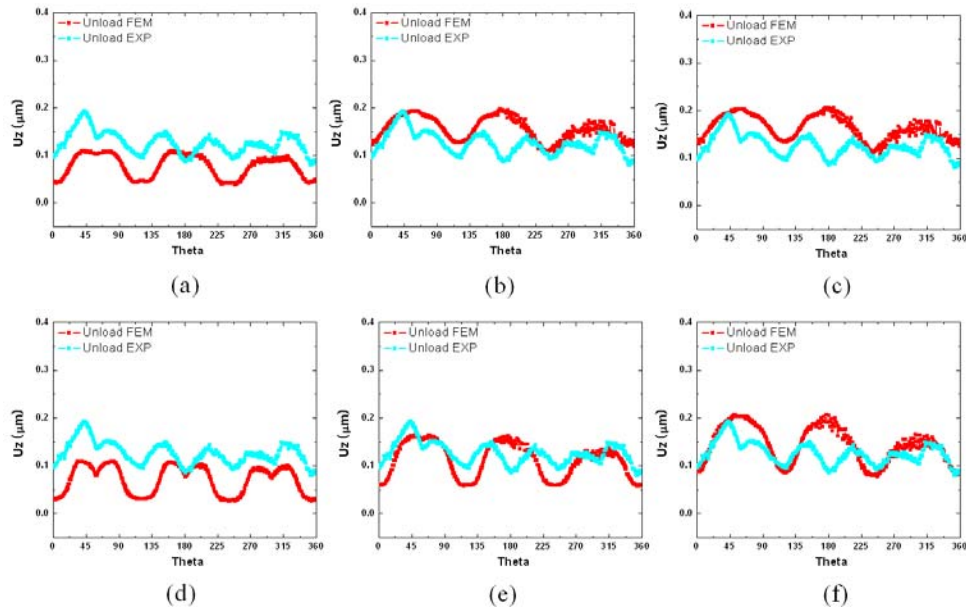
Figure III-4-15. Surface displacement along the line defined by pile up, which is indicated with dotted line in figure III-4-13 (a), from nanoindentation simulation with (a) Taylor normal, (b) Taylor same, (c) Taylor highK, (d) Hetero normal, (e) Hetero same, (f) Hetero highK.

The other distribution in figure III-4-15 (b), (c), (e) and (f) is obtained with a small storage parameters set. The maximum and minimum heights of the displacement distribution from simulations are about 200nm and 100nm respectively, which are similar with the peak height of displacement distribution from experiment, and the height of third peak is about 30nm lower than the other two peaks. Although the height distributions of simulated curves have only three broad peaks, they are quantitatively similar to the experimental height distribution. Especially, the height distributions from figure III-4-15 (f) are quite similar to the height distribution from the experiment.

In conclusion, the best hardening parameters which allow a good reproduction of experimental results are parameters set named Hetero same, and Hetero highK. All of the results as shown in figure III-4-11 ~ 15 from these parameters sets give quite reasonable quantitative results compared to the results from the experiment.

4.3 Best fitted results from simulation

Finally, the initial dislocation density and plastic parameters that allow the best reproduction of the experimental results are selected. In the next section the results of quantitative comparison between nanoindentation tests from experiments and simulations with the best fitting parameters

are presented.

Figures III-4-16 to III-4-20 show the quantitative comparison between the experimental and simulated results of nanoindentation. The surface orientations of tested samples are (111), (001), (110), (123) and (111) with low initial dislocation density. Appropriate initial dislocation densities are adopted for all orientations. The initial dislocation densities for nanoindentation simulations are $1.56\times10^{14}/m^2$, $1.2\times 10^{14}/m^2$, $1.2\times10^{14}/m^2$ and $3.0\times10^{13}/m^2$ for the samples with (110), (111), (001) and (123) surface orientations respectively. The initial dislocation density for (111) with low initial dislocation density is $6.0\times10^{12}/m^2$. The parameters set named Hetero same is used for all the simulations.

The comparison is relative to surface morphology, surface displacement through the contact boundary and surface displacement through the pile-up boundary. The left and right figures in figure III-4-16~20 (a) present surface morphology extracted from simulation and measured experimentally. All the results from simulation as shown in figure III-4-16~20 (a), (b) and (c) show that the simulation reproduces the experimental results if the appropriate initial dislocation density and parameters for plasticity are used. Both the results from experiment and simulation show the symmetry of each surface orientation, which are 3-fold, 4-fold, 2-fold, irregular 2-fold and 6-fold for (111), (001), (110), (123) and (111) orientation surface respectively. Simulation reproduces the results of applied load with indentation depths, stiffness with indentation depth, indentation modulus and contact area from experiments as it can be seen in figure III-4-4, 7, 8 and 9.
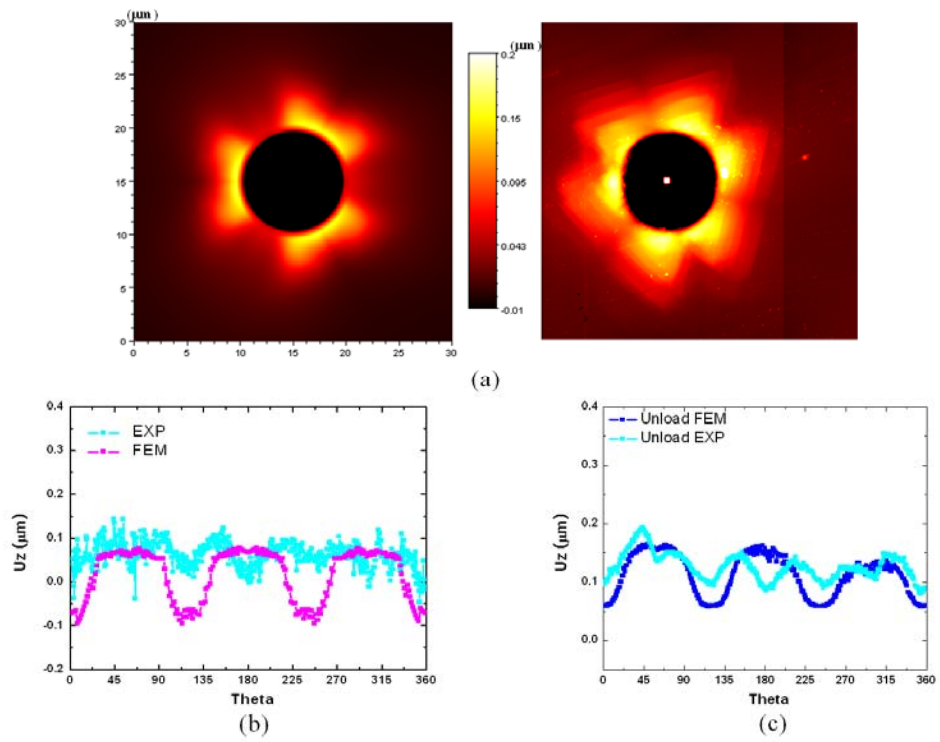
Figure III-4-16. Quantitative comparison between experiment and simulation of (111) nanoindentation.
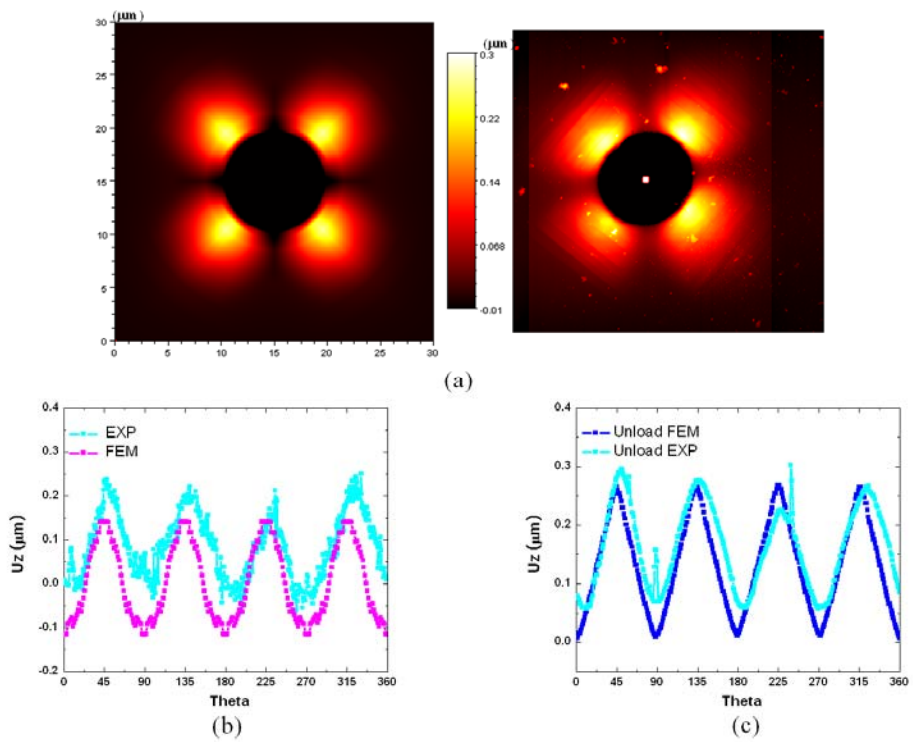

Figure III-4-17. Quantitative comparison for (001) nanoindentation.
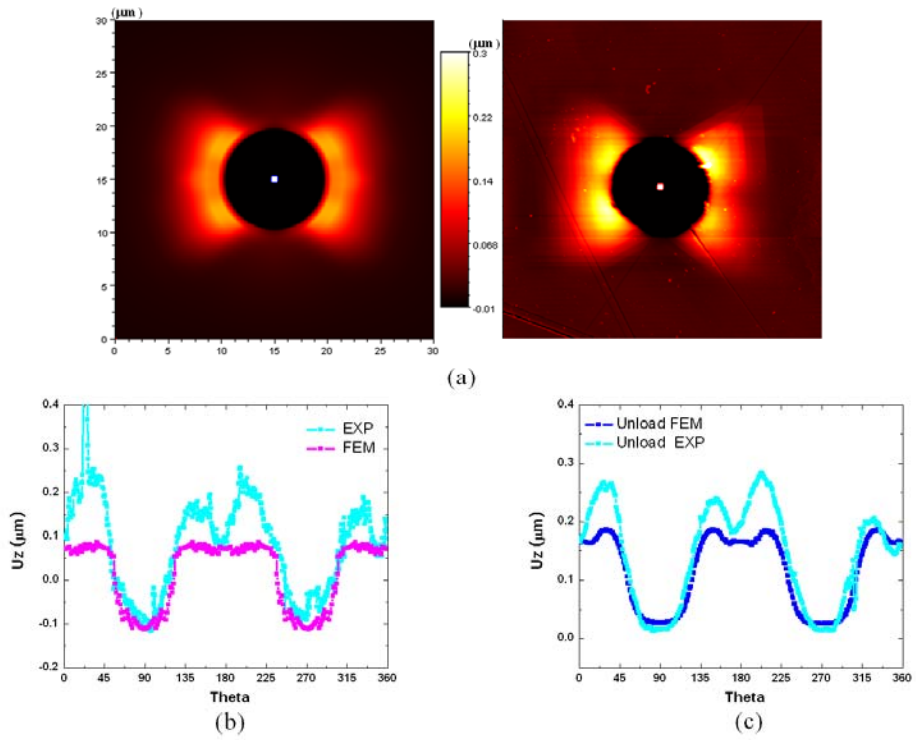
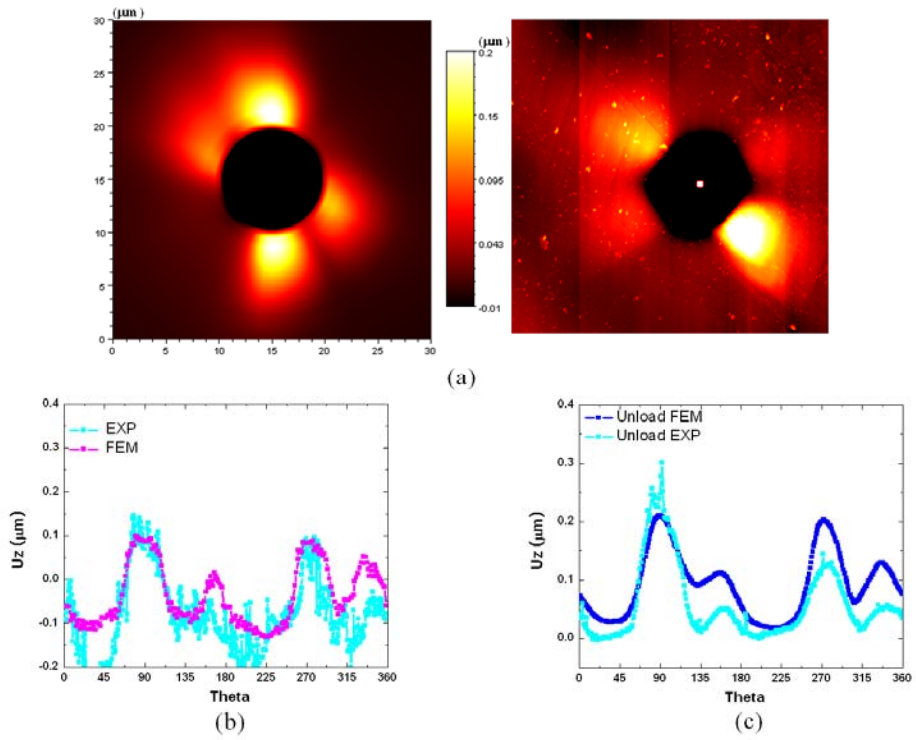Figure III-4-18. Quantitative comparison for (110) nanoindentation.

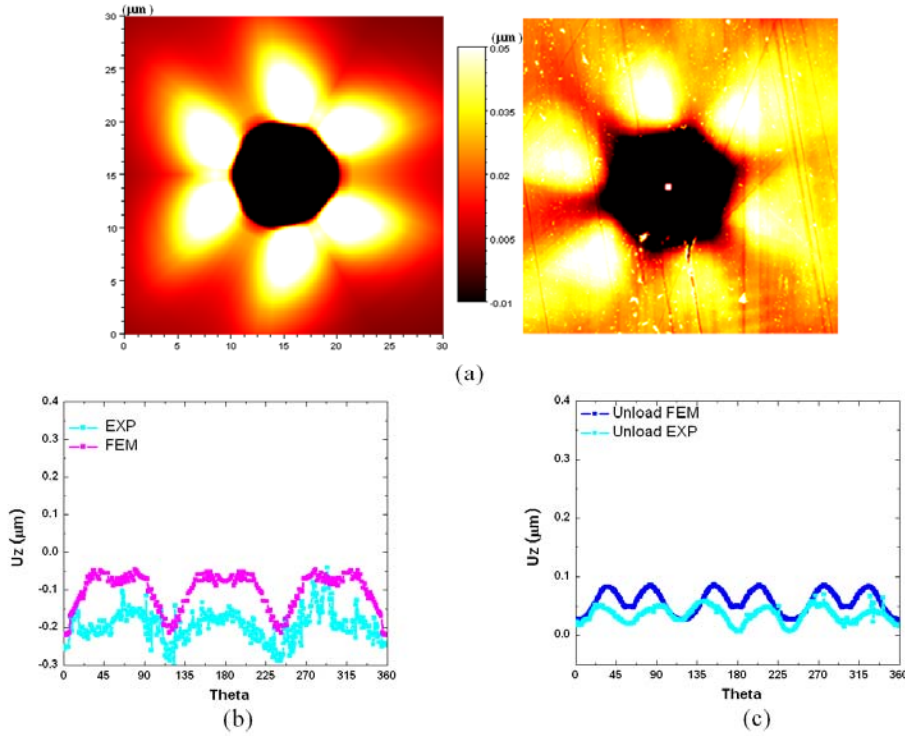Figure III-4-19. Quantitative comparison for (123) nanoindentation.

Figure III-4-20. Quantitative comparison for (111) nanoindentation with low initial dislocation density.

4.4 Prospective

The numerical analysis of local rotation beneath the imprint has become one of interesting issue, because it could be a key information to verify recent theories related to Nye tensor [Nye53] such as Cosserat theory which counts extra hardening from the local rotation. The crystal plasticity model used in this thesis can calculate the local rotation during and after nanoindentation, and it can be compared to the experimental observation by using electro back-scattered diffraction (EBSD) technique. The comparison will give many interesting results.

The crystal plasticity model used in this thesis is only concerning the isotropic hardening which is not good for cyclic loading conditions [BTF01 and Mec99]. To improve the model for complex loading condition, it should be modified by implanting kinematic hardening model. Déprés have proposed physics based kinematic hardening model [Dép04]. His model can be merged with the crystal plasticity model used in this thesis. This modification will expand application boundary of the model especially for cyclic loading conditions.

The other possibility to improve the model used in this thesis is to modify evolution rule. Recently, Kubin *et al.* have proposed new evolution rule, which counts the heterogeneous behavior with various loading orientation of anisotropic material [KDH08]. His evolution rule

can also be merged with the model easily. This modification will improve the accuracy to retrieve anisotropic deformation behavior and imprints after nanoindentation.

4.5 What should be retained from this section

- FEM simulation can reproduce experimental results from various surface orientations successfully
  - Load displacement curves
  - Stiffness and indentation modulus
  - Contact area
  - Surface morphology

- Surface morphology depends on
  - Initial dislocation density
  - Hardening parameters

5. Size effect of nanoindentation reproduced by FEM simulation

Indentation size effect (ISE) appears when sample size is decreased. At the beginning, there have been some discussions between researchers about the fact that unexpected environmental effect may explain the indentation size effect [TS81, PT79, Sam86, LGH93 and MC95]. All of these suggestions have contributed to clarify the indentation size effect. It has become clear that the inherent size dependence in nanoindentation is not an artifact caused by these unexpected environmental effects [SWB93, FMA94, MC95, PAF96, SE98, NG98, Gur02, ES02, KPM06, RMP07 and RMP08].

Theoretically, some models such as strain gradient model and geometrically necessary dislocation based models can explain the indentation size effect [GHN99, AB00, HGN00, FH01, ES03 and Mug04]. Recent theories to explain the indentation size effect introduce extra degrees of freedom or extra constitutive equations. Though simulations using the theories would be able to reproduce size effect from simple loading state of material, the required computer time due to the actualization of the numerous variables introduced by the model makes it practically impossible. Moreover, most of size effect theories have no rules about contact conditions. Hence, it is difficult to simulate the indentation size effect by using these theories and there has not been simulation of the indentation size using these models yet. Therefore, the searches for models that allow the reproduction of the indentation size effect is still an important challenge.

On the other hand, because the size effect theory we proposed in section II-2 has no extra degree of freedom or constitutive equations, it can also use the classical contact theories used in finite element method. Therefore, our size effect theory can be used to simulation with complex loading conditions including contact boundary condition. We have done the nanoindentation simulation using the size effect theory we proposed, where the theory is implanted to the user material subroutine in ABAQUS FEM package [ABA04].

In this section we apply the size effect theory proposed in section II-2 to the case of nanoindentation. Simulations are performed using ABAQUS with the dedicated VUMAT routine.

5.1 Environmental explanation for size effect

Various articles have reported the size effect at the nanoindentation experiment [TS81, PT79, Sam86, LGH93 and MC95]. Although the indentation size effect seems a natural state of the material because the indentation size effect is observed even within controlled environment, it is reported that one of the reasons for indentation size effects may be due to some artifacts such as indenter surface quality or material surface roughness [SWB93, FMA94, MC95, PAF96, SE98,

NG98, Gur02, ES02, KPM06, RMP07 and RMP08].

The report about size effect due to some artifacts insists on the fact that the effect origin between inherent material characteristic and experimental conditions should be clarified. Therefore, before simulation considering the size effect as intrinsic to the material, it is worth simulating size effect including specific experimental condition. Here, the simulations are done using classical crystal plasticity theory which cannot reproduce any size effect.

In general, the surface of sample material is polished mechanically for flattening the surface before nanoindentation experiment. After this treatment, the surface is polished again electrically or chemically to get rid of the hardened layer due to the mechanical polishing, to avoid any effect of the hardened layer on nanoindentation experiment.

In order to get rid totally of the hardened layer effect, the chemical polishing requires a sufficient time. Despite, there is no reference about the chemical polishing time because there is no idea about the depth of hardened layer. Therefore, it is worth understanding the effect the hardened layer by comparing the results between simulation of nanoindentation on sample with and without the hardened layer.

To understand the effect of the hardened layer, nanoindentation simulation with hardened layer is designed as shown in figure III-5-1. Thickness of the layer is set to 300nm and the layer has one of the two initial dislocation densities which are 300 and 1500 times higher than the initial density of the bulk material. The indentation surface orientation and initial density of the bulk material are set to (111) direction and 1.2×10^{12} /m^2, respectively. Other parameters for this simulation and indentation conditions are identical to those of the previous simulations of section III-3. After the simulation, hardness values corresponding to the bulk sample without hardened layer and the sample with a layer involving the 2 initial densities of dislocation are calculated and compared.
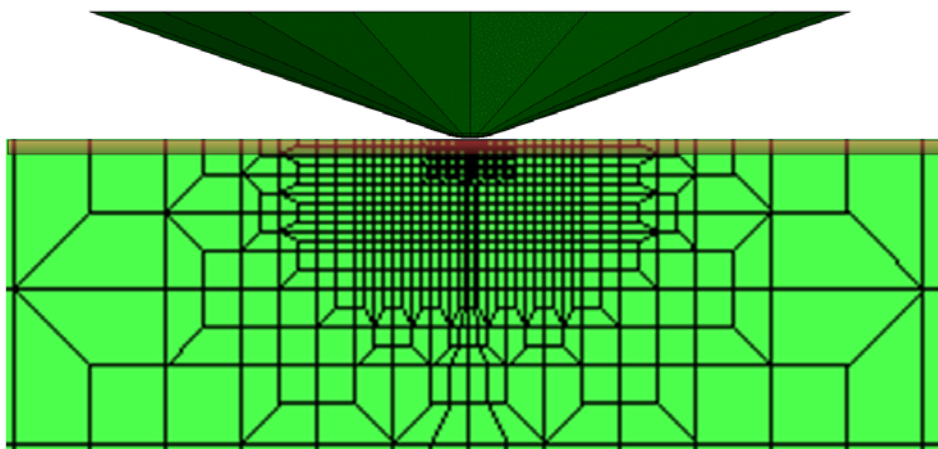

Figure III-5-1.   Mesh used for nanoindentation simulation including a hardened layer

Figure III-5-2 shows the hardness versus indentation depth curves extracted from nanoindentation simulations where an ideal material and sample with two different hardened layers are considered.
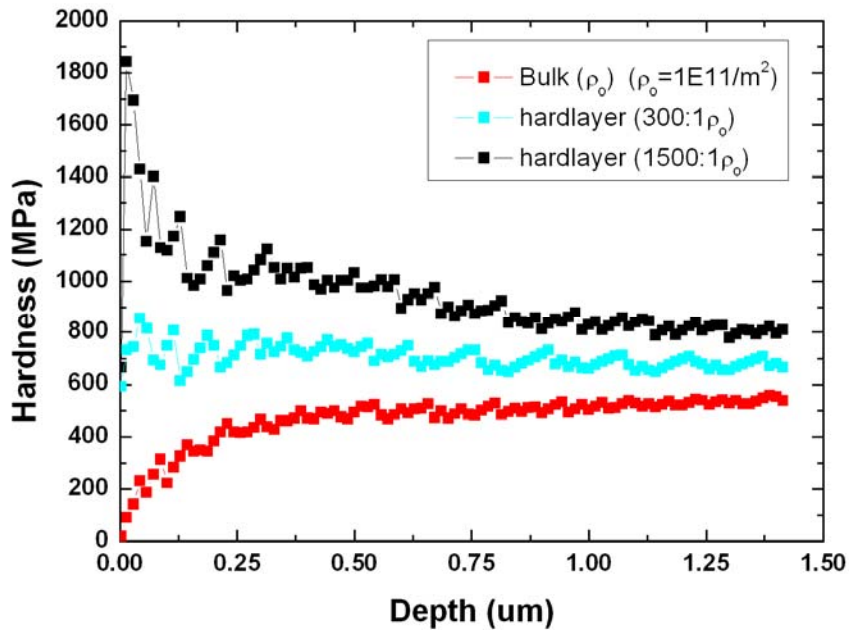

Figure III-5-2.Hardness versus indentation depth curves extracted from nanoindentation simulations of ideal bulk material and sample with two different hardened layers

If there is no hardened layer as shown by red symbol in figure III-5-2, hardness is increasing with increasing depth at the beginning of the indentation. It is because of the sphere type tip front. The hardness value from the nanoindentation with the sphere shape indenter tip is naturally increasing with indentation depth. When the indentation depth is greater than 200nm which is the depth corresponding to the transition between sphere to cone shape of the tip, the hardness values stabilizes around 500MPa even with increasing indentation depth. The cone type indenter increases both force and contact area with a dependence to the square of indentation depth. Therefore, the hardness value is constant when increasing indentation depth.

On the other hand, hardened layer changes the tendency of hardness curve with indentation depth from the beginning. Because the hardness is affected by only the hardened layer at the beginning of indentation and the hardness is increasing with the initial dislocation density of the material, the initial hardness from the simulation with hardened layer, where the layer has much higher initial dislocation densities than the initial dislocation density of the bulk material, should be greater than the hardness from the simulation with pure bulk material, as shown by the cyan and black symbol. The simulations with hardened layer, which have 300 and 1500 times higher

initial dislocation density, give about 800MPa and 2GPa at the beginning, respectively. The huge high hardness values are decreasing with indentation depth, because it starts to be affected by the smaller initial dislocation density of the bulk material below the hardened layer. Especially, the hardened layer, which has 1500 times higher initial dislocation density than the initial dislocation density of bulk material, make the hardness decrease dramatically with indentation depth down to 1.0GPa. The tendency of hardness curves with indentation depths of the black symbols looks like general tendency of the indentation size effect.

As a result, we can reproduce the indentation size effect from the hardness value with indentation depth by just using the hardened layer. This means that though mechanical polishing is good way to flatten the surface of a material, it could induce indentation size effect. Hence, the hardened layer due to the mechanical polishing should be cancelled clearly in order to get rid of that kind of size effect due to the surface preparation.

5.2 Results from FEM simulation using the simplified strain gradient model

The mesh and indenter shape used for the finite element modeling is shown in figure III-4-1 (a) and (b). Orientation of the indented surface is set to (001). The maximum indentation depth is set to 1500nm. In order to get rid of the effect of the indenter tip morphology, a perfect conical indenter tip was used. The other simulation conditions and parameters are the same as the conditions and parameters described in section III-3. The only difference comes from the additional stress theory introduced to account for the size effect. In this formalism, the internal length L_g needs to be defined. Here we propose that this length represents the size of the plastic volume, i.e. L_g is calculated as the triple root of the total plastic deformation volume. L_g is continuously updated with the time steps.

Figure III-5-3 shows the surface displacement morphology of the (001) indented surface obtained at indentation depth of 1500nm during loading state. The surface morphology shows a four-fold symmetry involving four pile-up peaks and four sink-in zones located between the peaks. This surface morphology is quite similar to the experimental results as shown in figure III-2-6 (a). It is found that the extra stresses introduced to account for size effects does not change the tendency of the surface morphology generally obtained in the case of (001) surface orientation.
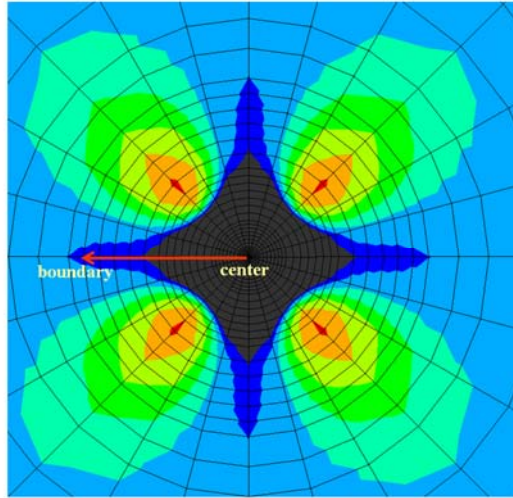
Figure III-5-3. The surface displacement morphology of (001) surface orientation from nanoindentation simulation with size effect theory

Figure III-5-4 gives the square root of the applied loading force versus the indentation depth. It is found that the relationship is not perfectly linear as expected for self similar indenter with a constant value of the hardness.
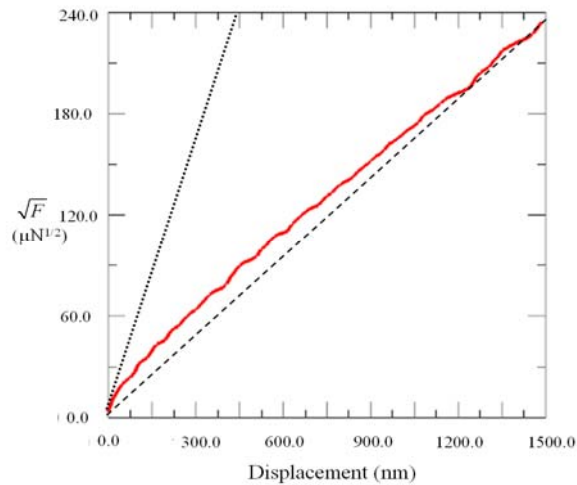

Figure III-5-4. Square root of the applied load plotted versus the indentation depth.

The value indeed increases with the indentation depth but the slope is not a constant. First, the slope is very stiff which as depicted by the dashed line. Then, the slope is decreasing with increasing indentation depth up to about 1200nm. Finally, for depths above 1200nm, the slope is almost constant. This is obviously a direct evidence of indent size effect simulated by FEM.

Figure III-5-5 plots the evolution of the hardness versus the indentation depth. Despite the fluctuations observed for low values of the depth, it is found that the hardness clearly decreases with indentation depth.
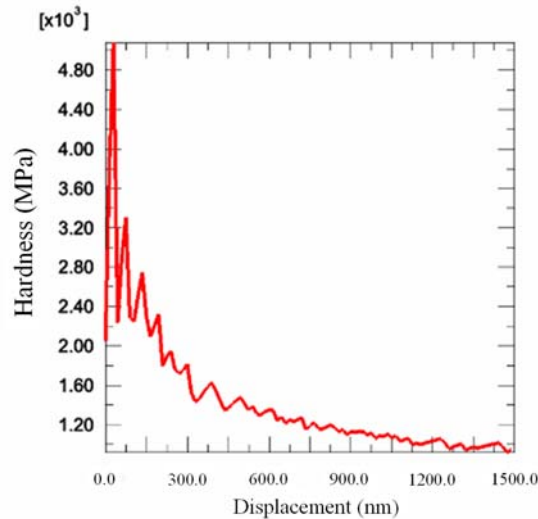

Figure III-5-5. Hardness versus indentation depth calculated from the strain gradient model

Hardness at a depth of 50nm is about 3GPa and decreases down to 1 GPa for 1200nm depth. Above this depth, the hardness of 1.0GPa is almost constant.

The fluctuations in the curve are due to the mesh size. Indeed, the hardness is computed as the ratio of the load and the size of the contact surface which is computed by the total area of the elements in contacts between the indenter and the tip. Although the applied force is continuously increasing with the indentation depth, the contact area is digitized by the number of elements in contact. Thus, the fluctuation amplitude can be reduced by decreasing the mesh size, but it can never disappear.

Figure III-5-6 gives the evolution of the hardness with the square root of inversed indentation depth. Nix and Gao have proposed that indentation size effects lead to a linear relationship with a slope which quantify the intensity of the indentation size effect [NG98]. The FEM results indeed show a line as plotted in figure III-5-6.
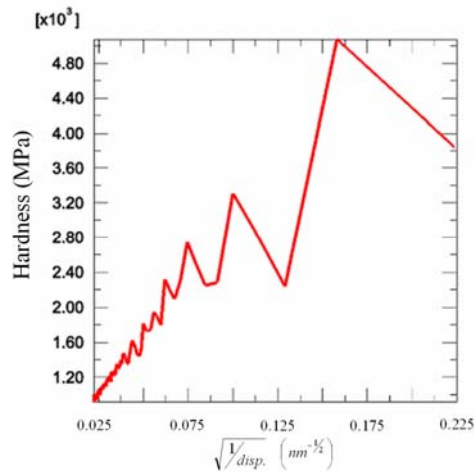
Figure III-5-6. Hardness value plotted versus the square root of inversed indentation depth.

The three figures above demonstrate that the model reproduce the indentation size effect like in real experiments at least qualitatively. This comes from the extra stresses introduced in the model and which is related to the inverse of the internal length (taken here as the size of the plastic zone) as shown in figure III-5-7. Since the size of the plastic zone is increasing with the indentation depth, this extra stress is large at the beginning of indentation, and continuously decreases with increasing indentation depth as shown in figure III-5-8.
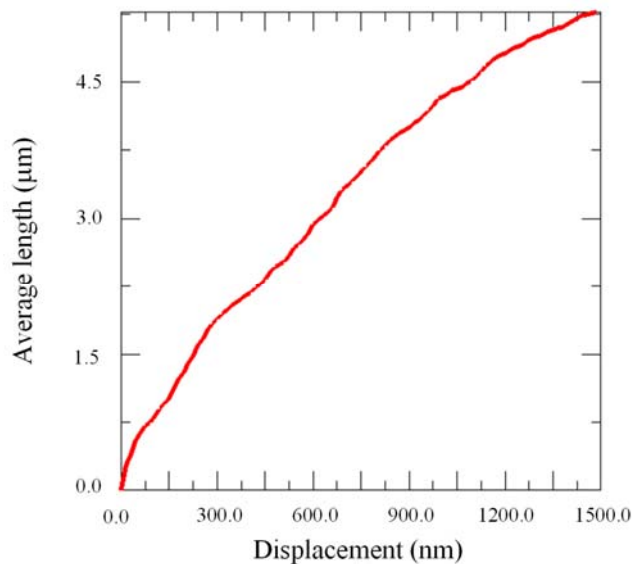

Figure III-5-7.   Characteristic global length scale with the indentation depth from nanoindentation simulation with size effect theory

In this figure the 9 curves correspond to 9 points located on the line indicated in figure III-5-3. The red line depicts the extra stress at the center point, and the cyan line depicts the extra stress

at the last point, the farthest from the indentation axis. For a given point, one can see that the extra hardening starts after a given amount of depth. This critical depth corresponds to the instant when the plastic zone reaches the probing point. Then, the generated extra stress increases up to a maximum value which level decreases when the distance to the indentation axis increases. After the extra stress reaches the maximum peak, it continuously decreases with increasing indentation depth with a decreasing rate lower than that of the central point.
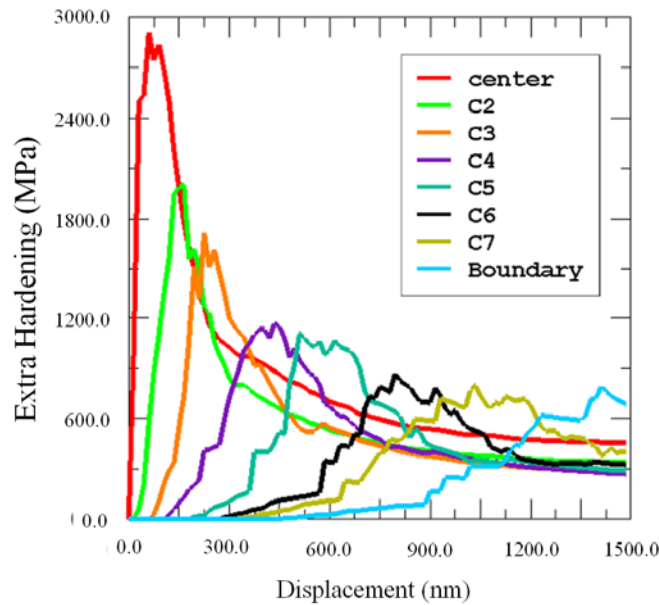

Figure III-5-8. Extra stress effect with indentation depth at 9 different points located on the line from the center to boundary as shown in figure III-6-3

According to equation (II-2-44), there are three parameters that may affect the extra stress: the difference between the local strain and the global strain, the total dislocation density and the global length scale. We have already explained the effect of the internal length. The total dislocation density is increasing with indentation depth. A larger value for the total dislocation density will decrease the extra stress. The difference between the local strain and averaged strain is also reduced with the increasing indentation depth. These two behaviors may explain why the extra stress decreases with the indentation depth after it has reached the maximum extra stress.

5.3 What should be retained from this section

- Simulation of hardened layer without size effect theory
  - Decreasing hardness with increasing indentation depth

- Nanoindentation with simplified size effect theory
  - Reproduce indentation size effect successfully
  - Due to increasing length scale with indentation depth

6. Dislocation Dynamics simulations of nanoindentation

Nanoindentation is an ideal case for applications of the DD method at least for indentation depth of the order of 100nm. Indeed, for these range of depth, the plastic volume is smaller than a micron and thus, the number of dislocation lines to handle is limited. Consequently, the computing time required to perform a typical nanoindentation test is still reasonable (about one week).

On the other hand, DD simulations as detailed in II-3 do not possess all the ingredients needed to reproduce nanoindentation experiments. Indeed, DD can perfectly simulate the behavior of ensemble of existing dislocations including their multiplication through Frank-Read mechanism but they cannot predict the apparition of new dislocations. And in the case of low penetration indentations, there is evidence of dislocation nucleation. This phenomenon being relevant from the atomic scale, this could be incorporated in DD simulations using Molecular Dynamics simulations.

The second ingredient needed to perform DD simulations of nanoindentation is a method to impose the indentation loading that is to say the image force on the free surface and the contact between the indenter and the surface. This will be done here by coupling the DD code with the finite element code CAST3M [CAS07]. Such a coupling was already realized in the past [FVC97 and Fiv97]. In this thesis we propose a new algorithm aiming at imposing a realistic loading.

Theoretically it would be necessary to use the anisotropic expressions of the dislocation stress field as introduced in section II-3.2. However, this would dramatically increase the computation time so that in the following we will only use the isotropic expressions.

6.1 Nucleation criterion computed from Molecular Dynamics simulations

<u>Conditions of the Molecular Dynamics</u>

MD simulations are performed using the embedded atom method (EAM) with the inter-atomic potential dedicated to Nickel developed by Voter. The figure III-6-1 (a) depicts the schematic diagrams of simulated volume and conditions. The simulated volume is typically a parallelepiped box of 224 x 284 x 285 A^3 (1675080 atoms). The indenter is represented by a spherical repulsive potential of radius R = 120 Å.

The position of the center of the sphere is imposed step by step (displacement control). The normal to the indented surface is chosen as (111). Periodic boundary conditions are applied on the (-101) and (1-21) side of the box. The atoms lying on the bottom surface are forbidden to

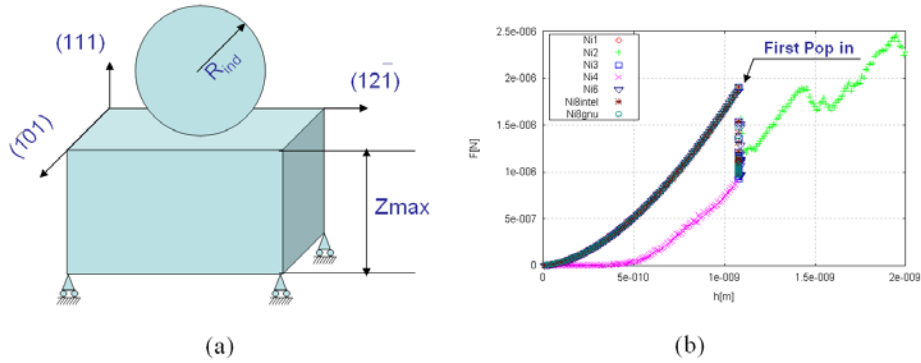move alone the (111) direction but the other in plane directions are allowed (See figure III-6-1 (a)).

Figure III-6-1. (a) Schematic representation of simulated volume and conditions for nanoindentation simulation using MD. (b) Applied load displacement curve calculated by MD

Results of the Molecular Dynamics simulations

A simulation campaign has been performed using both molecular static and MD simulations which confirmed that the indentation induced dislocations do not depend upon the loading rate. As shown in the loading curves given in figure III-6-1 (b), after an initial elastic stage, discontinuity is observed in the force displacement curve which is the signature of dislocation pop-in. The process for the formation of the dislocations beneath the indenter is rather complex as illustrated by the snapshots printed in figure III-6-2. In this figure, only the atoms for which the number of neighbors does not correspond to that of a perfect FCC crystal are plotted. This way, dislocation leading and tail partials appears in red (dark) and atoms in the stacking fault in yellow (clear).

After an elastic deformation of the volume (figure III-6-2 (a)), defects appear beneath the indenter (figure III-6-2 (b)). These defects consist of three extrinsic defects lying in the three (111) planes activated by the indentation. Each defect is made of an assembly of three adjacent stacking fault planes. This structure is unstable and rapidly transforms into intrinsic defects (figure III-6-2 (c)) then into three half loops of dislocations touching the free surface (figure III-6-2 (d)). Each loop is lying in the two slip system sharing a common Burgers vector. These loops expend in the volume and cross-slip events finally emit a closed prismatic loop which can easily glide on the cylinder based on the Burgers vector (figure III-6-2 (e-f)).
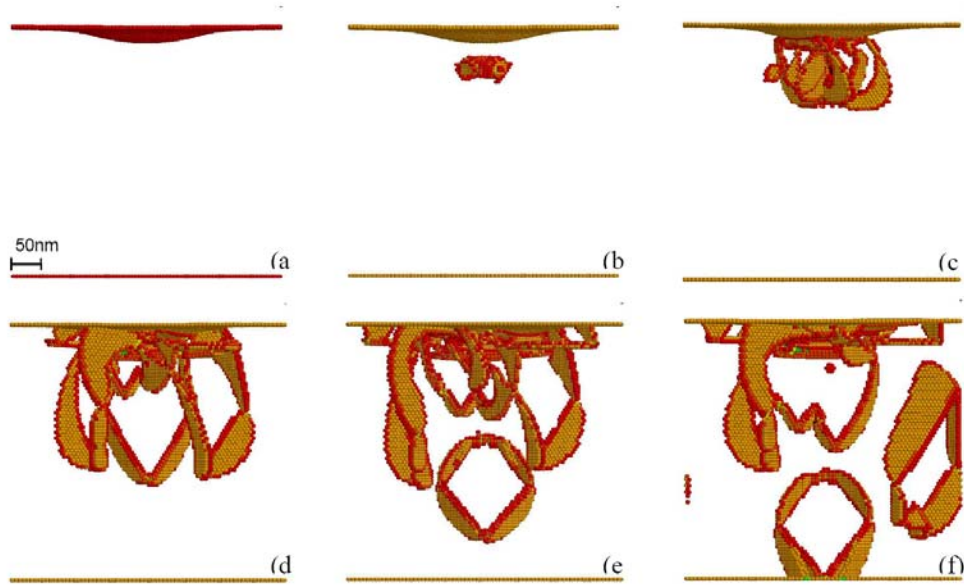
Figure III-6-2. The process for the formation and movement of the dislocations beneath the indenter

In figure III-6-2 (f), two loops are completely formed and a the expansion of a third one on the left is prohibited by the periodic boundary conditions which reintroduce the prismatic loop escaping from the right side of the box. When changing the size of the simulation box, we observe that three identical prismatic loops are simultaneously nucleated when indentation along the (111) direction. Moreover, when the indenter is further pushed in the crystal, more and more prismatic loops are introduced with a size directly related to the contact area between the indenter and the surface.

This nucleation mechanism will be used in the DD simulation presented below. For DD, the details of the formation of the prismatic loops are not accounted for and only the final shape and position of the prismatic loops are conserved as given in figure III-6-3.
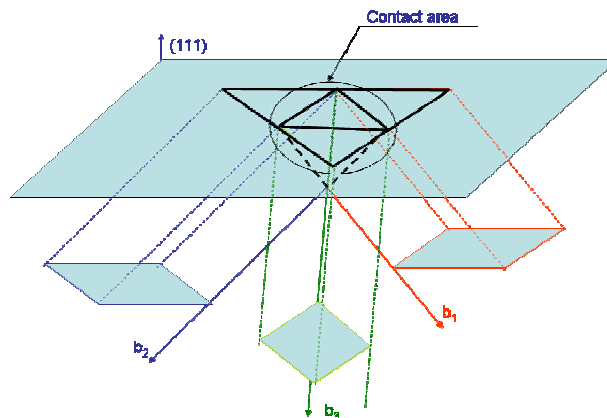

Figure III-6-3. Schematic representation of the prismatic loops to introduce in DD.

This means that at this upper scale, pure perfect prismatic loops will be introduced in the DD simulation box each time the load sufficient to make them progress in the volume.

6.2 DD algorithm used for nanoindentation simulations

Coupling DD and FEM

Figure III-6-4 depicts the superposition method used for the coupling between FEM and dislocation dynamics in the case of nanoindentation. Superposition can be applied since both FEM and DD make use of linear elasticity.
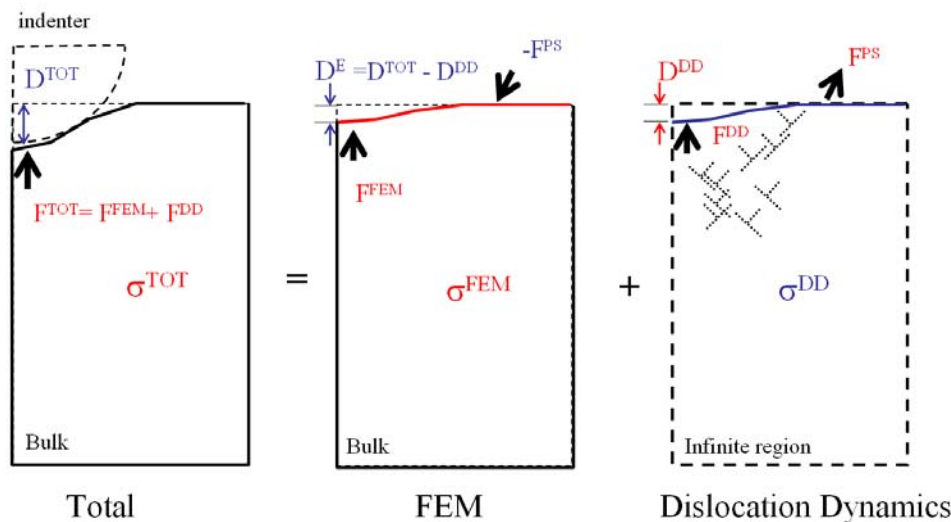

Figure III-6-4. Superposition method used to couple FEM and DD for nanoindentation

The objective is to compute the stress field to apply on the dislocation segments corresponding to a given imposed displacement $\mathbf{D^{TOT}}$ of the indenter. This stress field is obtained by the summation of the elastic field $\sigma^{\mathbf{FEM}}$ computed by FEM and the internal stress $\sigma^{\mathbf{DD}}$ induced by all the dislocations present in the simulation box. The latter being valid only for infinite medium, it induces forces $\mathbf{F^{PS}}$ on the surface and displacements $\mathbf{D^P}$ in the contact region. FEM calculations are then used to enforce the actual boundary condition on the surface: A displacement $\mathbf{D^{TOT}}$-$\mathbf{D^{DD}}$ is applied in the contact region and a force $-\mathbf{F^{PS}}$ is imposed on the remaining free surface. FEM then solve this elastic boundary problem and give the stress field $\sigma^{\mathbf{FEM}}$.

In the following; the code CAST3M [CAS07] is used as the FEM solver and TRIDIS [TRI09] is for dislocation dynamics. CAST3M is a pseudo commercial and open source based program. For the coupling, different communications between the CAST3M and TRIDIS are required. This is done by including TRIDIS inside CASTEM as a subprogram [Fiv97]. The coupled code

is now referred as KTRIDIS.

Nanoindentation algorithm

Figure III-6-5 depicts the general flow chart used in KTRIDIS program to realize the nanoindentation simulations. In practice this algorithm is written in GIBI, the meta-language used in CAST3M.

At the beginning, the mesh is designed using the CAST3M operators. Then boundary conditions are imposed to bottom nodes of the mesh as done in the FEM crystal plasticity case: all degrees of freedom are canceled. This boundary condition is not changed during the entire simulation.
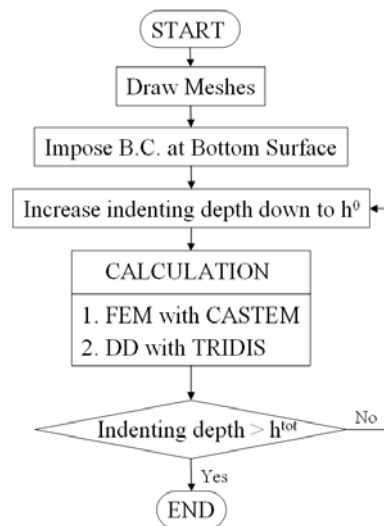

Figure III-6-5. Flow chart of KTRIDIS used for nanoindentation simulations.

Then, the indenter position is moved down to the desired indentation depth and the block *CALCULATION* starts to calculate the indentation force using both FEM and DD solvers. During this step, the elastic stress field inside the bulk material is calculated by the FEM solver and the results of the previous DD calculation. The surface displacement and surface forces due to the dislocation are recursively updated by the TRIDIS routine up to an equilibrium position. Details of this procedure are given below. This means that the loading is quasi-static. Finally, all the results are stored and next calculation with updated indentation depth is started. The routine is repeated until the final indentation depth is reached. The unloading state can also be calculated if we impose the indenter position to move upward.

Figure III-6-6 depicts the flow chart of the calculation part in figure III-6-5. The calculation begins by obtaining the values of surface displacement ($\mathbf{d}^{DD}$) and force ($\mathbf{F}^{s,DD}$) from the

dislocation positions and the surface displacement ($\mathbf{d^{FEM}}$) from the FEM elastic field computed at the previous step. The values are then used for detecting both the contact area and the displacements to impose as boundary conditions of this step. Surface forces from the dislocations are imposed at the surface of the bulk material as image forces. Then, the elastic stress field due to the imposed boundary condition is calculated and recorded, for the following TRIDIS calculation. After this FEM calculation is done, we can estimate if the contact points are over constraint or not. This notion of constraint is detailed below. If some over constraint points are found, they are removed and the FEM calculation is repeated.
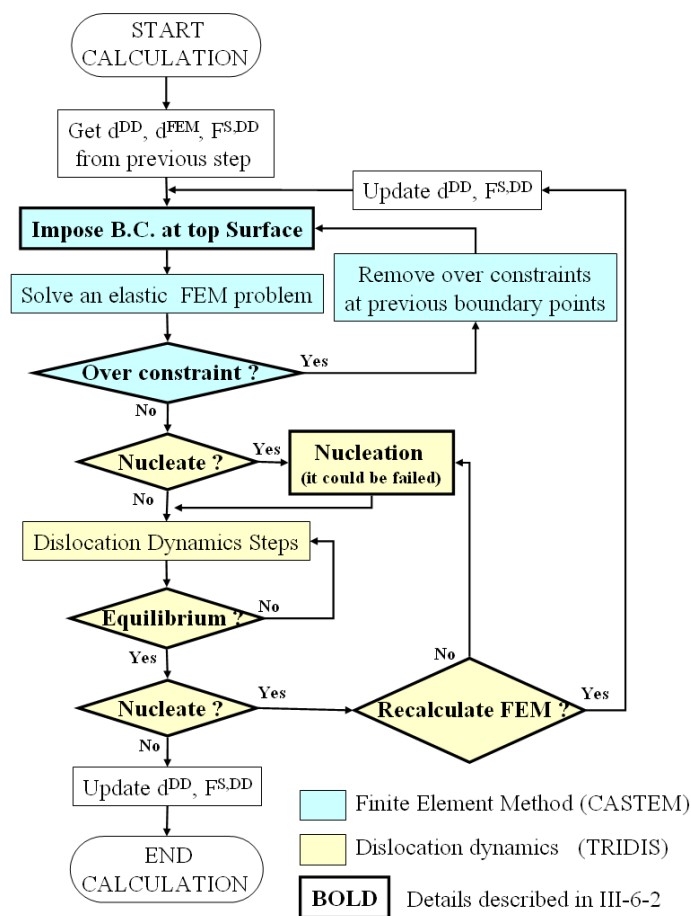
Figure III-6-6. Flow chart of calculation part of the main nanoindentation algorithm.

The TRIDIS calculation is starting with the elastic stress field calculated just before. The calculation is divided in two parts, the first one concerns nucleation of new dislocation loops and the second one deals with moving the dislocations within the elastic stress field.

At first, it is decided if nucleation of dislocation loops is needed or not. If it does, new dislocation loops are generated and the boundary conditions are updated. If no nucleation is

159

needed, the dislocations are moved other a few time steps within the elastic field. The dislocation motion is repeated until the dislocations all reach an equilibrium state. After this step the algorithm checks again if nucleation of new dislocation loops is needed or not. If it does not, the TRIDIS calculation is ended with recording the surface displacement and force field for the calculation of next step. If it does, the whole loop of TRIDIS calculation is repeated. Sometimes, it may be needed to repeat the FEM calculation during the nucleation process. In this case, the calculation is done from the beginning with the updated results from the TRIDIS calculations. Details about the boundary conditions on the top surface nodes, checking method of over constraint points and nucleation and equilibrium procedure for the TRIDIS calculation are described in the following paragraphs.

Boundary conditions on the contact nodes

Figure III-6-7 illustrates the boundary condition to apply on the nodes of the top surface in contact with the indenter. In the detection algorithm, we first need to compute the number of contact nodes and the corresponding amount of displacement to impose in order to fit with the geometry of the indenter.
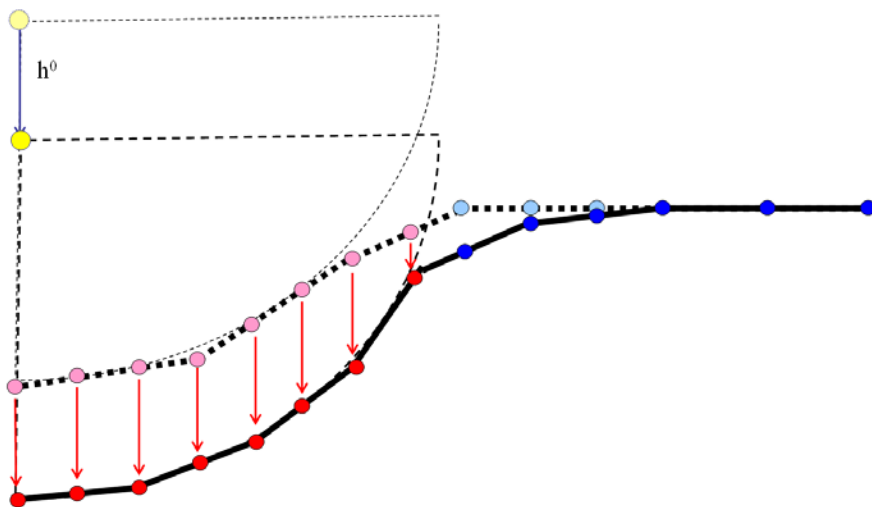
Figure III-6-7.   Boundary condition of top surface nodes corresponding to a spherical indentation.

A node is considered as a contact node if it is inside the indenter tip. Then the node should be forced to move down due to the action of the indenter tip. To do so, we have to impose displacement boundary conditions (Dirichlet conditions). The amount of displacement is calculated from the distance between the tip surface and the position of the node. Displacement is imposed along the indentation axis. The perpendicular displacements are let free. In practice,

we have programmed two geometries for the indenter, spherical and perfect cone. In this thesis, only results regarding the spherical tip will be given.

Checking over constraint points

The procedure used to find out the constraint points is shown in figure III-6.8.
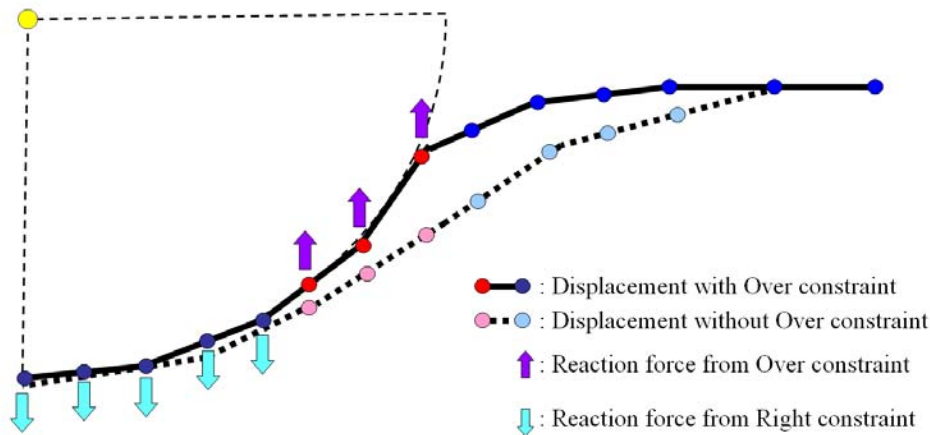

Figure III-6-8. Method used to find the over constraint points.

After any FEM calculation, a reaction force is obtained for each node for which the displacement was imposed. Normally, the direction of the reaction forces should be same as the direction of imposed displacement. Therefore, the direction of this reaction forces should be negative in regards to the surface normal direction. However, it may happen that the force direction is opposed because of the plastic displacement induced by the dislocations. The points which have a reaction force direction opposed to the indentation direction are the *over-constraint nodes*. In reality they should not be given an imposed displacement conditions because their stable positions are already below the indenter surface (see figure III-6-8).

Therefore, the direction of the reaction forces is checked after each FEM calculation. If some of the displacement imposed points have an opposite direction of reaction force, we recalculate the FEM solution without imposing the displacement on the over-constraint points. This checking routine is repeated until all of the constraint points have the same reaction force direction.

Validation test: fully elastic case

The boundary condition for nanoindentation simulation described above is now verified in the case of fully elastic material properties where the elastic modulus and Poisson ratio are 112000MPa and 0.34, respectively. Figure III-6-9 shows results of a (111) indentation using a spherical tip of radius 150nm
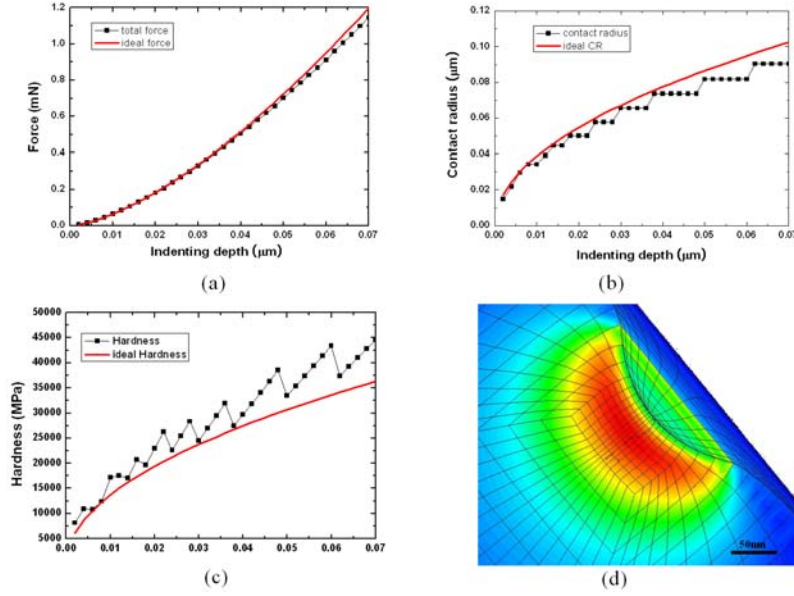
Figure III-6-9. The indentation results in case of elastic material indented with a spherical indenter (tip radius = 150nm) (a) applied force displacement curves (b) contact radius (c) hardness (d) stress distribution.

The force displacement curves, contact radius, hardness and Von Mises stress distributions with deformed shape are shown in (a), (b), (c) and (d) of the figure III-6-9, respectively. These results are now compared with theoretical predictions.

Theoretically, the force, contact radius and hardness during indentation by sphere indenter are estimated using the following equations:

$$P_{ind} = \frac{4}{3} E \sqrt{R_{ind}} x_{ind}^{3/2} \tag{III-6-1}$$

$$R_{cont} = \sqrt{R_{ind} x_{ind}} \tag{III-6-2}$$

$$H = \frac{P_{ind}}{\pi \times R_{cont}^2} = \frac{4}{3\pi} \sqrt{\frac{x_{ind}}{R_{ind}}} \tag{III-6-3}$$

Results show that the force computed by FEM using our algorithm for the detection of the contact nodes is about 5% lower than the theoretical expectations. In figure III-6-9 (b), the contact radius from the FEM calculations is slightly lower that the theoretical contact radius because of mesh effects. As a consequence, this increases the hardness value compared to the theoretical hardness as shown in figure III-6-9 (c). Discrepancies may come because we impose the surface displacement only through the surface normal direction. Because all of the surface nodes are free to move in the plane perpendicular to the surface normal direction, the surface

162

nodes can then penetrate into the indenter. This can reduce the applied force.

Although there are some differences between the FEM results and the theory, the discrepancies are quite reasonable (less than 5% on the loading curve). This validates the surface boundary conditions we described above and the proposed algorithm will be retained for the DD simulations.

Dislocation nucleation algorithm

Basically, the DD simulation starts the nanoindentation calculation without any dislocations inside the material. As said before, DD simulations can not predict the apparitions of new dislocations. This feature should be incorporated through rules that can emerge from experiments or atomic modeling. In this work we chose to get rid of the empirical assumptions and experimental fittings procedure. Thus all the information about the nucleation criterion comes from the molecular dynamics simulations described in section III-6.1.

A nucleation criterion should answer two questions:

(i) when the nucleation starts and finishes,

(ii) what are the shape and position of the new nucleated dislocation.

First part of the question is answered in figure III-6-10.

The master curve referred as the '*Nucleation criterion*' comes from the MD simulations results shown in figure III-6-1 (b). For a given indentation depth, when the loading force is found higher than the nucleation criterion, new dislocation loops are generated until the current point satisfies the nucleation criterion. After each nucleation stage, the indentation depth is increased because of the displacement field induced by the generated dislocation loops. The indentation force is once again compared to the value predicted by the nucleation criterion at the increased indentation depth. If the force is still higher than the nucleation criterion, other new dislocations are nucleated. Therefore, dislocations are introduced until the indentation force is lower than the nucleation criterion at the final updated indentation depth.

For the following, this nucleation process will be called as the *explicit method*. The advantage of this method is that it needs a single FEM calculation for one step of indentation simulation so that the total calculation time is reduced.
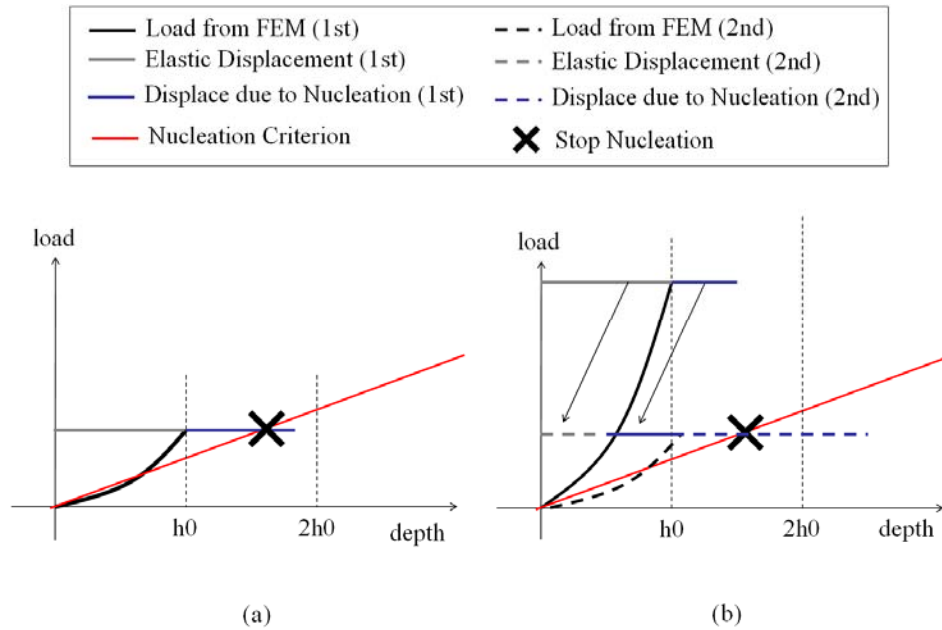
Figure III-6-10. Schematic description of the nucleation criterion (a) explicit method (b) quasi-implicit method

Sometimes, because the indentation force is very high in comparison to the nucleation criterion at the given depth, the nucleation criterion will never be satisfied just by increasing the total indentation depth as shown in figure III-6-10 (b). In that case, the explicit algorithm is changed into a *quasi-implicit method* aiming at reducing the indentation force. In that case, the FEM calculation is repeated using decreasing values for the indentation depth. These depths are calculated by subtracting the depth induced by the nucleated dislocation from the previous depth. After this recalculation of the force (which requires a new FEM solution), the explicit algorithm is applied to satisfy the nucleation criterion. Although, this quasi-implicit method will take more time than the explicit algorithm, this method will minimize the number of generated dislocations required to satisfy the nucleation criterion at a given step of calculation.

Figure III-6-11 answers the second question of the nucleation method: where the nucleation takes place and what is the shape of nucleated dislocation. Once again, answers are taken out from the molecular dynamics as shown in figure III-6-3. Generated Dislocation loops are prismatic loops made by edge dislocations on two slip systems sharing the same Burgers vector. In DD simulations however, one should conserve the material volume. Thus, two kinds of prismatic loops are simultaneously introduced: on interstitial prismatic loop inside the material and one vacancy prismatic loops located outside the material. The later is a virtual dislocation loop required to get a unique value of the dislocation displacement at the surface.
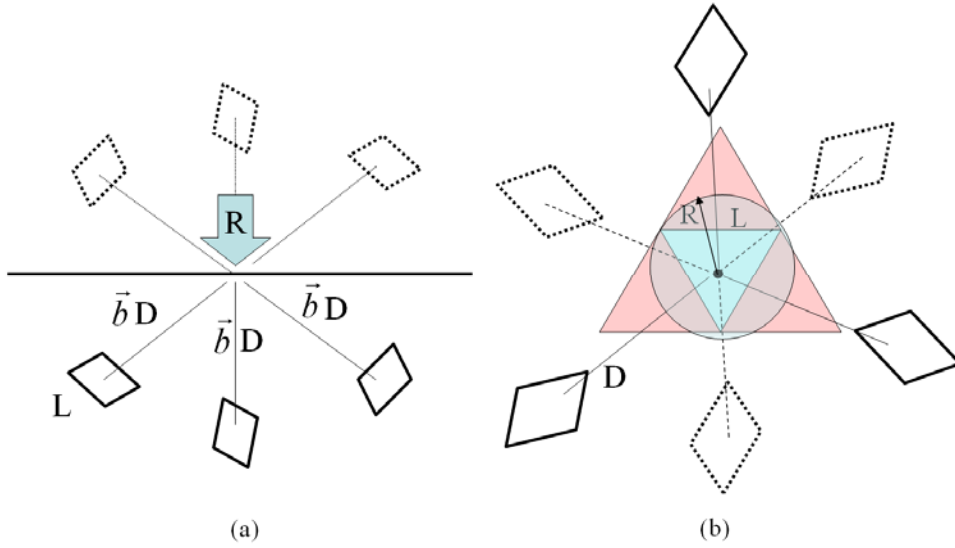
Figure III-6-11. Shapes of the nucleated prismatic loops (a) front section view (b) top view. Dashed lines show the virtual vacancy loops, continuous lines show the interstitial loops.

The position of the inner interstitial prismatic loops is defined by the distance from the center of indented surface through the Burgers vector direction of the given prismatic loop as shown in figure III-6-11 (a). The distance is calculated according to the position of maximum value of the resolved shear stress computed elastically (Hertz predictions):

$$d_{max} = 0.48 R_{cont} \qquad \text{(III-6-4)}$$

where the R_{cont}, and d_{max} are respectively the contact radius at the given indentation depth and distance to the surface computed along the indentation axis.

The size of the prismatic loop is also calculated from the contact radius using the following equation (see also figure III-6-11 (b)).

$$L_{loop} = \sin 60^o \times R_{cont} \qquad \text{(III-6-5)}$$

Checking equilibrium in dislocation dynamics

On one hand, the FEM simulation is based on static state, which implies an equilibrium state between the external forces and the internal material reactions. On the other hand, the DD calculation is based on succession of dynamic states (out of equilibrium), which induces instabilities and time dependencies. Therefore, for the coupling the two simulation method, FEM and dislocation dynamics, one of them should change its basal state. The easiest one is changing dislocation dynamics into static state, because repeating TRIDIS simulation with same external stress field will give the equilibrium state.

Figure III-6-12 illustrates the method developed to detect the equilibrium state during the DD calculation. The summation of the surface forces due to the dislocations inside the material, (black line), is used to check the equilibrium state. This force should be stable when all the dislocation segments will have reached an equilibrium position.
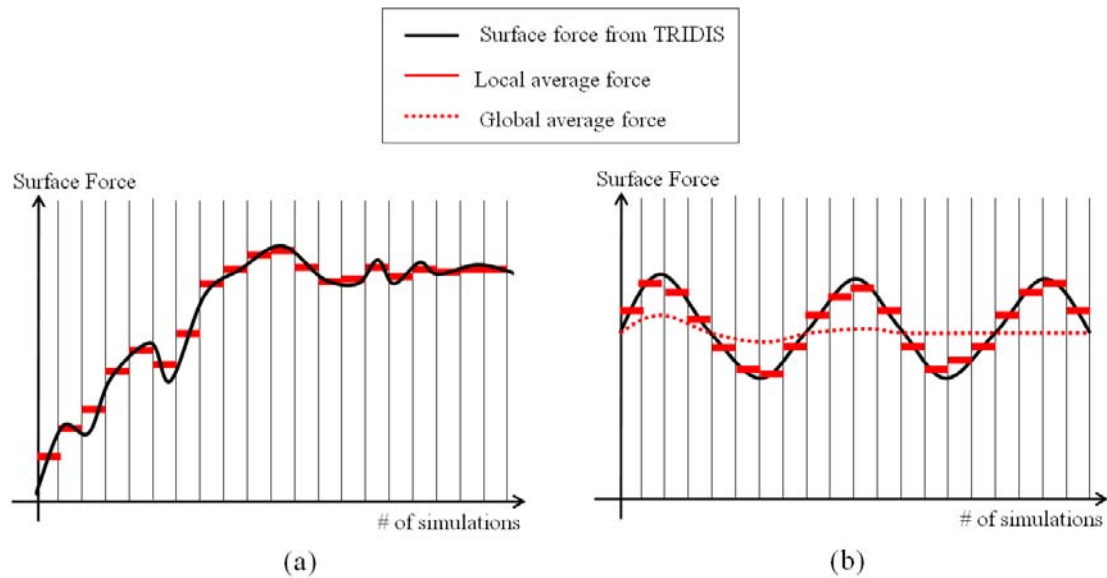

Figure III-6-12. Method used to check the equilibrium state during the DD calculations
(a) using local derivative (b) using global average

Two methods have been implemented. The first one is uses the *local derivative* as shown in figure III-6-12 (a). Firstly, the averaged surface force is calculated for every simulation set made from several calculations (red line in figure III-6-12 (a)). Then, the average value is compared with the one of the previous simulation step. If the differences do not exceed a given criterion, it is decided that the DD calculations have reached an equilibrium state.

Sometime, the equilibrium state can not be found because of the fluctuation as shown in figure III-6-12 (b). In that case the *global average* value is used in place of the local derivative. The average is obtained from integration of the surface forces curve (see dotted red line in figure III-6-12 (b)). When the global average value is stable, it is assumed that the DD calculations have reached an equilibrium state.

In the simulations presented below, a simulation set is composed of five DD steps. In practice, the local derivative procedure is first used. If the difference between two local averages is less than 2.0%, we assume the equilibrium state is reached. If not, the global average is computed and compared to the previous one. If the second difference between two global averages is less than 0.5 %, it is decided that the dislocations reached the equilibrium state. If both the

comparisons fail to detect the equilibrium state, the DD steps are repeated until one of the two criteria is satisfied.

6.3 Dislocations dynamics simulation of (111) nanoindentation in copper single crystal

<u>Mesh design</u>

Figure III-6-13 shows the mesh used for the nanoindentation simulations. The cross section of mesh is shown in figure III-6-13 (a). There are 5 by 5 coarse meshes. One mesh at the top center is divided into very fine meshes close to the contact regions. The radius and height of the bulk material is respectively 2μm, and 4μm. The length and height of fine mesh region is respectively set to 1.5 times and 3 times as long as the indenter radius (see figure III-6-12 (b)).
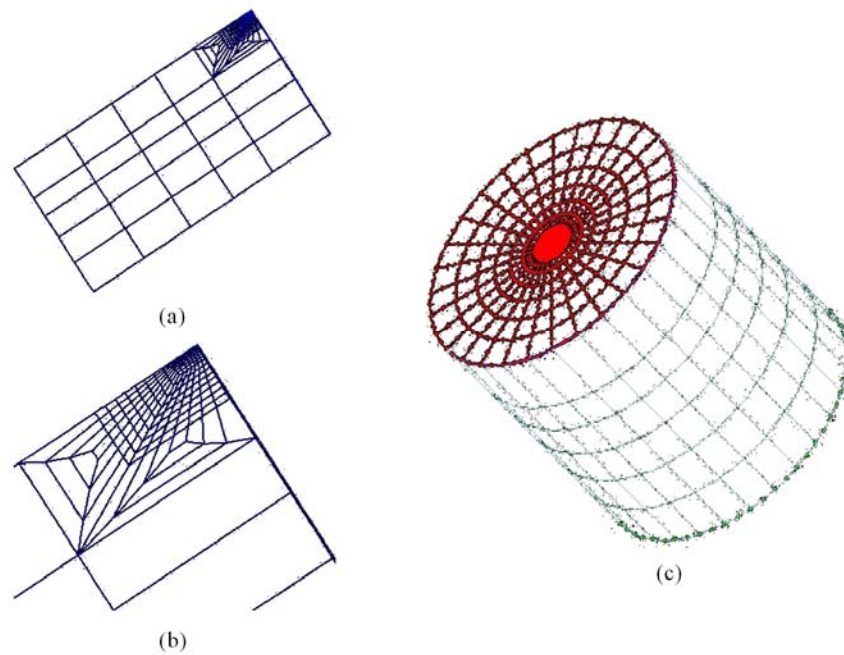
Figure III-6-13. FEM mesh used for the nanoindentation simulation
(a) Cross section of mesh (b) Zoom of the refined zone (c) 3D view of the entire mesh.

The fine mesh consists of three different parts. At the top center point, there is a squared fine mesh made of 64 elements. The length and height of this region is set to 0.5 times and 1 time as long as the indenter radius, respectively. Beside the square mesh region there are two trapezoid regions. These regions wrap the fine mesh in order to grow the mesh size. The 3D volume is obtained by rotating the cross section with 30 angular directional meshes as shown in figure III-

6-13 (c). The nodes at the top and bottom surfaces are picked for imposing the boundary conditions in the FEM calculations. They are represented as the red and green points in figure III-6-13 (c).

The general elastic properties selected to model copper material (here assumed to be isotropic) are 112000MPa for Young elastic modulus and 0.34 for Poisson ratio.

DD results: force, contact radius and hardness

Figure III-6-14 shows the results obtained from KTRIDIS in term of force, contact radius, hardness and displacement. Several unloading stages have been simulated at different indentation depth: 10nm, 30nm, 60nm and 100nm (see figure III-6-14 (a)). In figure III-6-14 (a), the total force is the summation of the elastic field and the dislocation field. The force criterion is the MD master curve shown in figure III-6-1 (b).
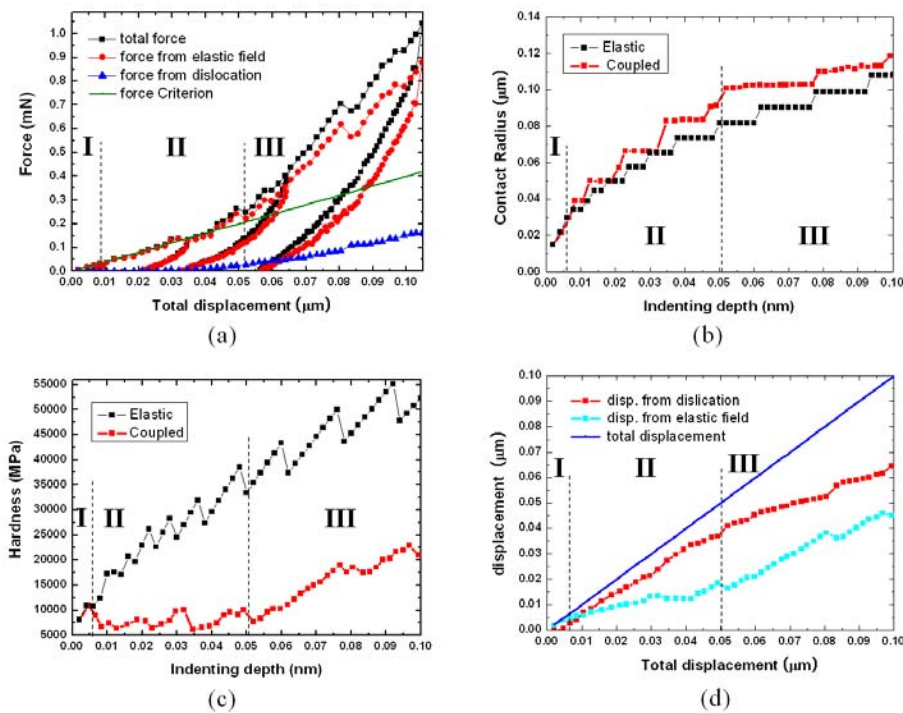
Figure III-6-14. DD simulation results .(a) force displacement curves, (b) contact radius vs. displacement, (c) hardness vs. displacement, (d) displacement fields

One can distinguish three periods in the loading curve of figure III-6-14 (a). During the first period (I), the total force only comes from the elastic field because there is no dislocation inside the material. The period ends at about 5nm indentation depth when the total force is high

enough to nucleate dislocation loops. Once, the total force is higher than the force criterion, dislocation loops are nucleated in the materials so that the total forces exactly follow the by force criterion. This corresponds to period (II). During this period the force computed from the dislocation fields starts to increase but the magnitude is very weak compared to the force of the elastic field. Period (III) starts after 50nm when the total force does not follow the force criterion anymore. During this stage, the slope of the loading curve is higher than the slope of the force criterion, and continuously increases with the indentation depth. At 100nm, the force coming from the dislocation field is reaches up to about 20% of the force of the elastic problem. This behavior appears when the dislocation density in the nucleation region is too high to allow introducing new dislocation loops. No loop is introduced in the simulation so that the force criterion cannot be fulfilled.

After the unloading, the remaining indentation depth is about half of the maximum depth. This means half of the depth is recovered. This will be discussed further in next paragraph.

The evolution of the contact radius with the indentation depth is given in figure III-6-14 (b). Results are compared to the contact radius obtained from FEM simulation in the case of a perfectly elastic material as shown in figure III-6-9 (b). During the first period, the two contact radii are the same, but the DD simulations give higher values of contact radius in the second and third period. This is due to the expansion of the dislocation loops inside the material which pile-up at the surface and increases the plastic zone size.

The evolution of the hardness is shown in figure III-6-14 (c). Generally, the hardness from sphere indenter test will increase with the indentation depth. If the material is fully elastic, the hardness is related to the square root of the depth as described in equation (III-6-3) and shown in figure III-6-9 (c). Here, in the case of DD simulations, the tendency of the hardness does not follow this general expectation. During the second period, the hardness is almost stable. It starts to increase with indentation depth only during the third period. The tendency of the increasing slope during the third period is quite similar to tendency that obtained for elastic materials. This shows that the indentation size effect may depend on the nucleation mechanism during the indentation. Although no final conclusion could be derived from this single DD simulation, one can however conclude that dislocation starvation decreases the indentation size effect.

The evolution of the indentation depth computed from the elastic and dislocation is given in figure III-6-14 (d) as functions of the total depth. During the first period, the total displacement just comes from the elastic field. During the second period, the displacement induced by the dislocation field increases with a stiff slope. This means that progressively, most of the indentation depth is given by the plastic displacement i.e. the nucleation and development of dislocation loops occurring during the second period. However, the slopes of the two kinds of displacement are changed in the third period. The slope of the elastic curve is still increasing

and that of the dislocations is decreased. This comes from the interruption of the new dislocation generation.

<u>Surface displacement distributions</u>

Figure III-6-15 shows the surface distribution of the different components of the displacement and the Von Mises stress obtained at 30nm indentation depth. The displacement computed from the elastic field is shown in figure III-6-15 (a). It displays a three-fold symmetry complimentary to that of the DD field given in figure III-6-15 (b).
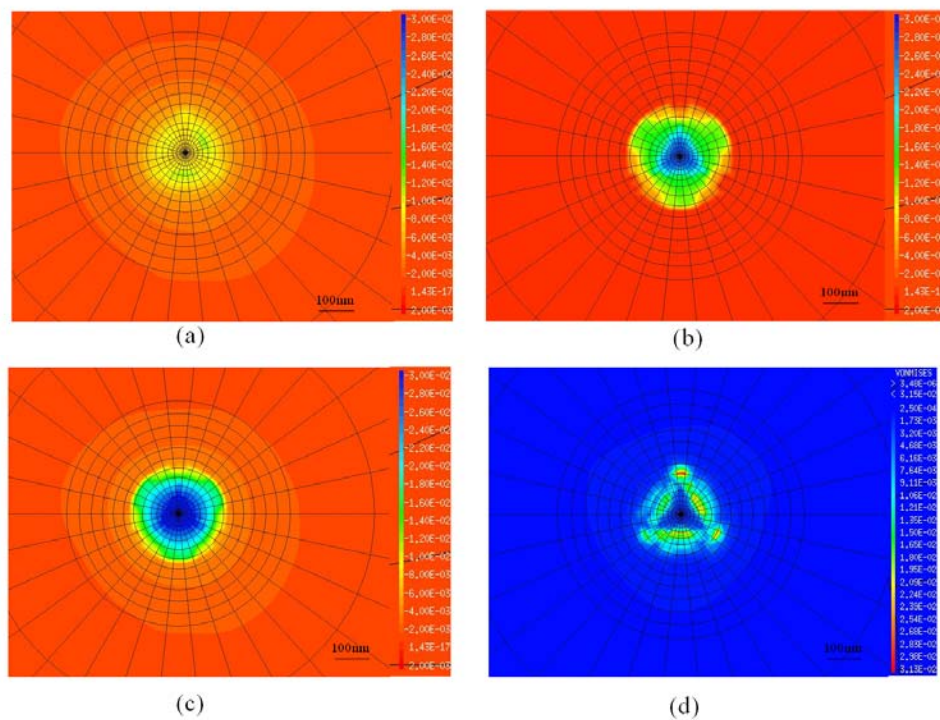
Figure III-6-15. Surface displacement distribution at 30nm indentation depth, (a) displacement from elastic field, (b) displacement from dislocation field, (c) total displacement, (d) Von Mises stress distribution due to elastic displacement.

These distribution shapes are similar to the shape of nucleated dislocation loops as obtained in MD (see figure III-6-3 and figure III-6-11 (b)). This shows that the displacement induced by the dislocation field is strongly related to the shape of the nucleated dislocation loops and this stands all along the indentation process. Let remember here that the cross-slip was not allowed in the present simulations so that the dislocation lines have less flexibility than in reality. Results may be different if cross-slip is accounted for, but today, there is no satisfactory cross-slip rules to implement in DD when the applied loading is as complex as in nanoindentation. Indeed, in

practice cross-slip rules refer to a given local stress and in nanoindentation this critical stress is always overcome so that cross-slip events are very easy.

The summation of the two kinds of displacements gives the total displacement distribution as shown in figure III-6-15 (c). The distribution shape is close to that coming from the dislocation. It means that most of the indentation displacement is accommodated by the dislocations. Globally this shape distribution is the closest to the actual shape of the spherical tip, as expected. The Von Mises stress distribution due to the elastic displacement field at the surface is shown in figure III-6-15 (d). This distribution reflects the shape of contact surface. The contact shape has again a three-fold symmetry and is similar to the region of maximum displacement from the elastic field. A popular assumption about contact surface during indentation is that the contact surface has a circular shape whose radius is the same as the contact radius. However, the DD simulation demonstrates that the contact surface does not include an inner triangular region centered on the indenter axis.

Evolution of the dislocation microstructure during indentation

Figure III-6-16 gives snapshots of the dislocation microstructure during indentation up to 100nm. Figure III-6-16 (a) shows the dislocations introduced just after the first nucleation process. There are three interstitial dislocation loops right below the surface and three vacancy virtual dislocation loops positioned outside the material. In figure III-6-16 (b)-(f), the virtual segments are not figured out. The shape is exactly the same as in figure III-6-11 (b). Once the dislocation loops are generated, they glide down along their own Burgers vector direction, and another set of dislocation loops is generated. At the beginning of indentation, dislocation nucleation and dislocation motion is repeated. See figure III-6-16 (b) for the dislocation microstructure obtained at 5nm indentation depth. The length of the generated loops increases with the contact radius. Consequently, the line tension of the edge segments forming the loops decreases with the penetration depth. On the other hand, the stress field at the location of the nucleated loops increases with the indentation depth. Thus, when the stress field at a given edge segment becomes higher than the line tension, each side of generated loops can act as a Frank-Read source and glissile loops are generated as shown in figure III-6-16 (c) which gives the microstructure obtained at a penetration depth of 10nm. Some parts of the glissile loops escape the material through the free and print slip lines on the indented surface.

171

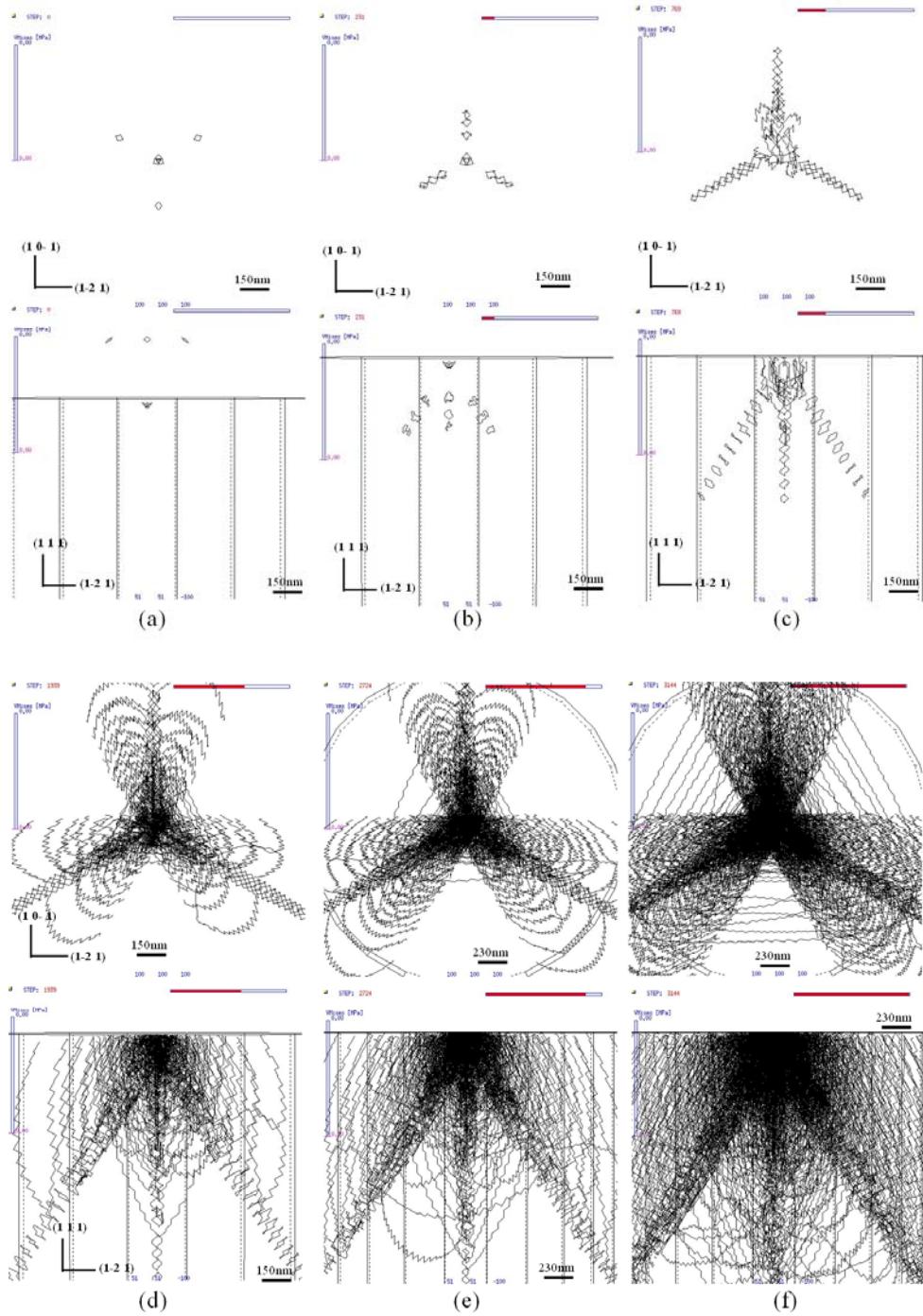Figure III-6-16. Dislocation microstructure obtained at different depths .

(a) just after the first generation of dislocation loops,

(b) after 5nm, (c) after 10nm, (d) after 30nm, (e) after 60nm (f) after 100nm indentation depth

For larger penetration depth, the dislocation lines are composed of two kinds of dislocation loops. One is prismatic loops as generated by the nucleation process. These loops are stacked on

their cylinder defined by their initial shape and the Burgers vector. The biggest prismatic loops are the closest to the indenter. The other type of dislocation is made of glissile loops generated from the side of the prismatic loops. Since one prismatic loop is composed by edge dislocations on two conjugate slip systems, it can make four glissile loops. Each glissile loop has ellipsoidal shape imposed by the effective stress. Increasing the penetration depth induce more and more glissile loop as shown in figure III-6-15 (d-f) for indentation depth varying from 30nm to 60nm and 100nm.

Residual displacement

Figure III-6-17 (a-f) shows the total surface displacement distribution before and after unloading from penetration depth of 10nm, 30nm and 60nm, respectively. The areas of deformed regions are dramatically reduced after unloading. It is found that 30 ~ 50 % of the deformation is recovered after unloading. This reflects the large elastic recovery found on the loading curves of figure III-6-14 (a).

During the unloading stage, the displacement induced by the elastic filed should be recovered, but the dislocations displacement can persist unless dislocations inside the material reach the free surface or disappear by annihilation. According to figure II-6-14(d), the displacement reached at 30nm and 60nm are about 25nm and 50nm, respectively. This is higher than the remaining displacement after unloading. Therefore, we can expect that some of dislocations are disappear during the unloading stage.

Figure III-6-18 shows the dislocation microstructure after unloading from 10nm, 30nm and 60nm indentation depth, respectively. Most of the glissile loops have disappeared. A possible explanation for this recovery is the effect of the image forces acting at the surface. They can easily attract the dislocations near to the surface and make them disappear. As shown in figure III-6-16 most of the glissile loops are located just below the surface, precisely where they are strongly affected by the image force.

In reality, this unloading process should also be influenced by cross-slip which could entangle the dislocations in the materials. Without cross slip, the dislocation motion is certainly more recoverable.
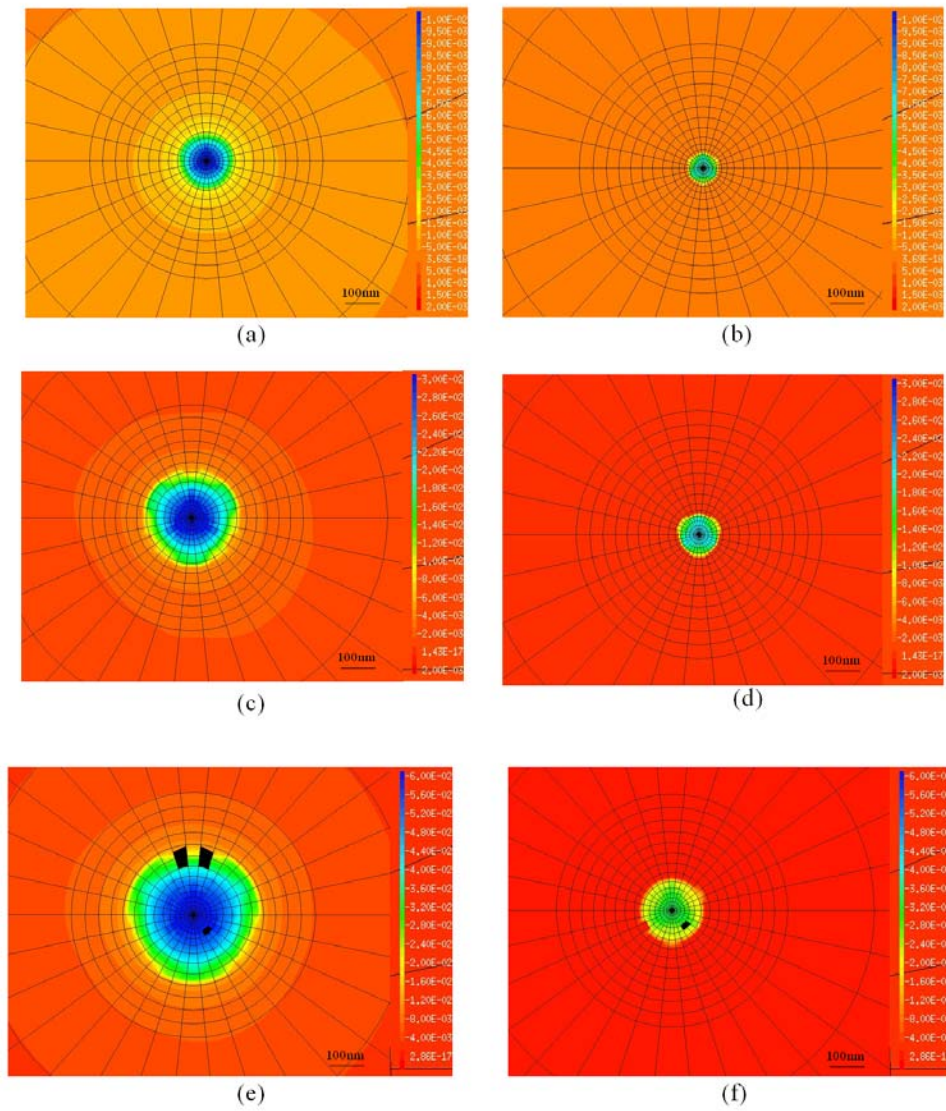
Figure III-6-17. Total surface displacement distribution before and after unloading
(a) before unloading from 10nm indentation depth, (b) after unloading from 10nm indentation
depth, (c) before unloading from 30nm indentation depth, (d) after unloading from 30nm
indentation depth, (e) before unloading from 60nm indentation depth (f) after unloading from
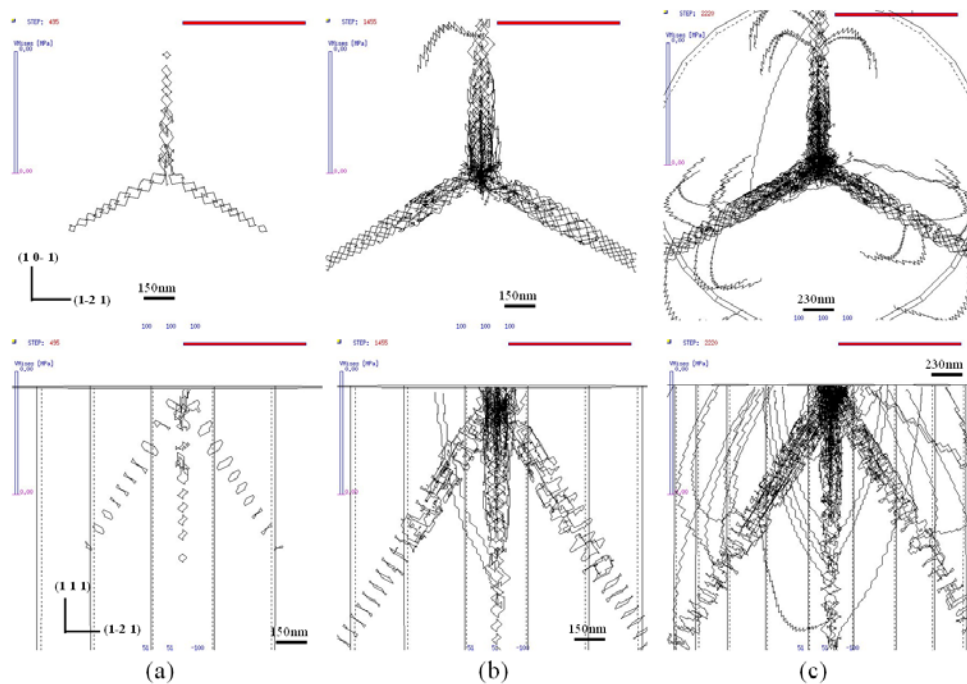60nm indentation depth

Figure III-6-18. The dislocation distributions with indentation depth after unloading state (a) after unloading from 10nm indentation depth, (b) after unloading from 30nm indentation depth, (c) after unloading from 60nm indentation depth

Concluding remarks on the dislocation dynamics simulation

It can be concluded from this study that indentation simulation can be done at the micron scale using KTRIDIS i.e. a coupling between DD and FEM. The coupled simulation can give not only the force displacement curves during loading and unloading stage, displacement distribution from elastic and dislocation fields but also the dynamic evolution of the dislocation microstructure during the indentation.

DD simulations can also be used to test the effect of parameters. Such a study has already been started and we have analyzed the effect of cross-slip, or tip geometry (cone and sphere). DD simulations also showed a new light on size effect which seems to be related to the nucleation mechanism.

6.4 Prospective

The DD code used in this thesis uses dislocation stress fields established for isotropic media. Therefore, this model should have lack of expecting accuracy for anisotropic material. It can now be improved using the expressions given in section II-3. However, the major problem is

that the computation time of DD code for anisotropic media is more than 100 times slower than the DD code for isotropic media. It means that one calculation for 100 nm indentation depth using the DD code for anisotropic media will need more than 100 months, which is totally out of range. Therefore, the DD code for anisotropic media should be improved in term of calculation speed for example by using parallel computing technique and probably on the recent graphic card: the general purpose graphic programmable units (GPGPU).

A key parameter of the DD simulation presented in this thesis is the nucleation process. In this study, the nucleation condition for indentation using spherical indenter is taken out from results of molecular dynamics. However, this could not apply to other geometry like conical indentations for example. One would need to realize similar MD simulations which are not available yet. In this case, an alternative way consists of using the experimental results to get the master curve and assuming a shape for the nucleated dislocations.

Practically, the ideal solution would be to define a nucleation procedure which does not depend upon any predefined criterion. One possibility is to express the number of dislocations to introduce as a function of the penetration depth according to the geometrically necessary dislocations needed to be introduced in order to accommodate the indentation at a given depth. Then, DD simulations would be predictive. Such an work is now in progress.

Finally, the dislocation dynamics model can calculate the local rotation during and after nanoindentation using the Nye tensor as described in equation (II-2-40). It would be interesting to compare the distributions of the local rotations obtained by DD and those obtained by crystal plasticity. The ultimate goal would be to compare both to experimental observation performed using electro back-scattered diffraction (EBSD) technique.

6.5 What should be retained from this section

- Coupling FEM, DD and MD
  - Stress field calculated by FEM
  - Dislocation movement calculated by DD
  - Nucleation criterion from MD
- Three phases during calculation
  - Phase 1 : Elastic phase
  - Phase 2 : Nucleation phase
    - Prismatic loops generated and move down through their burgers vector (dominant)
    - Glissile loops generated at the prismatic loops (weak)
    - Indentation Size effect obtained
  - Phase 3 : Dislocation evolution phase
    - No more nucleated prismatic loops
    - Glissile loops generated at the prismatic loops (dominant)
    - Dismissed indentation size effect

IV. Conclusion

The work presented in this document required several numerical developments performed at different scales: namely at the continuum level with finite element implantations and at the discrete sub-micron scale with dislocation dynamics simulations. The topics developed during this thesis are the following.

At the continuum level, a **dislocation density based crystal plasticity model** has been implanted into the ABAQUS user material subroutines for both implicit and explicit calculations. The codes have been validated in the case of tensile simulations with various kinds of loading orientations. It is shown that such a numerical tool can perfectly reproduce the deformation behavior expected for single crystals and give access to the evolution of the dislocation densities.

At the continuum scale again, size effect is addressed using a **simplified strain gradient model** which does not require any extra degree of freedom or any new governing equation. The proposed model calculates the extra stress due to the difference between global averaged strain and local strain. The model displays size effects in simple situations like simple shear and tensile loading condition.

At the discrete level, expressions for the **dislocation stress field of anisotropic media** are developed. The expression is compared to the isotropic case. Although, the formula for anisotropic media will be useful in the future for obtaining the exact internal stress field in the case of strongly anisotropic material such as copper single crystal, the computation time is too important to be used on single processors. This implantation in the dislocation dynamics code needs to be optimized on parallel computing.

Following these numerical developments, applications have been performed in the case of indentation loading conditions.

Nanoindentation experiments and FEM simulations have been performed with various surface orientations and initial dislocation densities. Results have been analyzed in term of load-depth curve, indentation stiffness, indentation modulus and contact area. The experimental results obtained with 4 different surface orientations are quantitatively reproduced by the crystal plasticity model provided the initial dislocation density and hardening parameters are adapted.

When applied to nanoindentation, the simplified strain gradient model was able to reproduce the well known indentation size effect (the hardness decreases when the penetration depth increases)

Finally, **dislocation dynamics simulations** of (111) nanoindentation have been performed using a code coupled to FEM routines needed to account for the complex boundary conditions. A nucleation criterion has been introduced to specify the shape, location and time of apparition of new dislocation during the indentation process. The criterion has been obtained from molecular dynamics simulations. Results of dislocation dynamics simulations have been analyzed in term of mechanical response, size effect and dislocation microstructure.

V. References

[Aif87] E. C. Aifantis, *International Journal of Plasticity*, **3** (1987), 211.

[Aif99] E. C. Aifantis, *International Journal for Fracture*, **95** (1999), 299.

[Asa] R. J. Asaro, *Advances in Applied Mechanics*, 23, San Diego: Academics Press.

[Ash70] M. F. Ashby, *Phil. Mag.*, **21** (1970), 399.

[AB00] A. Acharya, J. L. Bassani, *J. Mech. Phys. Solids*, **48** (2000), 1565.

[ABA04] ABAQUS version 6.5, Analysis User's manual, Hibbitt, Karlsson and Sorensen, Pawtucket, RI, 2004

[ACO08] J. Alcala, O. Casals, J. Ocenasek, *Journal of the Mechanics and Physics of Solids*, **56** (2008), 3277.

[AG90] R. J. Amodeo, N. M. Ghoniem, *Phys. Rev.*, **41** (1990), 6958.

[AHB73] P. Asaro, J. Hirth, D. Barnett, J. Lothe, *Phys. Stat. Sol. (b)*, **60** (1973), 261.

[AN85] R.J. Asaro and A. Needleman, *Computers and Structures*, **18** (1985), 923.

[AR77] R. J. Asaro and J. R. Rice, *J. Mech. Phys. Solid*, **25** (1977), 309.

[AT65] A. G. Atkins, D. Tabor, *Journal of Mechanics and Physics of Solids*, **13** (1965), 149.

[Bar72] D. Barnett, *Phys. Stat. Sol. (b)*, **49** (1972), 741.

[Bas90] J. L. Bassani, *Appl. Mech. Rev.*, **45** (1990), 320.

[Bro67] L. Brown, *ibid.*, **15** (1967), 363.

[Bur39] J.M. Burgers, *Proc. Kon. Ned. Akad. Wetenschap.*, **42** (1939), 378.

[BAS75] S. I. Bulychev, V. P. Alekin, M. Kh. Shorshorov, A. P. Ternovskii, G. D. Shnyrez, *Zavod. Lab.*, **41** (1975), 1137.

[BB33] W.H. Bragg and W. L. Bragg, *The Crystalline State*, London : Bell, 1933.

[BBS80] D. Bacon, D. Barnett, R. Scattergood, *Prog. Mater. Sci.*, **23** (1980), 51.

[BFN93] A. F. Bower, N. A. Fleck, A. Needleman, N. Ogbonna, *Proc. R. Soc. Lond. A*, **441** (1993), 97.

[BK04] F. M. Borodich, L. M. Keer, *Int. J. Solids Struct*, **41** (2004), 2479.

[BKA89] S. Brown, K. Kim and L. Anand, *Int. J. Plasticity*, **5**(1989), 95.

[BKA92] C. A. Bronkhorst, S.R. Kalidindi and L. Anand, *Phil. Trans. R. Soc. Lond A*, **341** (1992), 443.

[BS95] S. Biwa, B. Storakers, *J. Mech. Phys. Solids*,**43** (1995), 1303.

[BSF03] J. L. Bucaille, S. Stauss, E. Felder, J. Michler, *Acta Mater.*, **51** (2003), 1663.

[BSS04] J. L. Bucaille, S. Stauss, P. Schwaller, J. Micher, *Thin Solid Films*, **447-448** (2004), 239.

[BTF01] P. Balland, L. Tabourot, M. Fivel, *J. Phy.*, **4** (2001), 381.

[BW91] J. L. Bassani and T. Y. Wu, *Proc. R. Soc. Lond. A*, **435** (1991), 21.

[Cha06] L. Charleux, *PhD These*, Institut National Polytechnique de Grenoble (2006).
[CAS07] CASTEM 2007,

[CC03] T. W. Capehard, Y.T. Cheng, *J. Mater Res*, **18** (2003), 827.
[CDS03] N. Chollacoop, M. Dao, S. Suresh, *Acta Mater*, **51** (2003), 3713.
[CFP05] S. Catalao, X. Feaugas, Ph. Pilvin and M.-Th. Cabrillat, *Materials Science and Engineering A*, **400-401** (2005), 349.
[CL04a] Y. P. Cao, J. Lu, *Acta Mater.*, **52** (2004), 1143.
[CL04b] Y. P. Cao, J. Lu, *J. Mater. Res.*, **19** (2004), 1703.
[CO92] A. M. Cuitino and M. Ortiz, *Modelling Simul. Mater. Sci. Eng.*, **1** (1992) 225.
[COA07] O. Casals, J. Ocenasek, J. Alcala, *Acta Mater.* , **55** (2007), 55.
[CSK90] R. C. Cammarata, T. E. Schlesinger, C. Kim, S. B. Qadri, A. S. Edelstein, *Appl. Phys. Lett*, **56** (1990), 1862.
[CV01] X. Chen, J. J. Vlassak, *J. Mater. Res.*, **16** (2001), 2974.

[Dép04] C. Déprés, *PhD These*, Institut National Polytechnique de Grenoble (2004).
[Doe87] M. F. Doerner, *PhD thesis*, Stanford University (1987).
[DCV01] M. Dao, N. Chollacoop, K. J. Van Vliet, T. A. Venkatesh, S. Suresh, *Acta Mater*, **49** (2001), 3899.
[DF02] L. Dupuy and M. Fivel, *Acta Mater.*, **50** (2002), 4873.
[DKH06] B. Devincre, L. Kubin and T. Hoc, *Scripta Mater.*, **54** (2006), 741.
[DN86] M. F. Doerner, W. D. Nix, *J. Mater. Res.*, **1** (1986), 601.
[DNF93] M. S. De Guzman, G. Neubauer, P. Flinn, W. D. Nix, *Materials Research Symposium Proceedings*, **308** (1993), 613.
[DY03] A. DiCarlo, H. T. Y. Yang, *J. Mater Res.*, **18** (2003), 2068.

[EG07] B. Eidel, F. Gruttmann, *Comput. Mater. Sci.*, **39** (2007), 172.
[EM67] U. Essmann and H. Mughrabi, *Philosophical Magazine A*, **40** (1967) no 6, 731.
[ER00] J.A. Ewing and W.Rosenhain, *Phil. Trans. R. Soc.*, **193** (1900), 353.
[ES02] A. A. Elmustafa, D. S. Stone, *Acta Mater.*, **50** (2002), 3641.
[ES03] A. A. Elmustafa, D. S. Stone, *J. Mech. Phys. Solids*, **51** (2003), 357.
[EVK01] G. E. Exadaktylos, I. Vardoulakis, S. K. Kourkoulis, *International Journal of Solids and Structures*, **38** (2001), 4091.

[Fis02] A. Fischer-Cripps, *Nanoindentations*, Spring-Verlag, New York, 2002.

[Fiv97] M. Fivel, *PhD These*, Institut National Polytechnique de Grenoble (1997).

[For08] S. Forest, *CISM lecture Udine*, Italy, 2007

[FBC00] S. Forest, F. Barbe and G. Caillentaud, *International Journal of Solids and Structures*, **37** (2000), 7105.

[FBZ80] P. Franciosi, M. Berveiller and A Zaoui, *Acta Metall.*, **28** (1980), 273.

[FCS97] S. Forest, G. Cailletaud, R. Sievert, *Arch. Mech.*, **49** (1997), 705.

[FDS03] D. Feichtinger, P. M. Derlet, H. V. Swygenhoven, *Phys. Rev. B.*, **67** (2003), 024113.

[FF04] M. Fivel, S. Forest, *Techniques de L'ingénieur M4017*, 2004

[FH97] N. A. Fleck, J. W. Hutchinson, *Advances in Applied Mechanics*, **33** (1997), 295.

[FH01] N. A. Fleck, J. W. Hutchinson, *J. Mech. Phys.. Solids*, **49** (2001), 2245.

[FMA94] N.F. Fleck, G. M. Muller, M.F. Ashby, J.W. Hutchinson, *Acta Mater.*, **42** (1994), 475.

[FRC98] M. C. Fivel, C. F. Robertson, G. R. Canova, L. Boulanger, *Acta Mater.*, **46**(1998), 6183.

[FRS04] Z. Fan, J. Y. Rho, J. G. Swadener, *J. Mater. Res.*, **19** (2004), 114.

[FS93] J. S. Field, M. V. Swain, *J. Mater. Res.*, **8** (1993), 297.

[FS95] J. S. Field, M. V. Swain, *J. Mater. Res.*, **10** (1995), 101.

[FSA02] S. Forest, R. Sievert, E. C. Aifantis, *Journal of the Mechanical Behavior of Materials*, **13** (2002), 219.

[FVC97] M. Fivel, M. Verdier, G. Canova, *Mater. Sci. Engng A*, **234-236** (1997), 923.

[FWK89] L. J. Farthing, T. P. Weihs, D. W. Kisker, J. J. Krajewski, M. F. Tang, D. A. Stevenson, *Mater. Res. Soc. Symp. Proc.*, **130** (1989), 123.

[FWT01] M. Futakawa, T. Wakui, Y. J. Tanabe, I. Ioka, *Mater. Res.*, **16** (2001), 2283.

[Gia02] A. E. Giannakopoulos, *Int. J. Solids Struct.*, **39** (2002), 2495.

[Gur02] M. E. Gurtin, *J. Mech. Phys. Solids*, **50** (2002), 5.

[GHN99] H. Gao, Y. Huang, W.D. Nix, J.W. and Hutchinson, *J. Mech. Phys. Solids*, **47**(1999), 1239.

[GJS06] X. -L. Gao, X. N. Jing, G. Subhash, *Int. J. Solids. Struct*, **43** (2006) 2193.

[GLV94] A. E. Giannakopoulos, P. -L. Larsson, R. Vestergaard, *Int. J. Solids Struct.*, **31** (1994), 2679.

[GS90] A. E. Giannakopoulos, S. Suresh, *Scripta Mater.*, **40** (1990), 1191.

[GS99] A. E. Giannakopoulos, S. Suresh, *Acta Mater.*, **47** (1999), 2153.

[Hil62] R. Hill, *J. Mech. Phys. Solids*, **10** (1962), 1.

[Hil66] R. Hill, *J. Mech. Phys. Solid*, **14** (1966), 99.

[HGN00] Y. Huang, H. Gao, W. D. Nix, J. W. Hutchinson, *J. Mech. Phys. Solids*, **48** (2000), 99.

[HGW03] X. Han, N. M. Ghoniem, Z. Wang, *Philosophical Magazine*, **83** (2003), 3705.

[HL82] J. P. Hirth, J. Lothe, *Theory of dislocations Second edition*, John Wiley & Sons, New York, 1982

[HPO01] E. G. Herbert, G. M. Pharr, W. C. Oliver, B. N. Lucas, J. L. Hay, *Thin Solid Films*, **398** (2001), 331.

[HR72] R. Hill and J. R. Rice, *J. Mech. Phys. Solid*, **20** (1972), 401.

[HR82] R. Hill and J. R. rice, *J. Mech. Phys. Solid*, **30** (1982), 5.

[HS77] K. S Havner and A. H. Shlaby, *Proc. R. Soc. Lond A*, **358** (1977), 47.

[HSZ89] R. Hill, B. Storakers, A. B. Zdunek, *Proc. R. Soc. Lond. A*, **423** (1989), 301.

[HT99] N. Huber, C. Tsakmakis, *J. Mech. Phys. Solids*, **47** (1999), 1569.

[IO68] V. Indenbom, S. Orlov, *J. Appl. Math. Mech.*, 32 (1968), 414.

[Joh70] K. L. Johnson, *J. Mech. Phys. Solids*, **18** (1970), 115.

[Joh85] K. L. Johnson, *Contact Mechanics*, Cambridge University Press, Cambridge, 1985.

[JB67] P. J. Jackson and Z. S. Basinski, *Can. J. Phys.*, **45** (1967), 707.

[Koc70] U. F. Kocks, *Metall. Trans.*, **1** (1970), 1121.

[Koc94] U. F. Kocks, *Materials Science and Engineering A*, **175** (1994), 49.

[KB66] U. F. Kocks and T. J. Brown*, Acta Metall.*, **14** (1966), 87.

[KBA92] S.R. Kalidindi, C.A. Bronkhorst and L. Anand, *J. Mech. Phys. Solids*, **40** (1992), 537

[KCC92] L.P. Kubin, G. Canova, M. Condat, B. Devincre, V. Pontikis, Y. Brechet, *Diffusion Defect Data - Solid St. Data B*, **23-24** (1992), 455.

[KDH08] L. Kubin, B. Devincre and T. Hoc, *Acta Mater.*, **56** (2008), 6040

[KLB08] G. Kermouche, J. L. Loubet, J. M. Bergheau, *Mechanics and Materials*, **40** (2008), 271

[KM01] S. Kucharski, Z. Mroz, *Mater. Sci. Eng. A*, **318** (2001), 65.

[KPH98] C. L. Kelchner, S. J. Plimpton, J. C. Hamilton, *Phys. Rev. B*, **58** (1998), 11085.

[KPM06] D. Kiener, R. Pippan, C. Motz, H. Kreuzer, *Acta. Mater.*, **54** (2006), 2801.

[KWD01] M. E. Kassner, M. A. Wall and M. A. Delos-Reyes, *Materials Science and Engineering A*, **317** (2001), 28.

[Lak86] R. S. Lakes, *International Journal of Solids and Structures*, **22** (1986), 56.

[Len896] P. Lenard, *Hertz's Miscellaneous Papers*, Macmillan, London, 1896.

[Li65] J. C. M. Li, *Acta Metall.*, **13** (1965), 931.

[Lot67] J. Lothe, *Phil. Mag.*, **15** (1967), 353.

[LBY05] Y. Liu, B. Wang, M. Yoshino, S. Roy, H. Lu, R. Komanduri, *J. Mech. Phys. Solids*, **53** (2005), 2718.

[LGH93] H. Li, A. Ghosh, Y. H. Han, R. C. Bradt, *J. Mater. Res.*, **8** (1993), 1028.

[LPK05] Y. M. Lee, J. Y. Park, S. Y. Kim, S. Jun, S. Im, *Mech. Mater.*, **37** (2005), 1035.

[LSB02] H. C. Lichtenegger, T. Schoberl, M. H. Bartl, H. Waite, G. D. Stuchy, *Science*, **298** (2002), 389.

[LSG96] P. -L. Larsson, E. Soderlund, A. E. Giannakopoulos, D. J. Rowcliffe, R. Vestergaard, *Int. J. Solids Struct.*, **33** (1996), 221.

[LYC03] D. C. C. Lam, F. Yang, A. C. M. Chong, J. Wang, P. Tong, *Journal of the Mechanics and Physics of Solids*, **51** (2003), 1477.

[LZF03] E. T. Lilleodden, J. A. Zimmerman, S. M. Foiles, W. D. Nix, *J. Mech. Phys. Solids*, **51** (2003), 901.

[Man73] J. Mandel, *Int. J. Solids Structures*, **9** (1973), 725.

[Mec99] H. Mecking, *Mater. Sci. Eng.*, **7** (1999), 669.

[Mot56] B. W. Mott, *Micro-indentation Hardness Testing*, Butterworths, Guildeford, 1956.

[Mug04] H. Mughrabi, *Mater. Sci. Eng. A*, **387-389** (2004), 209.

[Mur63] T. Mura, *Phil. Mag.*, **8** (1963), 843.

[Mur87] T. Mura, *Micromechanics of Defects in Solids* , Dordrecht, Martinus Nijhoff, 1987.

[MA91] H.-B. Muhlhaus and E. C. Aifantis, *International Journal of Solids and Structures*, **28** (1991), 845.

[MA03] M. Mata, J. Alcala, *J. Mater. Res.*, **18** (2003), 1705.

[MA04] M. Mata, J. Alcala, *J. Mech. Phys. Solids*, **52**(2004) 145.

[MAA02] M. Mate, M. Anglada, J. Alcala, *J. Mater. Res.*, **17** (2002), 964.

[MAS04] R. Mulford, R. J. Asaro, R. J. Sebring, *J. Mater. Res.*, **19** (2004), 2641.

[MAS06] A. M. Minor, S. A. S. Asif, Z. W. Shan, E. A. Stach., E. Cyrankowski, T. J. Wyrobek, O. L. Warren, *Nat. Mater.*, **5** (2006), 697.

[MC91] L. Meric and G. Cailetaud, *J. Eng. Mater. Tech.*, **113** (1991) 171.

[MC95] Q. Ma, D. R. Clarke, *J. Mater. Res.*, **10** (1995), 853.

[MCA06] M. Mate, O. Casale, J. Alcala, *Int. J. Solds. Struct.*, **43** (2006), 2193.

[ME68] R. D. Mindlin, N. N. Eshel, *Int. J. Solids Struct.*, **4** (1968), 109.

[MF99] S. D. Mesarovic, N. A. Fleck, *Proc. R. Soc. Lond. A*, **455** (1999), 2707.

[MK81] H. Mecking and U. F. Kocks, *Acta Metall.*, **29** (1981), 1865.

[ML70] H. Mecking and K. Lucke, *Scripta Metall.*, **4** (1970) no 6, 427.

[MM76] T. Mura, T. Mori, *Phil. Mag.*, **33** (1976), 1021.

[MY03] X. L. Ma, W. Yang, *Acta Mech. Sin.*, **19** (2003), 485.

[Nie] remerciements au Prof. M. Niewczas, McMaster Uni. Pour la provision de monocristaux de feu Prof. Z. S. Basinski

[Nye53] J. F. Nye, *Acta Metall.*, **1** (1953), 153.

[NEB02] A. Nayebi, A. R. El, O. Bartier, G. Mauvoisn, *Mech. Mater.*, **34** (2002), 243.

[NG98] W. D. Nix and H. Gao, *J. Mech. Phys. Solids*, **46** (1998), 411.

[NK66] Y. Nakada and A. S. Keh, *Acta Metall.*, **14** (1966), 961.

[Oha87] T. Ohashi, *Transactions of the Japan Institute of Metals*, **28** (1987), 906.

[OP92] W. C. Oliver, G. M. Pharr, *J. Mater. Res.*, **7** (1992), 1564.

[Pol22] V. M. Polanyi, *Naturwissenschaften*, **10** (1922), 411.

[PAF96] W. J. Poole, M. F. Ashby, N. A. Fleck, *Scripta Mater.*, **34** (1996), 559.

[PAN83] D. Pierce, R. J. Asaro and A. Needleman, *Acta. Metall.*, **31** (1983), 1951.

[PHO83] J. B. Pethica, R. Hutchings and W. C. Oliver, *Phil. Mag. A*, **48** (1983), 593.

[PK50] M.O. Peach, J. S. Koehler, *Phys Rev.*, **80** (1950), 436.

[POB92] G. M. Pharr, W. C. Oliver, F. R. Brotzen, *J. Mater. Res.*, **7** (1992), 613.

[PT79] J. B. Pethica, D. Taylor, Surf. *Sci.*, **89** (1979), 182.

[RKC65] B. Ramaswami, U. F. Kocks and B. Chalmers, *Trans. Metall. Soc. AIME*, **233** (1965), 927.

[RMP07] M. Rester, C. Motz, R. Pippan, *Acta Mater.*, **55** (2007), 6427.

[RMP08] M. Rester, C. Motz, R. Pippan, *Scripta Mater.*, **59** (2008), 742.

[RZH98] M. Rhee, H. Zbib, J. Hirth, H. Huang, T. Diaz de la Rubia, *Modelling Simulation Mater. Sci. Engng.*, **6** (1998), 467.

[Sam86] L. E. Samuels, *Microindentation Techniques in Materials Science and Engineering*, ASTM STP 889, Philadelphia: ASTM, 1986.

[Sch24] E. Schmid, *Proc. Int. Congr. Appl. Mech. (Delft)*, (1924), 342.

[Sch99] K. Schwarz, *J. appl. Phys.*, **85** (1999), 108.

[Sci] Scilab, logiciel © INRIA-ENPC.

[Shi04] C. S. Shin, *PhD These*, Institut National Polytechnique de Grenoble (2004).

[Sne65] I. N. Sneddon, *Int. J. Eng. Sci.*, **3** (1965), 47.

[SE98] J. S. Stolken, A. G. Evans, *Acta Mater.*, **46** (1998),411.

[SF99] J. Y. Shu, N. A. Fleck, *J. Mech. Phys. Solids*, **47** (1999), 297.

[SFV01] J. Y. Shu, N. A. Fleck, E. Van der Giessen, A. Needleman, *Journal of the Mechanics and Physics of Solids*, **49** (2001), 1361.

[SL04] Y. L. Shen, R. W. Leger, *J. Mech.*, **20** (2004), 1.

[SM06] D. Saraev, R. E. Miller, *Acta Mater.*, **54** (2006), 33.

[SMC05] B. Shiari, R. E. Miller, W. A. Curtin, *J. Eng. Mater. Technol. Trans. ASME*, **127** (2005), 358.

[SP01] J. G. Swadener, G. M. Pharr, *Philos. Mag. A*, **81** (2001), 447.

[SP04] N. Schwarzer, G. M. Pharr, *Thin Solid Films*, **469-470** (2004), 194.

[SS41] I.S. Sokolnikoff and E.S. Sokolnikoff, *Higher Mathematics for Engineers and Physicists*, McGraw-Hill, New York, 1941.

[ST61] N. A. Stilwell, D. Tabor, *Proc. Phys. Soc.*, **78** (1961), 169.

[SWB93] N. A. Stelmashenko, M. G. Walls, L. M. Brown, Y. V. Milman, *Acta Metall.*, **41** (1993), 2855.

[Tab48] D. Tabor, *Proc. R. Soc. Lond. A*, **332** (1948), 247.

[Tab51] D. Tabor, *The Hardness of Metals*, Clarendon Press, Oxford, 1951.

[Tay34] G. I. Taylor, *Proc. Roy. Soc.* A, **165** (1934), 362.

[Tay38] G. I. Taylor, *J. Inst. Metals*, **62** (1938), 307.

[Teo75] C. Teodosiu, *Eng. Trans.*, **23** (1975), 157.

[TE23] G. I. Taylor and C. F. Elam, *Proc. Roy. Soc. A*, **102** (1923), 647.

[TE25] G. I. Taylor and C. F. Elam, *Proc. Roy. Soc. A*, **108** (1925), 28.

[TF97] L. Tabourot, M. Fivel, E. Rauch, *Mater. Sci. Eng. A*, **234-236** (1997) , 639.

[TH98] C. Teodosiu and Z. Hu, *Proceedings of the 9th Riso International Symposium on Materials Science* (1998), 149.

[TP04] B. Taljat, G. M. Pharr, *International Journal of Solids and Structures*, **41** (2004), 3891.

[TRI09] TRIDIS version 2.21, CASTEM 2009

[TS76] C. Teodosiu and F. Sidoroff, *International Journal of Engineering Science*, **41** (1976), 713.

[TS81] D. M. Turley, L. E. Samuels*, Metallography*, **14** (1981), 275.

[TS07] T. Tsuru, Y. Shibutani., *Phys. Rev. B*, **75** (2007), 035415.

[TZK98] B. Taljat, T. Zacharia, F. Kosel, *Int. J. Solids Struct.*, **35** (1998), 4411.

[VCB03] J. J. Vlassak, M. Ciavarella, J. R. Barber, X. Wang, *J. Mech. Phys. Solids*, **51** (2003), 1701.

[VFG98] M. Verdier, M. Fivel, I. Groma, *Modelling Simulation Mater. Sci. Engng.,* **6** (1998),

755.

[VN93]J. J. Vlassak, W. D. Nix, *Phil. Mag. A*, **67** (1993), 1045.

[VN94] J. J. Vlassak, W. D. Nix, *J. Mech. Phys. Solids*, **42** (1994), 1223.

[Wen87] G. J. Weng*, Int. J. Plast.*, **3** (1987), 315.

[Wil66] J. R. Willis, *J. Mech. Phys. Solids*, **14** (1966), 163.

[Wil70] J. Willis, *Phil. Mag.*, **21** (1970), 931.

[Wit60] R. de Wit, *Solid State Phys.*, **10** (1960), 249.

[Wit67] R. de Wit, *Phys. Stat. Sol.*, **20** (1967), 567.

[WRK04] Y. Wang, D. Raabe, C. Kluber, F. Roters, *Acta Mater.*, **52** (2004), 229.

[XH96] Z. C. Xia, J. W. Hutchinson, *Journal of the Mechanics and Physics of Solids*, **10** (1996), 1621.

[YKJ04] J. H. Yoon, S. J. Kim, H. Jang, *Mater. Sci. Forum*, **449-452** (2004), 89.

[YL81] J. F. C. Yang, R. S. Lakes, *Journal of Biomechanical Engineering*, **103** (1981), 275.

[ZPV01] A. Zervos, P. Papanastasiou, I. Vardoulakis, *International Journal of Solids and Structures*, **38** (2001), 5081.

[ZRR08] N. Zaafarani, D. Raabe, F. Roters, S. Zaefferer, *Acta Mater.*, **56** (2008), 31.

[ZRS06] N. Zaafarani, D. Raabe, R. N. Singh, F. Roters, S. Zaefferer, *Acta Mater.*, **54** (2006), 1863.

[ZVO04] J. Zhu, K. J. Van Vliet, S. Ogata, S. Yip, S. Suresh, *J. Mech. Phys. Solids*, **52** (2004), 691.